multi-Risk sciEnce for resilienT commUnities undeR a changiNgclimate

Codice progetto MUR: **PE00000005** – CUP LEAD PARTNER: **F83C22001660002**

Deliverable title: Multiscale modeling framework for contaminants transport and reaction with uncertainty quantification

Deliverable ID: DV 4.3.2

Due date: October 31st, 2025 (postponed to February 15th, 2026)

Submission date: November 30th, 2025

AUTHORS

A. Guadagnini, L. Ceresa, C. Recalcati (POLIMI)

P. Ballirano, A. Pacella, A. Marconato (UNIROMA1)

C. Lubello, B. Pagliaccia, R. Gori (UNIFI)

D. Varrica, M.G. Alaimo, D. Piazzese (UNIPA)

M. Falzarano, A. Polettini (UNIROMA1)

A. Cincinelli, L. Sforzi (UNIFI)

Andrea Bottacin-Busolin, Nirman Bhagat, Andrea Marion (UNIPD)

I. Colzi, S. Falsini, C. Gonnelli, A. Papini, B. Chiavacci (UNIFI)

G. Capobianco, E. Gorga, S. Serranti (UNIROMA1)

M. Antonelli, B. Cantoni, J. Ianes (POLIMI)

D. Di Trapani, S. Bifulco, M. Capodici, A. Cosenza, F. De Marines, M. Farina, I. Verginelli, G. Viviani (UNIPA)

1 Technical references

Project Acronym	RETURN
Project Title	multi-Risk sciEnce for resilienT commUnities undeR a changiNg climate
Project Coordinator	Domenico Calcaterra UNIVERSITÀ DEGLI STUDI DI NAPOLI FEDERICO II domcalca@unina.it
Project Duration	December 2022 – November 2025 (36 months)

Deliverable No.	DV 4.3.2
Dissemination level*	PU
Work Package	WP3 (VS4) - Enhancing capability to observe, model, and assess environmental hazards
Task	T 4.3.1 - Contaminant fate and transport models in water, groundwater and soils; innovative approaches to monitoring environmental pollution and quantification and reduction of uncertainty
Lead beneficiary	POLIMI/UNIFI
Contributing beneficiary/ies	POLIMI, UNIFI, UNINA, UNIPA, UNIPD, UNIROMA1, UNIPA

* PU = Public

PP = Restricted to other programme participants (including the Commission Services)

RE = Restricted to a group specified by the consortium (including the Commission Services)

CO = Confidential, only for members of the consortium (including the Commission Services)

1.1 Document history

Version	Date	Lead contributor	Description

2 ABSTRACT

The present document provides details on the results/products of the activities conducted until month 36 in the framework of WP4.3 (“Enhancing capability to observe, model, and assess environmental hazards”), task T4.3.1 (“Contaminant fate and transport models in water, groundwater and soils; innovative approaches to monitoring environmental pollution and quantification and reduction of uncertainty”).

In compliance with the executive working plan of the whole project, T4.3.1 involves using innovative techniques to detect and measure contaminants in different environmental compartments as well as in animal and plant organisms to provide the framework for risk assessment of anthropic activities. Target contaminants include microplastics (from both conventional plastics and bioplastics), elongated mineral particles (EMP), hydrocarbons, heavy metals, antibiotics, drugs, pesticides, and other contaminants of emerging concern (CECs). A range of approaches including advanced analytical determination, lab-scale studies, full-scale monitoring, theoretical assessment of contaminant dispersion in the environment, modelling of transformation/transport/bioaccumulation/biomagnification mechanisms, quantification of hazard and risk related to the presence of contaminants have been developed and used at different time/space scales to determine the evolution and transformation of contaminants in terrestrial water ecosystems, groundwater and soils. Specific attention has also been paid to the evaluation and quantification of uncertainty in the assessment and modelling of hazard and risk.

Task T4.3.1 is complementary to the companion task T4.3.2 that focuses on the same issues for marine ecosystems, so that the approaches adopted and the results obtained should be regarded to contribute jointly to the objectives and outputs of the RETURN project indicated in the following layout.

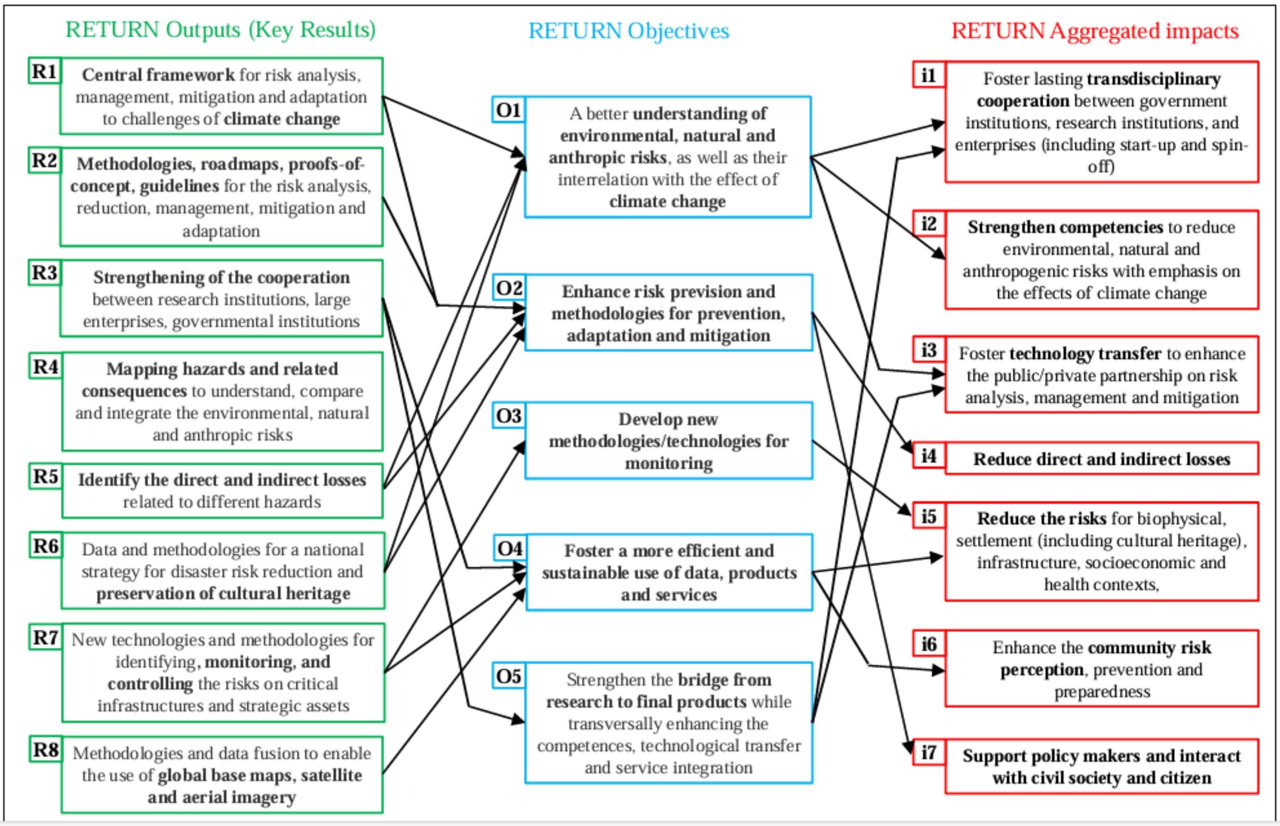

In particular, the investigation activities of T4.3.1 delivered as the final output of the project are grouped based on four main thematic areas, which were aimed at achieving the objectives of spoke VS4 (indicated in parentheses):

1. Methods and protocols for the identification and quantification of environmental contaminants [O1, O3]
2. Development, application and validation of methods for advanced environmental monitoring [O1, O2]

3. Data analysis and modelling of transport, diffusion, transformation and degradation of contaminants [O4, O5]
4. Prediction and estimation of the effects of contaminants on human health, flora and fauna and environmental quality [O2, O5]

Multiple activities were implemented during the project within the thematic areas outlined above, involving multiple competences, adopting various perspectives and approaches and yielding numerous final results, as summarised below.

1. **Development, application and validation of methods and protocols for the detection and quantification of contaminants in the environment:**
    i. Development of advanced methodologies for the detection and characterization of microplastics (MPs) in wastewater (UNIFI) [R2];
    ii. Advanced identification/classification of micro-bioplastics in organic matrices through SWIR hyperspectral imaging (UNIROMA1) [R2, R7].
2. **Development, application and validation of methods for advanced environmental monitoring:**
    i. Spatial distribution, contamination index, and geochemical baseline of trace elements in Sicilian soils (UNIPA) [R1, R4, R7];
    ii. Direct measurements of vapour emissions in contaminated site by means of dynamic flux chambers (UNIPA) [R1, R2, R3];
    iii. Methods for detecting microplastics in groundwater and drinking water (UNIFI) [R2, R7];
    iv. Monitoring and modelling of MPs diffusion at river basin scale (UNIFI) [R4, R7];
    v. Conceptual framework and material flow analysis for the assessment of bioplastic flows in the environment (UNIROMA1) [R1, R2, R7].
3. **Data analysis and modelling of transport, diffusion, transformation and degradation of contaminants:**
    i. Fundamental studies of geochemical processes in porous systems under uncertainty (POLIMI) [R2, R7];
    ii. Simulations of contaminant transport with varying bed topography in wetlands (UNIPD) [R6, R7];
    iii. Hydrodynamic modelling of microplastic transport in river systems (UNIPD) [R6, R7];
    iv. Anaerobic co-digestion of commercial bioplastics and food waste and related potential environmental issues (UNIROMA1) [R2, R7].
4. **Prediction and estimation of the effects of contaminants on human health, flora and fauna and environmental quality:**
    i. Modifications of fibrous erionite phagocytized by human THP-1 macrophages (UNIROMA1) [R1, R7];
    ii. Risk assessment for microplastics in groundwater and drinking water (UNIFI);
    iii. Prediction of micropollutant fate in the water environment: integrated risk assessment and targeted mitigation strategies (POLIMI) [R1, R2, R4, R7];
    iv. Risk-based approaches for managing multiple water (re-)use scenarios: from gaps to a one-health approach (POLIMI) [R4, R7];
    v. Assessment of the environmental impact of microplastics and bioplastics with regard to effects on plant-pollinator interactions, resistance to pathogens and plant physiology, and persistence in soils (UNIFI, UNIROMA1) [R1, R2, R4].

Efforts to efficiently integrate the multiple competences of the participants to T4.3.1 (encompassing the fields of chemistry, geology/mineralogy, hydrogeology, fluid mechanics, biology/botanic, civil and environmental engineering) were made in order to attain the main target of WP4.3, involving the development of advanced methodologies and tools to observe, model and assess environmental hazards as thoroughly and comprehensively as possible.

3 Table of contents

4 Multiscale modeling framework for contaminants transport and reaction with uncertainty quantification

4.1 Fundamental studies of geochemical processes in porous systems under uncertainty (POLIMI)

Contributors: A. Guadagnini, L. Ceresa, C. Recalcati

4.1.1 Introduction

The work is geared towards the recognition that uncertainty is inherently plaguing our ability to assess reactive transport processes taking place in porous systems across different spatial scales. Uncertainties arise from our lack of knowledge surrounding mechanistic processes driving reactions at the fundamental level. This, in turn, imprints onto our predictive capabilities of critical scenarios such as, e.g., migration of contaminants in underground groundwater bodies. As such, setting modeling approaches in a stochastic context embedding model and parametric uncertainty is recognized as the only viable way to accurately assess reactive transport processes.

In this broad context, we pursue to diverse research lines, associated with different spatial scales. *Research Line 1* investigates mechanistic processes driving evolution of mineral-water interfaces at the fundamental (nanoscale) level and their impact of mineral weathering rate heterogeneity. *Research Line 2* focuses on a laboratory-scale geochemical system and develops a robust theoretical framework to model complex reaction networks underpinning fate of Emerging Organic Contaminants including estimation and predictive uncertainty. Key results associated with *Research Line 2* are included in Deliverable DV4.3.1 and remaining tasks are related to finalizing publications (Ceresa et al., 2025). Hence, the rest of this Chapter focuses on *Research Line 1*.

Recent micro- and nanoscale investigations that relying on high resolution imaging techniques such as Atomic Force Microscopy (AFM), Vertical Scanning Interferometry, Digital Holographic Microscopy, or X-ray microtomography document that mineral-water interfaces subject to dissolution/precipitation evolve according to highly heterogeneous patterns (Putnis & Ruiz-Agudo, 2021; Bibi et al., 2018; Noiriel et al., 2020). Nanoscale surface details have been identified as the key factors responsible for marked spatial heterogeneities of rates that are experimentally documented to exhibit several-fold variations across the same interface (Arvidson et al., 2003; Fischer et al., 2012). Starting from mineral-water interfaces, the action of these local phenomena then manifests across various (spatial and temporal) scales. Accurate assessment and modeling of dissolution/precipitation kinetics must incorporate the inherently (stochastic) multiscale nature of these fundamental processes. In this context, analysis of *rate spectra*, i.e., probability densities of reaction rates, enables one to encapsulate critical details of reaction rate heterogeneity in interpretive and modeling efforts (Fischer et al., 2014). Quantification of the way main statistical features of rate spectra transition with scale is key to transfer information across (spatial and temporal) scales. Yet, this major research aspect is still largely unexplored in geochemical contexts, hindering significant advancements to our understanding of the effects of fundamental processes underpinning the stark heterogeneity of reactions at mineral-water interfaces.

In this context, we focus on characterizing statistical scaling of nanoscale-resolved reaction rates. We develop a sound mathematical framework providing a unified description of key features of rate spectra and their scaling. Our original model extends the Gaussian Mixture (GMIX) model (Siena et al., 2023) presented in Deliverable DV4.3.1 to include non-Gaussian traits of each component (or *mode*) of the mixture. We then identify links between key statistical features of rate spectra and mechanistic processes driving mineral-water interface evolution.

4.1.2 Methodologies

4.1.2.1 *Experimental methods*

Our analyses rely on a dataset comprising a collection of five spatial maps of nanoscale-resolved mineral dissolution rates. These are related to temporal observations obtained through (in situ and real-time) AFM imaging of the topography of the interface between flowing water and a pure calcite sample. Spatial distributions of dissolution rates are obtained from the difference of measurements of the mineral surface topography, $z(\mathbf{x}, t)$, as

$$R(\mathbf{x}, t) = \frac{z(\mathbf{x},t) - z(\mathbf{x},t+\Delta t)}{\Delta t \cdot V_m}. \qquad (1)$$

Here, $\mathbf{x}$ is a position vector, $V_m = 36.93$ cm^3 mol^{-1} is calcite molar volume, and $\Delta t = 16.43$ min coincides with the acquisition time. The observation window comprises a (19.5×8.7) µm^2 portion of the calcite crystal surface. Data support (i.e., measurement scale) is $dl = 19.5$ nm, corresponding to a discretization of the observation window through a 1000×455 uniform grid. Key elements of the experimental setup and protocols established in the context of *Research Line 1* are included in Deliverable DV4.3.1, the full set of details being available in Recalcati et al. (2024).

4.1.2.2 *Modeling approaches*

The functional dependence of the main statistical features of nanoscale-resolved dissolution rate on scale is assessed upon relying on the analysis of sample structure functions. These are defined as

$$S_N^q(s) = \frac{1}{N(s)} \sum_{n=1}^{N(s)} |\Delta R_n|^q, \qquad (1)$$

where $\Delta R_n = R(\mathbf{x}_1) - R(\mathbf{x}_2)$ is a spatial increment of R evaluated at (omnidirectional) separation distance or lag $s = |\mathbf{x}_1 - \mathbf{x}_2|$; $N(s)$ is the number of increments at lag s. Structure functions are said to exhibit a power-law scaling behavior if $S_N^q(s) \propto s^{\xi(q)}$. Here, $\xi(q)$ is a scaling exponent depending solely on the order of the statistical moment, q. Symptoms of power-law scaling behaviors are detected for a wide variety of variables of interest in diverse contexts. Examples include, e.g., fluid (Biferale et al., 2004) and fluvial (Nikora and Goring, 2001) turbulence, planetary topography (Landais et al., 2015, 2019), hydraulic conductivity (Liu & Molz, 1997; Tennekoon et al., 2003), sediment transport rate (Singh et al., 2009), and air-permeability (Siena et al., 2012). Experimental evidences of power-law scaling are generally limited to an interval of lags $s \in [s_L, s_U]$, s_L and s_U corresponding to a lower and an upper cut-off, respectively. These delineate interval below and above which a deviation from power-law scaling is observed (see, e.g., Neuman et al., 2013 and references therein). Sometimes, distinct power-law scaling regimes are observed in sample structure functions (Kantelhardt, 2011). This behavior, typically referred to as *cross-over* in power law-scaling, can stem from analysis grounded on lumping within a unique population data that are otherwise associated with mechanisms/attribute acting at distinct (spatial) scales. The emergence of multiple scaling regimes is documented for sample structure functions associated with a variety of attributes/processes associated with a wide range of observation domains. Examples include, e.g., pore-scale Lagrangian velocities (Siena et al., 2014), deep borehole porosity (Guadagnini et al., 2015), fluctuations of magnetic field (Kiyani et al., 2009) and intensity (Leonardis et al., 2012; Roberts et al., 2020) of solar plasma, or planetary surface topography (Landais et al., 2015, 2019).

Within each power-law scaling regime, the scaling exponent can be estimated through linear regression of log sample structure functions versus log separation distance. The functional relationship between $\xi(q)$ and q defines the way according to which statistics transition with scale. A linear behavior of ξ with q, i.e., $\xi(q) = Hq$ (H being the Hurst exponent) indicates that the field is self-affine (Molz et al., 1997). Otherwise, ξ can also exhibit a non-linear trend with q. The Hurst exponent is estimated through linear regression of $\xi(q)$ near the origin. It provides a measure of the degree of persistence of the underlying random field. If $H < 0.5$, the system exhibits an anti-persistent behavior, i.e., high and low values tend to alternate rapidly in space. Otherwise, $H > 0.5$ indicates persistence, i.e., high and low values tend to alternate mildly in space.

Dissolution rate fields are modeled according to the Generalized sub-Gaussian Mixture (GSG-MIX) modeling framework. Key analytical expressions of the GSG-MIX model are included below, the full set of details about their derivation being available in Recalcati et al. (2025a). A graphical illustration of the conceptual framework underpinning the GSG-MIX model is depicted in Figure 1. Dissolution rate maps are viewed as correlated bimodal random field (Figure 1.a), i.e.,

$$R(\mathbf{x}) = J(\mathbf{x}) R_A(\mathbf{x}) + (1 - J(\mathbf{x})) R_B(\mathbf{x}). \tag{2}$$

Here, $J(\mathbf{x})$ is a random indicator independent of each component of the mixture (Figure 1.b), $R_m(\mathbf{x})$, and distributed according to a Bernoulli distribution with parameter p_m (with $p_A = p$ and $p_B = 1 - p$). The components of the mixture are viewed as independent of each other and distributed according to a GSG distribution, i.e.,

$$R_m(\mathbf{x}) = G_m(\mathbf{x}) U_m(\mathbf{x}). \tag{3}$$

Here, $G_m(\mathbf{x})$is a spatially correlated Gaussian field and $U_m(\mathbf{x})$ is a subordinator, i.e., positive (spatially uncorrelated) random function independent of $G_m(\mathbf{x})$ (see Figure 1.c). The resulting probability density function (pdf), f_R, reads

$$f_R(r) = \frac{1}{\sqrt{2\pi}} \sum_{m=A,B} \frac{p_m}{\sigma_{G_m}} \int_0^\infty f_{U_m}(u) e^{-\frac{(r-\mu_m)^2}{2\sigma_{G_m}^2 u^2}} \frac{du}{u}, \tag{4}$$

where μ_m and σ_{G_m} are mean and scale parameter associated with each mode of the mixture, and $f_{U_m}(u)$ is the distributional form of $U_m(\mathbf{x})$. Integration of Eq. (4) yields the (raw) moment-generating function associated with the GSG-MIX pdf, i.e.,

$$\langle Y^q \rangle = \frac{2^{q/2}}{\sqrt{\pi}} \Gamma\left[\frac{q+1}{2}\right] \sum_{m=A,B} p_m \sigma_{G_m}^q \int_0^\infty u^q f_{U_m}(u) du, \tag{5}$$

where $\Gamma[\cdot]$ is the gamma function.

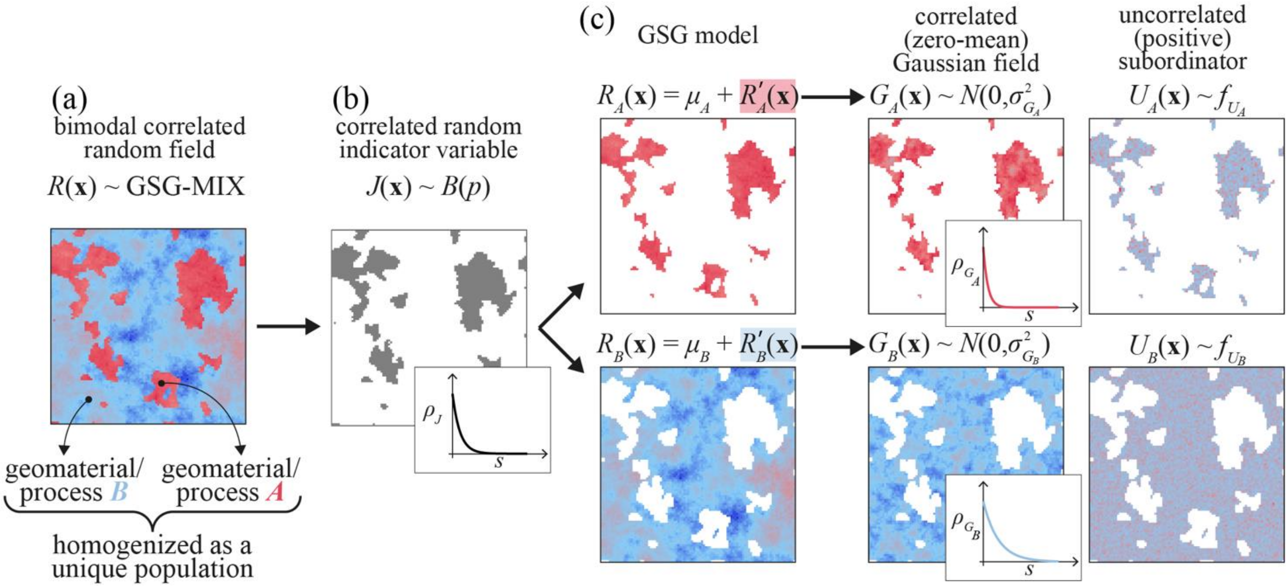

Figure 1. Conceptual framework underlying the Generalized sub-Gaussian mixture (GSG-MIX) model; (a) bimodal (spatially correlated) random field, $R(\mathbf{x})$, distributed according to a GSG-MIX theoretical model; (b) spatially correlated random indicator variable $J(\mathbf{x})$ (distributed according to a Bernoulli distribution with parameter p, $B(p)$) describing the architecture of the two regions within the domain; (c) randomly heterogeneous spatial distribution of each component $R_m(\mathbf{x})$ ($m = A, B$) of the GSG mixture across the domain.

The pdf of spatial increments of dissolution rate, $f_{\Delta R}$, reads

$$f_{\Delta R}(\Delta r) = \frac{1}{\sqrt{2\pi}} \sum\nolimits_{m=A,B} \frac{p_m^2 + C_J}{\sigma_{G_m}} \int_0^\infty \int_0^\infty \frac{f_{U_m}(u_1) f_{U_m}(u_2)}{k} e^{-\frac{\Delta r^2}{2k^2 \sigma_{G_m}^2}} du_2 du_1 + \\ + \frac{p(1-p) - C_J}{\sqrt{2\pi}} \sum\nolimits_{\substack{m=A,B \\ n=B,A}} \int_0^\infty \int_0^\infty \frac{f_{U_m}(u_1) f_{U_n}(u_2)}{h} e^{-\frac{(\Delta r - \mu_m + \mu_n)}{2h^2}} du_2 du_1, \tag{6}$$

with $k = \sqrt{u_1^2 + u_2^2 - 2\rho_{G_m} u_1 u_2}$ and $h = \sqrt{\sigma_{G_m}^2 u_1 + \sigma_{G_n}^2 u_2}$ $(m = A, B, n \neq m)$. Here, ρ_{G_m} is the correlation of the Gaussian field underlying each mode of the mixture and C_J is the covariance of the indicator. Analytical expressions for structure functions are obtained upon integration of Eq. (6) as

$$S_N^q = \frac{2^{\frac{q+1}{2}}}{\sqrt{2\pi}} \Gamma\left[\frac{q+1}{2}\right] \Bigg\{ \sum\nolimits_{m=A,B} (p_m^2 + C_J) \sigma_{G_m}^q \int_0^\infty \int_0^\infty k^q f_{U_m}(u_1) f_{U_m}(u_2) du_2 du_1 + \big[p(1-p) - \\ C_J\big] \sum\nolimits_{\substack{m=A,B \\ n=B,A}} \int_0^\infty \int_0^\infty h^q f_{U_m}(u_1) f_{U_n}(u_2) M\left[-\frac{q}{2}, \frac{1}{2}, -\frac{(\mu_m - \mu_n)^2}{2h^2}\right] du_2 du_1 \Bigg\}, \tag{7}$$

with $\mathrm{M}[\cdot]$ being gamma and confluent hypergeometric function. Following Riva et al. (2015), Guadagnini et al. (2018), Siena et al., (2019, 2021), and Li et al. (2022), we rely on a lognormal subordinator to characterize each mode of the mixture, i.e.,

$$f_{U_m}(u) = \frac{e^{-\frac{\log^2 u}{2(2-\alpha_m)^2}}}{\sqrt{2\pi} u (2 - \alpha_m)}, \tag{8}$$

where $\alpha_m \in (0,2)$ is the shape parameter associated with each mode of the mixture. A GSG-MIX formulation embedding such a distributional form of the subordinator tends to a GMIX model if $\alpha_m \to 2$, i.e., each mode of the mixture is described by a Gaussian distribution. Otherwise, non-Gaussian traits of each component are heightened as α_m departs from 2.

Model parameters embedded in Equations (4-8) are estimated upon relying on a custom Bayesian classification algorithm providing (*i*) the spatial distribution of the indicator and (*ii*) estimates of p, μ_m, σ_{G_m}, and α_m. Correlation functions associated with the Gaussian field underlying each component of the mixture, ρ_{G_m}, and C_J are inferred after classification relying upon the method of moments.

4.1.3 Results

Figure 2.a depicts the spatial distribution of sample dissolution rates at acquisition time $t_5 = 102$ min. The dissolution pattern is dominated by the presence of a deep etch pit (denoted as MP_1 in Figure 2.a) located around the center of the observation window and a secondary etch pit (MP_2) in the south-east corner. A comprehensive description of the dataset is included in Deliverable DV4.3.1, the full set of details being available in Recalcati et al. (2024).

Interpretation of temporal dynamics of the local mineral topography is grounded on a conceptual picture according to which step edges propagate across the surface of a dissolving crystal as a train of sequential steps that migrate in a wave-like manner. This scenario is also described as a stepwave mechanism of crystal dissolution (Lasaga & Lüttge, 2001; 2003). In this context, experimental observations document that emanation of steps from a localized crystal defect is not continuous over time. Otherwise, it appears to follow a pulsating behavior (Fischer & Lüttge, 2018). In turn, the pattern associated with spatial maps of dissolution rates is a direct consequence of this behavior and is characterized by the presence of well-defined regions (each corresponding to a rate pulse) centered at a given screw dislocation (Figure 2.a). As a consequence of such a pulsating nature, high and low rate dissolution pulses tend to alternate. As an example, Figure 2.b provides a depiction of rate pulses emanating along the profile AA' (corresponding to crystallographic direction $[\bar{4}41]_+$). One can recognize the presence of a sequence of hills and valleys corresponding to stepwaves associated with high, mild, and low values (denoted as sw_{a-e} in Figures 2.a-b).

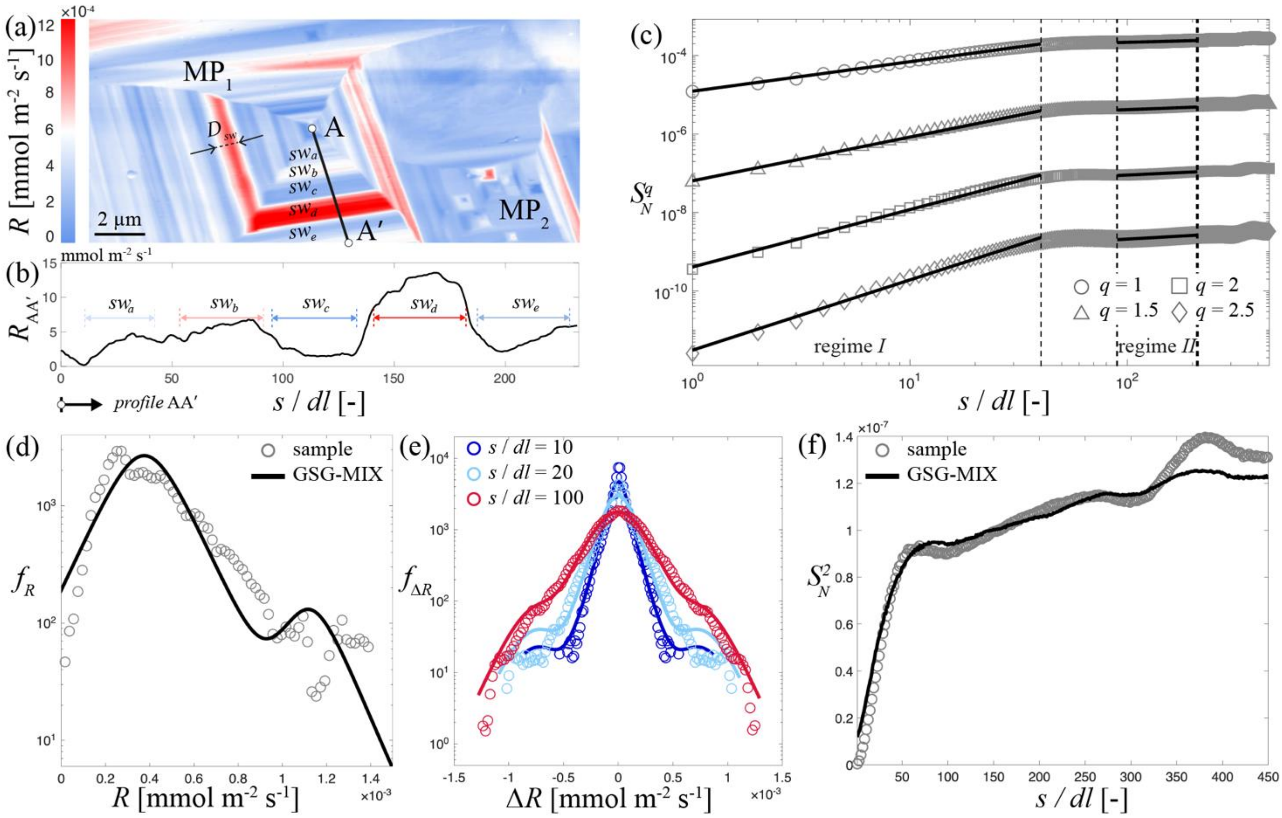

Figure 2. (a) Spatial map of nanoscale-resolved absolute dissolution rates, R, at time $t_5 = 102$ min. (b) Vertical profile of $R(t_5)$ along AA ʹ. (c) Sample structure functions, S_N^q, of order $q = 1, 1.5, 2$ and 2.5 associated with $R(t_5)$ depicted in (a). Results of linear regressions (in log-log scale) associated with power-law scaling regimes I and II are also depicted (continuous black lines). Demarcation of the two power-law scaling regimes is delineated through vertical dashed lines. Probability density function (pdf) of (d) dissolution rate, f_R, and (e) associated spatial increments, $f_{\Delta R}$, evaluated at lags $s/dl = 10, 20$, and 100. GSG-MIX modeling results (continuous curves) are juxtaposed to sample pdfs (circles). (f) Sample second order structure function, S_N^2, versus (normalized) lag, s/dl,for $R(t_5)$. Analytical expression evaluated according to the GSG-MIX model (Equation 7) is juxtaposed to its sample counterpart.

Sample structure functions associated with $R(t_5)$ of order $q = 1, 1.5, 2$, and 2.5 are depicted in Figure 2.c. The emergence of a cross-over between two scaling regimes can be clearly detected. A first regime (hereafter termed *regime I*) can be observed within the (dimensionless lag) interval $1 < s^I/dl < 40$. A second scaling regime (denoted as *regime II*) is otherwise comprised between $90 < s^{II}/dl < 210$. A breakdown in power-law behavior is then observed at the largest lags. Similar patterns are observed at all times.

At all orders q, log-log regression lines (depicted as continuous black lines in Figure 2.c) yield a coefficient of determination > 0.99 and > 0.96 for the power-law scaling regimes I and II, respectively. The ensuing scaling exponents, i.e., $\xi^I(q)$ and $\xi^{II}(q)$, are depicted versus q for various times in Figure 3.a and 3.b, respectively. Whereas $\xi^I(q)$ is linear with q at all times, $\xi^{II}(q)$ exhibits a nonlinear (concave) trend. The observation of a self-affine behavior at small scales coupled with a concave trend of $\xi(q)$ at larger lags is documented as a trait that is shared by various quantities of interest exhibiting cross-over phenomena between diverse scaling regimes. These include, e.g., deep borehole neutron porosity (Guadagnini et al., 2015) solar wind plasma turbulence (Kiyani et al., 2009; Roberts et al., 2020), or surface topography of planetary bodies (Landais et al., 2015; 2019).

Values of the Hurst exponent associated with regimes I and II, i.e., H^I and H^{II}, obtained from linear regression (continuous lines in Figures 3.a-b) are depicted versus time in Figure 3.c. Both H^I and H^{II} are virtually constant in time (a small oscillation being detected solely for H^{II} at t_4) and yield average values $\overline{H}^I = 0.70$ and $\overline{H}^{II} = 0.16$, respectively. These findings document that the two regimes are associated with starkly distinct behaviors, regime I exhibiting a marked persistence while regime II displays highly anti-persistent characteristics.

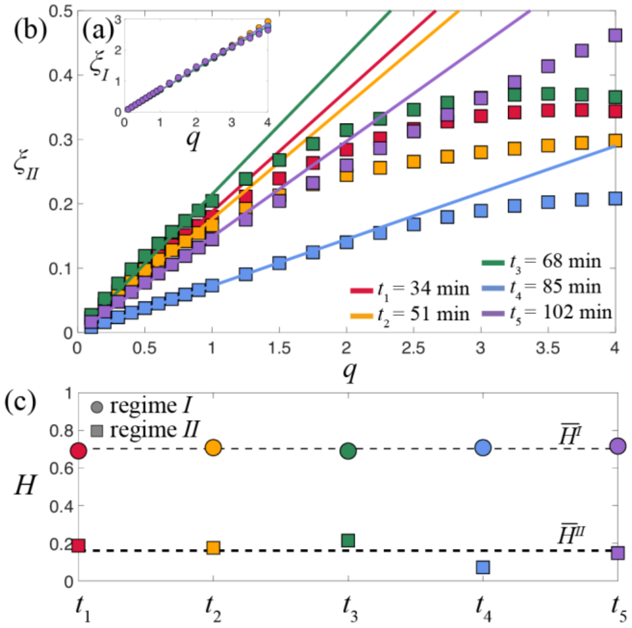

Figure 3. Scaling exponent, $\xi(q)$, versus structure function order, q, for power-law scaling regimes (a) I and (b) II at different times. (c) Temporal dependence of the Hurst exponent, H, associated with regime I (circles) and II (squares).

Emergence of a cross-over between regimes I and II is inherently related to conceptual approach employed to model the system behavior. Whereas dissolution rate values are distributed across various spatial regions, each corresponding to distinct stepwaves and/or dissolution mechanisms (see Figure 2.a), we view R at each time through a homogenized random field. Under such a conceptual picture, distinct scaling regimes can arise if processes (or attributes) within each spatial region act at distinct length scales. At all times, transition between the two scaling regimes is observed to take place at $s/dl \approx 40$. This value aligns with the average size of dissolution stepwaves, D_{sw}, i.e., $D_{sw} = 37 \pm 6\ s/dl$ (Figure 2.a).

We interpret scaling regimes I and II as being associated with a single dissolution pulse and the entire etch pit encompassing the space-time window of observation, respectively. This interpretation is further sustained by the degree of persistence associated with each of these two regimes. The high persistence associated with regime I is consistent with the tendency of each pulse to display similar rate values (see Figure 2.a-b). Otherwise, regime II corresponds to increments taken across diverse pulses. Given the pulsating nature of emanation of chains of steps from the etch pit center, high and low dissolution stepwaves alternate in space. This yields the marked anti-persistence of the signal within the interval of (dimensionless) lags $[90{,}210]$. Lumping data associated with dissolution pulses characterized by different strengths into a unique population also yields striking multimodal traits of sample PDFs of R and ΔR (see Figures 2.d-e). These features, along with key aspects of descriptive statistics associated with sample PDFs of R and ΔR, are fully consistent with a description grounded on the GSG-MIX modeling framework.

Theoretical structure functions based on the GSG-MIX modeling framework and evaluated through Equation (7) for $q = 2$ are juxtaposed to their sample counterparts in Figure 2.f. We recall that setting $q = 2$ is tantamount to examining (spatial) variograms, which are inherently linked to covariance functions of the quantity of interest. Modeling results show a remarkable agreement with sample data and document the exceptional ability of the GSG-MIX framework to capture the main traits exhibited by sample structure functions such as the cross-over at $s/dl \approx 40$ (vertical dashed line in Figure 2.f), as well as those of sample PDFs of R and ΔR (Figures 2.d-e).

Our work has critical implications in the broader context of characterizing and modeling geochemical processes taking place in porous systems. Starting from mineral-water interfaces, dissolution/precipitation reactions can alter pore-scale geometry, yielding formation (or closing) of preferential flow paths as well as exposure of new mineral surfaces (and/or new mineral phases, eventually containing potentially hazardous compounds) to reactions. Changes of the local geometry of pore spaces alter fluid velocities at the level of individual pores. In turn, distributions of chemical concentrations and their gradients (acting as dissolution/precipitation drivers) are impacted. The ensuing variations of pore water geochemical signature further contribute to enhance (or reduce) heterogeneity of surface reactivity in a continuous feedback loop (Fischer & Lüttge, 2017). The effect of these processes then propagates to larger spatial scales, imprinting variations in effective (continuum scale) attributes such as, for example, porosity or permeability. In this perspective, setting our analysis and interpretation in a stochastic environment responds to the dire need of a sound approach capable to encapsulating the effect of surface details driving self-organization of mineral-water interfaces in (conceptual and mathematical) modeling frameworks. As such, our study opens new ground to future studies aiming at transferring statistics of rates of dissolution (or of other types of geochemical reactions) across scales upon anchoring these on physical processes governing evolutionary patterns of mineral surface morphology at the fundamental level.

4.1.4 Scientific products and dissemination

Research papers

Recalcati, C., Riva, M., & Guadagnini, A. (2025). *Evidence of power-law scaling regimes for nanoscale-resolved reaction rates at mineral-water interfaces*. Geophysical Research Letters, 52, e2025GL118357. https://doi.org/10.1029/ 2025GL118357.

Recalcati, C., Yivlialin, R., Duò, L., Guadagnini, A., & Bussetti, G. (2025). *A novel experimental platform to monitor solid/water interfaces under freeze–thaw cycles*. Journal of Microscopy, https://doi.org/10.1111/jmi.70017.

Ceresa, L., Riva, M., & Guadagnini, A. (2025). *A multi-model perspective for stochastic inverse modeling of diclofenac dynamics in porous media*. Water Resources Research 61, e2024WR039684, https://doi.org/10.1029/2024WR039684.

Recalcati, C., Guadagnini, A., & Riva, M. (2025). *Characterization of spatially heterogeneous environmental variables through multi-modal Generalized Sub-Gaussian distributions*. Water Resources Research, 61, e2024WR038487, https://doi.org/10.1029/2024WR038487.

Sprocati, R., Guadagnini, A., Ceresa, L., Gallo, A., & Rolle, M. (2025). *Global sensitivity analysis of mass transfer and reaction dynamics for electrokinetic transport in porous media*. Advances in Water Resources, 196, 104887, https://doi.org/10.1016/j.advwatres.2025.104887.

Starnoni, M., Sanchez-Vila, X., Recalcati, C., Riva, M., and Guadagnini, A. (2024). *Process modeling of mineral dissolution from nano-scale surface topography observations*. Geophysical Research Letters, 51(16), e2024GL110030, https://doi.org/10.1029/2024GL110030.

Recalcati, C., Siena, M., Riva, M., Bollani, M., & Guadagnini, A. (2024). *Stochastic assessment of dissolution at fluid-mineral interfaces*. Geophysical Research Letters, 51, https://doi.org/10.1029/2023GL108080.

Conference presentations

Recalcati, C., Riva, M., & Guadagnini, A. (2025, May). *Statistical scaling of nanoscale mineral dissolution rates*. In Goldschmidt2025 Conference.

Guadagnini, A., Varouchakis, E., Ceresa, L., Recalcati, C., & Riva, M. (2025, July). *Space-time correlations associated with nanoscale dissolution patterns at calcite-water interfaces*. In Goldschmidt2025 Conference.

Recalcati, C., Riva, M., & Guadagnini, A. (2025, May). *Statistical scaling of nanoscale spatially heterogeneous dissolution rates at mineral-water interfaces*. In InterPore2025 Annual Meeting.

Guadagnini, A., Bussetti, G., Yivlialin, R., Duò, L., & Recaclati, C. (2025, May). *Controlling ice formation at the interface between a solid and a liquid in view of nano-scale imaging resolution*. In InterPore2025 Annual Meeting.

Recalcati, C., Siena, M., Bollani, M., Riva, M., & Guadagnini, A. (2024, September). *Stochastic characterization of dissolution at fluid-mineral interfaces*. In IDRA2024 Conference.

Ceresa, L., Riva, M., & Guadagnini, A. (2024, September). *Diclofenac dynamics in porous media*. In IDRA2024 Conference.

Recalcati, C., Siena, M., Riva, M., & Guadagnini, A. (2024, June). *Scalable statistical behavior of mineral dissolution rates*. In Symposium on microscopic characterization of the solid/liquid interface, Sondalo (SO).

Recalcati, C., Siena, M., Bollani, M., Riva, M., & Guadagnini, A. (2024, June). *Quantification of mineral dissolution via Atomic Force Microscopy*. In Symposium on microscopic characterization of the solid/liquid interface, Sondalo (SO).

Ceresa, L., Riva, M., & Guadagnini, A. (2024, June). *Stochastic Inverse Modeling of Diclofenac Dynamics in Groundwater*. In GeoEnv2024 Conference.

Recalcati, C., Siena, M., Bollani, M., Riva, M., & Guadagnini, A. (2024, April). *Investigation of mineral dissolution kinetics through Atomic Force Microscopy*. In EGU2024 General Assembly Conference.

Ceresa, L., Guadagnini, A., Riva, M., & Porta, G. M. (2023, July). *Modeling the fate of Diclofenac in soil-water systems*. In Goldschmidt 2023 Conference.

Recalcati, C., Siena, M., Riva, M., & Guadagnini, A. (2023, July). *Stochastic modeling of calcite dissolution rates from microscale observations*. In Goldschmidt 2023 Conference.

Recalcati, C., Siena, M., Riva, M., & Guadagnini, A. (2023, May). *Direct nanoscale investigation of calcite dissolution kinetics*. In Interpore 2023 Conference.

4.1.5 References

Arvidson, R. S., Ertan, I. E., Amonette, J. E., & Luttge, A. (2003). Variation in calcite dissolution rates:: A fundamental problem?. Geochimica et cosmochimica acta, 67(9), 1623-1634.

Bibi, I., Arvidson, R. S., Fischer, C., & Lüttge, A. (2018). Temporal evolution of calcite surface dissolution kinetics. Minerals, 8(6), 256.

Biferale, L., Boffetta, G., Celani, A., Lanotte, A., & Toschi, F. (2005). Particle trapping in three-dimensional fully developed turbulence. Physics of Fluids, 17(2).

Ceresa, L., Riva, M., & Guadagnini, A. (2025). A multi-model perspective for stochastic inverse modeling of diclofenac dynamics in porous media. Water Resources Research, 61(7), e2024WR039684.

Fischer, C., Arvidson, R. S., & Lüttge, A. (2012). How predictable are dissolution rates of crystalline material?. Geochimica et Cosmochimica Acta, 98, 177-185.

Fischer, C., Kurganskaya, I., Schäfer, T., & Lüttge, A. (2014). Variability of crystal surface reactivity: what do we know?. Applied Geochemistry, 43, 132-157.

Fischer, C., & Luttge, A. (2017). Beyond the conventional understanding of water–rock reactivity. Earth and Planetary Science Letters, 457, 100-105.

Fischer, C., & Luttge, A. (2018). Pulsating dissolution of crystalline matter. Proceedings of the National Academy of Sciences, 115(5), 897-902.

Guadagnini, A., Neuman, S. P., Nan, T., Riva, M., & Winter, C. L. (2015). Scalable statistics of correlated random variables and extremes applied to deep borehole porosities. Hydrology and Earth System Sciences, 19(2), 729-745.

Guadagnini, A., Riva, M., & Neuman, S. P. (2018). Recent advances in scalable non-Gaussian geostatistics: The generalized sub-Gaussian model. Journal of hydrology, 562, 685-691.

Kantelhardt, J. W. (2011). Fractal and multifractal time series. In Mathematics of Complexity and Dynamical Systems (pp. 463-487). Springer, New York.

Kiyani, K. H., Chapman, S. C., Khotyaintsev, Y. V., Dunlop, M. W., & Sahraoui, F. (2009). Global scale-invariant dissipation in collisionless plasma turbulence. Physical review letters, 103(7), 075006.

Landais, F., Schmidt, F., & Lovejoy, S. (2015). Universal multifractal Martian topography. Nonlinear Processes in Geophysics, 22(6), 713-722.

Landais, F., Schmidt, F., & Lovejoy, S. (2019). Multifractal topography of several planetary bodies in the solar system. Icarus, 319, 14-20.

Lasaga, A. C., & Lüttge, A. (2001). Variation of crystal dissolution rate based on a dissolution stepwave model. Science, 291(5512), 2400-2404.

Lasaga, A. C., & Lüttge, A. (2003). A model for crystal dissolution. European Journal of Mineralogy, 15(4), 603-615.

Leonardis, E., Chapman, S. C., & Foullon, C. (2012). Turbulent characteristics in the intensity fluctuations of a solar quiescent prominence observed by the Hinode Solar Optical Telescope. The Astrophysical Journal, 745(2), 185.

Li, K., Wu, J., Nan, T., Zeng, X., Yin, L., & Zhang, J. (2022). Analysis of heterogeneity in a sedimentary aquifer using Generalized sub-Gaussian model based on logging resistivity. Stochastic Environmental Research and Risk Assessment, 36(3), 767-783.

Liu, H. A., & Molz, F. J. (1997). Multifractal analyses of hydraulic conductivity distributions. Water Resources Research, 33(11), 2483-2488.

Molz, F. J., Liu, H. H., & Szulga, J. (1997). Fractional Brownian motion and fractional Gaussian noise in subsurface hydrology: A review, presentation of fundamental properties, and extensions. Water Resources Research, 33(10), 2273-2286.

Neuman, S. P., Guadagnini, A., Riva, M., & Siena, M. (2013). Recent advances in statistical and scaling analysis of earth and environmental variables. Advances in hydrogeology, 1-25.

Nikora, V., Goring, D., McEwan, I., & Griffiths, G. (2001). Spatially averaged open-channel flow over rough bed. Journal of Hydraulic engineering, 127(2), 123-133.

Noiriel, C., Oursin, M., & Daval, D. (2020). Examination of crystal dissolution in 3D: a way to reconcile dissolution rates in the laboratory?. Geochimica et Cosmochimica Acta, 273, 1-25.

Putnis, C. V., & Ruiz-Agudo, E. (2021). Nanoparticles formed during mineral-fluid interactions. Chemical Geology, 586, 120614.

Recalcati, C., Siena, M., Riva, M., Bollani, M., & Guadagnini, A. (2024). Stochastic assessment of dissolution at fluid-mineral interfaces. Geophysical Research Letters, 51(7), e2023GL108080.

Recalcati, C., Guadagnini, A., & Riva, M. (2025). Characterization of spatially heterogeneous environmental variables through multi-modal Generalized sub-Gaussian distributions. Water Resources Research, 61(3), e2024WR038487.

Riva, M., Neuman, S. P., & Guadagnini, A. (2015). New scaling model for variables and increments with heavy-tailed distributions. Water Resources Research, 51(6), 4623-4634.

Roberts, O. W., Thwaites, J., Sorriso-Valvo, L., Nakamura, R., & Vörös, Z. (2020). Higher-order statistics in compressive solar wind plasma turbulence: High-resolution density observations from the magnetospheric multiscale mission. Frontiers in Physics, 8, 584063.

Siena, M., Guadagnini, A., Riva, M., & Neuman, S. P. (2012). Extended power-law scaling of air permeabilities measured on a block of tuff. Hydrology and Earth System Sciences, 16(1), 29-42.

Siena, M., Guadagnini, A., Riva, M., Bijeljic, B., Pereira Nunes, J. P., & Blunt, M. J. (2014). Statistical scaling of pore-scale Lagrangian velocities in natural porous media. Physical Review E, 90(2), 023013.

Siena, M., Riva, M., Giamberini, M., Gouze, P., & Guadagnini, A. (2019). Statistical modeling of gas-permeability spatial variability along a limestone core. Spatial Statistics, 34, 100249.

Siena, M., Bussetti, G., Recalcati, C., Riva, M., Duò, L., & Guadagnini, A. (2021). Statistical characterization of heterogeneous dissolution rates of calcite from in situ and real-time AFM imaging. Transport in Porous Media, 140(1), 291-312.

Siena, M., Recalcati, C., Guadagnini, A., & Riva, M. (2023). A Gaussian-Mixture based stochastic framework for the interpretation of spatial heterogeneity in multimodal fields. Journal of Hydrology, 617, 128849.

Singh, A., Fienberg, K., Jerolmack, D. J., Marr, J., & Foufoula-Georgiou, E. (2009). Experimental evidence for statistical scaling and intermittency in sediment transport rates. Journal of Geophysical Research: Earth Surface, 114(F1).

Tennekoon, L., Boufadel, M. C., Lavallee, D., & Weaver, J. (2003). Multifractal anisotropic scaling of the hydraulic conductivity. Water Resources Research, 39(7)

4.2 Modifications of fibrous erionite phagocytized by human THP-1 macrophages (UNIROMA1)

Contributors: P. Ballirano, A. Pacella, A. Marconato

4.2.1 Introduction

Erionite (ERI) is an “intermediate” zeolite that belongs to the small pore family. It crystallizes in the hexagonal crystal system, space group $P6_3/mmc$ and has an average formula $K_2(Na,Ca_{0.5})_8[Al_{10}Si_{26}O_{72}] \bullet 30H_2O$. The framework of erionite consists of columns of alternating cancrinite (ε) cages, and double 6-rings (d6r) plus erionite cages (23-hedra). The unit cell hosts two cancrinite cages and two d6r alternating along 0, 0, *z*, and two erionite cages running, respectively, along 1/3, 2/3, *z*, and 2/3, 1/3, *z*. Cages host EF cations and H_2O and, in particular, the small ε cage allocate a K^+ ion at its centre whereas the large erionite cage potentially contains several cation sites prevalently residing at or near the axis of the cage. Moreover, K-rich erionite samples (> 2 atoms per formula unit a.p.f.u. K^+) display a further EF cation site which is placed at the centre of the boat-shaped eight-ring forming the walls of the erionite cage. H_2O is distributed among six OW sites radiating from the axis of the cavity whose distribution, as in the case of EF cations, is dictated by prevention of short contacts.

Recent substantial work has been devoted to analysing in detail the cation exchange properties of erionite fibres finalized to building a solid background for modelling their interaction with biological environments. The relevant interest of this topic is related to the unambiguous link of inhalation by humans of erionite fibres with the onset of malignant mesothelioma (MM). In fact, *in vivo* studies have proved the strong tumorigenic activity of erionite that has been accordingly included in the Group 1 Human-Carcinogenic list by the International Agency for Research on Cancer (IARC). Erionite occurs worldwide and, in particular, a high rate of MM observed in several villages of Central Anatolia have been related to inhalation of erionite fibres since the 1970s. Starting from the pioneering paper by Ballirano and Cametti, where fibres were incubated in artificial lysosomal fluid (ALF) and Gamble’s solution, following the complications to control the stability of these simulated lung fluids (SLFs) over a large span of time, many papers adopted simplified formulations or focused on the ability of erionite to upload specific cations. Simulated formulations lack most of the organic components and, in the case of the simplified ones, even some minor inorganic salts are substituted to avoid possible interference with the released cations during analytical procedures. However, it is unclear whether those simplifications represent a sufficiently close approximation of the conditions to which fibres are subjected in the biological compartment after inhalation and inside the cells after phagocytosis. In a recent work, it has been described for the first time, by synchrotron micro-X-ray fluorescence, the spatial distribution of metals and other cations in macrophage cells after the phagocytosis of erionite fibres up to four days of incubation. The results of this research ruled out the intracellular Ca^{2+} binding by the fibres, in exchange with Na^+, as one of the mechanisms of toxicity of erionite fibres, a hypothesis that has been proposed, among others, to explain erionite hazard potential.

4.2.2 Case study description

To shed further light into these complex mechanisms, in this work we describe, by a multi analytical approach, the structural modifications induced by the *in vitro* phagocytosis of erionite fibres by THP-1 cell line derived macrophages mimicking the action of the cellular first line of defence in the alveolar space against inhaled harmful stimuli. Moreover, we report the results of a thorough structural investigation aimed at identifying possible experimental interferences induced by manipulation during experiments that, coupled with the careful check of control samples, will shed new perspectives toward the comprehension of the mechanism(s) inducing toxicity of erionite in comparison to simplified models.

4.2.3 Methodologies

Fibres of erionite were studied by a multi-analytical approach: scanning electron microscopy (SEM) to characterize from the chemical point of view the fibres pre and post incubation, powder X-ray diffraction (PXRD) to characterize from the structural point of view fibres pre and post incubation.

The human monocytic cell line THP-1 was cultured at 37 °C in a humidified 5% CO_2 atmosphere. THP-1 cells were cultured in RPMI-1640 with L-glutamine and 10% FBS.

Erionite toxicity was initially evaluated by the MTT assay to assess the degree of cell damage given by the erionite working concentration used in the following experiments.

To obtain the phagocytosed erionite fibres THP-1 cells were seeded at 3×10^6 cells/plate in 10-cm plates and differentiated to M0 macrophages. Then, M0 macrophages were treated with 50 µg/mL of erionite for 1d, 7d and 14d (THP-1-1d, -7d, -14d). Additionally, a control containing only pristine erionite fibres was prepared as well. Experiments were carried out in duplicate. A significant number of erionite fibres were found inside macrophages already after 1d of incubation and all fibres in the petri dishes were internalised after 7/14d of exposure.

The quantity of recovered fibres phagocytosed by THP-1 cells was of the order of a few hundred µgrams for each experiment. During the whole process, fibres may enter in contact with different chemical-physical environments since pH ranges from 4.5 to 5 within the lysosome (luminal environment maintained at the proper pH by proton pumping vacuolar ATPases) to 7.4 within the cytosol. Apart from the main experiments, additional ones were performed to investigate the possible occurrence of interferential effects during the manipulation of fibres pre- and post-incubation and to provide additional hints on the effect of single physical-chemical parameters.

4.2.3.1 Analytical methods

Fibres of erionite from Rome (Oregon, USA) were chosen for the following experiments. The pristine material (PRI) was enriched in erionite content (up to ca. 95 wt%). It is classified as erionite-Na, based on its formula $K_{2.40}(Na_{3.30}Mg_{0.72}Ca_{0.35})[Al_{7.78}Si_{28.22}O_{72.04}] \bullet 29.75H_2O$. The material contains ca. 4 wt.% of chabazite, traces of quartz (ca. 0.1 wt%) and minor clays as impurities.

Fibre length and diameter were in the range of ca. 5–70 µm and 0.1–3.0 µm, respectively, with most fibres (65%) showing length below 20 µm and width less than 5 µm. For experiments in THP-1-derived macrophages, sterile fibre suspensions were prepared.

4.2.3.2 Experimental methods

The chemical composition of the PRI fibres and those after immersion in ALF was determined using a Quanta 400 SEM equipped with an EDS Genesis system. The analysis of the fibres after phagocytosis from THP-1 derived macrophages revealed E% values markedly outside the admitted range of ±10% (up to 40%), so that it was not possible to obtain reliable crystal chemical formulae, likely due to both possible occurrence of a layer of organic material with variable thickness on the fibre surface and fibre alteration following the phagocytosis process. Nonetheless, in this case a qualitative interpretation of the spectra is given.

PXRD data were collected using a Bruker AXS D8 Advance operating in transmission mode, θ/θ geometry. The instrument is fitted with focusing mirrors and a position sensitive detector VÅntec-1 placed after radial Soller slits. Pristine material contains minor chabazite and quartz plus clay minerals (identified as nontronite, an iron-rich phyllosilicate). Preliminary analysis of the diffraction data pointed out to the significant reduction of the clays content upon incubation/internalization.

To measure the mitochondrial damage induced by erionite fibres, cells were stained with the mitochondrial proton gradient ($\Delta\Psi$)-sensitive fluorescent dye JC-1. After cells were stained with JC-1 following the manufacturer's instructions, images were immediately acquired in fluorescence mode using a Nikon Eclipse Ti2 confocal microscope equipped with a PLAN APO λD 60x oil objective. The resulting images (3.0 × digital zoom) were obtained acquiring the green fluorescence (emission at 527 nm) and the red fluorescence (emission at 590 nm).

4.2.3.3 Modelling approaches

The crystal chemical formulae were calculated based on 36 (Si+Al) a.p.f.u., assuming a water content of 18.5 wt% (corresponding to ca. 30 a.p.f.u.). Both the balance error formula E% and the K content test (K content $\geq$ 2 atoms per unit formula) were used for selecting the positive analyses.

Diffraction data were evaluated by performing a mixed Pawley-Rietveld method, successfully adopted for similar samples, using Topas V6 and the Fundamental Parameters Approach. Refined structural parameters of erionite included fractional coordinates and site occupancy fraction (s.o.f.) of EF cations and H_2O sites.

To measure the mitochondrial damage, the red/green fluorescence intensity of selected ROIs in each image (at least five microphotographs taken for each condition) was quantified after background subtraction with the ImageJ software v1.8.0, and the results were expressed as the mean red/green ratio ± SD of the different samples.

4.2.4 Results

Erionite toxicity on human THP-1-derived macrophages was evaluated by the MTT assay to assess the degree of cell damage caused by the working concentration used in the following experiments. The assay showed that, at the highest fibre concentration tested, 50 μg/mL, the mortality rate of macrophages ranged from ca. 20% after 1d to ca. 40% after 14d of incubation. Therefore, this concentration was considered optimal, since it could ensure a significant fibre uptake without excessive cell damage that would compromise the retrieval of *bona fide* internalised fibres.

Cell parameters of THP-1 phagocytosed fibres indicate a generalized compression of the cell with respect to PRI. The refined values of the site scattering (s.s.) at the EF cation sites and H_2O sites is summarized in Fig. XX. We found the complete depletion of Ca1 and Ca3 and a relevant reduction of s.s. at Ca2 for THP-1-1d. In the case of THP-1-7d and -14d the s.s. increases somewhat and limited s.s. is observed at Ca1. We observe a very minor reduction of s.s. at K2 with respect to PRI, significantly smaller than that observed for ALF 14d. The minor release of K^+ ions into the cellular environment is reasonably hindered by the abundance of such cation inside the cells where the fibres are located.

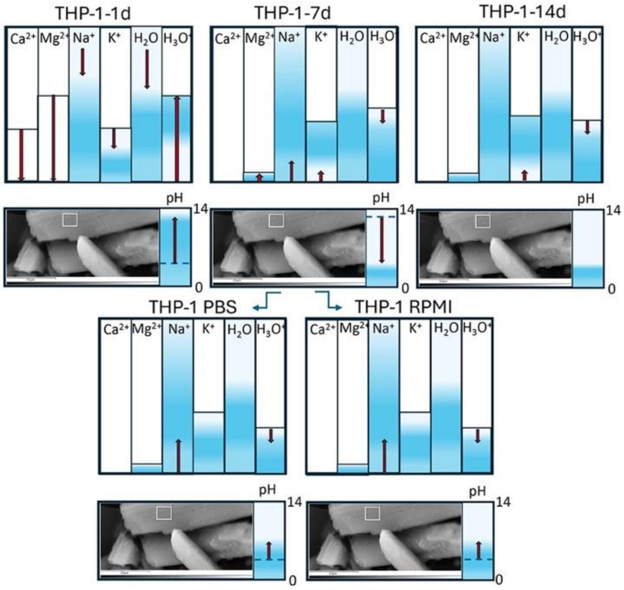

Fig. XX A pictorial representation of the various processes, as deduced from the structural analyses.

The total EF cation s.s. decreases dramatically from 114(2) e^- of PRI to 73.8(13) e^- of THP-1-1d and to ca. 81 e^- in the case of increased incubation times. The decrease of s.s. at the EF cation sites experienced by the THP-1 phagocytosed fibres is coupled to a significant redistribution of s.s. at the various OW sites where H_2O is expected to be located. We observed an increase of the s.s. of both EF cations and OW sites passing from THP-

1-1d to -7d and -14d. Explanation to this behaviour may be linked to the very quick complete release of Ca from erionite structure to the biological environment that is followed by a small re-equilibration process driven by the cations available within the lysosomal fluid and possibly by pH modifications. The s.s. redistribution at OW sites of the fibres internalised by THP-1 macrophages is obtained without the occurrence of large displacement of the various sites. However, the bonding system is different. In the following we will discuss the structural features of THP-1-1d sample as representative of the effect of the interaction of the erionite fibres with THP-1 macrophages owing to the minor structural differences existing among the fibres residing into the cellular environment for longer periods (i.e., 7d and 14d). Both XRPD and SEM data showed that after internalization in THP-1 macrophages erionite fibres undertake a significant release of extra-framework cations and there is no evidence of Na^+ or K^+ binding from the cellular fluid. Protonation of oxygen atoms of the framework has been previously invoked to justify a small charge unbalance of ca. 1.5 e^- per formula unit (pfu) occurring because of minor EF cation release in simulated lung fluids. However, in the present case the expected charge mismatch is very large, as indicated by the significant reduction of s.s. at EF cation sites and an extended protonation of the framework without loss of crystallinity (not observed) seems implausible.

As previously pointed out, THP-1-1d shows even a more dramatic reduction of s.s. at EF cation sites of ca. 40 e^-. The precipitation of calcite apparently suggests the abrupt increase of the pH in the internalization environment occurring in the first day. Conversely, its absence in fibres phagocytosed for longer times (i.e., 7d to 14d) together with the increase of s.s. at EF cation sites in the same samples, points to a subsequent restoration of the original acidic pH around the fibres. A possible explanation of the main mechanism of charge compensation is that the release of cations by the fibres (indicated as X for simplicity in the following) is largely counterbalanced by the uptake of hydronium ions from the cellular fluids according to one or more of the following simplified equations:

1) $X^+_{(eri)} + 2H_2O \Leftrightarrow X^+_{(soln)} + H_3O^+_{(eri)} + OH^-_{(soln)}$;

2) $X^{2+}_{(eri)} + 4H_2O \Leftrightarrow X^{2+}_{(soln)} + 2H_3O^+_{(eri)} + 2OH^-_{(soln)}$:

3) $X^{2+}_{(eri)} + 2H_2O + X^+_{(soln)} \Leftrightarrow X^{2+}_{(soln)} + X^+_{(eri)} + H_3O^+_{(eri)} + OH^-_{(soln)}$.

In particular, the process outlined by equation 1) is well documented for several zeolite species, both as pristine or activated, immersed in water or aqueous solutions and produces a pH increase in the solution caused by the fast release of OH^-. It is subsequently followed by a slow pH decrease arising from hydrolysis of the framework and partial release of hydronium ions. The efficiency of the process strongly depends on the pH and is favoured by acidic conditions i.e. those typically occurring within lysosomes. It is worth noting that, in the present case, X represents K^+, Na^+, Ca^{2+}, and Mg^{2+} in the simplified equations.

The fibres incubated for 7d in THP-1 and subsequently exposed for 1d to PBS and RPMI (THP-1 PBS and RPMI), mimicking the re-immersion in the extracellular environment after the release of fibres from dead macrophages, show a partial recovery of the s.s. at both OW sites and EF sites indicating a relevant upload of cations from the media that should be essentially Na^+. The trend of structural convergence toward the corresponding control PBS and RPMI samples indicate the possible extended reversibility of the ionic exchange process occurred inside THP-1 macrophages after phagocytosis. This would imply that at each ingestion/reingestion cycle in the lung environment, the erionite fibres would discharge the predominant Na^+ and/or K^+ cations in exchange for the abundant H_3O^+ inside the acidic phagolysosomes and subsequently recharge them when released again into the neutral, sodium-rich extracellular milieu, after macrophage cell death. An important consequence of this phenomenon would be that at each macrophage cell reingestion the fibres regain one of the erionite toxicity characteristics in a perpetual way. In fact, the H_3O^+ upload on the fibre surface would cause a significant alteration of the acidic pH of the phagolysosomes that would be necessarily reestablished by the hyperactivation of the ATP-dependent proton pumps in the organelle membranes with an energetic cost for the cells possibly affecting the mitochondrial and cell homeostasis. If our hypothesis turns out to be true, a great deal of erionite toxicity after cellular ingestion would be centred on the mitochondria, with the compromission of cell respiration mechanisms and of the ATP production rate. To shed light on the hypothesis of the cell mitochondrial suffering and function compromission after erionite fibre internalization, THP-1 M0 macrophages were incubated with erionite fibres up to 3d and then their mitochondrial inner membrane potential was measured by use of the mitochondrial proton gradient (ΔΨ)-sensitive fluorescent probe JC-1. In THP-1 M0 macrophages a significant compromission of the electron transport chain and of the ATP-synthase activity in the organelles was observed after erionite fibre exposure at 24h and 3d of incubation leading to a 40% and 50% ΔΨ decrease in cells with phagocytosed fibres, respectively, as compared to control, healthy cells.

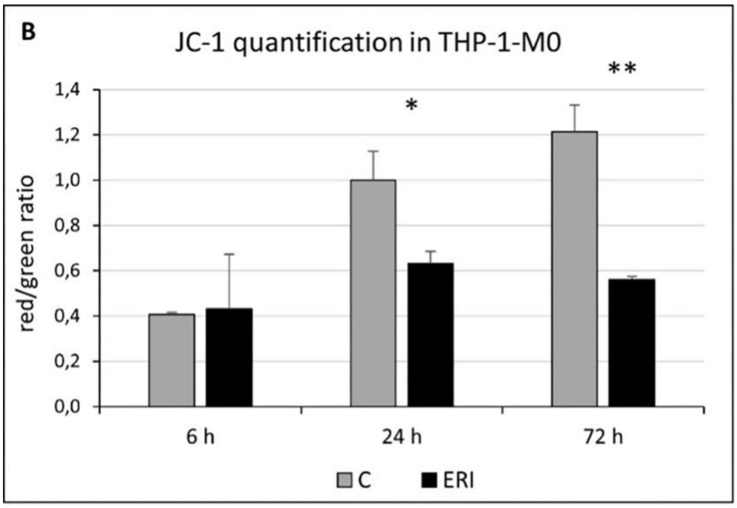

Fig. XX. Quantification of mitochondrial damage in THP-1 M0 cells. Quantification of the red/green fluorescence ratio measured by confocal microscopy. Results are the mean ± SD of five different microphotographs and asterisks indicate significance in Tukey test (ANOVA p<0.001; Tukey vs. C, **p<0.001, *p<0.005, respectively).

These data seem to confirm that, although in an unexpected way, erionite ion exchanging capacity indeed has a role in the cytotoxicity of this mineral which is surprisingly exerted by sequestering H_3O^+ ions from the fluid of the lysosomes in which the fibres are compartmentalized inside the cells, increasing the pH of the organelles. Consequently, the increased activity of the membrane proton pumps of the organelle to restore the acidic pH, would lead to a significant ATP expenditure and mitochondrial suffering in the cells, compromising the cellular functions and homeostasis.

4.2.5 Scientific products and dissemination

Ballirano, P., Pacella, A., Mirata. S., Passalacqua, M., Di Carlo, M.C., Arrizza, L., Montereali, M.R., Scarfì, S. (2025) – Fibrous erionite modifications following THP-1 macrophage phagocytosis: An insight into the mechanisms of interaction with biological systems. Journal of Hazardous Materials, 490, 137546. DOI:10.1016/j.jhazmat.2025.137546

Press review:

https://life.unige.it/erionite

https://www.uniroma1.it/it/notizia/erionite-la-fibra-killer-peggiore-dellamianto-individuato-un-potenziale-meccanismo-di

https://www.corriere.it/salute/sportello_cancro/25_marzo_26/l-erionite-il-minerale-killer-piu-pericoloso-dell-amianto-ecco-il-meccanismo-che-lo-rende-tossico-3773c540-97fd-4ccd-8753-84443ddadxlk.shtml https://www.ansa.it/canale_scienza/notizie/fisica_matematica/2025/03/23/scoperto-il-segreto-dellerionite-killer-peggiore-dellamianto_99ee6e2a-3aec-4332-b817-72cc957e9af8.html

https://www.ilsole24ore.com/art/erionite-scoperto-segreto-minerale-killer-AGhBpljD

https://tg24.sky.it/scienze/2025/03/24/erionite-zeolite-studio

https://www.msn.com/it-it/notizie/tecnologiaescienza/scoperto-il-segreto-dell-erionite-killer-peggiore-dell-amianto/ar-AA1B5HzS

https://www.wired.it/article/erionite-tossica-mesotelioma-meccanismo-tossicita-scoperta/

https://www.rainews.it/tgr/liguria/video/2025/06/erionite-minerale-fibra-killer-studio-universita-di-genova-4f959b49-a880-44b0-9b2d-8533f1f6a31b.html

4.3 Development of advanced methodologies for the detection and characterization of microplastics (MPs) in wastewater (UNIFI)

Contributors: C. Lubello, B. Pagliaccia, R. Gori

4.3.1 Introduction

The current state-of-the-art knowledge regarding the occurrence, fate and removal of microplastics (MPs) in wastewater treatment plants (WWTPs) is affected by a high degree of variability in the available literature data. The existing discrepancies among scientific reports in terms of MPs concentrations and removals arise not only from differences in the monitored facilities – such as wastewater source, type of sewer system, treatment configuration, etc. – but also from the diverse methodological approaches applied for sampling and analysis. The lack of reference and/or harmonized protocols therefore hinder direct comparison among literature, hampering the establishment of standardized assessment frameworks.

Multiple techniques can be applied for the detection and characterization of MPs in wastewater. Regardless of the specific methods employed, the MPs analysis workflow involves the following key stages: (i) sample collection (e.g. containers, autosamplers, separate pumping and filtration systems, etc.), (ii) sample processing for the removal of organic matter (e.g. chemical digestion) and eventually for the separation of non-plastic items (density-based separation treatment), and (iii) sample analysis for counting and chemical and physical description of MPs. Particular attention is given to the analytical method used for MPs identification. To date, chemical assignment can be carried out through non-destructive techniques – such as Raman/micro-Raman spectroscopy (Becucci et al., 2022; Kardel et al., 2025; Li et al., 2024; X. Liu et al., 2019) and Fourier transform infrared (FTIR)/micro-FTIR spectroscopy (Bayo et al., 2020; Gies et al., 2018; Murphy et al., 2016; Talvitie et al., 2017) – or destructive methods including thermal analysis-related techniques such as pyrolysis-gas chromatography-mass spectrometry (Py-GC-MS) (Peñalver et al., 2020). A non-destructive technique recently introduced for the analysis of MPs is the Laser Direct InfraRed (LDIR) chemical imaging spectroscopy, which provides comprehensive information on both chemical nature and size/morphological characteristics of plastic particles ≥ 10 μm according to a highly automated and time-effective approach. LDIR employs the latest semiconductor Quantum Cascade Laser (QCL) technology as infrared source, coupled with fast-scanning optics, to provide high-quality imaging and spectral data in the wavenumber range 975 – 1800 cm^{-1} (Dong et al., 2022; Liu et al., 2022). Despite its enormous advantages in terms of speed and automation of operations, this technique is still poorly studied for application on wastewater monitoring compared to more conventional spectroscopic techniques.

Bearing in mind above, a highly automated and time-effective Laser Direct InfraRed (LDIR)-based method was developed and fine-tuned within the framework of WP4.3 – Task 4.3.1 – for the detection and characterization of MPs in both raw and treated wastewater. Reliable experimental protocols and advanced analytical approaches were specifically designed and optimized to enhance the accuracy, reliability and reproducibility of MPs analysis, covering the entire workflow – from sampling to particle detection/characterization. Specially produced MPs were first used in the methodology development and validation stages. Well-established techniques were employed to evaluate the reliability of collected data. The robustness of the tailored protocols was then assessed by analyzing real wastewater samples taken at a large municipal WWTP in Tuscany (Italy).

The methodologies described in this chapter were then used within the project for cross-WP activities: in particular, the tailored protocols were applied for the large-scale monitoring of MPs in WWTPs, conducted in the framework of WP4.5 – Task 4.5.1, providing reliable and robust experimental and analytical tools to get valuable insights into the MPs behaviour across the urban water cycle.

4.3.2 Methodologies

4.3.2.1 Production of reference MPs

Specially produced MPs covering a broad range of polymer types, sizes and shapes were first used for methodology development and validation purposes. Particularly, reference particles were obtained by grinding common plastic items in ABS, PET and HDPE and then sieving them in the size range 38 – 106 µm. Synthetic aqueous samples to be tested as standards were obtained by dispersing known quantities of specially produced MPs (10 mg/L for each of the three polymers, i.e. ABS, PET and HDPE) in ultrapure water (**Figure 1**).

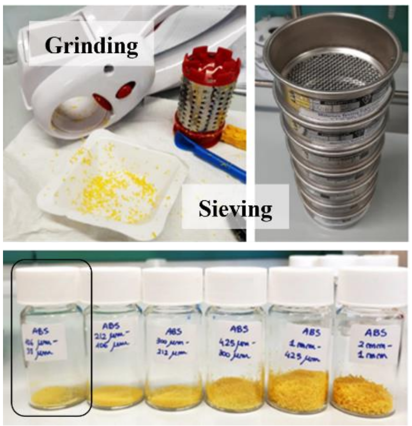

Figure 1: Specially produced MPs for methodology development and validation.

4.3.2.2 Sample processing for MPs extraction

A multi-stage pretreatment protocol was fine-tuned for MPs extraction. Samples were first subjected to chemical digestion by Fenton reaction for the removal of organics by adapting the protocol proposed by (Al-Azzawi et al., 2020). A density-based separation step was then provided to remove most of non-plastic particles. Digested samples were hence vacuum-filtered (nylon filter of 5 µm mesh size), recovering material retained on the filter by backwashing it with a 60 % (w/w) $ZnCl_2$ aqueous solution (ρ ≈ 1.65 g/cm^3). The eluate thus recovered (i.e. extracted particles in $ZnCl_2$ solution) was left in a glass separating funnel for 2 hours to ensure density separation of plastic particles (floating) and non-plastic particles (settling). The supernatant was collected and vacuum-filtered (nylon filter of 5 µm mesh size), while the extracted particles were recovered by filter backwashing with 5 mL ethanol (EtOH). At the end of the pretreatment procedure, particle dispersions in EtOH were thus obtained.

An additional step of concentration was provided before Fenton reaction in the case of real wastewater to increase the analysis representativeness: pristine samples were hence vacuum-filtered (nylon filter of 5 µm mesh size), recovering the material retained on the filter by backwashing it with a lower volume of ultrapure water. The concentrated wastewater samples were then pretreated following the method described above (i.e. Fenton reaction + density-based separation + vacuum-filtration/backwashing).

The MPs recovery rate was estimated by applying the developed MPs extraction protocol on synthetic aqueous samples containing specially produced MPs: visible images of the filter after vacuum-filtration and backwashing were collected and compared by exploiting the LDIR-High magnification function, thus enabling particle counts over the subsequent treatment stages.

Chemical digestion is reported to potentially degrade plastic particles depending on the chemicals and operations used. The suitability of the selected chemical treatment was therefore addressed by collecting and comparing both Attenuated Total Reflectance-Fourier Transform Infrared (ATR-FTIR) and LDIR spectra of specially produced MPs before and after Fenton reaction. For more details on the acquisition workflow and parameters refer to the sections below. Significant alteration or degradation caused by Fenton reaction on the filter used for sample processing were ruled out by collecting and visually comparing high magnification-visible images of the filter before and after chemical digestion (**Figure 2**). Releases of nylon particles upon filtration were also excluded in preliminary experiments treating blank control samples.

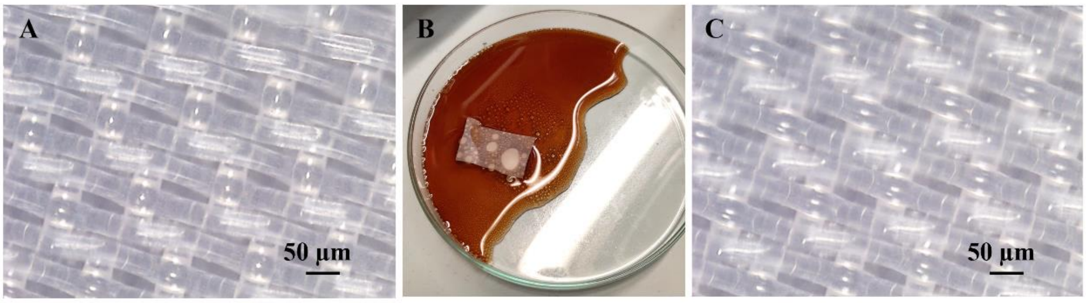

Figure 2: Visible image of the pristine filter used for sample processing (**A**), its chemical digestion by Fenton reaction (**B**) and visible image of the same filter and after chemical treatment (**C**).

4.3.2.3 Quality Assurance/Quality Control (QA/QC)

Quality Assurance and Quality Control (QA/QC) procedures were implemented to prevent cross- and self-contamination during all processing and analytical stages. The entire experimental procedures were carried out under a fume hood (covering apparatus with aluminum foil to minimize airborne plastics contamination during manipulation), all equipment were thoroughly rinsed before use, all reagents employed in the sample processing were preliminarily 0.8 µm-filtered and the usage of plastic materials was avoided as much as possible. Blank control samples – consisting of equivalent volumes of ultrapure water stored in the same collection tanks used for sampling – were subjected to all treatment stages provided for the experimental samples. MPs from self- and cross-contamination were considered during data analysis by applying a selective subtraction method. This method involved identifying and removing particles from the experimental dataset that closely corresponded to those found in the blank controls, following this matching approach: priority was given to polymer type, followed by size, and finally particle morphology.

4.3.2.4 Laser Direct InfraRed (LDIR)-based analysis for MPs counting and characterization

The analysis of MPs was carried out with an Agilent 8700 LDIR under the microplastic-dedicated workflow within the Agilent Clarity software (version 1.5.58). A total of 4 depositions of 5 µL each of the MPs dispersion in EtOH (for a total of 60 µL analyzed) were dropped on each microscope reflective slide (Kevley Low-e Microscope slide). The slides were placed in the sample base and left in a dust-free environment until ethanol evaporated. The base was introduced in the LDIR camera on the sample stage, which automatically moved to the sample compartment when the software was initiated. By selecting the "*Particle Analysis*" mode, the LDIR system automatically generates IR/high-resolution visible images and IR spectra of each particle detected within the selected portion of the slide. The acquisition workflow can be described as follows. The analysis initially provides counting and physical description of detected particles through a broad range of dimensional and geometrical parameters (**Table 1**) by rapidly scanning the sample area at a single wavenumber (1442 cm^{-1}) with the optics moving at high speed over the sample (*SCAN* mode). The system then switches to a *SWEEP* mode, with the optics parked at a single point over the sample, to collect full IR spectra of all detected particles in the wavenumber range between 975 and 1800 cm^{-1}. Spectra thus acquired are automatically cross-referenced with a built-in database provided by the Clarity software (Microplastics 2.0) for the real-time chemical identification. The quality of the spectral matching is expressed with the Hit Quality Index (*HQI*), a parameter ranging between 0 and 1 describing how closely the sample spectrum matches that in the reference library.

Table 1: Description of the geometrical and dimensional parameters provided by the LDIR-based particle analysis.

Parameter	Description
Width (w) and Height (h)	They are calculated by measuring the base and height of the rectangle, respectively, in which the particle is enclosed.
Area (A)	It is calculated based on the pixel enclosed by width and height.
Diameter (d)	It is calculated by equivalating the area A to the circle area by using equation $A = \pi \cdot d^2/4$
Aspect ratio (AR)	It is the ratio of width to height ($AR = w/h$)
Perimeter (p)	It is calculated as the length of the line that defines the boundary of the particle.
Eccentricity	It is geometric parameter characterizing the particle shape. It is equal to 0 for circles, while for ellipses it ranges from 0 to 1. A value close to 1 suggests a high aspect ratio.
Circularity	It measures how close to a circle the particle is. A perfect circle will have a circularity of 1, while other shapes will have a circularity < 1.
Solidity	It is calculated as the ratio of the particle area over the area of its convex hull. Therefore, a particle with a rectangle-like shape will have a high solidity (close to 1). A fiber that is curving will have a low solidity since its area is small compared to its bounding area.

The LDIR-based particle analysis workflow is summarized in **Figure 3**.

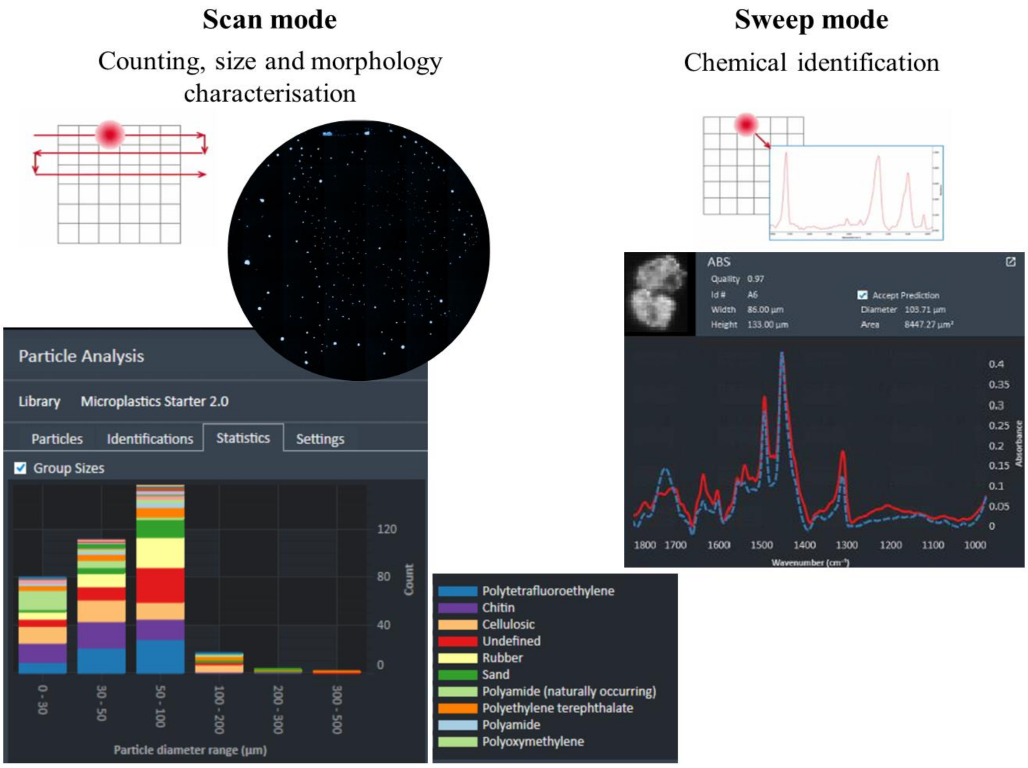

Quality 0.97
Id # A6
Width 86.00 μm
Height 133.00 μm
Diameter 103.71 μm
Area 8447.27 μm²

Figure 3: LDIR-based particle analysis workflow.

Once the particle analysis was completed, data were exported from the Clarity software and further processed as below. Only plastic particles < 5 mm chemically identified with a *HQI* ≥ 0.80 were considered, while non-plastic materials detected by LDIR (e.g. chitin, sand and natural polyamide) were excluded from elaboration. Different data elaboration scenarios were proposed including or not including particles recognized as "*Cellulosic*" by the LDIR-based particle analysis. In this regard, it is worth noting that this polymeric class is associated in the default spectral library with a large variety of cellulose-derived materials of both natural and chemically modified/semi-synthetic origins. As a function of the parameters *Circularity* and *Aspect Ratio* (*AR*) particles were classified into fibers ($AR \leq 0.33$ or $AR \geq 3$), spheres ($Circularity > 0.9$), pellets ($0.6 < Circularity \leq 0.9$) and fragments ($0.33 < AR < 3$ and $Circularity \leq 0.6$). A characteristic size was assigned to each particle depending on its morphology, i.e. maximum length (width / height) for fibers and diameter for all other particles.

In the case of wastewater samples, taking the recovery rate into account, the MPs concentrations in the collected 24-h composite samples were hence calculated and expressed as number of items per liter (MPs/L) net of the blank. Results related to characterization of detected particles in terms of polymer type, size and shape were reported as percentage data with respect to the total of MPs found in the sample under observation (Eq. 1):

$$MP_i\, relative\ abundance = \frac{n°\ MP_i}{n°\ MP_{TOT}} \cdot 100\% \tag{1}$$

where $n°\ MP_i$ is the number of particles of each polymer / size / morphology class and $n°\ MP_{TOT}$ is the total number of particles identified in the samples under observation.

4.3.2.5 Methodology validation on specially produced MPs

The robustness of data collected by LDIR-based particles analysis on standard samples produced as above was addressed by means of well-established techniques. Particularly, to validate the outcome of the LDIR measurements in terms of polymer identification, plastic particles were also analyzed by ATR-FTIR spectroscopy (IR-Affinity-1S, Shimadzu) by collecting spectra in the wavenumber range 600 – 4000 cm^{-1} (64 scans, resolution = 4 cm^{-1}, no spectrum correction applied) and comparing them with database and literature data. To be noticed that in the case of ATR-FTIR chemical assignment was carried out by manually comparing acquired spectra with literature data while LDIR performed it via automated spectrum matching with the built-in library. Additionally, the size distributions given by the LDIR-based particle analysis for the tested MPs dispersed in ultrapure water were compared to those acquired by using a laser diffraction method (Mastersizer 3000, with Hydro SM, Malvern Panalytical). The parameters set in the Mastersizer software were the following: particle geometry [non-spherical], refractive index [1.52], absorbance index [1], dispersant [water], number of replicates [20], agitation speed [1800 rpm] and density [1.04 g/cm^3 for ABS, 1.38 g/cm^3 for PET and 0.95 g/cm^3 for HDPE]. Three replicates were prepared and tested for each polymer (i.e. ABS, PET, HDPE) for both methods (LDIR and Mastersizer).

4.3.2.6 Methodology validation on wastewater samples

A large municipal WWTP in Tuscany (Italy) was preliminarily selected as case-study to assess the reliability and robustness of the proposed methodology. The plant, having a potentiality of 600000 PE, has in use a treatment train consisting of mechanical pretreatments, a biological treatment to remove organics and nitrogen, a chemical co-precipitation of phosphorous and a secondary settling stage to separate the clarified effluent from sewage sludge ($WWTP_A$). Average 24-h composite samples of raw wastewater (IN) and final effluent (OUT) were collected by autosamplers. Preliminary analyses were carried out to identify the minimum representative volume to be processed for MPs detection and characterization. To this aim, depending on the expected content of MPs in the sample under observation, aliquots of different volumes were collected from the 24-h composite IN and OUT samples, keeping them under continuous mechanical agitation to ensure homogeneity in the sub-sampling procedure (i.e. 0.1, 0.5 and 1 L for IN, and 1, 2 and 5 L for OUT), transferred into glass bottles and stored at 4 °C before being processed. For each volume aliquot, three sub-samples were collected and analyzed as above. The MPs concentrations of both IN and OUT samples were reported (net of the blank) as average value ± standard deviation among n. 3 replicates. The average MPs removal efficiency of the monitored WWTP was hence calculated as follows (Eq. 2):

$$Removal\ efficiency = \frac{C_{IN} - C_{OUT}}{C_{IN}} \cdot 100\% \tag{2}$$

where C_{IN} and C_{OUT} (MPs/L) are the average MPs concentrations detected in IN and OUT, respectively.

4.3.3 Results

4.3.3.1 Method development and validation on specially produced MPs

The multi-stage protocol for MPs extraction allowed an average particle recovery rate of 96 ± 4 % (**Figure 4**), in line and even higher compared to those reported in the literature (Bäuerlein et al., 2022; Hildebrandt et al., 2022).

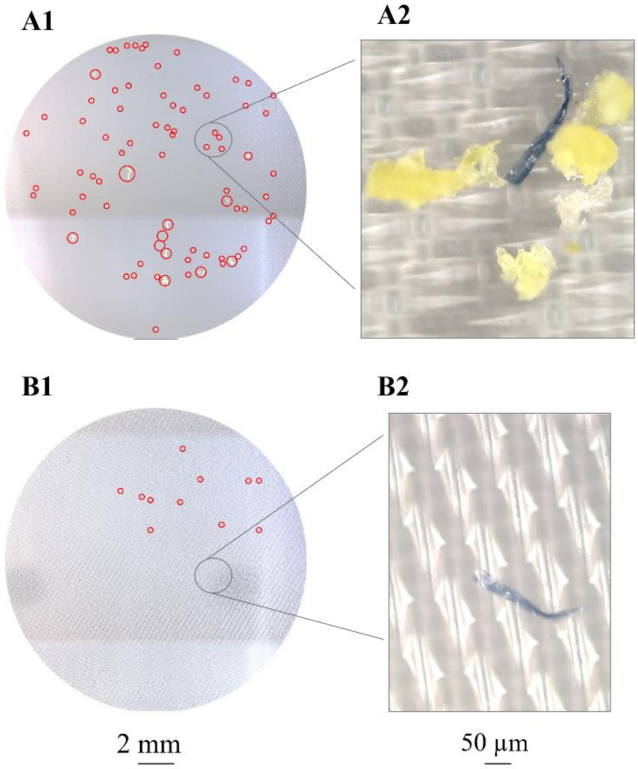

Figure 4: Determination of the particle recovery rate in experiments carried out by treating aqueous samples containing ABS, PET and HDPE particles sieved in the 38 – 106 µm size range (10 mg/L for each polymer) with the development pretreatment method. The figure shows the LDIR-derived visible images of the filter after vacuum-filtration (**A1**) and subsequent backwashing (**B1**) and high-magnification details of them (**A2** and **B2**, respectively). Particles that remained on the filter after filtration and backwashing are highlighted by red circles.

The spectra collected by ATR-FTIR and LDIR for the specially produced MPs in ABS, PET and HDPE displayed a good correspondence in their diagnostic peaks within the 975 – 1800 cm^{-1} spectral range (**Figure 5**). For more details on peak assignment refer to **Table A1** in *Appendix*. Both techniques hence confirmed the chemical nature of the tested plastic particles. Particularly, the targeted polymers were correctly identified by LDIR-based particle analysis with a high confidence level ($HQI \geq 0.95$), thus highlighting the reliability and robustness of the LDIR-based method, even if based on the collection of IR spectra in a limited spectral range (975 – 1800 cm^{-1}) with respect to ATR-FTIR spectroscopy. For both ATR-FTIR and LDIR analyses, no significant differences were found in the IR spectra of pristine and chemically digested MPs, meaning that Fenton reaction did not significantly alter the chemical nature of plastic particles. Indeed, it is documented in the literature that the use of Fenton reagent enables a rapid breakdown of organic compounds, significantly reducing reaction time compared to pure chemicals such as H_2O_2, without adversely affecting the integrity of MPs (Sun et al., 2019).

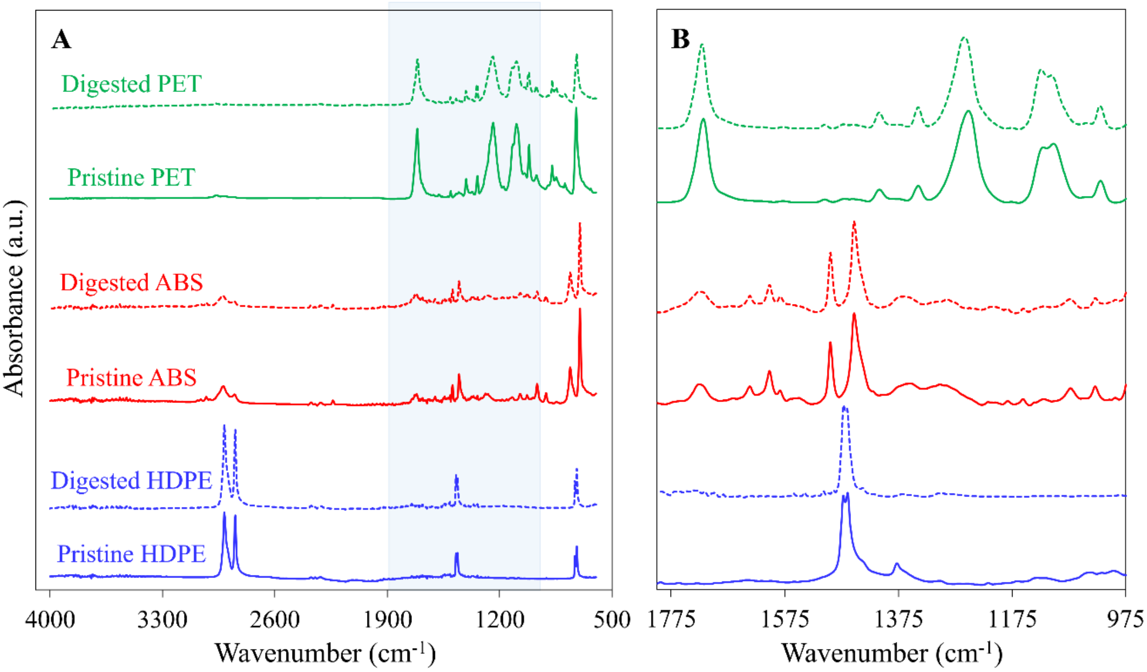

Figure 5: Spectra collected by ATR-FTIR (**A**) and LDIR-based particle analysis (**B**) before and after chemical digestion by Fenton reaction (in continuous and dotted lines, respectively) for ABS, PET and HDPE particles in red, green and blue, respectively. In sub-figure (**A**), the portion of ATR-FTIR spectra between 975 cm^{-1} and 1800 cm^{-1} where the LDIR acquisition is carried out is highlighted by a light blue rectangle (resolution = 4 cm^{-1} for both techniques).

Figures 6 shows the results of the LDIR-based particle analysis in terms of size and morphology distributions of specially produced MPs in ABS, PET and HDPE. Most of particles were found in the size range expected from sieving, i.e. 38 – 106 µm (61 %, 56 % and 59 % for ABS, PET and HDPE particles, respectively), thus suggesting the reliability of the LDIR-based particle analysis. However, size distributions broader than expected from sieving operations were observed. This can be reasonably due to the fact that particles in the form of fibers and/or fragments with elongated shape could more easily pass longitudinally through the sieve openings despite their length (Ziajahromi et al., 2017). On the other hand, other particles may not pass through the sieve even if sufficiently small due to their irregular morphology (Michielssen et al., 2016; Sun et al., 2019).

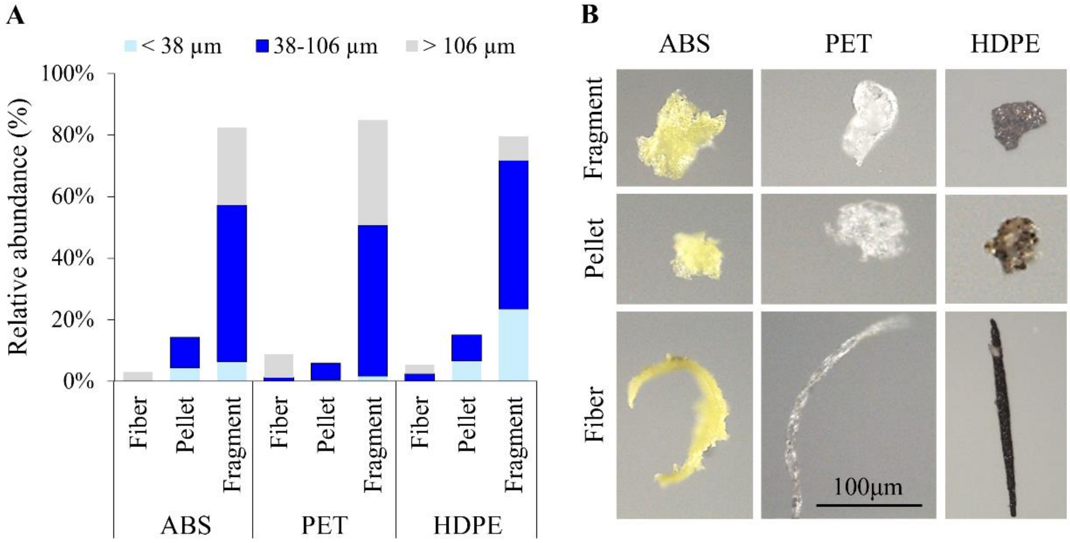

Figure 6: Size and shape cross-classification of ABS, PET and HDPE particles sieved in the 38 – 106 µm size range (**A**) and their visible images acquired by LDIR-High magnification (**B**). Data reported in sub-figure (**A**) refer to all particles analyzed, i.e. 468, 422 and 166 particles in ABS, PET and HDPE, respectively.

In this study, the particle size was determined according to a shape-dependent approach: maximum length of the rectangle enclosing the particle for fibers and diameter for the other morphologies (**Table 1**). However, diameter (D)-based size distributions were also reported to enable direct comparison with data obtained via Mastersizer in terms of characteristic diameters D10, D50 and D90 (**Table 2**). Minor discrepancies were found between the D50 median values, which were within the expected range from sieving (38 – 106 µm) for both methods, thus suggesting the reliability of the LDIR-based method for particle size assignment. Larger differences were observed for D10 and D90: this was likely influenced by the different measurement principles of the two methods. While the Mastersizer uses laser diffraction to assess particle size distribution, the LDIR system identifies particles and measures their dimension through infrared imaging of the sample area at a specific wavenumber (1442 cm^{-1}). Moreover, given the potential heterogeneity of the samples analyzed with each technique, slight variations in the measured size distributions were reasonable. Bearing in mind the above, the overall consistency of the results obtained with the two methods confirmed the reliability and robustness of the LDIR-based approach for the particle size analysis.

Table 2: Characteristic diameters D10, D50 and D90 obtained from the diameter-based particle size distributions acquired by both LDIR- and Mastersizer-based particle analyses. The comparative measurements were performed with synthetic aqueous samples containing ABS, PET and HDPE particles sieved in the 38 – 106 µm size range (10 mg/L for each polymer). D10, D50 and D90 represent the particle diameter for which 10 %, 50 % and 90 % of particles, respectively, are smaller.

Specially produced MPs	Mastersizer			LDIR		
	D10 (µm)	D50 (µm)	D90 (µm)	D10 (µm)	D50 (µm)	D90 (µm)
ABS	18	87	176	37	81	137
PET	37	98	299	52	92	177
HDPE	16	62	129	25	51	92

4.3.3.2 Methodology validation on wastewater samples

The minimum volume to be collected from the 24-h composite influent (IN) and effluent (OUT) samples to ensure representative MPs analysis was determined following the sub-sampling procedure described above (**Figure 7**). The representative volume is expected to be closely linked to the MPs concentration in the targeted matrix and should therefore be determined on a case-by-case basis. In general, lower MPs contents require larger sample volumes to be processed to enable reliable detection and quantification. A decreasing trend in the MPs concentration was observed in IN as the analyzed volume increased, indicating stabilization toward a representative value. This trend was less marked in OUT, suggesting that larger volumes may be necessary to capture the reasonably lower MPs content in the treated effluents. Based on this preliminary assessment, 1 L and 5 L aliquots were identified among the tested volumes as sufficiently representative for the methodological objectives of this study and thus selected for complete processing and characterization.

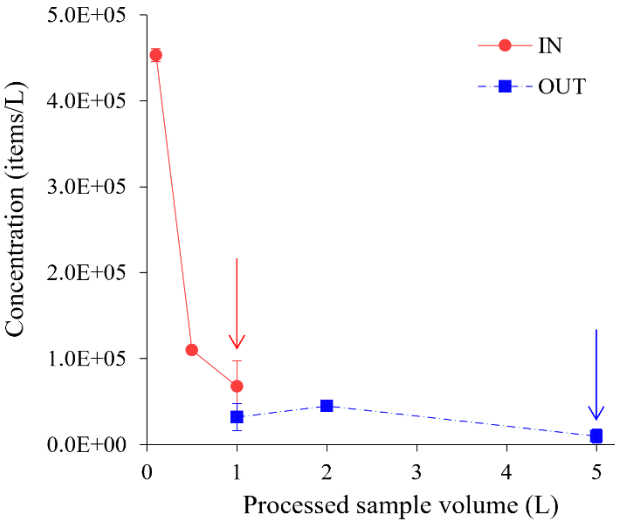

Figure 1: MPs concentrations (including cellulosic particles) estimated from the LDIR-based particle analyses for 24-h composite influent (IN) and effluent (OUT) samples as a function of the sub-sample volume processed (data presented as average value ± standard deviation among n. 3 replicates).

Referring to the most representative volume aliquots (**Figure 7**), the average particle concentrations found in the 24-h composite samples were $6.76\times10^4 \pm 3.00\times10^4$ MPs/L and $9.88\times10^3 \pm 8.21\times10^3$ MPs/L for IN and OUT, respectively. The relatively large standard deviations observed in the concentration data likely resulted from the discrete and non-uniform distribution of particles within the aqueous phase. In reason of that, despite the precautions adopted in the sub-sampling procedure, a certain degree of heterogeneity among the processed sub-samples is expected. Additionally, the small volume analyzed via LDIR – limited to 60 µL out of a total 5 mL EtOH dispersion containing the extracted MPs – may have contributed the observed variability, potentially hindering the accurate collection of the full particle size and type distribution in the sample under observation. These findings underscore the importance of accounting for both processed volume and potential distribution variability of sub-samples when interpreting quantitative MPs data, especially in matrices like wastewater.

Based on the concentration data presented above, an average removal efficiency of approximately 85 % was estimated for the monitored WWTP. This removal rate was in line with that reported for plant configurations not equipped with advanced tertiary treatment processes (Kardel et al., 2025). In contrast, more remarkable differences were highlighted in terms of MPs concentrations with respect to the available literature data. Indeed, among the reviewed scientific publications, the MPs concentrations typically range from only a few items per liter (Bayo et al., 2020; Pittura et al., 2021) to many thousands of items per liter (Hidayaturrahman & Lee, 2019; Simon et al., 2018) in raw wastewater, while decreasing by at least one order of magnitude in the final effluents. Such a huge variability can be attributed not only to the diverse WWTP-related conditions – such as wastewater source, type of sewer system, treatment configuration, etc. – but also to the different methods applied for MPs detection and characterization.

The cross-classification of particles found in the processed samples in terms of polymer type, size and shape is displayed in **Figure 8**. The polymers identified in both raw wastewater and final effluent likely originated from domestic discharges and urban runoff, given the plant served by a combined sewer system. The latter could help explain the notable presence of rubber particles, which accounted for approximately 20 % and 7 % of the total MPs in IN and OUT, respectively. One of the potential production paths for rubber particles is tire erosion across roads/highways in the urban area served by the plant (Jan Kole et al., 2017). Similarly, micro-sized rubber items could also be generated and dispersed directly in the treatment site due to vehicle traffic occurring within the plant itself. Among the various polymers detected, cellulosic items were the most prevalent in both IN and OUT, representing around 32 % and 54 % of the total particles, respectively. As previously discussed, this category includes both naturally occurring cellulose and chemically modified or semi-synthetic derivatives. The widespread occurrence of cellulose-based particles in wastewater is well-documented in the literature. Gies et al. (2018) reported that modified cellulose and cotton fibers represented about 59 % and 7 % of the chemically identified particles, respectively, in the influent of a large WWTP in Canada. Similarly, Talvitie et al. (2017) found that cotton and viscose fibers accounted for a substantial fraction – about 44 % and 9 %, respectively – of particles present at various treatment stages and in the final effluent of a WWTP in Finland. Cellulose-derived fibers are widely used in the textile industry, particularly for clothing production (Dris et al., 2018), and their presence in wastewater can largely be attributed to household laundry activities. In this study, cellulose-derived fibers accounted for 14 % of the total particles detected in IN, supporting the hypothesis that domestic washing machines are a key source of fibers entering the sewer system (Hernandez et al., 2017). Polypropylene (PP)-based fibers – comprising about 7 % of MPs in the influent – also could originate from synthetic textiles, further highlighting the contribution of domestic laundering to secondary MPs pollution, even in urban areas with limited industrial inputs (Becucci et al., 2022). In addition to rubber, PP, and cellulosic materials – which together represented more than 60 % of the particles detected in both raw and treated wastewater – other polymers such as PET, polytetrafluoroethylene (PTFE) and polyamide (PA) were also identified. These were likely associated with common consumer products including synthetic textiles, carpets, single-use plastic items, etc. Additionally, limited contents polymethyl methacrylate (PMMA) and polyurethane (PU) particles were observed exclusively in IN, thus indicating their complete removal over the treatment train. Regarding the morphological classification of detected MPs, it was found that the relative content of fibers – about 25 % and 39 % of total particles in IN and OUT, respectively – increased in the final effluent, thus suggesting the plant was less effective in removing this kind of items. Fragments represented approximately 43 % of the particles detected in IN, with their relative abundance decreasing down to 32 % in the final effluent. This trend is consistent with previous studies, which report that fragments, together with fibers, are among the most prevalent particle morphologies in wastewater. For instance, Liu et al. (2019) observed that the relative content of fragments in the samples collected from a large municipal WWTP in China ranged between 30 % and 46 % of MPs depending on the sampling point. Similarly, Becucci et al. (2022) found that fragments and fibers together accounted for about 77 % of MPs present in the final effluent of an Italian WWTP. In this study, no spherical particles were observed, supporting the hypothesis that most MPs discharged into wastewater had a secondary origin, likely formed through degradation and/or fragmentation of larger plastic items rather than being released as primary microbeads. Pellets represented about 32 % and 29 % of total particles in IN and OUT, respectively. Most of pellets were associated with the smallest size classes: particularly, 86 % and 63 % of them in IN and OUT, respectively, were smaller than 30 µm. Most particles identified in this study – approximately 80 % in both IN and OUT – had a characteristic size lower than 100 µm. In particular, particles < 30 µm represented a relevant fraction (45 % and 29 % in IN and OUT, respectively). These findings are in line with literature data. For example, Li et al. (2024) reported that only 3.3 – 5.1 % of MPs in raw wastewater and 6.2 – 23.0 % of MPs in final effluent exceeded 100 µm in size across three municipal WWTPs in China. It is worth noting that the particle size distributions are known to be influenced by the sampling methodology and, particularly, by the mesh size used in the case of filtration/sieving operations (Sun et al., 2019). In this study, the lowest detectable size was 10 µm considering both the mesh size employed for vacuum-filtered (5 µm) and the detection limit of the LDIR analytical system operating under its automated microplastic-dedicated workflow (10 µm). Comparison of IN and OUT data revealed that the WWTP was less effective in removing particles between 30 and 50 µm in size, the relative content of which almost doubled in the final effluent (from 14 % to 29 %). Similar trends are reported in the literature. For instance, Talvitie et al. (2017b) observed an increase in the percentage of MPs in the 20 – 100 µm size class from 40 % in the influent to 70 % in final effluent of a Finnish WWTP, while Liu et al. (2019) documented that MPs between 20 and 300 µm in size accounted for about 50 % and 73 % of particles found in the influent and effluent, respectively, of a Chinese WWTP. In this study, the relative abundance of particles < 30 µm decreased by 37 % in OUT. However, it should be considered that around 25 % of the particles smaller than 30 µm in size detected in the influent were composed of cellulose-based materials (**Figure 8**). When cellulosic particles were excluded from the dataset, it can be noted the relative content of this smallest size class (< 30 µm) increased from 29 % in IN to 54 % in OUT (**Figure 9**), thus suggesting a decreases in the removal efficiency towards MPs < 30 µm. This evidence highlights that the definition of polymers/materials to be included in the dataset for analysis can strongly influence the particle size distribution obtainable, thus representing a point of attention depending on the wastewater source and specific research goal.

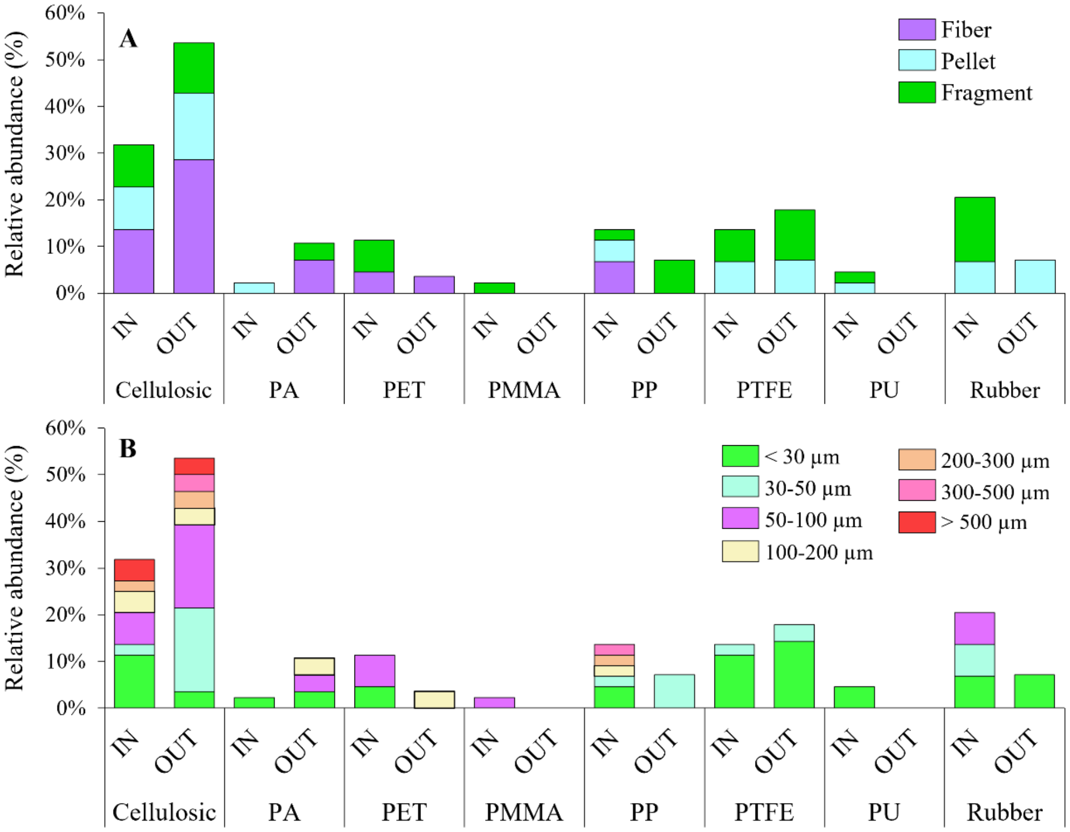

Figure 8: Chemical identification of particles detected in both raw and treated wastewater, which are in turn classified according to their morphology (**A**) and size (**B**). Data are presented as percentage relative contents referring to all particles found in the 1 L- and 5 L-aliquots of IN and OUT samples, respectively.

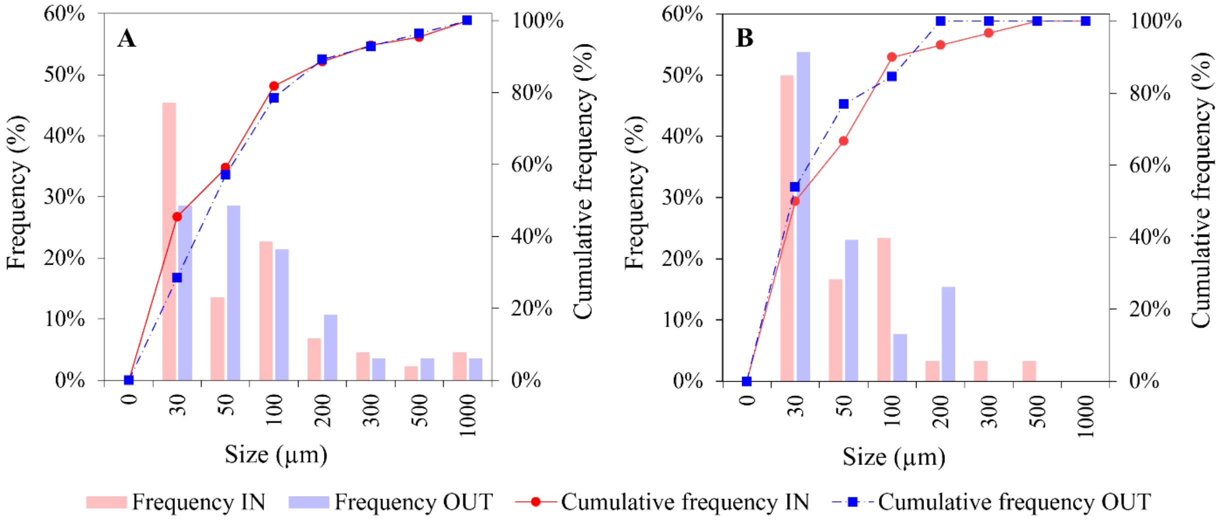

Figure 9: Size distribution of particles detected in IN and OUT samples considering two distinct datasets: one that includes cellulosic particles (**A**) and the other that excludes cellulosic particles (**B**).

Taking all the above into account, the results obtained showed coherent patterns, with no substantial discrepancies with respect to the existing literature framework. The trends observed in terms of MPs occurrence, fate and characteristics over the treatment train were consistent with the source of the analyzed wastewater and in line with the findings from previous scientific reports. This general agreement reinforces the reliability of the collected data and underscores the effectiveness of the LDIR-based method as a robust approach for detecting and characterizing MPs in both raw and treated wastewater.

4.3.3.3 Remarks on the applicability of the LDIR-based method for MPs analysis

All the results described above proved that LDIR is a suitable technique for the analysis of MPs in wastewater. One of the main advantages of this method is its time-effectiveness compared to more conventional spectroscopic techniques: the average measurement time per particle of the LDIR-based particle analysis is typically in the range between 6 and 9 s (Dong et al., 2022) and further decreases for particles > 50 µm. The duration of the overall sample analysis – including counting, physical description and chemical identification –strictly depends on the number, size and shape of the particles present. The decrease in the acquisition time is ascribed to the fact that the LDIR system uses a QCL as IR source coupled with fast-scanning optics to rapidly scans the sample area at a single wavenumber to locate, count and physically describe plastic particles before spectra acquisition (Scircle et al., 2020). With respect to other chemical imaging systems (e.g. FPA-based FTIR), LDIR can hence automatically focus on single particles, thus avoiding empty spaces present within the analyzed surface. The LDIR-based analysis provides complete characterization of particles present in the sample under observation through a fully automated workflow. Of major interest is the feasibility of collecting a broad range of size- and shape-related parameters (**Table 1**) that could be useful for modelling purposes, for instance to study the particle behaviour in the settling units.

On the other hand, at the development stage described in this chapter, the LDIR-based method presented many limitations, mainly related to the reliability of quantitative results obtained by analyzing small volume aliquots of the MPs dispersion in EtOH (on the order of 60 µL vs. 5 mL of total volume). This could increase the risk of collecting data that do not reflect the effective concentration and/or distribution of MPs, leading to potential underestimation or overestimation of their presence in the samples under observation, especially in the case of diluted matrices. Additionally, by placing only a few µL of sample on the reflective slides before analysis, the influence of cross-contamination from airborne MPs could be amplified. In the case of low-concentration samples, the small volumes analyzed may not provide sufficient data to guarantee statistical robustness, further affecting the reliability of the measurement. To overcome this critical issue, methodological advancements were provided in the analysis of a wide range of wastewater samples, as detailed in deliverable DV 4.5.2: in particular, the volume of the particle dispersion in EtOH analyzed by LDIR was increased up to reach stable and reliable quantitative assessments. Other implementations of the method proposed regarded its validation across a broader range of wastewater types – such municipal vs. industrial wastewater, effluent of different process units, etc. – as emerged from the more extensive monitoring campaigns carried out within the framework of WP4.5 – Task 4.5.1: this approach helped address the method versatility on distinct wastewater sources and treatment configurations, offering further insights into its potential across diverse real-world applications.

4.3.4 Conclusions

This study enabled the tailoring of a highly effective LDIR-based method for the identification and characterization of MPs in both raw and treated wastewater. The method was developed and validated through laboratory-scale trials by first using specially produced reference particles. Key outcomes from this first methodological stage included:

i. **High recovery efficiency**:

The processing protocol for MPs extraction – including vacuum-filtration and subsequent filter backwashing with EtOH – allowed to achieve a particle recovery rate of approximately 96 %.

ii. **Chemical integrity maintenance upon chemical digestion**:

Any significant degradation of MPs occurred during Fenton reaction, thus confirming the applicability of the selected chemical digestion method.

iii. **Reliable particle characterization**:

LDIR analysis accurately identified polymer types and size distributions, showing agreement with reference techniques such as ATR-FTIR and laser diffraction (Mastersizer).

The robustness of the proposed methodological approach was further proved by collecting and analyzing real wastewater samples from a large municipal WWTP. The results of the monitoring campaign in terms of particle concentrations / characteristics and removal efficiency were in line with the existing literature framework and consistent with the source of the analyzed wastewater, thus strengthening the reliability of the protocols applied.

In conclusion, this work helped overcome some of the methodological limitations currently hindering the research on MPs, by providing an accurate, automated, reproducible and time-efficient approach for their quantification in wastewater. The protocols developed in this study would therefore offer a robust and scalable framework for the routine monitoring of MPs across the entire wastewater treatment system, paving the way for more accurate assessments of their environmental pathways.

4.3.5 References

Al-Azzawi, M. S. M., Kefer, S., Weißer, J., Reichel, J., Schwaller, C., Glas, K., Knoop, O., & Drewes, J. E. (2020). Validation of sample preparation methods for microplastic analysis in wastewater matrices-Reproducibility and standardization. Water, 12(9), 2445. https://doi.org/10.3390/w12092445

Andrés, M.S., Chércoles, R., Navarro, E., de la Roja, J.M., Gorostiza, J., Higueras, M., & Blanch, E. (2023). Use of 3D printing PLA and ABS materials for fine art. Analysis of composition and long-term behaviour of raw filament and printed parts. Journal of Cultural Heritage, 59, 181–189. https://doi.org/10.1016/j.culher.2022.12.005

Bäuerlein, P. S., Hofman-Caris, R. C. H. M., Pieke, E. N., & ter Laak, T. L. (2022). Fate of microplastics in the drinking water production. Water Research, 221, 118790. https://doi.org/10.1016/j.watres.2022.118790

Bayo, J., Olmos, S., & López-Castellanos, J. (2020). Microplastics in an urban wastewater treatment plant: The influence of physicochemical parameters and environmental factors. Chemosphere, 238. https://doi.org/10.1016/j.chemosphere.2019.124593

Becucci, M., Mancini, M., Campo, R., & Paris, E. (2022). Microplastics in the Florence wastewater treatment plant studied by a continuous sampling method and Raman spectroscopy: A preliminary investigation. Science of the Total Environment, 808, 152025. https://doi.org/10.1016/j.scitotenv.2021.152025

Bernardino, C. A. R., Mahler, C. F., Fernandes, J. O., Lopes, C. S. C., Braz, B. F., Archanjo, B. S., Santelli, R. E., & Cincotto, F. H. (2023). Evaluation of microplastic contamination by metals in a controlled environment: A risk to be considered. Environmental Monitoring and Assessment, 195, 691. https://doi.org/10.1007/s10661-023-11389-1

Chaudhary, A. K., & Vijayakumar, R. P. (2020). Effect of chemical treatment on biological degradation of high-density polyethylene (HDPE). Environment, Development and Sustainability, 22, 1093–1104. https://doi.org/10.1007/s10668-018-0236-6

Dong, M., She, Z., Xiong, X., Ouyang, G., & Luo, Z. (2022). Automated analysis of microplastics based on vibrational spectroscopy: are we measuring the same metrics? Analytical and Bioanalytical Chemistry, 414, 3359–3372. https://doi.org/10.1007/s00216-022-03951-6

Dris, R., Gasperi, J., Rocher, V., & Tassin, B. (2018). Synthetic and non-synthetic anthropogenic fibers in a river under the impact of Paris Megacity: Sampling methodological aspects and flux estimations. Science of the Total Environment, 618, 157–164. https://doi.org/10.1016/j.scitotenv.2017.11.009

Gies, E. A., LeNoble, J. L., Noël, M., Etemadifar, A., Bishay, F., Hall, E. R., & Ross, P. S. (2018). Retention of microplastics in a major secondary wastewater treatment plant in Vancouver, Canada. Marine Pollution Bulletin, 133, 553–561. https://doi.org/10.1016/j.marpolbul.2018.06.006

Hernandez, E., Nowack, B., & Mitrano, D. M. (2017). Polyester Textiles as a Source of Microplastics from Households: A Mechanistic Study to Understand Microfiber Release during Washing. Environmental Science and Technology, 51(12), 7036–7046. https://doi.org/10.1021/acs.est.7b01750

Hidayaturrahman, H., & Lee, T. G. (2019). A study on characteristics of microplastic in wastewater of South Korea: Identification, quantification, and fate of microplastics during treatment process. Marine Pollution Bulletin, 146, 696–702. https://doi.org/10.1016/j.marpolbul.2019.06.071

Hildebrandt, L., El Gareb, F., Zimmermann, T., Klein, O., Kerstan, A., Emeis, K.C., & Pröfrock, D. (2022). Spatial distribution of microplastics in the tropical Indian Ocean based on laser direct infrared imaging and microwave-assisted matrix digestion. Environmental Pollution, 307, 119547. https://doi.org/10.1016/j.envpol.2022.119547

Jan Kole, P., Löhr, A. J., Van Belleghem, F. G. A. J., & Ragas, A. M. J. (2017). Wear and tear of tyres: A stealthy source of microplastics in the environment. International Journal of Environmental Research and Public Health, 14(10), 1265. https://doi.org/10.3390/ijerph14101265

Kardel, F., Saedi, Z., Fouladiestarabadi, A., Babanezhad, D., & Abbasi, S. (2025). The abundance, removal efficiency, and characteristics of microplastics in three urban wastewater treatment plants (WWTPs) on the southern coast of the Caspian Sea. Environmental Monitoring and Assessment, 197(1), 108. https://doi.org/10.1007/s10661-024-13525-x

Kauts, S., Mishra, Y., Yousuf, S., Bhardwaj, R., Singh, S. K., Alshabrmi, F. M., Abdurahman, M., Vamanu, E., & Singh, M. P. (2023). Toxicological Profile of Polyethylene Terephthalate (PET) Microplastic in Ingested Drosophila melanogaster (Oregon R+) and Its Adverse Effect on Behavior and Development. Toxics, 11(9), 782. https://doi.org/10.3390/toxics11090782

Li, Y., Qin, T., Bai, X., Wu, W., Chen, X., Shen, M., Qin, L., Dou, Y., & Duan, X. (2024). Occurrence and Removal of Microplastics in Tertiary Wastewater Treatment Plants: A Case Study of Three Plants in Zhengzhou, China. Processes, 12(4), 803. https://doi.org/10.3390/pr12040803

Liu, N., Cheng, S., Wang, X., Li, Z., Zheng, L., Lyu, Y., Ao, X., & Wu, H. (2022). Characterization of microplastics in the septic tank via laser direct infrared spectroscopy. Water Research, 226, 119293. https://doi.org/10.1016/j.watres.2022.119293

Liu, X., Yuan, W., Di, M., Li, Z., & Wang, J. (2019). Transfer and fate of microplastics during the conventional activated sludge process in one wastewater treatment plant of China. Chemical Engineering Journal, 362, 176–182. https://doi.org/10.1016/j.cej.2019.01.033

Michielssen, M. R., Michielssen, E. R., Ni, J., & Duhaime, M. B. (2016). Fate of microplastics and other small anthropogenic litter (SAL) in wastewater treatment plants depends on unit processes employed. Environmental Science: Water Research and Technology, 2(6), 1064–1073. https://doi.org/10.1039/c6ew00207b

Murphy, F., Ewins, C., Carbonnier, F., & Quinn, B. (2016). Wastewater Treatment Works (WwTW) as a Source of Microplastics in the Aquatic Environment. Environmental Science and Technology, 50(11), 5800–5808. https://doi.org/10.1021/acs.est.5b05416

Peñalver, R., Arroyo-Manzanares, N., López-García, I., & Hernández-Córdoba, M. (2020). An overview of microplastics characterization by thermal analysis. Chemosphere 242, 125170. https://doi.org/10.1016/j.chemosphere.2019.125170

Pittura, L., Foglia, A., Akyol, Ç., Cipolletta, G., Benedetti, M., Regoli, F., Eusebi, A. L., Sabbatini, S., Tseng, L. Y., Katsou, E., Gorbi, S., & Fatone, F. (2021). Microplastics in real wastewater treatment schemes: Comparative assessment and relevant inhibition effects on anaerobic processes. Chemosphere, 262, 128415. https://doi.org/10.1016/j.chemosphere.2020.128415

Scircle, A., Cizdziel, J. V., Tisinger, L., Anumol, T., & Robey, D. (2020). Occurrence of microplastic pollution at oyster reefs and other coastal sites in the Mississippi sound, USA: Impacts of freshwater inflows from flooding. Toxics, 8(2), 35. https://doi.org/10.3390/TOXICS8020035

Simon, M., van Alst, N., & Vollertsen, J. (2018). Quantification of microplastic mass and removal rates at wastewater treatment plants applying Focal Plane Array (FPA)-based Fourier Transform Infrared (FT-IR) imaging. Water Research, 142, 1–9. https://doi.org/10.1016/j.watres.2018.05.019

Sun, J., Dai, X., Wang, Q., van Loosdrecht, M. C. M., & Ni, B. J. (2019). Microplastics in wastewater treatment plants: Detection, occurrence and removal. Water Research, 152, 21–37. https://doi.org/10.1016/j.watres.2018.12.050

Talvitie, J., Mikola, A., Setälä, O., Heinonen, M., & Koistinen, A. (2017). How well is microlitter purified from wastewater? – A detailed study on the stepwise removal of microlitter in a tertiary level wastewater treatment plant. Water Research, 109, 164–172. https://doi.org/10.1016/j.watres.2016.11.046

Ziajahromi, S., Neale, P. A., Rintoul, L., & Leusch, F. D. L. (2017). Wastewater treatment plants as a pathway for microplastics: Development of a new approach to sample wastewater-based microplastics. Water Research, 112, 93–99. https://doi.org/10.1016/j.watres.2017.01.042

4.3.6 Scientific products and dissemination

Pagliaccia, B., Ascolese, M., Vannini, E., Carretti, E., Lubello, C., Gori, R. (2025). Methodologic insights aimed to set-up an innovative Laser Direct InfraRed (LDIR)-based method for the detection and characterization of microplastics in wastewaters, Science of The Total Environment 967, 178817. https://doi.org/10.1016/j.scitotenv.2025.178817

Pagliaccia, B., Ascolese, M., Lubello, C., Dugheri, S., Caffaz, S., Fibbi, D., Gori, R., Insights on the fate and removal of microplastics and microparticles in wastewater treatment plants, ECOMONDO, 3–6/11/2025, Rimini (Italy). Oral presentation.

Pagliaccia, B., Ascolese, M., Lubello, C., Dugheri, S., Fibbi, D., Gori, R., Insights on the fate and removal of microplastics in wastewater treatment plants: Unveiling the impact of textile industry, Symposium on Microplastics in the Environment and Water, 18–19/09/2025, Singapore. Oral presentation.

Pagliaccia, B., Ascolese, M., Vannini, E., Fibbi, D., Carretti, E., Lubello, C., Gori, R., Development of an innovative Laser Direct InfraRed (LDIR)-based methodology for monitoring microplastics in wastewater treatment plants, XII International Symposium on Environmental Engineering (SIDISA 2024), 1–4/10/2024, Palermo (Italy). Oral presentation.

4.4 Spatial distribution, contamination index, and geochemical baseline of trace elements in Sicilian soils (UNIPA)

Contributors: D. Varrica, M.G. Alaimo, D. Piazzese

4.4.1 Introduction

Soil plays a crucial role in ecosystems as it is a dynamic habitat that supports a variety of biological processes. The topsoil layer is of particular interest as degradation may occur due to atmospheric deposition, anthropogenic activities, and/or natural geochemical processes. In this study, the Sicily region, known for its significant lithological heterogeneity, was selected as a pilot site to define reference values for major, trace elements, and REEs in topsoils. The lack of analytical data on current topsoil conditions led to the selection of the Sicily region. The methodological approach used represents the first attempt to define the regional geochemical baseline (Varrica et al. 2024). The samples were analyzed for major (Ca, Fe, K, Mg, Mn, Na, P, Sr, and Ti) and trace (B, Ba, Bi, Co, Li, Ni, Rb, Se, and U) elements, and Rare Earth Elements. The objectives of this research include the following: 1) establish baseline values: determine the natural concentrations of major, trace, and rare earth elements (REE) in unpolluted soils; 2) spatial distribution mapping: analyze and map the spatial variability of these elements in the study area, and predict the distribution of each element's concentrations, even in unsampled areas.

4.4.2 Methodologies

A total of 83 topsoil samples (depth of 0-20 cm) were collected far from anthropogenic sources (i.e., extra-urban roads, urban areas, industrial areas, cultivated land) in the Sicilian territory. Data were analyzed statistically, and all tests were considered significant at $p<0.05$ using the software XLSTAT and ProUCL 5.1 software. Regional Geochemical Baseline (RGB) values for major, trace elements, and REEs were determined using a statistical approach by the UTL95-95 BCA Bootstrap method. The spatial distribution of the elements was determined through stochastic simulations on a convex-concave boundary at a 5 km resolution, yielding detailed geochemical maps that predict each element's concentration even in unsampled areas.

4.4.3 Results

The distribution patterns of major and trace elements are closely linked to the geological features of the area. The calculated Regional Geochemical Baseline (RGB) values are below the Italian and GEMAS regulatory limits, indicating that the regional approach provides more specific and significant indications than the European and Italian reference values. The contamination status of the topsoil layer was assessed by comparing several contamination indicators, including the Enrichment Factor (EF), Contamination Factor (CF), Geoaccumulation Index (I_{geo}), and Pollution Load Index (PLI). All indices highlight an uncontaminated condition. A geostatistical approach was used to produce spatial geochemical maps, which allow the prediction of element distributions in unsampled areas. The spatial geochemical distribution maps of each element in the topsoil provide valuable information about their concentrations, distributions, and origins. The determination of RGB values and the production of detailed geochemical maps can provide essential support to local authorities in managing soil contamination in Sicily.

4.4.4 Scientific products and dissemination

Federica Lo Medico, Daniela Varrica, Marino Vetuschi Zuccolini, Marianna Miola, Giovanna Scopelliti, Maria Grazia Alaimo (2025). Geochemical baseline values and spatial distribution of major, trace, and rare earth elements in unpolluted soils of the Sicily region (Italy). Environ Geochem Health 47:167
https://doi.org/10.1007/s10653-025-02475-z

4.5 Monitoring and modelling of MPs diffusion at river basin scale (UNIFI)

Contributors: C. Lubello, B. Pagliaccia, R. Gori

4.5.1 Introduction

Microplastics (MPs) are recognized as ubiquitous contaminants in all environmental compartments, raising increasing concerns due to their potential adverse effects on living organisms and ecosystems. Wastewater treatment plants (WWTPs) represent one of the main pathways through which they enter freshwater systems. Even in the absence of dedicated process units, WWTPs are typically reported to be effective in removing MPs, trapping most of them into sewage sludge. The fate and removal of MPs within treatment trains is expected to be governed by a complex interplay of factors – including plant configuration, operating conditions, sewer system characteristics and physical/chemical properties of particles themselves – thus highlighting the need for ongoing research to advance the current state-of-the-art knowledge. Despite the relatively high removal performance, the absolute loads of MPs released into receiving water bodies with treated effluents could remain substantial, given the large volumes of wastewater processed daily. To date, comprehensive mass-balance assessments at the river basin scale are still poorly unexplored. In this context, the present study aimed to estimate the cumulative MPs emissions from wastewater sources across the Arno River basin (Tuscany, Italy), providing valuable insights into the contribution of WWTPs to the MPs contamination of freshwater ecosystems. Despite the specific case-study proposed, the significance of this work might be also found in the development of a versatile and robust methodological framework for river basin-scale assessments, that can be readily adapted to other catchments and used for multiple purposes.

It is wort noting that part of the activities described in this chapter were carried out in close synergy with WP4.5 – Task 4.5.1. A common data framework was shared between the two work packages and jointly interpreted from complementary perspectives. In particular, the monitoring campaigns generated a much larger dataset than that required for the river basin-scale elaboration performed in WP4.3. While the present study relies exclusively on raw wastewater and final effluent data, the achievements of activities conducted within WP4.5 – Task 4.5.1 – are based on additional measurements collected at multiple sections along both the wastewater and sludge treatment lines, providing deeper insights into the fate, occurrence and behavior of MPs and other microparticles of interest within WWTPs.

4.5.2 Methodologies

An integrated suite of analytical and experimental tools was employed to estimate the fluxes of MPs emitted from wastewater (WW) discharges into the Arno river basin. Particularly, the river basin-scale assessments were based on a deterministic approach which combined literature and multi-site field data.

4.5.2.1 Literature review

An extensive literature review was carried out to strengthen and extend the outcome of the monitoring campaigns. In total, 41 peer-reviewed scientific publications addressing the occurrence and fate of MPs in WWTPs were examined. For each study, the following categories of information were collected:

- Details on the plant in terms of population served, treatment configuration, wastewater source, etc.;
- Sampling, pretreatment and analytical methods applied for MPs detection and characterization;
- MPs concentrations at different stages along the wastewater treatment train (expressed as number of items per liter);
- MPs removal efficiencies, expressed as overall performance and, where available, as stage-specific removal rates.

The large set of literature data thus obtained was further processed to provide a comprehensive assessment of the current state-of-the-art knowledge regarding the presence and removal of MPs in a variety of wastewater treatment configurations.

4.5.2.2 *Monitoring campaigns*

Monitoring campaigns were conducted at three WWTPs within the Arno river basin (**Table 1**): the selected facilities had major differences in terms of treatment trains in use and WW source (municipal vs. industrial), thus enabling a broader evaluation of the removal efficiency exerted by different treatment configurations and the influence of specific industrial contributions. In particular, $WWTP_B$ and $WWTP_C$ were selected as reference plants for assessing the level of MPs pollution coming from the textile and tanning industrial districts, respectively, which are two of the main industrial areas within the river catchment.

24-h composite samples of raw wastewater (IN) and treated effluent (OUT) were collected through autosamplers at the selected WWTPs. These samples were then transferred to the laboratory for processing and analysis, thus acquiring a complete set of data concerning not only the MPs concentrations – expressed as number of items per liter [MPs/L] – but also their distributions in terms of chemical composition and geometrical features. To this aim, a reliable and robust method based on the recently introduced Laser Direct InfraRed (LDIR) chemical imaging technique was specifically developed and fined-tuned within the project. LDIR uses the latest quantum cascade laser technology, coupled with fast-scanning optics, to provide high-quality images and spectral data in the wavenumber range from 975 to 1800 cm^{-1}. The microplastic-dedicated LDIR workflow first provides a rapid imaging of sample area by using an IR light at a single wavenumber instead of visible cameras to locate, count and describe size and shape of particles. For each detected particle, full spectra are then acquired, while chemical identification is automatically carried out via real-time spectral matching with built-in libraries (Dong et al., 2022; Liu et al., 2022; Samandra et al., 2022; Scircle et al., 2020). The method therefore allows quantification and comprehensive characterization of MPs ≥ 10 µm through a fully automated workflow and with measuring times significantly reduced compared to more conventional spectroscopic techniques. Of major interest is its feasibility of acquiring a broad set of data concerning size and shape of detected particles, which could be used for modelling and predicted analyses. For more details on pretreatment and analytical methods applied refer to deliverable the related section in this deliverable. Briefly, sample processing for MPs extraction consisted of a multi-stage protocol including (i) sample concentration by vacuum-filtration (5 µm-mesh), (ii) Fenton reaction for organic matter digestion, (iii) density-based separation for inorganics removal and (iv) particle recovery by vacuum-filtration and subsequent filter backwashing with ethanol (EtOH). Quality Assurance and Quality Control (QA/QC) procedures – including the analysis of blank control samples – were implemented to prevent (and quantify) cross- and self-contamination during all sampling, processing and analytical stages. The particle dispersion in EtOH was analyzed by LDIR for MPs quantification and characterization. Data on chemical assignments were directly used to determine the polymer distribution of detected particles. Regarding size and morphology characterization, based on the parameters aspect ratio and circularity given by LDIR-based particle analysis, MPs were classified into fibers (aspect ratio ≥ 3 or ≤ 0.33), spheres (circularity ≥ 0.9), pellets ($0.6 \leq$ circularity < 0.9) and fragments ($0.33 <$ aspect ratio < 3; circularity < 0.6) (Liu et al., 2022), and a characteristic size was assigned to each of them (i.e. maximum length for fibers and equivalent diameter for the other shapes). Data analysis finally focused on defining the MPs budget across the treatment trains and assessing their removal efficiency. In the framework of this work, the evaluations were limited exclusively to MPs, excluding all kinds of cellulosic microparticles found in the processed samples.

Shape-dependent models available in the literature (Barchiesi et al., 2023; Simon et al., 2018) were applied to predict the volume of each particle i found in the processed samples (V_i, μm^3) by exploiting the numerous 2D geometrical parameters given by the LDIR-based particle analysis. Knowing the density of particle i (ρ_i, g/cm^3) and its volume, particle mass (m_i, g) was easily calculated: $m_i = V_i \cdot \rho_i$: in this way, numerical concentrations [MPs/L] were converted to a mass basis [µg MPs/L].

Table 1: Brief description of the monitored WWTPs in terms of wastewater source, design capacity and treatment train.

	WWTP$_A$	**WWTP$_B$**	**WWTP$_C$**
Wastewater source	Municipal	Municipal + industrial (textile)	Municipal + industrial (tanning)
Design capacity	600000 PE	900000 PE	850000 PE
Treatment train	• Physical pretreatments • Biological section for organics and nitrogen removal (activated sludge) + phosphorus co-precipitation	• Physical pretreatments • Primary sedimentation • Biological section for organics and nitrogen removal (activated sludge) • Coagulation-flocculation • Final ozonation • Refining section for water reclamation	Line S2 (municipal + industrial WW): • Physical pretreatments • Primary sedimentation • Biological section for organics and nitrogen removal (activated sludge) • Coagulation-flocculation • Final ozonation Line S2 (municipal WW): • Physical pretreatments • Membrane bioreactor (MBR) section • Deoxygenation

4.5.2.3 Data elaboration at river basin scale

Data elaboration at river basin scale was carried out with a differentiate approach depending on the wastewater (WW) source.

In the case of both untreated municipal WW and treated municipal WW with negligible industrial inputs (i.e. conveyed to WWTPs receiving only urban discharges), the following approach was applied. All the WW discharges were first classified based on their population served (as population equivalent, PE) and treatment train in use. In total, 1783 WW discharges, with a sewer coverage of 93 % (as PE), were identified and used for analysis (**Figure 1**). WWTP$_A$ (**Table 1**) is the largest municipal WWTP among those reported in **Figure 1** and it was strategically selected as reference urban plant within the basin for conducting dedicated monitoring campaigns. The results obtained by analyzing raw wastewater samples from WWTP$_A$ were considered representative of all mapped discharges: the hypothesis was therefore that all municipal WW in **Figure 1** had the same average MPs (numerical / mass) concentration of that revealed for WWTP$_A$. The value of the MPs flux entering WWTP$_A$ ($Q_{MPs,IN,REF}$) – calculated on both numerical basis [MPs/y] and mass basis [tons MPs/y] – was therefore associated with all WW discharges in **Figure 1** and then scaled according to their respective population served (as PE). In the case of treated WW, this value was reduced by an average removal efficiency estimated from literature data ($\%Removal$), depending on the treatment train in use. The total MPs (mass / numerical) load emitted at river basin scale was finally calculated as the sum of the contributions of all recorded WW discharges according to Eqs. 1 – 3:

$$MPs\ mass\ discharge_i = Q_{MPs,IN,REF} \cdot PE_i/538378 \tag{1}$$

$$MPs\ mass\ discharge_i = Q_{MPs,IN,REF} \cdot (1\ - \%Removal\,) \cdot PE_i/538378 \tag{2}$$

$$Total\ MPs\ mass\ discharge = \textstyle\sum_{i=1}^{n} MPs\ discharge_i + \ \sum_{j=1}^{m} MPs\ discharge_j \tag{3}$$

where:

- $MPs\ mass\ discharge_i$ [MPs/y or tons MPs/y] is the MPs load emitted into the river basin by the untreated municipal WW discharge i (with i=1, …, n);
- $MPs\ mass\ discharge_j$ [MPs/y or tons MPs/y] is the MPs load emitted into the river basin by the treated municipal WW discharge j (with i=1, …, m);
- PE_i [PE] is the population served by the untreated municipal WW discharge i;
- PE_j [PE] is the population served by the treated municipal WW discharge j;
- 538378 [PE] is the population served by the reference plant WWTP$_A$.

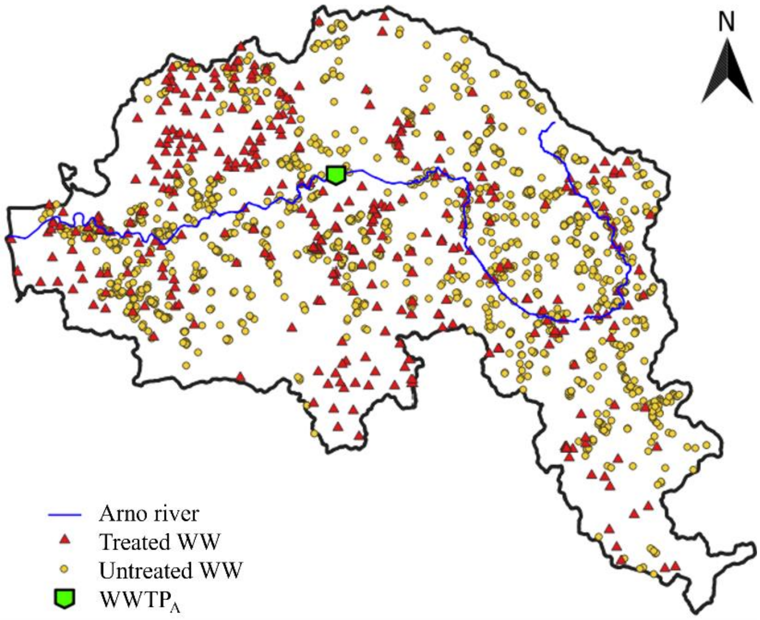

Figure 1: Treated and untreated municipal wastewater discharges in the Arno river basin geo-referenced in QGIS environment. Treated wastewater discharges refer to WWTPs treating only urban wastewater with negligible industrial inputs.

A similar approach was applied to estimate the MPs emissions at river basin scale from WWTPs treating both municipal and industrial wastewater. The analysis focused on three major industrial districts within the study area, including textile, leather-tanning and paper factories, respectively. The plants serving the three targeted industrial areas were classified according to their processed inflow, design capacity and treatment configuration. For the textile and leather-tanning districts, the assessment was based on the results emerged from the monitoring campaigns conducted at the corresponding reference plants, i.e. WWTP$_B$ and WWTP$_C$, respectively (**Table 1**): the average MPs concentrations found in both (untreated) municipal and industrial wastewater of WWTP$_B$ and WWTP$_C$ were hence assigned to all WW discharges across the respective districts. For the paper industrial area, where no field data were available, the average MPs concentrations in the industrial WW were estimated from literature data (47218 MPs/L / 21291 µg MPs/L; Steinfeld et al., 2025). The average MPs fluxes entering the plants within the targeted industrial districts were therefore calculated. For each plant, the MPs load emitted at river basin scale was finally estimated by applying an average removal efficiency derived from the collected literature dataset based on the specific treatment configuration in use. The overall MPs emissions in the Arno river basin were therefore calculated and expressed on both numerical basis [MPs/y] and mass basis [tons MPs/y], highlighting the impact of different WW sources.

4.5.3 Results

4.5.3.1 Literature review

The literature survey revealed a substantial variability in the MPs concentrations reported for both raw and treated wastewater, with values ranging from only a few items per liter (Bayo et al., 2020; Long et al., 2019; Magni et al., 2019; Pittura et al., 2021) to several thousand items per liter (Hidayaturrahman and Lee, 2019; Simon et al., 2018) (**Table A1** in *Appendix*). These discrepancies can be ascribed not only to the different site-specific conditions, such as type of sewer system, wastewater source, treatment train in use, etc., but also to the highly diverse sampling, pretreatment and analytical methods applied for particle detection and characterization (Sun et al., 2019). However, common trends were identified referring to the percentage removals across different treatment configurations that evidenced a higher consistency among the reviewed scientific reports (**Figure 2**). Specifically, the average removal efficiencies emerged from literature data for plants based on primary, secondary, tertiary and quaternary treatments were 66.2 ± 20.0, 89.0 ± 11.1, 93.1 ± 8.7 and 97.5 ± 3.2 %, respectively. For each treatment class, efficiency appeared strictly dependent on the process units applied. These removal patterns highlighted how the application of advanced technologies for wastewater treatment would contribute to significantly decrease the MPs load discharged into receiving water body, with the best performances typically recorded in the case of membrane-related processes (Talvitie et al., 2017).

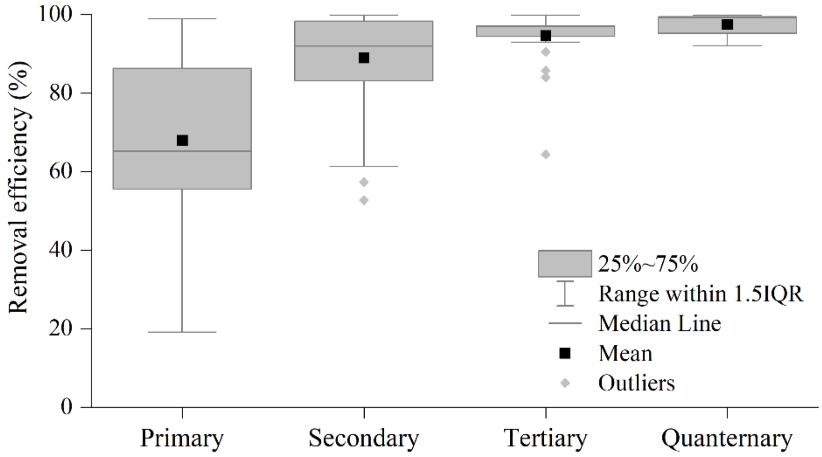

Figure 2: Literature data related to the MPs removal efficiency in WWTPs depending on the treatment train in use.

Literature data also revealed relatively good correlations between the removals of MPs and organic matter (BOD$_5$)/total suspended solids (TSS) (**Figure 3**). These results highlight the potential of using BOD$_5$ and TSS – parameters regularly monitored in WWTPs – as indirect indicators for estimating the MPs removal performance. Implementing these kinds of correlations to integrate them into predictive models could facilitate the development of simplified and robust tools for assessing the fate of MPs in WWTPs without the need for resource-intensive plastic-specific analyses.

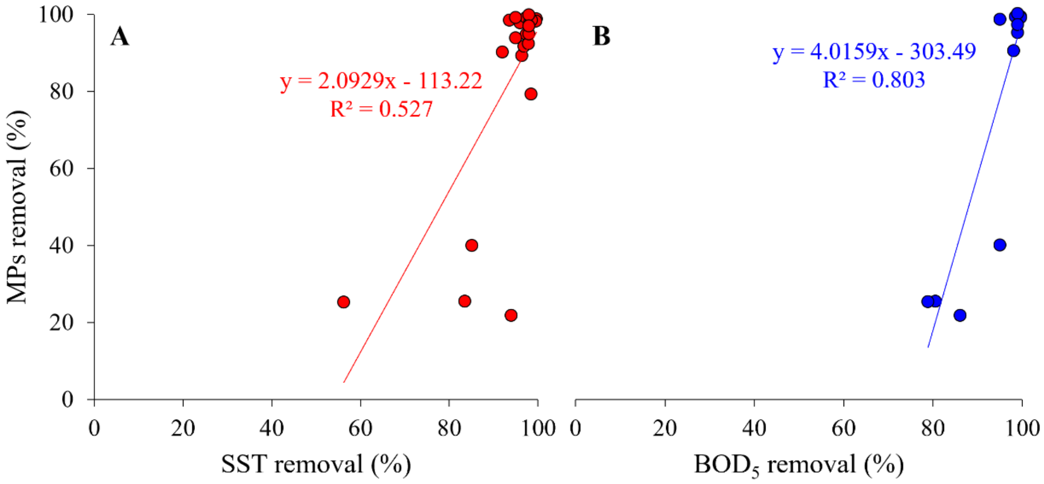

Figure 3: Correlations emerged from literature data between the removals of MPs and total suspended solids (TSS) (**A**) and between the removals of MPs and organic matter (as BOD$_5$) (**B**) in WWTPs.

4.5.3.2 *Monitoring campaigns*

An extract of the results of monitoring campaigns carried out within the project is presented in **Table 2**. For more details on the complete characterization of identified particles and related percentage removals refer to deliverable DV 4.5.2. The MPs concentrations detected at both the inlet and outlet sections of the monitored WWTPs varied based on the WW source and treatment train in use, with industrial inputs having a sector-dependent contribution to the MPs production. Referring to WWTP$_B$, it is worth noting that the MPs concentrations measured in the textile WW were lower compared to those observed in the mixed municipal and industrial influent. This evidence seems to contradict the common belief that identifies textile industrial processes as primary sources of MPs (Gambino et al., 2025). Many hypotheses could be made to explain this pattern. The temporal variability in industrial operations may contribute to the relatively low MPs concentrations observed in the textile WW. Industrial MPs emissions could fluctuate according to production cycles, maintenance activities or changes in textile processing steps. While 24-h composite samples allow to minimize the short-term (within-day) variability, they do not account for differences occurring across days, weeks or production phases. If sampling takes place during a period of reduced production, equipment cleaning and/or low fiber-intensive processing, the collected samples may underestimate typical MPs emissions. Furthermore, industrial wastewater streams could be high in volume but diluted in MPs concentration since many textile operations (e.g. fabric dyeing) typically use large quantities of water (Gambino et al., 2025). Taking all the above into account, when industrial streams are mixed with municipal wastewater, the combined MPs concentration could hence appear higher compared to the industrial component alone.

Looking at the untreated municipal WW, it could be observed that the content of MPs in $WWTP_C$ was significantly higher compared to that measured at $WWTP_A$ and $WWTP_B$. In this regard, it should be considered that the urban area served by $WWTP_C$ has no septic tanks, in contrast to the municipalities connected to $WWTP_A$ and $WWTP_B$. The absence of this pretreatment stage would reasonably contribute to the higher MPs concentrations observed in the raw municipal wastewater entering $WWTP_C$. More in general, it is worth noting that the level of MPs entering WWTPs can be reasonably influenced by a complex interplay of factors, including the catchment size, WW source, adjacent surrounding land use, etc.

The percentage removals revealed at the monitored WWTPs reflected the major differences among their wastewater treatment trains. Consistently with that emerged from the literature survey (**Figure 1**), the highest removal rate was observed for $WWTP_C$, which employes more advanced technologies (e.g. MBR processes). An intermediate removal efficiency was found for $WWTP_B$, that has in use tertiary treatments including coagulation-flocculation and final ozonation. The lowest removals were observed for $WWTP_{A,}$ which is based on a more simplified treatment scheme. Overall, these monitoring data demonstrated that, even in the absence of dedicated treatment stages, WWTPs are able to largely reduce the MPs content in wastewater, preventing their massive discharge into receiving water bodies.

Table 2: Extract of the results emerged from the monitoring campaigns conducted at various WWTPs in the study area in terms of average MPs concentrations in both raw wastewater and final effluent and related removal efficiency. Both concentrations and percentage removals are expressed on a numerical basis. Data are reported as average values ± standard deviations among the processed sample replicates.

		Average MPs concentration (MPs/L)	**Average MPs removal efficiency (%)**
$WWTP_A$	IN	10624 ± 2074	87.7%
	OUT	1309 ± 369	
$WWTP_B$	IN-Mixed [1]	42767 ± 693	97.2%
	IN-Ind [2]	2618 ± 55	
	IN-Mun	51495 [3]	
	OUT [4]	1194 ± 127	
$WWTP_C$	IN-Mun [5]	167078	99.8%
	IN-Ind [6]	189441 ± 13375	
	OUT [7]	341	

[1] Mixed municipal and textile industrial wastewater sampled where the two fluxes are mixed (after course screening).

[2] Textile industrial WW from separate sewer.

[3] MPs concentration attributed to the municipal WW conveyed to $WWTP_B$ (estimated from the average IN-Ind and IN-Mixed concentrations, knowing the partitioning between the industrial and urban volumetric flows).

[4] Final effluent discharged into receiving water body without entering refining section for water reclamation.

[5] Municipal WW from combined sewer.

[6] Tannery industrial WW from separate sewer.

[7] Final effluent discharged into receiving water body (consisting of effluents from both treatment lines).

A large variety of polymers were detected in the processed samples (**Figure 4**) – including acrylonitrile butadiene styrene (ABS), acrylic from textiles, ethylene vinyl acetate (EVA), polyamide (PA), polyethylene (PE), polyethylene terephthalate (PET), polypropylene (PP), polystyrene (PS), polytetrafluoroethylene (PTFE), polyurethane (PU), polyvinyl chloride (PVC), polylactic acid (PLA), polyoxymethylene (POM) and polymethyl methacrylate (PMMA) – thus highlighting the diverse and complex range of urban and industrial sources contributing to the MPs load in the WWTP. It is worth noting that rubber particles accounted for a relevant fraction at all sampling sites (except for textile industrial WW of $\mathrm{WWTP_B}$ and final effluent of $\mathrm{WWTP_C}$). Small rubber debris can largely originate from tire erosion across roads/highways in the urban area served by the combined sewer and/or directly within the plant (Kole et al., 2017), comprising from 29 % ($\mathrm{WWTP_A}$) to 53 % ($\mathrm{WWTP_B}$) of rubber particles found in raw wastewater. PA and acrylic, but also PP and PET particles, could be associated, among the various sources, with the loss of microfibers during garment laundering in households (Hernandez et al., 2017), thus pointing out the impact of synthetic textiles on the MPs pollution. Similarly, textile processes at industrial scale are also reported to release fibers during washing, dyeing and finishing operations (Gambino et al., 2025). Overall, the identified polymers could be commonly found in single-use packaging, consumer products, equipment, piping systems, coating, etc., thus being potentially released in the form of microparticles reaching WWTPs via urban runoff, domestic discharges and industrial wastewater. To be noticed that the specific profile of MPs in the targeted textile/tannery wastewater was likely influenced by a variety of factors related to the industrial processes themselves – such as production scale, type of processed fabric/leather and chemical formulations employed – which may contribute to both abundance and variability of MPs contamination.

While data elaboration at river basin-scale was limited exclusively to MPs, the analysis of collected samples also revealed a significant content of cellulose-based particles comprising a wide range of materials of both natural and chemically modified sources (**Table 3**). Among these, cellulose-based textiles (e.g. cotton, linen and viscose) represent a relevant fraction in the textile wastewater (with an average concentration of about 13293 items/L in the mixed municipal and industrial influent of $\mathrm{WWTP_B}$ located in the textile district).

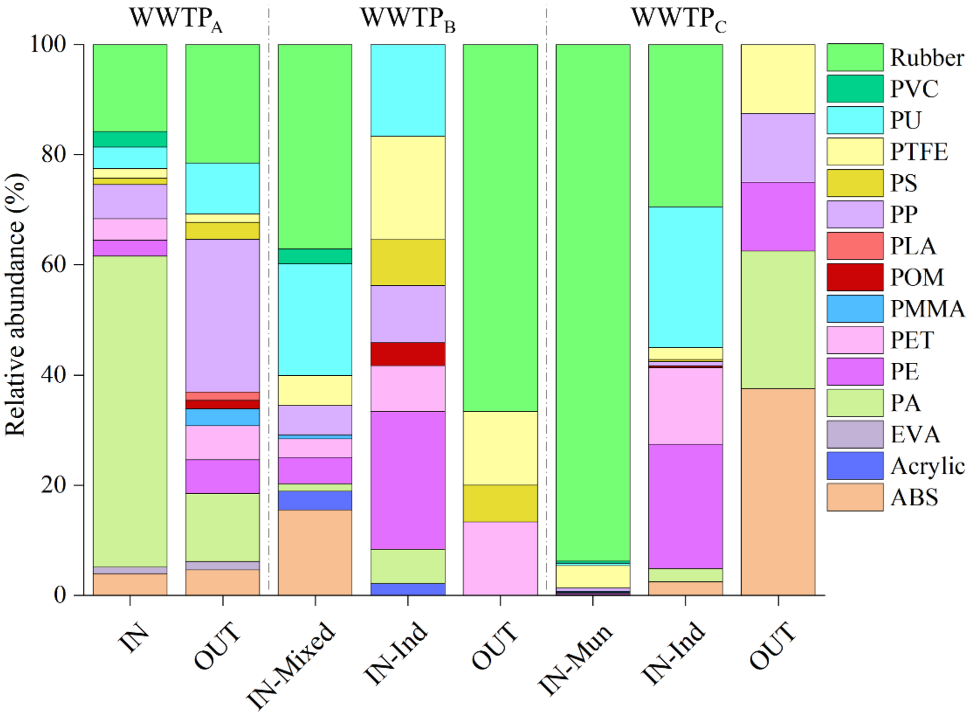

Figure 4: Chemical characterization of MPs found in raw wastewater and final effluents from $\mathrm{WWTP_A}$, $\mathrm{WWTP_B}$ and $\mathrm{WWTP_C}$.

Table 3: Average concentrations of cellulosic particles found in raw wastewater and final effluents from WWTP$_A$, WWTP$_B$ and WWTP$_C$.

WWTP$_A$		**WWTP$_B$**			**WWTP$_C$**		
IN	**OUT**	**IN-Mixed**	**IN-Ind**	**OUT**	**IN-Mun**	**IN-Ind**	**OUT**
3580 ± 1511	991 ±182	30342 ± 492	1837 ± 220	955 ±102	4107	46203 ± 31909	683

Most MPs had a characteristic size < 100 µm, with a relevant fraction of them (from 13 to 57 % depending on the sampling site) measuring less than 30 µm (**Figure 5**). Irregular fragments of secondary origin – i.e. likely originated from fragmentation/degradation of larger plastic debris – were generally the prevalent morphologies identified among the detected MPs (**Table 4**).

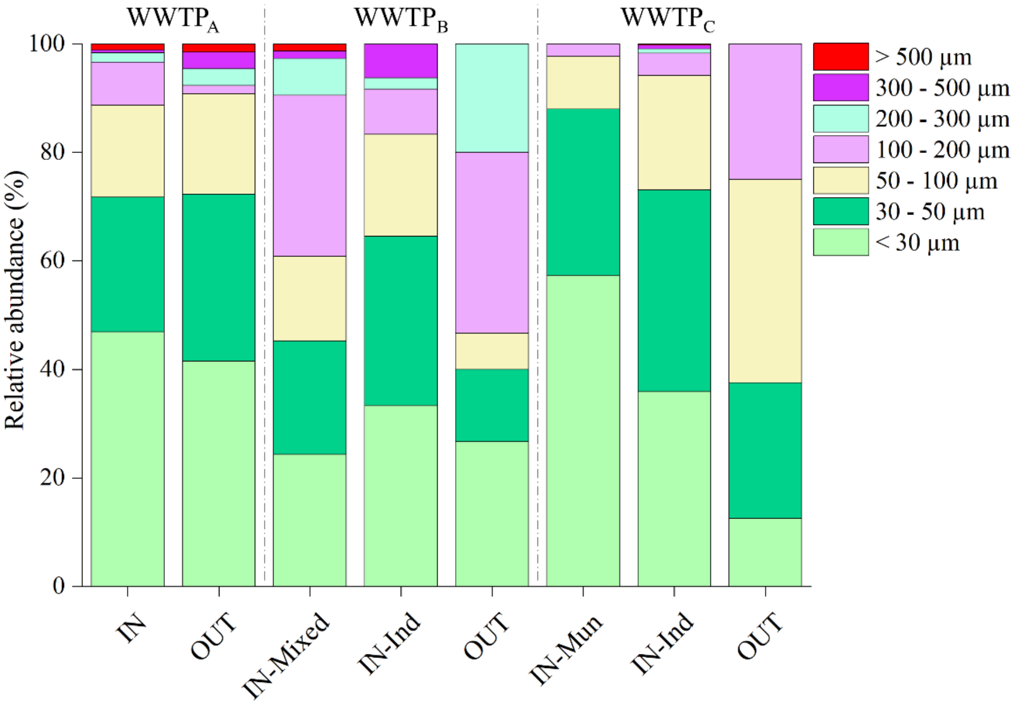

Figure 5: Size distribution of MPs found in raw wastewater and final effluents from WWTP$_A$, WWTP$_B$ and WWTP$_C$.

Table 4: Morphological classification of MPs found in raw wastewater and final effluents from WWTP$_A$, WWTP$_B$ and WWTP$_C$.

	WWTP$_A$		**WWTP$_B$**			**WWTP$_C$**		
	IN	**OUT**	**IN-Mixed**	**IN-Ind**	**OUT**	**IN-Mun**	**IN-Ind**	**OUT**
Fiber	13%	15%	7%	10%	0%	2%	2%	38%
Pellet	19%	34%	24%	46%	27%	38%	40%	13%
Fragment	68%	51%	69%	44%	73%	60%	58%	50%

Referring to the influents of all monitored WWTPs, the distribution of MPs in terms of polymer / size /shape was used to convert the MPs concentrations listed in **Table 2** on a mass basis (**Table 5**) thus enabling mass balance elaboration at river basin-scale.

Table 5: Average MPs (numerical /mass) concentrations found in the raw wastewater from WWTP$_{A}$, WWTP$_{B}$ and WWTP$_{C}$, that were used for data elaboration at river basin-scale.

Reference plant	**Wastewater class**	**Average MPs concentration**	
		(MPs/L)	**(µg MPs/L)**
WWTP$_{A}$	IN	10624	2014
WWTP$_{B}$	IN-Mixed	42767	35430
	IN-Mun	51495 [1]	42795 [1]
	IN-Ind	2618	1552
WWTP$_{C}$	IN-Mun	167078	6986
	IN-Ind	189441	40836

[1] MPs concentration attributed to the municipal WW conveyed to WWTP$_{B}$ (estimated from the average IN-Ind and IN-Mixed concentrations, knowing the partitioning between the industrial and urban volumetric flows).

4.5.3.3 Data elaboration at river basin scale

Data collected from WWTPs within the river catchment and their further analysis for mass / numerical balance purposes allowed to give a preliminary overview regarding the total MPs fluxes entering the targeted river basin through both municipal and industrial wastewater. The total MPs load released into the Arno river basin from wastewater discharges was estimated at 134 tons MPs/y ($4.37 \cdot 10^{14}$ MPs/y). Untreated WW (all of urban origin), even accounting for a minor fraction in terms of population served, would be responsible for approximately 20 % of to the total MPs mass emissions in the river basin (32 % on a numerical basis). This would highlight a critical issue for urban areas with limited sewer coverage that could potentially increase the MPs fluxes entering freshwater environments. The portion of the cumulative MPs emissions assigned exclusively to industrial WW would be only 4.5 % on a mass basis (3.9 % on numerical basis). This relatively small contribution would point out the potentially relevant role of municipal discharges, whose cumulative release of MPs at river basin scale would be influenced by a variety of factors such as treatment configuration in use, degree and type of industrialization of the surrounding area, etc. Moreover, these industrial and urban contrasting contributions could be also strongly affected by the volumetric flows of wastewater involved, which vary by several orders of magnitude between the recorded discharges. Despite the specific MPs (numerical / mass) load entering WWTPs, which are typically sector-dependent in the case of industrial discharges, the cumulative MPs emissions into receiving water bodies would be largely influenced by the level of technological advancement of the treatment configurations in use. A source with high emission potential equipped with enhanced treatment trains may ultimately exert a minor contribution to the discharge of MPs in the environment than a low-impact source that lacks adequate treatment capacity. Therefore, when considering MPs pollution at river basin scale, both input characteristics and treatment performance of the WWTPs should be considered.

To address the robustness of the above-described predictions, the estimated MPs fluxes released by WW discharges into the Arno river basin – expressed as number of items per day – were compared with those measured in the river water (50 cm-depth) at the outlet section by Monnanni et al. (2024). To allow a proper comparison between the two studies, only MPs > 60 µm were considered. It was found that the estimated load of MPs > 60 µm emitted at river basin scale by wastewater ($3.7 \cdot 10^{11}$ MPs/y) was approximately one order of magnitude higher than that observed at the river outlet ($2.4 \cdot 10^{10}$ MPs/y). This discrepancy would suggest that a substantial fraction of the discharged particles > 60 µm likely settle along the river course, accumulating in bed sediments and/or being retained along riverbanks before reaching the outlet section. Aware that no general conclusions can be drawn based on such a limited set of data, even considering that the different methodological approaches applied in the two studies could limit direct comparability, the overall pattern seems to be consistent, suggesting valuable insights into the fate of MPs released from wastewater discharges into receiving water bodies.

To be noticed that a larger set of multi-site field data would increase the representativeness of the river basin-scale assessments, allowing for more targeted identification of emission hotspots and highlighting the impact of specific industrial / urban sources of MPs. In this perspective, it should be emphasized that this work primarily focused on developing a reliable methodological framework to estimate the overall contribution of WW discharges to the cumulative MPs emissions rather than on providing a detailed prediction of their distribution within the catchment area. Considering that the production of MPs from urban sources can be estimated by monitoring the MPs flows entering WWTPs (and combined sewer overflows), the developed tool could also enable evaluations regarding the overall MPs production in a targeted area. According to preliminary estimates, referring only to municipal WW with negligible industrial inputs, a per capita production of 0.55 kg MPs/inhab/y was predicted within the Arno river basin.

4.5.4 Conclusions

In summary, this study provided a comprehensive assessment of the MPs fluxes entering the Arno river basin through both municipal and industrial wastewater discharges. The large set of multi-site field data collected through dedicated monitoring campaigns, reinforced by an in-depth literature review, not only enabled reliable river basin-scale assessments but also contributed to a deeper understanding of the occurrence, fate and removal of MPs across different wastewater treatment configurations. The total load of MPs emitted in the studied catchment from WW wastewater discharges was estimated at 134 tons MPs/y ($4.37 \cdot 10^{14}$ MPs/y). Despite the differences in the MPs loads entering WWTPs, strictly dependent on the characteristic of the urban and industrial areas served, the effectiveness of the treatment trains in use in removing MPs proved to have a primary role in limiting their overall emission in the environment.

Despite the results described above for the case-study area, this work provided a methodological framework for river basin-scale assessments that could be further implemented to expand its versatility and accuracy in a broader range of applications. From a management perspective, this could support risk-based prioritization of municipal and industrial wastewater discharges, where both the nature of the activities present in the targeted area and existing treatment facilities are evaluated to determine the need for additional control measures. Integrating sector-specific MPs emission factors into river basin-level modeling frameworks would enhance the accuracy of emission inventories and facilitate the identification of more targeted and effective mitigation strategies. In this regard, further implementation of the set of multi-site field data would help to increase the representativeness of the predictions in the catchment area.

4.5.5 References

Barchiesi, M., Kooi, M., & Koelmans, A. A. (2023). Adding Depth to Microplastics. Environmental Science and Technology, 57(37), 14015–14023. https://doi.org/10.1021/acs.est.3c03620

Bayo, J., Olmos, S., & López-Castellanos, J. (2020). Microplastics in an urban wastewater treatment plant: The influence of physicochemical parameters and environmental factors. Chemosphere, 238, 124593. https://doi.org/10.1016/j.chemosphere.2019.124593

Dong, M., She, Z., Xiong, X., Ouyang, G., & Luo, Z. (2022). Automated analysis of microplastics based on vibrational spectroscopy: are we measuring the same metrics? Analytical and Bioanalytical Chemistry, 414, 3359–3372. https://doi.org/10.1007/s00216-022-03951-6

Gambino, I., Terzaghi, E., Baldini, E., Bergna, G., Palmisano, G., & Di Guardo, A. (2025). Microcontaminants and microplastics in water from the textile sector: a review and a database of physicochemical properties, use in the textile process, and ecotoxicity data for detected chemicals. Environmental Science: Processes and Impacts, 27(2), 297–319. https://doi.org/10.1039/d4em00639a

Hernandez, E., Nowack, B., & Mitrano, D. M. (2017). Polyester Textiles as a Source of Microplastics from Households: A Mechanistic Study to Understand Microfiber Release during Washing. Environmental Science and Technology, 51(12), 7036–7046. https://doi.org/10.1021/acs.est.7b01750

Hongprasith, N., Kittimethawong, C., Lertluksanaporn, R., Eamchotchawalit, T., Kittipongvises, S., & Lohwacharin, J. (2020). IR microspectroscopic identification of microplastics in municipal wastewater treatment plants. Environmental Science and Pollution Research, 27(15), 18557–18564. https://doi.org/10.1007/s11356-020-08265-7

Hidayaturrahman, H., & Lee, T. G. (2019). A study on characteristics of microplastic in wastewater of South Korea: Identification, quantification, and fate of microplastics during treatment process. Marine Pollution Bulletin, 146, 696–702. https://doi.org/10.1016/j.marpolbul.2019.06.071

Jan Kole, P., Löhr, A. J., Van Belleghem, F. G. A. J., & Ragas, A. M. J. (2017). Wear and tear of tyres: A stealthy source of microplastics in the environment. International Journal of Environmental Research and Public Health, 14(10), 1265. https://doi.org/10.3390/ijerph14101265

Liu, N., Cheng, S., Wang, X., Li, Z., Zheng, L., Lyu, Y., Ao, X., & Wu, H. (2022). Characterization of microplastics in the septic tank via laser direct infrared spectroscopy. Water Research, 226, 119293. https://doi.org/10.1016/j.watres.2022.119293

Long, Z., Pan, Z., Wang, W., Ren, J., Yu, X., Lin, L., Lin, H., Chen, H., & Jin, X. (2019). Microplastic abundance, characteristics, and removal in wastewater treatment plants in a coastal city of China. Water Research, 155, 255–265. https://doi.org/10.1016/j.watres.2019.02.028

Luo, Y., Xie, H., Xu, H., Zhou, C., Wang, P., Liu, Z., Yang, Y., Huang, J., Wang, C., & Zhao, X. (2023). Wastewater treatment plant serves as a potentially controllable source of microplastic: Association of microplastic removal and operational parameters and water quality data. Journal of Hazardous Materials, 441, 129974. https://doi.org/10.1016/j.jhazmat.2022.129974

Magni, S., Binelli, A., Pittura, L., Avio, C. G., Della Torre, C., Parenti, C. C., Gorbi, S., & Regoli, F. (2019). The fate of microplastics in an Italian Wastewater Treatment Plant. Science of the Total Environment, 652, 602–610. https://doi.org/10.1016/j.scitotenv.2018.10.269

Monnanni, A., Rimondi, V., Morelli, G., Nannoni, A., Cincinelli, A., Martellini, T., Chelazzi, D., Laurati, M., Sforzi, L., Ciani, F., Lattanzi, P., & Costagliola, P. (2024). Microplastics and microfibers contamination in the Arno River (Central Italy): Impact from urban areas and contribution to the Mediterranean Sea. Science of the Total Environment, 955, 177113. https://doi.org/10.1016/j.scitotenv.2024.177113

Pittura, L., Foglia, A., Akyol, Ç., Cipolletta, G., Benedetti, M., Regoli, F., Eusebi, A. L., Sabbatini, S., Tseng, L. Y., Katsou, E., Gorbi, S., & Fatone, F. (2021). Microplastics in real wastewater treatment schemes: Comparative assessment and relevant inhibition effects on anaerobic processes. Chemosphere, 262. https://doi.org/10.1016/j.chemosphere.2020.128415

Samandra, S., Johnston, J. M., Jaeger, J. E., Symons, B., Xie, S., Currell, M., Ellis, A. V., & Clarke, B. O. (2022). Microplastic contamination of an unconfined groundwater aquifer in Victoria, Australia. Science of the Total Environment, 802, 149727. https://doi.org/10.1016/j.scitotenv.2021.149727

Scircle, A., Cizdziel, J. V., Tisinger, L., Anumol, T., & Robey, D. (2020). Occurrence of microplastic pollution at oyster reefs and other coastal sites in the Mississippi sound, USA: Impacts of freshwater inflows from flooding. Toxics, 8(2), 35. https://doi.org/10.3390/TOXICS8020035

Simon, M., van Alst, N., & Vollertsen, J. (2018). Quantification of microplastic mass and removal rates at wastewater treatment plants applying Focal Plane Array (FPA)-based Fourier Transform Infrared (FT-IR) imaging. Water Research, 142, 1–9. https://doi.org/10.1016/j.watres.2018.05.019

Steinfeld, F., Kersten, A., Schabel, S., & Kerpen, J. (2025). Microplastics in German paper mills’ wastewater and process water treatment plants: Investigation of sources, removal rates, and emissions. Water Research, 271, 123016. https://doi.org/10.1016/j.watres.2024.123016

Sun, J., Dai, X., Wang, Q., van Loosdrecht, M. C. M., & Ni, B. J. (2019). Microplastics in wastewater treatment plants: Detection, occurrence and removal. Water Research, 152, 21–37. https://doi.org/10.1016/j.watres.2018.12.050

Talvitie, J., Mikola, A., Koistinen, A., & Setälä, O. (2017a). Solutions to microplastic pollution – Removal of microplastics from wastewater effluent with advanced wastewater treatment technologies. Water Research, 123, 401–407. https://doi.org/10.1016/j.watres.2017.07.005

Talvitie, J., Mikola, A., Setälä, O., Heinonen, M., & Koistinen, A. (2017b). How well is microlitter purified from wastewater? – A detailed study on the stepwise removal of microlitter in a tertiary level wastewater treatment plant. Water Research, 109, 164–172. https://doi.org/10.1016/j.watres.2016.11.046

Yang, L., Li, K., Cui, S., Kang, Y., An, L., & Lei, K. (2019). Removal of microplastics in municipal sewage from China's largest water reclamation plant. Water Research, 155, 175–181. https://doi.org/10.1016/j.watres.2019.02.046

4.5.6 Scientific products and dissemination

Pagliaccia, B., Ascolese, M., Vannini, E., Carretti, E., Lubello, C., Gori, R. (2025). Methodologic insights aimed to set-up an innovative Laser Direct InfraRed (LDIR)-based method for the detection and characterization of microplastics in wastewaters, Science of The Total Environment 967, 178817. https://doi.org/10.1016/j.scitotenv.2025.178817

Pagliaccia, B., Ascolese, M., Lubello, C., Dugheri, S., Caffaz, S., Fibbi, D., Gori, R., Insights on the fate and removal of microplastics and microparticles in wastewater treatment plants, ECOMONDO, 3–6/11/2025, Rimini (Italy). Oral presentation.

Pagliaccia, B., Ascolese, M., Lubello, C., Dugheri, S., Fibbi, D., Gori, R., Insights on the fate and removal of microplastics in wastewater treatment plants: Unveiling the impact of textile industry, Symposium on Microplastics in the Environment and Water, 18–19/09/2025, Singapore. Oral presentation.

Pagliaccia, B., Ascolese, M., Vannini, E., Fibbi, D., Carretti, E., Lubello, C., Gori, R., Development of an innovative Laser Direct InfraRed (LDIR)-based methodology for monitoring microplastics in wastewater treatment plants, XII International Symposium on Environmental Engineering (SIDISA 2024), 1–4/10/2024, Palermo (Italy). Oral presentation.

Appendix

Table A1: Extract of the literature review on the detection and characterization of MPs in wastewater treatment plants (WWTPs): sampling and detection methods applied, monitoring results in terms of MPs concentrations in both raw wastewater (IN) and final effluent (OUT) and related removal efficiency.

Location	Population served	Wastewater type	Treatment configuration *	Sampling method	Sampling volume	Detection method	Finest mesh	IN concentration (items/L)	OUT concentration (items/L)	Removal (%)	References
China	$3.5\cdot10^6$ inhabitants served by 7 WWTPs	Domestic	Secondary	Pump system/ Filtration on sieve stacks	2.98 – 142.98 L (IN) 27.67 – 348.71 L (OUT)	Dissection microscope/ µ-Raman	43 µm	1.57 – 13.69 [3]	0.20 – 1.73 [3]	79.33 – 97.84 [1]	Long et al. (2019)
China	$1.2\cdot10^4$ inhabitants	Domestic	Secondary	Autosampler for collection in sewer pipes [2]	3 – 10 L (IN) 6 – 30 L (OUT)	Stereomicroscope/ µ-FTIR	10 µm	36.2 – 141.5 [3]	1.3 – 42.5 [3]	76.86 – 98.21 [3]	Luo et al. (2023)
China	$2.4\cdot10^6$ inhabitants	Municipal	Quaternary	Container	30 L	Microscope/ µ-FTIR	10 µm	12.03 ± 1.29	0.59 ± 0.22	95.16 ± 1.57	Yang et al. (2019)
Denmark	NA	Domestic and/or industrial	Secondary / Tertiary	Autosampler [2]	1 L (IN) 4.1 – 81.5 L (OUT)	FPA-based FTIR imaging	10 µm	2223 – 18285 [4]	19 – 447 [4]	99.3 [5]	Simon et al. (2018)
Finland	$8.0\cdot10^5$ inhabitants	NA	Tertiary / Quaternary	Container/Pumped filtration [8] Autosampler [2]	0.1 L (IN) [2, 6] 2 – 1000 L (OUT) [6] 2 – 13.5 L (OUT) [2]	Stereomicroscope/ FTIR	20 µm	380 ± 52.2 – 686.7 ± 155.0 [6, 7] 390 – 900 [2, 7]	0.7 ± 0.6 – 3.5 ± 1.3 [6, 7] 1.4 – 2.8 [2, 7]	95.0 – 98.5/ 99.9	Talvitie et al. (2017b)
Italy	$8.0\cdot10^4$ PE	Municipal	Tertiary	Autosampler [2]	25 L	Stereomicroscope/ µ-FTIR	63 µm	3.64	0.52	86	Pittura et al. (2021)
Spain	$2.1\cdot10^5$ PE	Municipal	Secondary	Container	0.5 – 3.7 L (IN) 2.7 – 17.0 L (OUT)	Stereomicroscope/ FTIR	0.45 µm	3.20 ± 0.67	0.31 ± 0.06	90.3	Bayo et al. (2020)
South Korea	NA	Industrial Municipal Municipal	Tertiary Quaternary Tertiary	Container	2 L	Microscope	1.2 µm	4200 31400 5840	33 297 66	99.2 99.1 98.9	Hidayaturrahman and Lee (2019)
Thailand	$5.8\cdot10^5$ PE $5.1\cdot10^4$ PE $5.2\cdot10^5$ PE	Municipal	Secondary	Container	5 – 10 L	Microscope/FTIR	330 µm	12.2 [8]	2 [8]	84 [8]	Hongprasith et al. (2020)

*** Quaternary treatment configurations refer to the application of advanced technologies, such as reverse osmosis, membrane bioreactors (MBRs), etc.**

[1] Data related to the results collected for the seven monitored WWTPs.

[2] Collection of 24-h composite samples.

[3] Data collected under both dry weather and wet weather conditions.

[4] Data related to the ten monitored WWTPs.

[5] Removal efficiency calculated from the median particle concentration among the ten monitored WWTPs.

[6] Collection of grab samples.

[7] Data given as microlitter particle concentrations.

[8] Data calculated as average values among the three monitored WWTPs.

4.6 Conceptual framework and material flow analysis for the assessment of bioplastic flows in the environment (UNIROMA1)

Contributors: M. Falzarano, A. Polettini (DICEA, University of Rome "La Sapienza")

4.1.1 Introduction

The pervasive presence of plastics and its more recent counterpart, bioplastics, in the environment represents one of the most pressing ecological challenges of our time. From vast ocean gyres of marine debris to microplastic particles found in air, soil, water, and even human and animal bodies, the potential long-term transfer and accumulation of such materials in the environmental compartments may pose threats and risks to ecosystems and human health. The environmental profile of bioplastics is often overlooked as there are pressing concerns regarding bioplastic residues ending up in the environment, in particular when they are designed to be single-use materials. Additional concerns arise from the generally limited consumer awareness regarding discarded bioplastics' fate that may lead to substantial littering or mismanagement. In any of these scenarios, it is therefore necessary to understand the fate of bioplastics and the risks their presence may pose to the natural compartments. So far, the impact of bioplastic debris on ecosystems has not yet been clarified, but there is evidence of micro-bioplastics accumulation and persistence in soil ([1]). Fine particles can also adsorb and transport heavy metals and toxic compounds, resulting in a potentially higher risk for living organisms (e.g., [2, 3]).

In order to effectively evaluate such hazards, it is therefore fundamental to identify univocally and quantitatively the potential sources of bioplastics, their fields of use and potential destinations once they are discarded, as well as the potential sinks for litter and microparticles.

Materials Flow Analysis (MFA) is regarded as a powerful tool when addressing the above-mentioned issues. MFA is a systematic, structured accounting method widely used to quantify the stocks (materials accumulated within a system) and flows (the transfer of materials into, through and out of a system) of a specific substance within defined spatial and temporal boundaries. MFA was chosen in this study since it is capable of providing a comprehensive, mass-balanced framework to understand the true scale and complexity of bioplastic flows and the potentially involved environmental compartments, providing information that can be used to implement appropriate management approaches, develop effective mitigation strategies and safeguard environmental sustainability.

The present study was specifically focused on packaging products made of polylactic acid (PLA) at a European scale (EU27), on account of the fact that the packaging sector largely dominates the current applications of bioplastics (reported global production capacity in 2024 for rigid and flexible packaging: 1.12 Mt/y, making up ~45% of the global bioplastics production [4]) and within the packaging market PLA is by far the most widespread bioplastic type (~54% of the overall production capacity [4]). The primary aim of the work was to provide a preliminary assessment of the flows of PLA-based bioplastics that may ultimately be released into the environmental compartments as a result of different end-of-life (EOL) transformation and transfer pathways.

4.1.3 Modelling approach

The estimation of the PLA-based bioplastic packaging flows was aimed at providing a macro-scale overview of the fate of such materials across their value chain at the EU27 scale, highlighting potential hotspots in their end-of-life management and identifying potential risks associated to their emissions to multiple environmental compartments. A specific focus of the study was the estimation of potential material losses in the environment that may occur as a result of mismanagement of bioplastic waste and incomplete biodegradation of the materials at different stages of treatment, which represent a major novel contribution of the work.

The time scale adopted for the analysis was the year 2024. The choice of an annual time horizon for the assessment of bioplastic flows appears to be reasonable for the packaging sector, which is characterized by rapid dynamics of materials consumption and waste generation.

The MFA model was built up on previous work conducted by various researchers [5–13] on flow estimation for the life cycle of conventional plastics. A static MFA model was adopted to describe the post-consumption fate of PLA packaging materials spanning the whole range of end-of-life management options and potential material losses. The system boundary of the present study includes the main phases involved in the life cycle of packaging bioplastics downstream of consumption, as illustrated in Figure 1. Each phase included in the general system layout (highlighted in Figure 1 with a specific color) represents one of the following conceptual stages which the value chain was modelled to be comprised of: i) PLA-based packaging consumption; ii) waste production; iii) waste collection; iv) recycling; v) waste processing (including sorting and treatment); vi) landfill disposal; vii) bioplastic losses from the above mentioned phases; viii) emission of macro- and microparticles towards the environmental compartments; ix) transfer and transformation of macro- and microparticles to the environmental compartments.

Each phase in the system was arranged to include different bioplastics waste management options belonging to the same block, generating specific nodes (processes) and related output flows depending on the characteristics of the process considered. In more detail, the overall model was structured so as to consist of 46 processes (1 consumption phase, 2 waste production phases, 5 waste collection options, 1 recycling system, 9 waste processing options, 1 disposal phase, 9 bioplastic losses, 5 macroparticles emissions to the environment, 7 microparticles emissions to the environment, 6 transfer processes to the environment) resulting in 117 flows. Table 1 provides a description of the nature and role of individual processes and flows, while Figure 2 shows the full system structure modelled. It is noted that some of the nodes in the system are redundant (as they include single input and output flows), but still they were included in the model to represent the conceptual end points for specific material flows. Furthermore, a number of nodes (namely, dedicated separate collection of bioplastics, chemical recycling and the related mass losses) were included for the sake of completeness to account for potential future recycling scenarios, but the related flows were set to zero to reflect the current management strategies of bioplastic waste in Europe, that at present do not involve dedicated chemical recycling options.

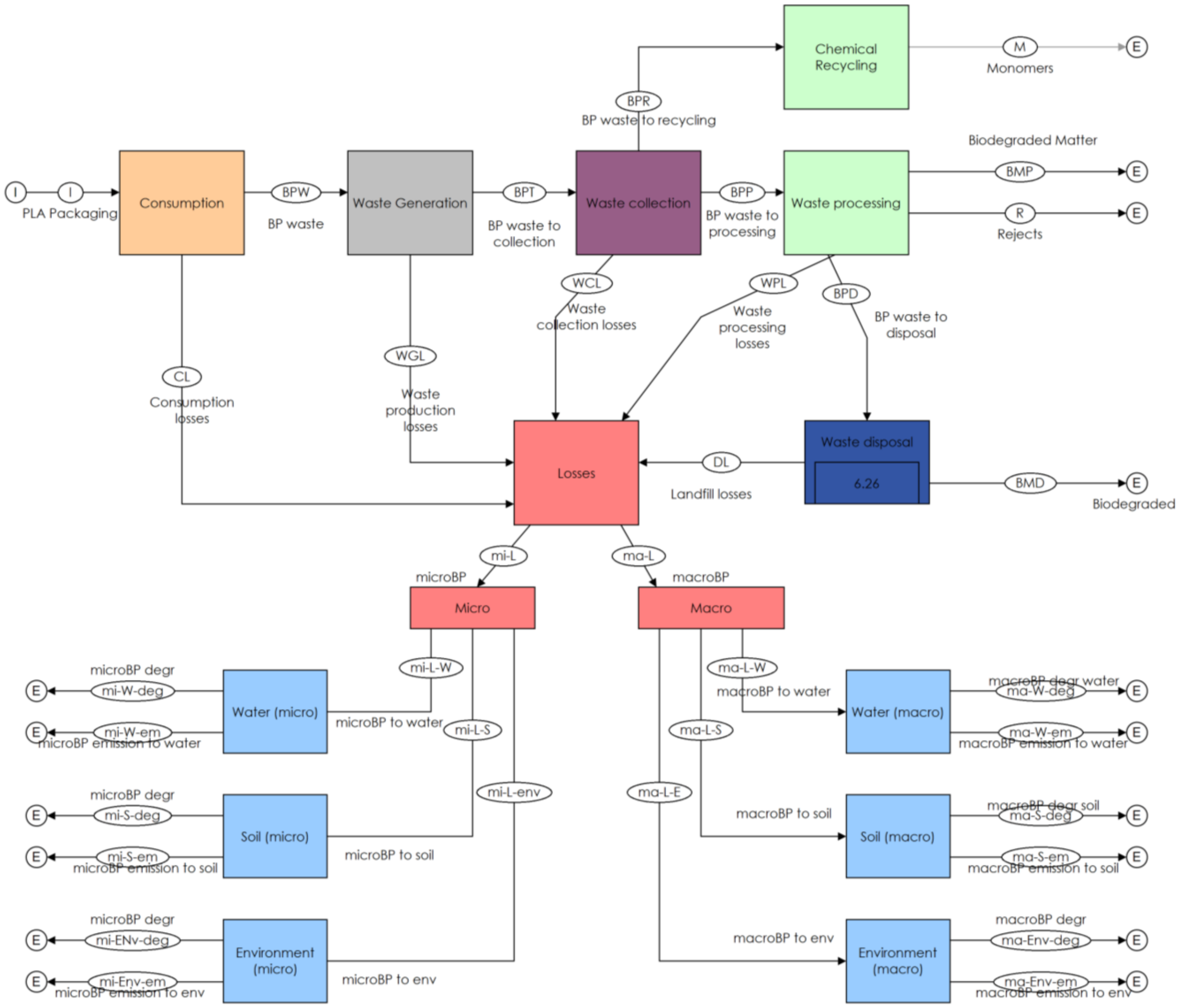

Figure 1. System boundaries and main components of the MFA model: consumption phase (orange); waste generation (grey); waste collection (purple); recycling and waste processing (green); landfill disposal (blue); losses of macro- and microparticles (red); transfer to the environmental compartments (light blue).

Table 1. Description of management phases and processes included in the model.

Stage no.	Stage	Description of processes involved	Generated flows
i	Consumption	Consumption of PLA-based bioplastic products (P1)	F1.1 (to waste generation) F1.2 (material losses [macro- and microparticles])
ii	Waste production	Post-consumption waste generation (P2)	F2.1 (to dedicated BP collection) F2.2 (to collection along with conventional plastics) F2.3 (to collection along with biowaste) F2.4 (wrongly collected along with other waste fractions) F2.5 (to collection along with residual waste) F2.6 (mismanaged) F2.7 (material losses [macroparticles])
		Waste mismanagement due to unaccounted waste, inappropriate treatment (e.g., by unauthorized third parties), littering or inappropriate/illegal disposal (P3)	F3.1 (mismanaged waste recollected and managed with residual waste) F 3.2 (material losses [macroparticles] from mismanaged waste)
iii	Waste collection	Dedicated bioplastic collection (future scenario to allow for chemical recycling of BPs) (P4)	F4.1 (PLA collected separately for chemical recycling to produce lactic acid monomer) F4.2 (material losses [macroparticles] from separate collection)

		Plastics collection and management (P5)	F5.1 (plastic flow to sorting) F5.2 (material losses [macroparticles]) from separate collection of conventional plastics)
		Biowaste collection and management (P6)	F6.1 (biowaste flow to biological treatment) F6.2 (material losses [macroparticles]) from separate collection of biowaste)
		Separate collection and management (other waste fractions) (P7)	F7.1 (flow of other separately collected waste fractions to sorting) F7.2 (material losses [macroparticles]) from separate collection of other waste fractions)
		Residual waste collection and management (P8)	F8.1 (flow of residual waste to sorting) F8.2 (material losses [macroparticles]) from residual waste collection)
iv	Recycling	Chemical recycling of BPs from dedicated collection (P9)	F9.1 (flow of chemically recycled PLA monomers to industrial processing [outside the system boundaries]) F9.2 (material losses [macroparticles]) from chemical recycling of PLA)
v	Waste processing (sorting and treatment)	Sorting (3) after separate collection of plastic waste and other waste fractions and after residual waste collection (P10, P11, P12)	F10.1 (flow of sorted PLA from plastics collection to chemical recycling) F10.2 (material losses [macro- and microparticles]) from plastics sorting) F10.3 (flow of rejects from plastic waste sorting to further processing along with residual waste) F10.4 (flow of sorted bioplastics to further processing along with biowaste) F11.1 (flow of rejects from sorting of other waste fractions to further processing along with residual waste) F11.2 (material losses [macro- and microparticles]) from sorting of other waste fractions) F12.1 (flow of BPs in sorted biodegradable waste to anaerobic digestion) F12.2 (flow of BPs in rejects from waste sorting to incineration) F12.3 (flow of BPs in rejects from waste sorting to final disposal) F12.4 (material losses [macro- and microparticles]) from waste sorting) F12.5 (flow of BPs in sorted biodegradable waste to aerobic stabilization) F12.6 (flow of BPs to further processing along with plastics)
		Separation of biowaste in view of biological treatment (P13)	F13.1 (flow of BPs in biowaste to composting) F13.2 (flow of BPs in biowaste to anaerobic digestion)
		Composting of biowaste (P14)	F14.1 (material losses [microparticles]) from composting) F14.2 (biodegraded matter during composting) F14.3 (flow of residual BPs in compost to the soil compartment) F14.4 (flow of residual BPs in compost to landfill disposal)
		Aerobic stabilization of biowaste (P16)	F16.1 (flow of residual BPs in the stabilized organic fraction to landfill disposal) F16.2 (biodegraded matter during aerobic stabilization) F16.3 (material losses [microparticles]) from aerobic stabilization)
		Anaerobic digestion of biowaste (P15)	F15.1 (flow of residual BPs in digestate to composting) F15.2 (biodegraded matter during anaerobic digestion) F15.3 (material losses [microparticles]) from anaerobic digestion) F15.4 (flow of residual BPs in digestate to the soil compartment) F15.5 (flow of residual BPs in digestate to landfill disposal)
		Anaerobic digestion of residual waste (P17)	F17.1 (flow of residual BPs in the stabilized organic fraction to landfill disposal) F17.2 (biodegraded matter during aerobic stabilization) F17.3 (material losses [microparticles]) from anaerobic digestion)
		Incineration of residual waste and sorting residues (P18)	F18.1 (gaseous emissions from incineration) F18.2 (material losses [microparticles]) from the storage/feeding units of the incinerator)

vi	Disposal	Landfill disposal of rejects (also includes a stock term to account for mass storage in the landfill site) (P19)	F19.1 (material losses [microparticles]) from landfill disposal) F19.2 (biogas generated in the landfill site) S1 (stock of undegraded BPs in the landfill)
vii	Losses	Bioplastic losses (9) from consumption, waste generation, waste mismanagement, waste collection, recycling, sorting/separation, composting/aerobic stabilization, anaerobic digestion, incineration, disposal (P20, P23, P25, P27, P30, P33, P35, P37, P39)	F20.1 (mass losses from consumption to microparticle generation) F20.2 (mass losses from consumption to macroparticle generation) F23.1 (mass losses from waste production to macroparticle generation) F25.1 (mass losses from waste collection to macroparticle generation) F27.1 (mass losses from recycling to microparticle generation) F27.2 (mass losses from recycling to macroparticle generation) F30.1 (mass losses from sorting to microparticle generation) F30.2 (mass losses from sorting to macroparticle generation) F33.1 (mass losses from disposal to microparticle generation) F35.1 (mass losses from incineration to macroparticle generation) F37.1 (mass losses from anaerobic digestion to microparticle generation) F39.1 (mass losses from composting/aerobic stabilization to microparticle generation)
viii	Emissions	Macroparticles emissions (5) from consumption, waste generation, waste mismanagement, waste collection, recycling, sorting/separation (P22, P24, P26, P29, P32)	F22.1 (flow of macroparticle losses from consumption to other environmental compartments) F22.2 (flow of macroparticle losses from consumption to the soil compartment) F22.3 (flow of macroparticle losses from consumption to the water compartment) F24.1 (flow of macroparticle losses from waste generation to other environmental compartments) F24.2 (flow of macroparticle losses from waste generation to the soil compartment) F24.3 (flow of macroparticle losses from waste generation to the water compartment) F26.1 (flow of macroparticle losses from waste collection to other environmental compartments) F26.2 (flow of macroparticle losses from waste collection to the soil compartment) F26.3 (flow of macroparticle losses from waste collection to the water compartment) F29.1 (flow of macroparticle losses from chemical recycling to other environmental compartments) F29.2 (flow of macroparticle losses from chemical recycling to the soil compartment) F29.3 (flow of macroparticle losses from chemical recycling to the water compartment) F32.1 (flow of macroparticle losses from waste sorting to other environmental compartments) F32.2 (flow of macroparticle losses from waste sorting to the soil compartment) F32.3 (flow of macroparticle losses from waste sorting to the water compartment)
		Generation of microparticles emissions (7) from consumption, recycling, sorting/separation, composting/aerobic stabilization, anaerobic digestion, incineration, disposal (P21, P28, P31, P34, P36, P38, P40)	F21.1 (flow of microparticle losses from consumption to other environmental compartments) F21.2 (flow of microparticle losses from consumption to the soil compartment) F21.3 (flow of microparticle losses from consumption to the water compartment) F28.1 (flow of microparticle losses from chemical recycling to other environmental compartments) F28.2 (flow of microparticle losses from chemical recycling to the soil compartment) F28.3 (flow of microparticle losses from chemical recycling to the water compartment) F31.1 (flow of microparticle losses from waste sorting to other environmental compartments)

			F31.2 (flow of microparticle losses from waste sorting to the soil compartment) F31.3 (flow of microparticle losses from waste sorting to the water compartment) F34.1 (flow of microparticle losses from landfill disposal to the soil compartment) F34.2 (flow of microparticle losses from landfill disposal to the water compartment) F36.1 (flow of microparticle losses from landfill disposal to the soil compartment) F36.2 (flow of microparticle losses from landfill disposal to the water compartment) F38.1 (flow of microparticle losses from anaerobic digestion to other environmental compartments) F38.2 (flow of microparticle losses from anaerobic digestion to the soil compartment) F38.3 (flow of microparticle losses from anaerobic digestion to the water compartment) F40.1 (flow of microparticle losses from composting/aerobic digestion to other environmental compartments) F40.2 (flow of microparticle losses from composting/aerobic digestion to the soil compartment) F40.3 (flow of microparticle losses from composting/aerobic digestion to the water compartment)
ix	Transfer to the environmental compartments	Transfer of macroparticles to water (P41)	F41.1 (macroparticles in the water compartment [net of biodegradation]) F41.2 (macroparticles biodegradation in the water compartment)
		Transfer of macroparticles to soil (P42)	F42.1 (macroparticles in the soil compartment [net of biodegradation]) F42.2 (macroparticles biodegradation in the soil compartment)
		Transfer of macroparticles to other environmental compartments (P43)	F43.1 (macroparticles in other environmental compartments [net of biodegradation]) F43.2 (macroparticles biodegradation in other environmental compartments)
		Transfer of microparticles to water (P44)	F44.1 (microparticles in the water compartment [net of biodegradation]) F44.2 (microparticles biodegradation in the water compartment)
		Transfer of microparticles to soil (P45)	F45.1 (microparticles in the soil compartment [net of biodegradation]) F45.2 (microparticles biodegradation in the soil compartment)
		Transfer of microparticles to other environmental compartments (P46)	F46.1 (microparticles in other environmental compartments [net of biodegradation]) F46.2 (microparticles biodegradation in other environmental compartments)

To fulfil the mass conservation principle, the sum of input flows for a given material/substance to a generic node must equal the sum of the output flows from the same node plus a storage term that represents the mass (if any) per unit time accumulated or depleted in the process (equation (1)):

$$\sum_{j=1}^{n_{F_{I,tot}}} F_{I,j} = \sum_{k=1}^{n_{F_{O,tot}}} F_{O,k} + \dot{m}_{stor} \qquad (1)$$

where *F* denotes the mass flow, *I* and *O* are the input and the output to and from the process, $n_{FI,tot}$ and $n_{FO,tot}$ are the numbers of input and output flows, and $\dot{m}_{stor,i}$ is the storage term. In the present model, the only process that was modelled with a storage term (stock) was the landfill disposal phase, while for all other nodes the accumulation term was set to zero.

The preservation of the mass balance was guaranteed by the use of transfer coefficients (TC) that describe the fractional partitioning of the total input mass to a given node into the individual output flows (equation (2)), imposing that all TCs for the node sum up to 1 (equation (3)).

$$TC_k = \frac{F_{O,k}}{\sum_{j=1}^{n_{F_{I,tot}}} F_{I,j}} \qquad (2)$$

$$\sum_{k=1}^{n_{FO,tot}} TC_k = 1 \tag{3}$$

The values of the individual TCs adopted in the model were derived from different sources, including: 1) studies on the assessment of traditional plastic flows [5, 6, 9–11, 13, 14], where applicable to bioplastics by analogy; 2) studies specifically related to the fate of bioplastics in waste treatment processes and in natural environments; 3) expert-based assumptions in the absence of available data.

Emission flows of macro- and micro- bioplastic particles to the environment were derived by quantifying the amount of material lost from the consumption and post-consumption phases, the generation of macro- and microparticles from such losses, their ultimate transfer to the environmental compartments as well as the extent of their biodegradation in such environments. By definition, macro- and microparticles were intended as bioplastics fragments or debris having an equivalent diameter > 5 mm and in the range 1 nm – 5 mm, respectively. The environmental compartments considered as potential final sinks for macro- and microparticles included terrestrial compartments ("soil"), aquatic environments ("water") and a general category "environment". The potential further fragmentation of macroparticles into microparticles after reaching the final sink was not implemented in the model, nor was the redistribution of plastics between different environmental compartments after release.

The graphical representation of the modelled system as well as the calculation of the mass flows from each node based on the assumed TCs were performed using the software STAN [15], v. 2.7.101.

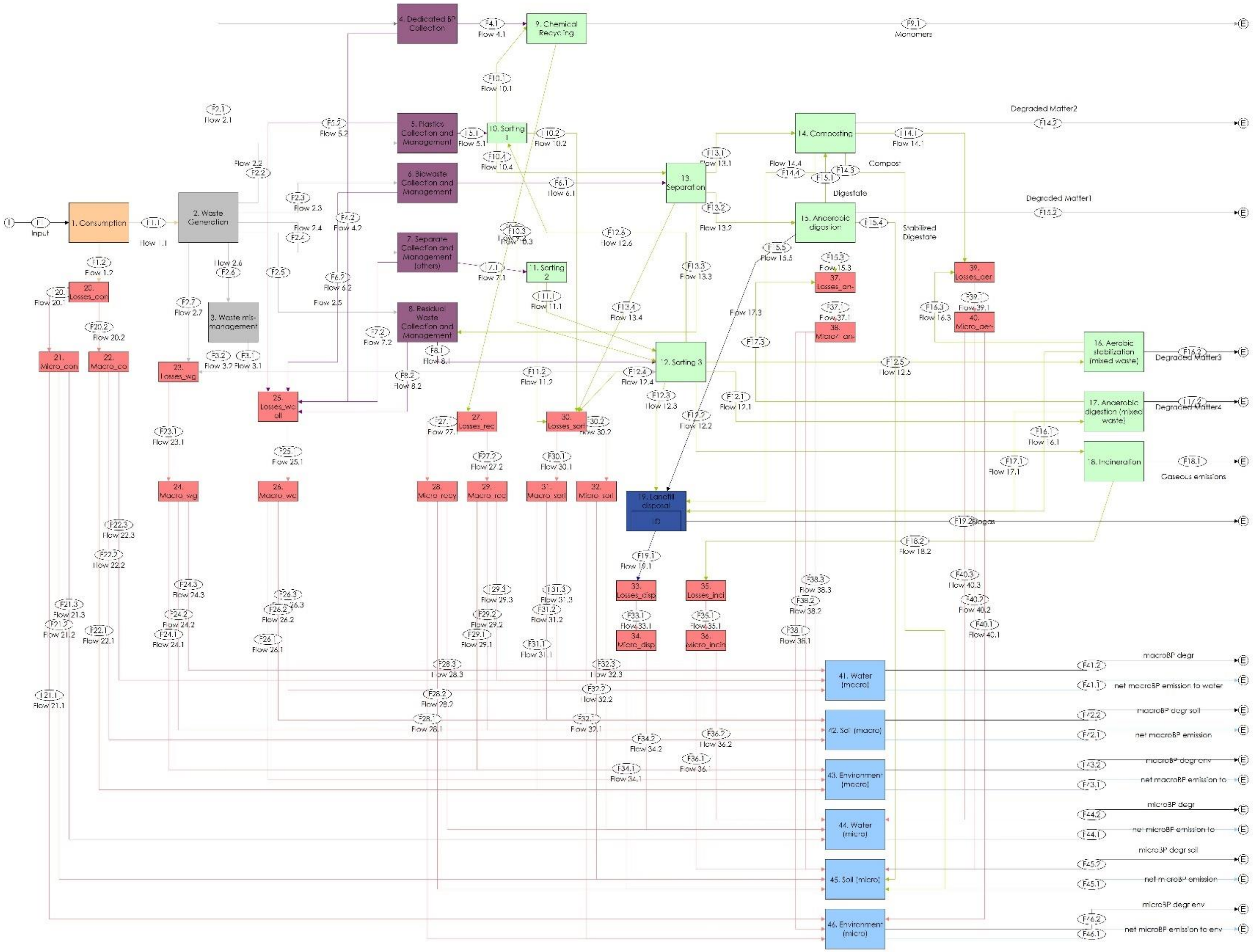

Figure 2. Layout of the modelled system

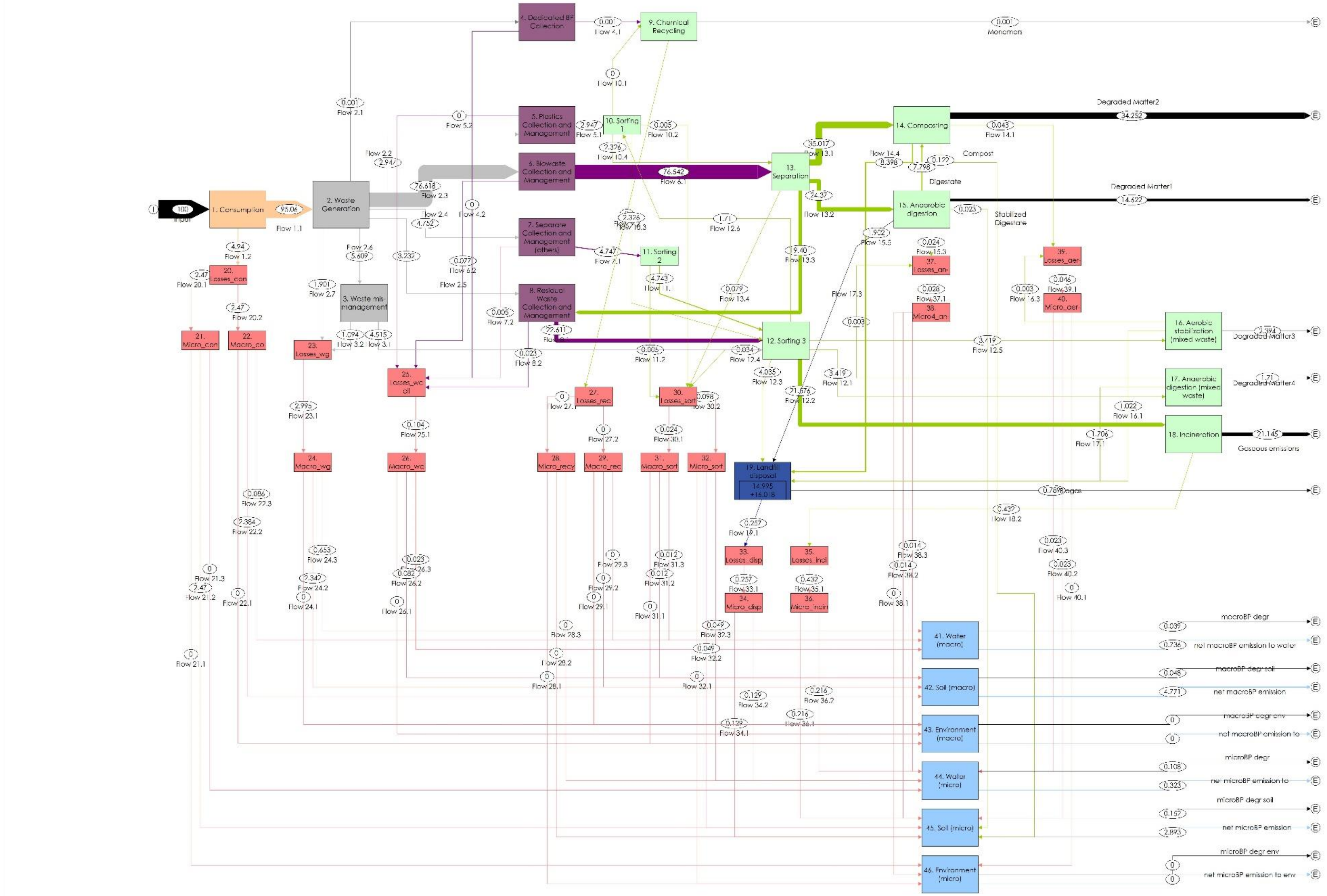

Figure 3. Results of flow estimation

4.1.4 Results

The results of the calculations performed on the modelled system are reported in Figure 3. Based on the assumptions made for the TCs of the processes involved, it was estimated that the bioplastic emissions to the environment due to mass losses and incomplete natural degradation of the material include about 71% of macroparticles and 29% of microparticles. Of the emitted particles, the soil compartment is the major sink (about 68%) of the total amount that reaches the environmental matrices.

The study demonstrates that an MFA framework can be used to estimate potential impacts from inappropriate management of end-of-life materials. The results may also be usefully analysed in order to identify possible mitigation strategies, involving environmental policies, clean-up strategies, material replacement strategies and others.

4.1.5 References

1. Fojt, J., David, J., Přikryl, R., Řezáčová, V., Kučerík, J.: A critical review of the overlooked challenge of determining micro-bioplastics in soil. Sci. Total Environ. 745, 140975 (2020). https://doi.org/10.1016/J.SCITOTENV.2020.140975
2. Afifah, N.M.R., Sathiaseelan, J.J., Waiho, K., Sung, Y.Y., Sui, L., Bhubalan, K.: Bioplastic microparticles exposure on brine shrimp, Artemia franciscana and the effects on survival, growth and intestinal microbiota composition. Polym. Degrad. Stab. 242, 111640 (2025). https://doi.org/10.1016/J.POLYMDEGRADSTAB.2025.111640
3. Zhang, Y., Zhang, L., Li, X., Wang, W., Wang, P., Cheng, R., Liu, Y., Yu, C., Wang, Y.: Environmental risks and regulatory gaps in bioplastics: A critical review of degradation pathways and ecosystem impacts. J. Hazard. Mater. Plast. 1, 100010 (2025). https://doi.org/10.1016/J.HAZMP.2025.100010
4. European Bioplastics e.V.: Bioplastics Market Development Update 2024, https://www.european-bioplastics.org/bioplastics-market-development-update-2024/, (2024)
5. Kawecki, D., Nowack, B.: Polymer-Specific Modeling of the Environmental Emissions of Seven Commodity Plastics As Macro- and Microplastics. Environ. Sci. Technol. 53, 9664–9676 (2019). https://doi.org/10.1021/ACS.EST.9B02900
6. Kawecki, D., Scheeder, P.R.W., Nowack, B.: Probabilistic Material Flow Analysis of Seven Commodity Plastics in Europe. Environ. Sci. Technol. 52, 9874–9888 (2018). https://doi.org/10.1021/ACS.EST.8B01513
7. Schwarz, A.E., Lensen, S.M.C., Langeveld, E., Parker, L.A., Urbanus, J.H.: Plastics in the global environment assessed through material flow analysis, degradation and environmental transportation. Sci. Total Environ. 875, 162644 (2023). https://doi.org/10.1016/J.SCITOTENV.2023.162644
8. Van Eygen, E., Feketitsch, J., Laner, D., Rechberger, H., Fellner, J.: Comprehensive analysis and quantification of national plastic flows: The case of Austria. Resour. Conserv. Recycl. 117, 183–194 (2017). https://doi.org/10.1016/J.RESCONREC.2016.10.017
9. Hsu, W.T., Domenech, T., McDowall, W.: How circular are plastics in the EU?: MFA of plastics in the EU and pathways to circularity. Clean. Environ. Syst. 2, 100004 (2021). https://doi.org/10.1016/J.CESYS.2020.100004
10. Van Eygen, E., Laner, D., Fellner, J.: Circular economy of plastic packaging: Current practice and perspectives in Austria. Waste Manag. 72, 55–64 (2018). https://doi.org/10.1016/J.WASMAN.2017.11.040
11. Amadei, A.M., Rigamonti, L., Sala, S.: Exploring the EU plastic value chain: A material flow analysis. Resour. Conserv. Recycl. 197, 107105 (2023). https://doi.org/10.1016/J.RESCONREC.2023.107105

12. Winterstetter, A., Veiga, J.M., Sholokhova, A., Šubelj, G.: Country-specific assessment of mismanaged plastic packaging waste as a main contributor to marine litter in Europe. Front. Sustain. 3, 1039149 (2022). https://doi.org/10.3389/FRSUS.2022.1039149
13. Jiang, D., Nowack, B.: Reconciling plastic release: Comprehensive modeling of macro- and microplastic flows to the environment. Environ. Pollut. 383, 126800 (2025). https://doi.org/10.1016/J.ENVPOL.2025.126800
14. Peano, L., Kounina, A., Magaud, V., Chalumeau, S., Zgola, M., Boucher, J.: Plastic Leak Project. (2020)
15. Cencic, O., Rechberger, H.: Material Flow Analysis with Software STAN. J. Environ. Eng. Manag. 18, 5 (2008)

4.7 Methods for detecting microplastics in groundwater and drinking water and risk assessment (UNIFI)

Contributors: A. Cincinelli, L. Sforzi

4.7.1 Introduction

Over the past three years, our research has advanced the understanding of microplastic (MP) contamination across multiple environmental compartments, with a particular focus on freshwater and groundwater systems. We conducted a global bibliometric analysis of MPs in groundwater, mapping current knowledge, assessing associated risks, and highlighting critical research gaps that hinder comprehensive risk evaluation. With the identification of spatial-temporal patterns of MP pollution in freshwater sediments, we characterized how these pollutants vary geographically and seasonally, shedding light on key drivers of their distribution. Building on this foundation, expanding from occurrence to ecological implications, our studies provided the first evidence of MPs within groundwater fauna and habitats, emphasizing the potential biological and ecological consequences of this contamination.

Monitoring studies of MP pollution in groundwater are necessary to develop targeted mitigation strategies to preserve human and environmental health. The interconnection between groundwater and drinking water resources represents a critical pathway in the assessment of MP contamination and its potential implications for human health, as groundwater constitutes one of the main sources of drinking water in many regions. Parallel to environmental investigations, we explored MP contamination in single-use water containers, addressing direct human exposure routes and implications for food safety.

Finally, recognizing the methodological challenges in this emerging field, we developed and validated a novel sampling device for MP determination in groundwater, successfully applying it across Italian aquifers to enhance sampling reliability and comparability. Collectively, these efforts contribute to understanding of MP pollution from methodological innovation to ecosystem and human health implications, supporting more informed management and policy strategies for plastic pollution mitigation.

4.7.2 Case study description

Three case studies were addressed, focusing on investigating MP contamination within freshwater and groundwater systems, integrating environmental monitoring, analytical development, and risk assessment approaches. Water and biological samples were collected to assess the occurrence, distribution, and potential transport pathways of MPs between surface and subsurface environments. The study combined field-based measurements with laboratory analyses to characterize MP types, sizes, and polymer compositions, while also evaluating their potential sources.

Particular attention was given to groundwater-dependent ecosystems, where the presence of MPs in fauna provided new insights into bioavailability and trophic transfer processes. In particular, the carried out research aims provide preliminary understanding of MP presence in different Italian groundwater bodies (caves and monitoring wells) influenced by human activities, by analyzing both water and fauna samples, to assess the potential MP ingestion by stygobitic invertebrates.

The development and validation of an innovative sampling device further strengthened the methodological framework, enabling standardized, reproducible collection of MP samples from groundwater. This second case study main goals were to validate an easy-to-implement and portable sampling device, suitable for investigating MPs from different kind of groundwater habitats. The method was validated through the use of polymeric standards and the applicability tested through sampling collection in natural conditions.

Complementary assessments on commercial single-use water containers offered a comparative perspective on human exposure to MPs through drinking water, representing the third case study of the project. Beverage cartons and plastic bottles water content were examined for assessing potential release from the packaging systems and to estimate daily intakes both for adults and children, thorugh consumption of packaged water.

Overall, this integrated case studies provided a comprehensive view of MP contamination across the aquatic continuum, linking environmental occurrence, ecological relevance, and potential risks to human health.

4.7.3 Methodologies

Discrepancies in extraction and detection methods lead to significant inconsistencies between the results of different studies. The final results are often significantly affected by the sampling protocol and sample pre- treatment and/or extraction. Owning to the lack of standardized procedures, a wide variety of approaches can be used to process the samples.

For this reason, we adopted an approach as consistent as possible for each sample we have worked on for MPs extraction and identification, starting with contamination control thorugh out all the analytical processing. Moreover, the implementation of a standardized methodology from sampling to data reporting, helped in environmental assessment and monitoring programs.

4.7.3.1 Analytical methods

Within this context, analytical methods for MP detection have evolved to include a combination of physical, chemical, and spectroscopic techniques aimed at improving recovery, identification, and quantification. Visual sorting under stereomicroscopy remains a preliminary but effective step, to classify the shape, color, and size of the polymeric items on each filter. Advanced spectroscopic tools such as Fourier-Transform Infrared spectroscopy coupled with microscopy (microFTIR), was used to chemically characterize the items to classify by polymeric nature.

Despite these advances, challenges persist in processing low-concentration samples, as typical of groundwater fauna, where small particle size complicate detection. Thus the complementary use of fluorescence microscopy staining filters with Nile Red fluorescence dye was employed to identify smaller items ingested by underground fauna. This strategy was justified by the direct relationship between an mouth opening of the organism and the size of MPs consumed.

Moreover, the integration of improved sampling methodologies, and quality assurance and quality control protocols, represents a key direction toward harmonizing methodologies and achieving inter-comparable, reliable data on microplastics in groundwater and related water resources.

4.7.3.2 Experimental methods

For the analysis of groundwater and Italian fauna in underground habitats, the collection included four samples of stygofauna pools and water samples, comprising two karst caves and two monitoring wells of a saturated alluvial aquifer. Once in the laboratory, the water samples were treated with 30% hydrogen peroxide for 48 hours at 60 °C, followed by density separation using a saturated NaCl solution with a volume-to-volume ratio of 1:2. The supernatant was then filtered. For fauna samples, the samples were treated with 30% hydrogen peroxide at 60 °C for 72 hours and filtered under vacuum. All samples were dried. After microFTIR spectroscopy, the fauna sample filters were stained with Nile Red for subsequent fluorescence spectroscopy.

A microplastic sampling device, which can be assembled in situ and allows several liters of water (200 L) to be filtered through a sequential mesh filtration system, has been validated for use in natural groundwater habitats. The system was validated with standard solutions supplemented with standard reference polymeric materials. To assess the applicability of the device in natural conditions, a sampling campaign was carried out involving thirteen selected habitats, including karst and unconsolidated groundwater aquifers.

To integrate the results obtained to risk assessment given water human consumption, drinking water packaged in beverage cartons and plastic bottles was analyzed and compared. A total of 10 single-use plastic bottles and 4 beverage cartons were purchased and analyzed. The contents of each packaged were vacuum filtered and dried. In this case, the filters were analyzed directly by visual inspection and microFTIR spectroscopy. Moreover, the estimated daily intake (EDI), expressed as MP/kg/day was calculated for adults and children.

4.7.4 Results

In the first case study investigating Italian groundwater habitats and fauna, MPs were detected in all groundwater samples. The abundances ranged from 18 items/L to 911 items/L, with a mean of 255 items/L The most common colors were black and red, accounting for 30% and 25%, respectively, while fibers and fragments were the only two morphology found, with fibers representing for more than 80%. The average sizes were in the range of 100- 500 µm, and 500 µm - 1 mm, both accounting for 34%. Cellulose was the most abundant polymer, with 82.7% on average, while polyethylene terephthalate PET, accounted for 58%. Other polymers found were polyamide PA (3.4%), polyacrylonitrile PAN (3.4%), polyethylene PE (2.2%), polysaccharide gums (1.7%), PP/PE blend (1.3%), polypropylene PP (0.9%) and ethylene-vinyl acetate EVA (0.3%). In fauna samples, the number of fluorescent particles ≥ 0.5 µm per biomass ranged from 130.5 items/g dw to 0.2 items/g dw. Pellets were the predominant shape followed by fragments and fibers. Concerning dimension, fragments were the largest fluorescent particles, with a mean size of 26 ± 30 µm, followed by fibers, 19 ± 10 µm, and pellets 1 ± 1 µm. microFTIR spectroscopic analysis was carried out for items larger than 5 µm. Cellulose was the predominant polymer, followed by polysaccharide gums. Also PET and PA traces were found.

Validation of the microplastic sampling device the recovery rate was higher than 70%. Fibers represented most abundant shape, followed by fragments and pellets. In general, the majority of the items were larger than 125 µm, followed by items in the range 124-75 µm, and 74-42 µm. The predominant polymer was artificial/textile cellulose, followed by PET.

For the analysis of packaged water, the results showed the presence of MPs in 55% of the samples. Single-use plastic bottles contained 7.6 ± 8.4 items/L, while beverage cartons contained 6.2 ± 1.4 items/L. The size ranged from 20 to 1000 µm, with the prevalence of black, and blue colors. The polymers detected were textile cellulose (78.2%), PE (12.8%), PET (6.0%), PP (1.5%), and PA (1.5%). Estimated daily intakes (EDI) were 0.56 ± 0.40 and 0.39 ± 0.09 MP/kg/day for children and 0.25 ± 0.18 and 0.18 ± 0.04 MP/kg/day for adults, in single-use plastic bottles and beverage cartons, respectively.

4.7.5 Scientific products and dissemination

Scientific publications

Monnanni, A., Rimondi, V., Morelli, G., Nannoni, A., Cincinelli, A., Martellini, T., Chelazzi, D., Laurati, M., Sforzi, L., Ciani, F., Lattanzi, P., & Costagliola, P. (2024). Microplastics and microfibers contamination in the Arno River (Central Italy): Impact from urban areas and contribution to the Mediterranean Sea. *Science of The Total Environment*, *955*, 177113. https://doi.org/10.1016/J.SCITOTENV.2024.177113

Sforzi, L., Santini, S., Sarti, C., Scopetani, C., Martellini, T., Mumtaz, A., Randazzo, D., & Cincinelli, A. (2025). Microplastic Pollution in Freshwater Sediments: Spatial–Temporal Patterns. *Current Pollution Reports*, *11*(1), 1–25. https://doi.org/10.1007/S40726-025-00373-7

Sforzi, L., Sarti, C., Santini, S., Martellini, T., & Cincinelli, A. (2024). Global status, risk assessment, and knowledge gaps of microplastics in groundwater: A bibliometric analysis. *Groundwater for Sustainable Development*, *27*, 101375. https://doi.org/10.1016/J.GSD.2024.10137

Sforzi, L., Tabilio Di Camillo, A., Di Lorenzo, T., Galassi, D. M. P., Balestra, V., Piccini, L., Cabigliera, S. B., Ciattini, S., Laurati, M., Chelazzi, D., Martellini, T., & Cincinelli, A. (2024). (Micro-)Plastics in Saturated and Unsaturated Groundwater Bodies: First Evidence of Presence in Groundwater Fauna and Habitats. *Sustainability (Switzerland)* , *16*(6), 2532. https://doi.org/10.3390/SU16062532

Laura Sforzi, Chiara Sarti, Costanza Scopetani, Samuele Ciattini, David Chelazzi, Alessandra Cincinelli, Tania Martellini (2026). Drinking or Not Drinking: Microplastic Contamination in Single-Use Water Containers. *Journal of Food Composition and Analysis,* 149, 108603. https://doi.org/10.1016/j.jfca.2025.108603

Dissemination

Poster presentation “Characterization of (micro-)plastics in groundwater bodies: insights from Italian aquifers”. Sforzi, L., Tabilio, A., Di Lorenzo, T., Balestra, V., Chelazzi, D., Ciattini, S., Martellini, T., Cincinelli, A.- 26/06/2023 – 30/06/2023 Naples (Italy), XXVII AIOL Conference

Oral presentation "Microplastiche, un inquinante emergente nelle acque sotterranee" Sforzi, L., Tabilio, A., Di Lorenzo, T., Balestra, V., Chelazzi, D., Martellini, T., Cincinelli, A.- 08/09/2023 Florence (Italy), Serra in serra: le opere sostenibili di Annarita Serra in mostra all'Orto botanico di Firenze- Workshop on plastic as environmental issue

Oral presentation "Presenza, caratterizzazione e potenziali rischi associati alle microplastiche nelle acque sotterranee" Sforzi, L., Cincinelli, A.- 22/05/2024 Florence Workshop Environmental degradation: Micro(bio)plastics

Oral presentation "Invisible ecosystems: microplastics in groundwater and their impact on biodiversity" Sforzi L., Sarti C., Tabilio Di Camillo A., Di Lorenzo T., Cabigliera B. S., Balestra V., Laurati M., Chelazzi D, Martellini T., Cincinelli A.- 06/06/2024 Ravenna (Italy), Plastiche e ambiente- Workshop on plastic pollution

Finanziato dall'Unione europea
NextGenerationEU
Ministero dell'Università e della Ricerca
Italiadomani
PIANO NAZIONALE DI RIPRESA E RESILIENZA

4.8 Effects of bed topography and data resolution in wetland modelling (UNIPD)

Contributors: Andrea Bottacin-Busolin[1], Gianfranco Santovito[2], Andrea Marion[1]

[1] Department of Industrial Engineering, University of Padova, Via Venezia 1, 35121 Padova, Italy

[2] Department of Biology, University of Padova, Via Ugo Bassi 58/B, 35131 Padova, Italy

4.8.1 Abstract

Understanding how small-scale bed features and the resolution of input data influence hydraulic behaviour and contaminant treatment is essential for reliable wetland modelling. This study investigated the combined effects of heterogeneous bed topography and spatial data resolution on hydrodynamics and solute transport in free water surface wetlands. Using synthetic wetlands generated from spatially correlated random fields of bed elevation and, where relevant, vegetation density, we analysed flow patterns, residence time distributions, and contaminant removal under varying degrees of topographic variability, correlation length, and grid resolution. Increased bed-elevation variability produces stronger dispersion and wider residence time distributions, reducing hydraulic efficiency and increasing sensitivity to specific spatial configurations of topographic features. Shorter correlation lengths promote complex flow structures, including dead zones and internal islands, while longer correlation lengths reduce residence time variance. Coarse-graining of topographic data yields modest median errors in nominal residence time but systematically underestimates residence time variance, with errors exceeding 10 and 35% grid sizes equal to and twice the correlation length, respectively. In contrast, outlet concentration errors remain relatively small, typically below 5% even when grid size exceeds the correlation length of bed features, indicating a stronger dependence on nominal residence time than on variance. Vegetation heterogeneity exerts limited influence relative to topography within the considered parameter ranges. Collectively, these results highlight the dominant role of bed topography in shaping wetland hydraulic and treatment performance and provide guidance on the spatial resolution required for dependable numerical modelling and field characterization.

4.8.2 Introduction

Constructed free-water surface (FWS) wetlands are widely used as nature-based solutions for treating urban and industrial wastewater. Their effectiveness in removing a broad range of contaminants, including organic matter, nutrients, suspended solids, and pathogens, has been demonstrated in numerous experimental and modelling studies (Vymazal 2014; Katsenovich et al. 2009; Zhang et al. 2015; Kotti et al. 2010; Cameron et al. 2003). Treatment efficiency arises not only from biogeochemical reactions but also from the underlying hydrodynamics and the interaction between water, vegetation, and topography (Arheimer and Wittgren 2002; Meng et al. 2014; Zhao et al. 2024). However, despite decades of research, the coupled interplay between wetland flow structure, microtopography, vegetation distribution, and contaminant transformation remains incompletely understood, making performance prediction challenging (Marion et al. 2014; Jiang and Chui 2022).

Hydraulic behavior is a primary determinant of wetland treatment efficiency because it governs how long water and solutes reside within the system. Ideally, flow through a wetland would approximate plug flow, where all fluid parcels experience the same residence time (Thackston et al. 1987; Vymazal 2014). In reality, variations in water depth, vegetation density, and bed elevation generate heterogeneous velocity fields, recirculation zones, and preferential flow paths. These features broaden residence time distributions, reduce hydraulic efficiency, and diminish contaminant removal (Kadlec and Wallace 2008; Carleton et al. 2001; Holland et al. 2004). Spatial variability in vegetation structure can either enhance retention and mixing or, if poorly aligned with flow direction, contribute to short-circuiting and rapid contaminant breakthrough (Sabokrouhiyeh et al. 2017; 2020; Vymazal 2013).

In addition to vegetation, small-scale elevation differences, such as hummocks, depressions, and ridges, play a central role in shaping flow patterns and transport processes. Microtopography creates spatial gradients in inundation depth, soil moisture, hydroperiod, and nutrient availability, which influence vegetation composition, biogeochemistry, microbial activity, carbon storage, and ecological resilience across wetland types (Moser et al. 2007; Diamond et al. 2020; Zheng et al. 2021; Vulliet et al. 2024; Wang et al. 2023; Keiser et al. 2024; Smith et al. 2024; Zhang et al. 2023; Harvey et al. 2025). These microtopographic features affect local velocities, mixing, and exchange processes, and thus are expected to influence solute transport and overall treatment performance. Yet their quantitative hydrodynamic impacts remain less explored than their ecological ones, particularly from a modelling perspective.

Another important and often overlooked aspect is the role of input data resolution. In practice, digital elevation models (DEMs), vegetation maps, and other spatial inputs are derived from field surveys or remote sensing data that are inherently resolution-limited. If critical spatial details are undersampled or smoothed, numerical models may fail to capture key hydrodynamic structures, leading to over- or underestimation of hydraulic efficiency and contaminant removal (Jarihani et al. 2015; Seenath 2018). Despite increasing recognition of this issue, no systematic framework has been proposed to quantify how input resolution interacts with the statistical structure of wetland heterogeneity to influence predictive accuracy.

To address these gaps, the present chapter reports on work in which we investigated the combined effects of bed topography and spatial data resolution on hydraulic and treatment performance in free water surface wetlands. Using two-dimensional shallow-water models and synthetic wetlands characterized by spatially correlated random fields of bed elevation and vegetation density, we evaluated how topographic variability, correlation length, and input coarse-graining influence flow patterns, residence time distributions, and contaminant removal. High-resolution fields were systematically coarse-grained and used as inputs to the numerical model, allowing direct comparison between simulations based on original and degraded representations of the same wetland. Prediction errors in nominal residence time, residence time variance, and outlet contaminant concentration were then quantified. Collectively, this work provided new insights into the mechanistic role of microtopography, clarified the sensitivity of wetland models to input resolution, and offered practical guidance for model setup, wetland design, and field data acquisition.

4.8.3 Methods

4.8.3.1 *Wetland Model*

A two-dimensional, depth-averaged numerical model was employed to simulate the flow field and solute transport in synthetic wetlands under steady-state conditions. The hydrodynamics are governed by the shallow-water equations, while solute transport is described using the depth-averaged advection-diffusion equation. This modeling approach is suitable for free-surface wetland systems where horizontal transport dominates over vertical processes, and where vertical stratification of velocity or concentration is minimal.

The model is capable of representing both laminar and turbulent flow, although the velocities and flow depths in the simulated wetlands are consistent with laminar flow conditions. Solute input is prescribed as a spatially uniform concentration across the inlet boundary, with no consideration of density-driven or thermally stratified flows. Vegetation is assumed to be emergent and to exert drag on the flow, with its distribution either uniform or spatially variable, depending on the simulation setup.

In this study, spatial heterogeneity in both bed elevation and vegetation density is represented using synthetic fields generated via a two-dimensional Gaussian random field model. This allows us to systematically explore the influence of spatial variability and resolution on model predictions. Specifically, we consider wetlands where either bed elevation varies while vegetation is uniform, or where the bed is flat and vegetation density is spatially heterogeneous. For both cases, high-resolution input fields are generated and then progressively coarse-grained to assess the impact of input resolution on key performance metrics.

The use of a depth-averaged modeling framework offers a computationally efficient yet physically meaningful way to assess how spatial detail in input data influences model outputs. However, this approach necessarily neglects vertical gradients in flow and concentration, and assumes fully emergent vegetation. As such, it may not capture all three-dimensional effects present in natural wetlands, especially under strongly stratified conditions. Nevertheless, this modeling framework allows quantification of resolution-dependent prediction errors in simplified but representative wetland systems.

4.8.3.2 Hydrodynamic Model

Assuming hydrostatic pressure, steady flow, and negligible wind and Coriolis effects, the depth-averaged flow field is governed by the two-dimensional shallow-water equations (e.g., Wu 2007):

$$\begin{aligned}
&\frac{\partial(h\,U_x)}{\partial x}+\frac{\partial\left(h\,U_y\right)}{\partial y}=\;0\\
&\frac{\partial(h\,U_x^2)}{\partial x}+\frac{\partial\left(h\,U_xU_y\right)}{\partial y}=-\,g\,h\frac{\partial z_s}{\partial x}-\frac{\tau_{bx}}{\rho}-\frac{\tau_{vx}}{\rho}\\
&\frac{\partial\left(h\,U_xU_y\right)}{\partial x}+\frac{\partial\left(h\,U_y^2\right)}{\partial y}=-\,g\,h\frac{\partial z_s}{\partial y}-\frac{\tau_{by}}{\rho}-\frac{\tau_{vy}}{\rho}
\end{aligned}$$

where U_x and U_y are the depth-averaged velocity components in the x and y directions, respectively; h is the local water depth; z_s is the free-surface elevation; ρ is the water density; and τ_b and τ_v denote the shear stresses due to bed friction and vegetation drag, respectively.

Bed friction is represented by a spatially uniform Manning's roughness coefficient, M = 0.025 s·m$^{-1/3}$, which accounts only for soil-scale roughness (Chow 1959). Larger-scale roughness effects associated with variable topography or vegetation distribution are not included in this parameter, as they are treated explicitly through the bathymetry and vegetation drag formulations.

Vegetation-induced drag is parameterized as a function of the local stem density n and stem diameter d, following the formulation of Sabokrouhiyeh et al. (2020). The simulations were carried out considering two different vegetation scenarios with uniform stem density and diameter. A first scenario uses a density of n = 500 stems·m^{-2} and a diameter of d = 3 mm, and a second scenario uses n = 250 stems·m^{-2} and d = 6 mm. These values fall within the ranges reported by Valiela et al. (1978) for the salt-marsh grass Spartina alterniflora.

Two classes of wetland configurations are considered in this study. In the first, spatial variability is introduced in the bed topography while vegetation density is kept uniform. In the second, the bed is flat and vegetation density varies spatially. In both cases, spatially correlated random fields are used to generate heterogeneous patterns of topography or vegetation, allowing a systematic exploration of their influence on model predictions.

Although vegetation distribution in natural wetlands often correlates with water depth (e.g., Hudon 2004), such interactions were not incorporated in this study because reliable empirical relationships for modeling these correlations are lacking. By treating bed-elevation and vegetation-density variability separately, our approach isolates their individual effects on hydrodynamic behavior and avoids potential confounding from their covariation.

4.8.3.3 Solute Transport Model

The transport and removal of a reactive solute within the wetland is described using a two-dimensional, depth-averaged advection-diffusion equation with a first-order reaction term:

$$\frac{\partial(h\,C)}{\partial t}+\frac{\partial(h\,U_xC)}{\partial x}+\frac{\partial\left(h\,U_yC\right)}{\partial y}=\frac{\partial}{\partial x}\left(hE_{xx}\frac{\partial C}{\partial x}+\,hE_{xy}\frac{\partial C}{\partial y}\right)+\frac{\partial}{\partial y}\left(hE_{yx}\frac{\partial C}{\partial x}+\,hE_{yy}\frac{\partial C}{\partial y}\right)-\,kC$$

where $C(x,y,t)$ is the depth-averaged solute concentration, h is the local water depth, U_x and $U_y$are the depth-averaged velocity components, and E_{ij} are the components of the effective dispersion tensor that incorporate turbulent mixing and shear dispersion effects. The parameter k represents the local areal removal rate (m·yr^{-1}), which is modeled as a linear function of vegetation density, following the approach of Sabokrouhiyeh et al. (2020).

Here, n is the local vegetation stem density, $\bar{n}$ = 500 stems·m^{-2} is the reference density used to normalize the relationship, equal to the mean density, and k_0 = 11.5 m·yr^{-1} is the reference areal removal rate, consistent with the average value for ammonia removal reported by Kadlec (2008) for a survey of 131 wetlands.

The dispersion tensor E_{ij} accounts for both local mixing and velocity shear induced by vegetation drag, and is parameterized as a function of stem density, stem diameter, local velocity, and water depth, following the approach described by Sabokrouhiyeh et al. (2020):

$$k = k_0 \frac{n}{\overline{n}}$$

Solute transformation occurs only in regions where water depth is positive; dry or intermittently inundated areas are excluded from transport and reaction processes. The model assumes the solute is introduced with uniform concentration at the inlet, and that no additional sources or sinks are present within the domain.

4.8.3.4 Numerical Simulations

All simulations were conducted on a rectangular wetland domain measuring approximately $L = 100$ m in length and $W = 50$ m in width. The inlet and outlet were both centrally located along the short sides of the domain, with a channel width of 5 m for each. A constant inflow rate of $Q = 4.8$ L s^{-1} was prescribed at the inlet, and the water surface elevation at the outlet was adjusted to achieve a mean residence time of 6 days across all simulations. This residence time is within the typical range for free-water surface wetlands (Kadlec and Wallace 2008; Serra et al. 2004). Given the fixed surface area, the average water depth remained constant at H = 0.5 m in all cases. Vegetation-induced hydraulic resistance was included through the drag formulation described in Section 4.8.3.2.

For solute transport, boundary conditions were defined as follows: a constant normalized concentration, $\hat{C}_{in} = 1$, was imposed at the inlet; an open (zero-gradient) condition was applied at the outlet; and impermeable, no-flux conditions were enforced along the remaining boundaries.

The governing equations for flow and solute transport were solved using a custom-built two-dimensional finite volume code. The hydrodynamic solver employs the Saint-Venant equations with a second-order time integration scheme, and a Van Leer flux-limited total variation diminishing (TVD) method for spatial advection (van Leer 1974). For scalar transport, the advection term is handled via the explicit wave-propagation algorithm available in the CLAWPACK library (LeVeque 1997; Calhoun and LeVeque 2000), while diffusion is treated using the implicit Crank-Nicolson scheme. The computational domain was discretized using a uniform Cartesian grid with 0.5 m resolution. A time step of 1 min was found to ensure numerical stability and convergence of all simulations.

4.8.3.5 Bed topography

Two-dimensional Gaussian random fields of bed elevation, $z_b(x, y)$, were generated using a spectral method, with given variance σ_h^2, and correlation lengths λ_x and λ_y in the streamwise (x) and lateral (y) direction, respectively. Note that, in the simulations performed in this study, the variations in free surface elevation are extremely small relative to the mean water depth, and therefore, the variance of bed elevation is, for all practical purposes, the same as the variance of water depth.

In the simulations, we considered three possible values of the normalized standard deviation of bed elevation, $\sigma_h/H = 0.2$, 0.4, and 0.6. For the latter case, we also considered two distinct correlation lengths $\lambda = 5$ m and 10 m, corresponding to 0.05 to 0.1 times the longitudinal size of the wetland, L, and 0.1 to 0.2 times the width of the wetland, W. We only considered isotropic fields of bed elevation, for which $\lambda = \lambda_x = \lambda_y$.

The values chosen for the standard deviation and correlation length were designed to span conditions from nearly flat beds to highly irregular topographies, while still remaining consistent with the assumptions of a depth-averaged shallow-water model. The selected variability in σ_h is comparable to that observed in natural wetlands (e.g., Price 1993), where features such as small ridges, depressions, and shallow channels can introduce substantial elevation differences. Considering this range makes it possible to capture a wide variety of plausible wetland morphologies and to derive findings that are relevant for both wetland analysis and design.

For each set of parameter values, we generated 200 random topographies and simulated the flow and mass transport through the wetland. Based on several tests, this was more than sufficient to obtain accurate statistics of the chosen performance metrics that are independent of the number of generated random fields.

4.8.3.6 Vegetation Distribution

In the absence of empirical relationships linking vegetation stem density to water depth, simulations with heterogeneous bed topography were conducted assuming a uniform vegetation density of $\bar{n}$ = 500 stems/m^2 and diameter d = 3 mm. These values fall within the ranges reported by Valiela et al. (1978) for Spartina alterniflora, and they provide representative conditions for emergent wetland vegetation. This approach allows us to isolate the influence of bed variability independently from vegetation heterogeneity.

Complementary simulations considered wetlands with flat beds, and thus a uniform flow depth of H = 0.5 m, but heterogeneous vegetation distributions. Random fields of stem density were generated with the same random field generator used for topography, but using an exponential covariance function following Sabokrouhiyeh et al. (2020). The analysis focused on wetlands with an average stem density $\bar{n} = 500$ stems/m^2, a standard deviation σ_n = 300 stems/m^2, and a correlation length $\lambda = 5\,m$. This level of variability is also consistent with reported ranges for the salt marsh grass Spartina alterniflora (Valiela et al. 1978). For these parameter values, 200 random realizations of vegetation density were generated.

4.8.3.7 Resampling Approach

The impact of data resolution on model predictions was assessed by comparing coarsened representations of bed elevation and vegetation density against a high-resolution benchmark. The benchmark corresponds to fields directly defined on the computational mesh used in the simulations, which has a grid size of 0.5 m.

To generate coarsened inputs, the high-resolution fields were resampled on a uniformly spaced square grid with grid size $\Delta x = \Delta y$. Since the wetland length L is twice its width W, the spacing was defined as $\Delta x = W/m_y$, where m_y is the number of intervals along the width. The first sampling point is placed at a distance $\Delta x/2$ from the wetland boundaries, ensuring that the grid is centered in the wetland and that the number of longitudinal nodes is twice the number of lateral ones. The coarsened fields were then linearly interpolated back onto the computational mesh for use in the simulations.

The number of sampling intervals m_y varied between 2 and 100, corresponding to coarsened grid sizes ranging from 25 m to 0.5 m. To enable comparison across different correlation lengths, the results are expressed in terms of the normalized grid size $\Delta x/\lambda$, where λ is the correlation length of the random field. Accordingly, $\Delta x/\lambda$ spans from 0.1 to 5 for $\lambda = 5$ m and from 0.05 to 2.5 for $\lambda = 10$ m.

Illustrative examples are shown in Figure 2 for a wetland topography with $\sigma_h/H = 0.6$. Figure 2a shows the case $m_y = 2$, corresponding to $4 \times 2 = 8$ sampling points, with the resulting interpolated bed elevation field on the computational mesh shown in Figure 2c. Figure 2b shows the case $m_y = 5$, corresponding to $10 \times 5 = 50$ sampling points, with the interpolated field shown in Figure 2d.

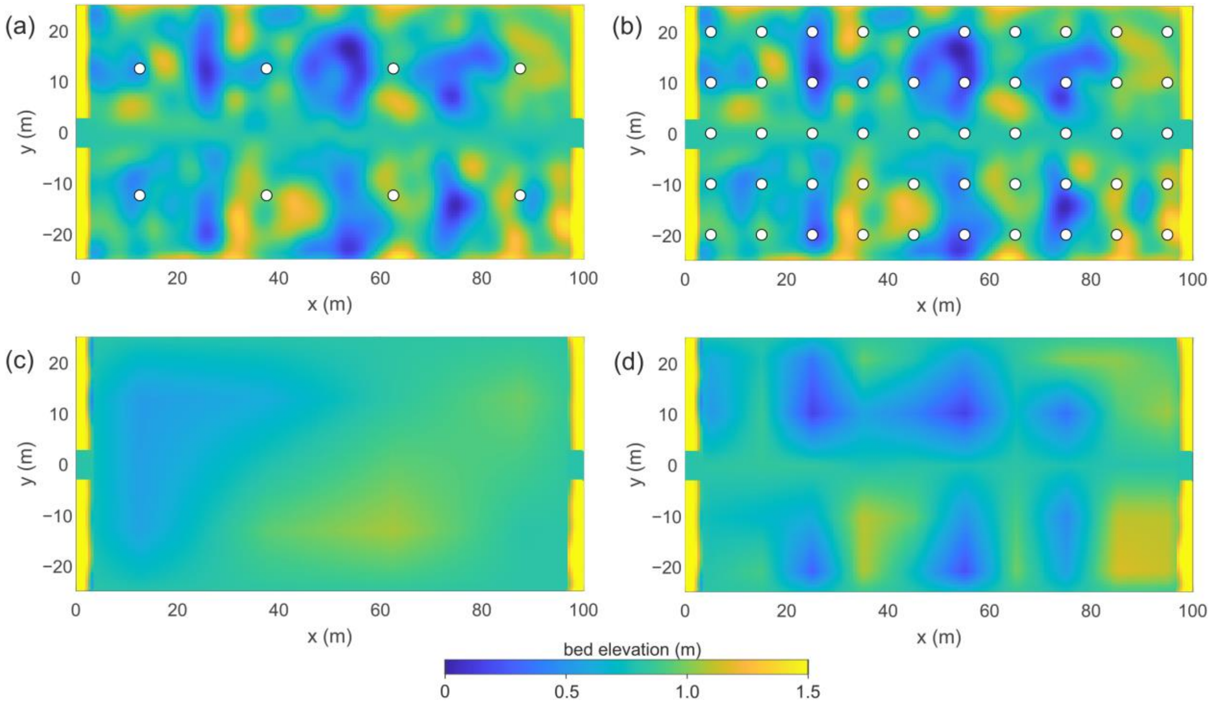

Figure 2. Examples of coarse-graining of bed elevation fields for a wetland with $\sigma_h/H = 0.6$. Panels (a, b) show sampling grids with $m_y = 2$ and $m_y = 5$ points across the wetland width, corresponding to 4 × 2 = 8 and 10 × 5 = 50 sampling points, respectively. Panels (c, d) show the corresponding interpolated bed elevation fields interpolated back onto the computational mesh with $\Delta x = 0.5$ m.

4.8.3.8 Efficiency Metrics

In this work, we imposed the discharge and the average flow depth so that the mean residence time was the same for all simulated wetlands. We then analyzed the hydraulic performance based on the residence time distributions (RTDs), looking in particular at the standard deviation of the residence time. The residence time distribution, $R(t)$, was calculated by simulating the transport of a passive tracer ($k = 0$ m yr^{-1}) with a constant concentration, C_0, at the inlet, and a concentration of zero in the wetland. The cumulative RTD, $R(t)$, was then calculated as the normalized output concentration, $C_{\text{out}}(t)/C_0$.

The first moment of the RTD is the mean residence time, t_m, i.e., the average time that a water parcel remains in the wetland. This is calculated from the complementary cumulative distribution function, $R_c(t) = 1 - R(t)$, as

$$t_m = \int_0^\infty R_c(t)\ dt,$$

The second central moment of the residence time, i.e., its variance, is calculated as

$$\sigma_t^2 = \int_0^\infty 2t\, R_c(t)\, dt - t_m^2$$

which provides a measure of the spreading around the mean value, t_m.

The numerical simulation of the transport of a passive scalar is protracted for a sufficiently long time so that $C_{\text{out}}/C_0 \approx 1$ at the end of the simulation, and $t_m \approx t_n = V/Q$, where V is the water volume in the wetland.

In general, a wetland can be modeled as a number (N) of continuous stirred tank reactors (CSTRs) in series (Kadlec and Wallace 2008). In the case of a single tank ($N = 1$), the wetland behaves as a well-mixed reactor, resulting in an exponential RTD with $\sigma = t_n$. Conversely, a model with a large number of tanks produces a system approaching plug flow, which corresponds to a variance of the residence time approaching zero. The number of tanks in series, N, can be determined from the inverse of the dimensionless variance ($\sigma_\theta = \sigma/t_n$):

$$N = \sigma_\theta^{-2} = \left(\frac{\sigma}{t_n}\right)^{-2}$$

and can be used to compute the dispersion efficiency of the wetland (Persson et al. 1999):

$$e_d = 1 - \sigma_\theta^2 = 1 - \frac{1}{N}$$

which is equal to 1 in the ideal limit of plug flow, as σ_θ approaches zero.

An alternative metric of wetland efficiency is the volumetric efficiency, e_v, which according to Persson et al. (1999) represents the effective volume of a wetland system and is defined as

$$e_v = \frac{t_m}{t_n}$$

where t_m is the mean residence time measured in a field tracer test. It is noted that, for a completely passive tracer, the mean residence time should equal the nominal residence time in the limit case where the distribution of the residence time is sampled for an infinitely long time and the tail of the distribution is accurately represented. In the present study, all simulated wetlands have the same water volume and flow rate, resulting in identical nominal residence times across all cases. Since the residence time distributions are reconstructed over a sufficiently long duration to allow for full mixing, we have $t_m \approx t_n$. Therefore, according to the definition above, $e_v \approx 1$ for all wetlands.

For the same reason, the hydraulic efficiency index, e_h, defined by Persson et al. (1999) as the product of volumetric efficiency and dispersion efficiency,

$$e_h = e_v \cdot e_d = \frac{t_m}{t_n}\left(1 - \frac{1}{N}\right)$$

is approximately equal to e_d in all simulations.

An alternative metric for the degree of mixing is based on the time taken for 90% of the injected tracer to leave the system, t_{90}, and is defined as follows:

$$\theta_{90} = \frac{t_{90}}{t_n}$$

Generally, higher values of θ_{90} indicate poor mixing, with $\theta_{90} \approx 1$ in the ideal case of complete mixing. Again, this parameter is correlated to the variance of the residence time, σ_t^2, as for the same t_n, higher values of σ_t imply higher values of θ_{90} and therefore lower degrees of mixing.

For the simulations with a reactive tracer, we also evaluated the concentration reduction efficiency:

$$E_c = \frac{C_i - C_o}{C_i} = 1 - \frac{C_o}{C_i}$$

In this study, the input flow rate is imposed, and steady-state conditions are assumed. Although evapotranspiration can be significant in some wetland systems, it is neglected here to focus on the dominant advective-dispersive transport processes; as a result, inflow equals outflow. Therefore, the ratio of the output mass rate to the input mass rate equals the ratio of the output concentration to the input concentration, and the concentration reduction efficiency also represents the mass removal efficiency.

4.8.3.9 Error Metrics

To assess the accuracy of the coarse-grained models, we evaluated three characteristic parameters that govern wetland performance. The first parameter is the nominal residence time, $t_n = V/Q$, where V is the water volume in the wetland and Q is flow rate. This parameter is widely used as the primary design criterion for constructed wetlands, as it ensures that solutes remain in the system long enough for treatment processes to occur (Kadlec and Wallace 2008). In all high-resolution benchmark simulations, the outlet water level was adjusted so that the nominal residence time is fixed at $t_n^* = 6$ days (see Section 4.8.3.4). The relative error in the coarse-grained model is then defined as

$$\Delta\hat{t}_n = \frac{t_n - t_n^*}{t_n^*}$$

where t_n is the value obtained from the coarse-grained model.

The second parameter is the variance of the residence time, σ_t^2, which characterizes the spread of solute travel times. The relative error in this parameter is defined as

$$\Delta\widehat{\sigma_t} = \frac{\sigma_t - \sigma_t^*}{\sigma_t^*},$$

where σ_t^* is the benchmark (high-resolution) value.

The third parameter is the outlet concentration in reactive transport simulations, C_{out}, which directly reflects contaminant removal efficiency. Its relative error is defined as

$$\Delta\hat{C}_{\mathrm{out}} = \frac{C_{\mathrm{out}} - C_{\mathrm{out}}^*}{C_{\mathrm{in}}}$$

where C_{out}^* is the outlet concentration from the benchmark model, and C_{in} is the inlet concentration. Normalizing by C_{in} rather than C_{out}^* provides a clearer measure of the deviation in predicted treatment performance relative to the influent load.

4.8.4 Results

4.8.4.1 *Effect of Bed Topography*

4.8.4.1.1 Flow Patterns

Examples of simulated wetlands with isotropic bathymetry fields are shown in Figure 3. Specifically, Figure 3a shows a wetland with a uniform water depth. The wetlands in Figure 3b, Figure 3c, and Figure 3d, have a non-uniform random bed elevation with correlation length $\lambda = 5$ m and a standard deviation $\sigma_h/H = 0.2, 0.4$, and 0.6, respectively. As previously mentioned, in all cases, the mean water depth is the same, i.e., $H = 0.5$ m. It can be seen that, for this value of the correlation length, if the standard deviation of bed elevation is sufficiently high, there can be a formation of internal dry zones, i.e., islands. For higher values of the correlation length, the occurrence of internal dry zones becomes less likely.

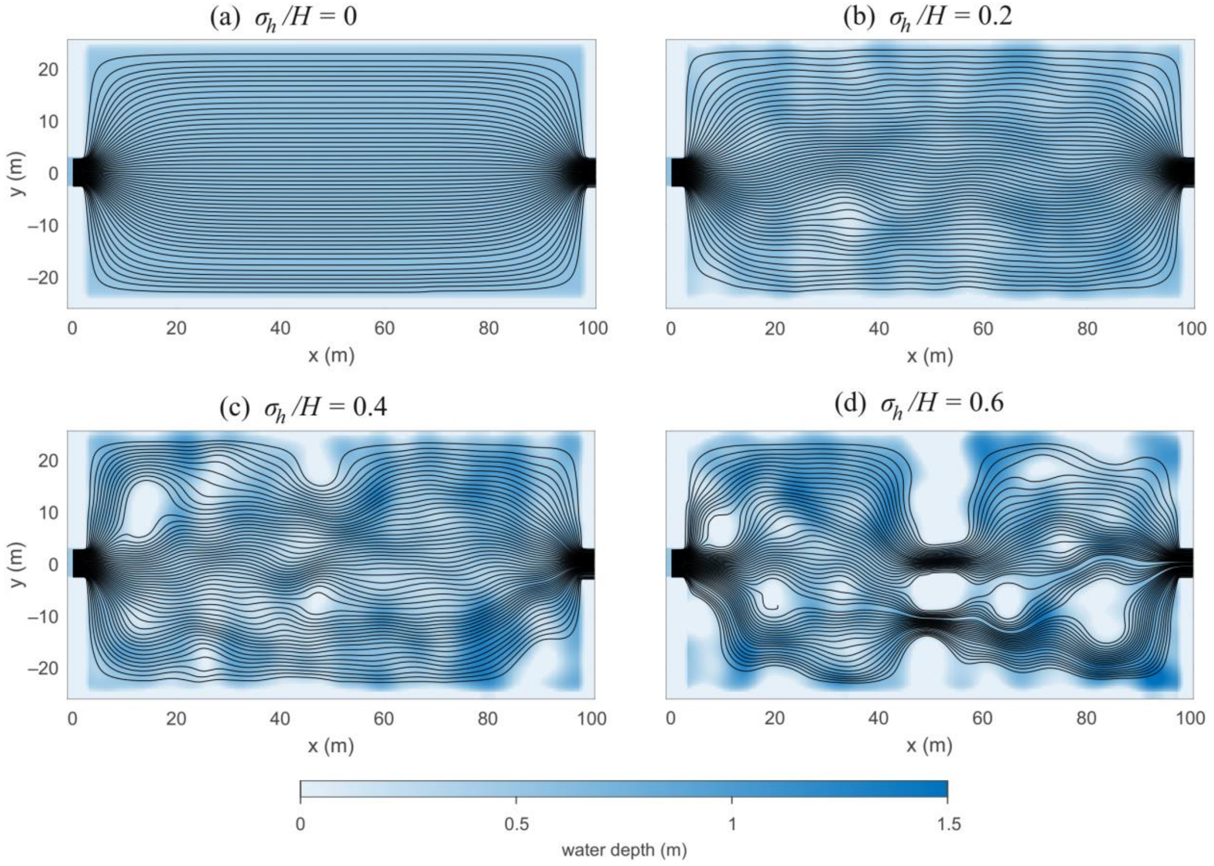

Figure 3. Example bathymetric maps and streamlines for wetlands with correlation lengths of $\lambda_x = \lambda_\gamma = 5$ m, an average water depth of $H = 0.5$ m, and the following normalized standard deviations of bed elevation: (a) $\sigma_h / H = 0$; (b) $\sigma_h / H = 0.2$; (c) $\sigma_h / H = 0.4$; (d) $\sigma_h / H = 0.6$.

Figure 3 also shows the streamlines obtained by considering 100 source points at the inlet, which are seen to become more irregular as the variance of bed elevation is increased. Figure 3a shows the case of a wetland with uniform bed topography, and therefore almost uniform flow depth. Figure 3b shows a wetland with $\sigma_h/H = 0.2$, in which the pattern of streamlines is very similar to that of a uniform wetland, but we make an exception for a higher variance of flow velocities due to the differences in water depth. A similar flow pattern is also found for $\sigma_h/H = 0.4$, but in this case, we can also observe small internal islands and lateral bars which act as breakwaters and significantly deflect the streamlines. For the wetland in Figure 3d, it can be seen that there is an island which causes a flow contraction and a partition of the flow into two main pathways. In this case, there is an additional obstruction induced by two large lateral bars, which create a wetland with the two main detention basins. A further partition of the flow is induced by small internal wetlands inside the second basin. This case well illustrates the complex flow patterns that can arise in the wetland with a large variance in bed elevation. In general, as the variance of bed elevation σ_h increases, larger lateral dead zones appear where lower velocities are found, and even internal dead zones can appear when internal dry zones are present.

4.8.4.1.2 Isotropic Bed Topography

We first investigated the hydraulic performance of a wetland with isotropic topography, i.e., wetlands with bed elevation fields in which the correlation lengths in the x and y directions are the same, $\lambda_x = \lambda_y$. Figure 4 shows the behavior of the standard deviation of the residence time, σ_t as a function of the standard deviation of bed elevation, σ_h. It can be seen that the average standard deviation of the residence time seems to follow a sigmoid function, which increases with the standard deviation of bed elevation, but reaches a horizontal asymptote for $\sigma_h/H \approx 0.6$. This implies that the hydraulic efficiency decreases on average for a higher σ_h/H. If we consider the definition of e_h provided in Section 4.8.3.8, the highest hydraulic efficiency among the simulated wetlands is obtained for $\sigma_h/H = 0$ and is equal to 0.96, whereas the minimum efficiency is obtained for $\sigma_h/H = 0.8$ and is equal to 0.64. Hence, the variation of the average hydraulic efficiency across the tested topographies is around 30%.

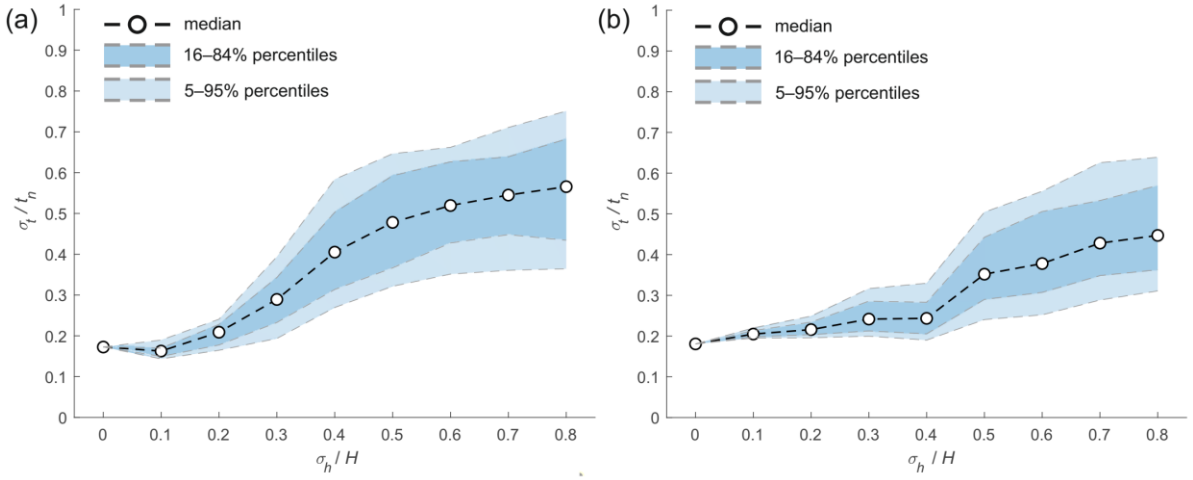

Figure 4. The standard deviation of the residence time as a function of the standard deviation of bed elevation for (a) n = 500 stems·m^{-2} and d = 3 mm, and (b) n = 250 stems·m^{-2} and d = 6 mm. In both cases, the normalized correlation length of the bed elevation is λ / H = 10. The increase in σ_t as the bed elevation variability becomes more pronounced implies a decrease in hydraulic efficiency.

In addition to the median value of σ_t/t_n, the graph in Figure 4 shows the range corresponding to the 16th and 84th percentiles, which is representative of the standard deviation of a normal distribution, and the range corresponding to the 5th and 95th percentiles, which is representative of the extreme values. It is observed that the spreading around the mean of σ_t/t_n also increases for increasing σ_h/H, which is consistent with the formation of more complex flow structures with lateral dead zones and internal dry zones as the topographical complexity increases. The range of variation of σ_t/t_n for $\sigma_h/H = 0.8$ is quite large, as the 5th percentile corresponds to $\sigma_t/t_n \approx 0.4$ and the 95th percentile corresponds $\sigma_t/t_n \approx 0.8$.

We then investigated the effect of the correlation length, λ, assuming a constant vegetation density in the wetland, so as to isolate the effect of bed topography. In all simulations, the normalized variance of the bed elevation σ_h/H is set to 0.8. The results are shown in Figure 5. It can be observed that σ_t/t_n decreases as the correlation length increases, and hence the hydraulic efficiency, e_h, is higher for larger correlation lengths. This is due to the formation of more complex flow patterns for smaller correlation lengths, characterized by the presence of lateral dead zones and internal dry zones. Note that, while the variance of σ_t/t_n is almost constant for the range of correlation lengths λ considered in the simulations, the range of variation of the most extreme values appears to decrease for increasing λ. This is likely due to the lower flow complexity, particularly the reduced likelihood of solute trapping in dead zones, which not only decreases the variance of the residence time but also narrows its range of variation.

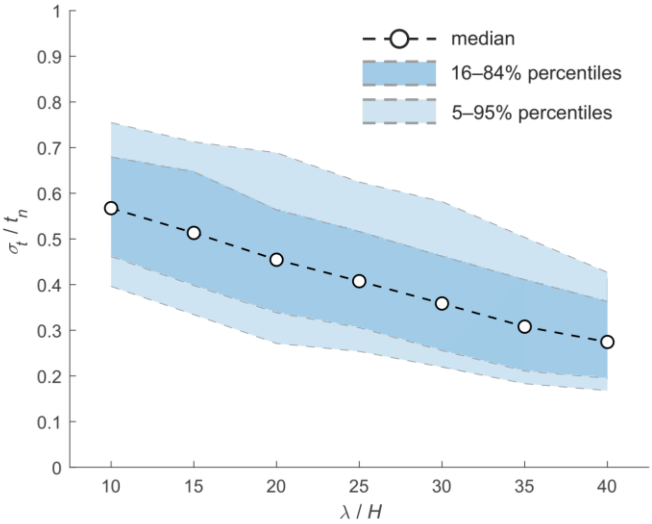

Figure 5. The standard deviation of the residence time as a function of the standard deviation of bed elevation for (a) n = 500 stems·m^{-2} and d = 3 mm, and (b) n = 250 stems·m^{-2} and d = 6 mm. In both cases, the normalized correlation length of the bed elevation is λ/H = 10. The increase in σ_t as the bed elevation variability becomes more pronounced implies a decrease in hydraulic efficiency.

4.8.4.1.3 Anisotropic Bed Topography

We evaluated the effect of anisotropic topography by considering different correlation lengths in the x- and y-directions, thus creating bed forms elongated in the two directions. In the simulations, we first set $\lambda_y =$ 5 m, which is to 0.1 times the width of the wetland, W, and varied λ_x from 5 to 20 m, i.e., from 10 to 40 times the average depth H, which corresponds to between 0.05 and 0.2 times the longitudinal length of the wetland, L. We then set $\lambda_x = 5$ m and varied λ_y from 5 to 20 m, i.e., from 0.05 to 0.1 the longitudinal size of the wetland. For all the topographies considered here, $\sigma_h / H = 0.8$.

Example bathymetric maps and streamlines for wetlands with anisotropic bed topography are shown in Figure 6. In particular, Figure 6a,b show two wetlands with bed forms elongated in the x direction, with $\lambda_x = 10$ m and $\lambda_x = 20$ m, respectively, whereas Figure 6c,d show wetlands with bed forms that are more elongated in the y direction, with $\lambda_y = 10$ m and $\lambda_y = 20$ m, respectively. It can be observed that increasing the longitudinal correlation length, λ_x, reduces the number of bed forms within the wetland, while increasing their size. This can lead to the formation of narrow preferential flow channels. In contrast, increasing the transverse correlation length, λ_y, results in bed forms that resemble baffles, creating larger lateral dead zones.

Figure 7a,b show the effect of the variation of the longitudinal and lateral correlation lengths, respectively. It can be seen that the standard deviation of the residence time decreases on average from $\sigma_t / t_n \approx 0.6$ to $\sigma_t / t_n \approx 0.4$ as λ_x is increased from $10H$ to $40H$, i.e., from 5 to 20 m, whereas the spreading around the mean does not differ substantially. Conversely, for an increasing λ_y, we do not observe a monotonic decrease in the standard deviation of the residence time. Instead, the maximum mean value of σ_t is found for $\lambda_y / L_y = 0.2$, i.e., $\lambda_y = 10$ m. The observed trends are likely to be due to a reduction in flow complexity as the correlation length of bed elevation becomes large relative to the size of the wetland.

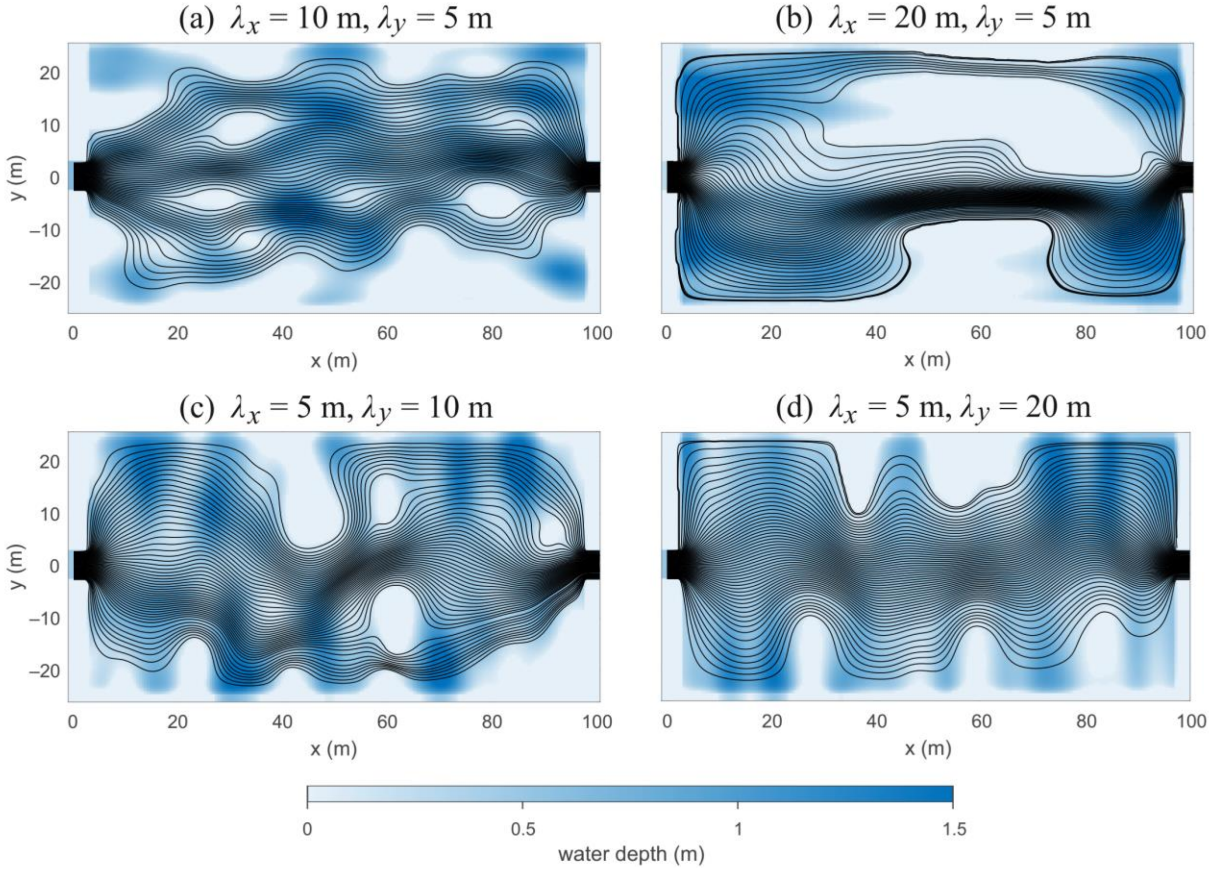

Figure 6. Example bathymetric maps and streamlines for wetlands with anisotropic topographies with $\sigma_h/H = 0.8$ and the following correlation lengths: (a) $\lambda_x = 10$ m and $\lambda_y = 5$ m; (b) $\lambda_x = 20$ m and $\lambda_y = 5$ m; (c) $\lambda_x = 5$ m and $\lambda_y = 10$ m; (d) $\lambda_x = 5$ m and $\lambda_y = 20$ m.

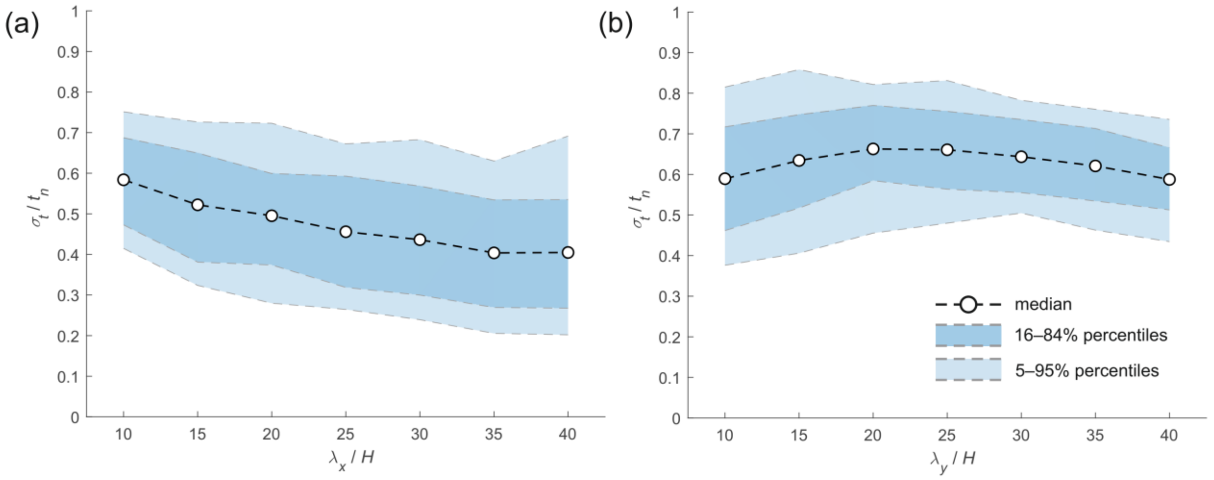

Figure 7. (a) Standard deviation of the residence time for wetlands with $\sigma_h/H = 0.8$ as a function of the correlation length of the bed elevation in the x direction. (b) Standard deviation of the residence time for wetlands with $\sigma_h/H = 0.8$ as a function of the correlation length of the bed elevation in the y direction. The results are based on wetlands with n = 500 stems·m^{-2} and d = 3 mm. It can be seen that increasing λ_x leads to a decrease in σ_t, and thus to higher hydraulic efficiency. In contrast, σ_t shows a convex trend with respect to λ_y, indicating a non-monotonic relationship.

4.8.4.1.4 Impact on Contaminant Removal Efficiency

The relationship between the variability of water depth and the concentration reduction efficiency was investigated by considering a non-zero reaction rate in the mass transport model, as explained in

Section 4.8.3.3. Figure 8 shows the results obtained for wetlands with a normalized correlation length of bed elevation $\lambda/H = 10$ and two different settings for vegetation: (a) $n = 500$ stems m^{-2} and $d = 3$ mm; and (b) $n = 250$ stems m^{-2} and $d = 6$ mm. In both cases, the areal removal rate, k, was set to 11.5 m yr^{-1}.

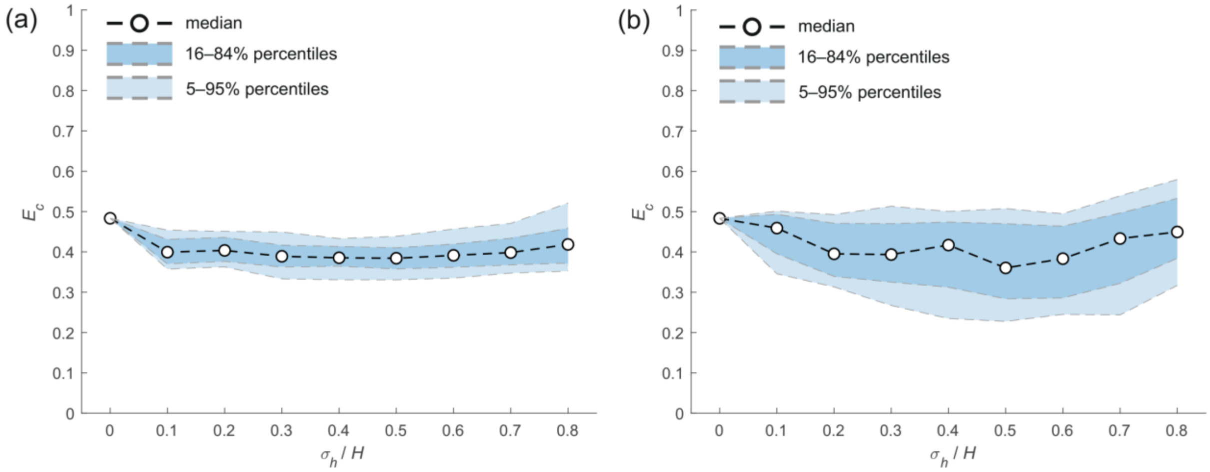

Figure 8. Concentration reduction efficiency as a function of the normalized standard deviation of bed elevation for wetlands with (a) n = 500 stems·m⁻² and d = 3 mm, and (b) n = 250 stems·m⁻² and d = 6 mm. In the simulations, the average water depth H is 0.5 m and the correlation length of the bed elevation λ is 5 m. The results show that the mean removal efficiency is lower in wetlands with non-uniform topography compared to the case with a uniform bed, with both the reduction and the variability in efficiency becoming more pronounced under sparser vegetation conditions.

The results show that mean removal efficiency is lower in wetlands with a non-uniform topography compared to those with uniform beds. This reduction is more pronounced under sparser vegetation conditions, with a difference of approximately 10% between the case of $\sigma_h/H = 0.5$ and the case of a flat bed. Moreover, substantial variability in removal efficiency is observed among the wetlands with the same standard deviation of bed elevation, with differences exceeding 30% for more heterogeneous topographies. This suggests that, although the statistical properties of the bed topography are identical, the relative positioning of the bed features can significantly influence flow patterns and short-circuiting, leading to divergent treatment outcomes. It is also apparent that variations in the removal efficiency are more pronounced for the second vegetation scenario, which is characterized by a smaller vegetation density but a larger stem diameter compared to the first scenario.

4.8.4.2 Sensitivity of Wetland Model Outputs to Data Resolution

4.8.4.2.1 Nominal Residence Time

Figure 9 presents the relative error in the nominal residence time, $\Delta\hat{t}_n$, as a function of the normalized grid size, $\Delta x/\lambda$, for four combinations of bed elevation variability and correlation length. In each panel, the median value across replicate realizations is shown together with the variability range defined by the 16th and 84th percentiles, which are representative of the standard deviation, and 5th and 95th percentiles, which are representative of the extreme values.

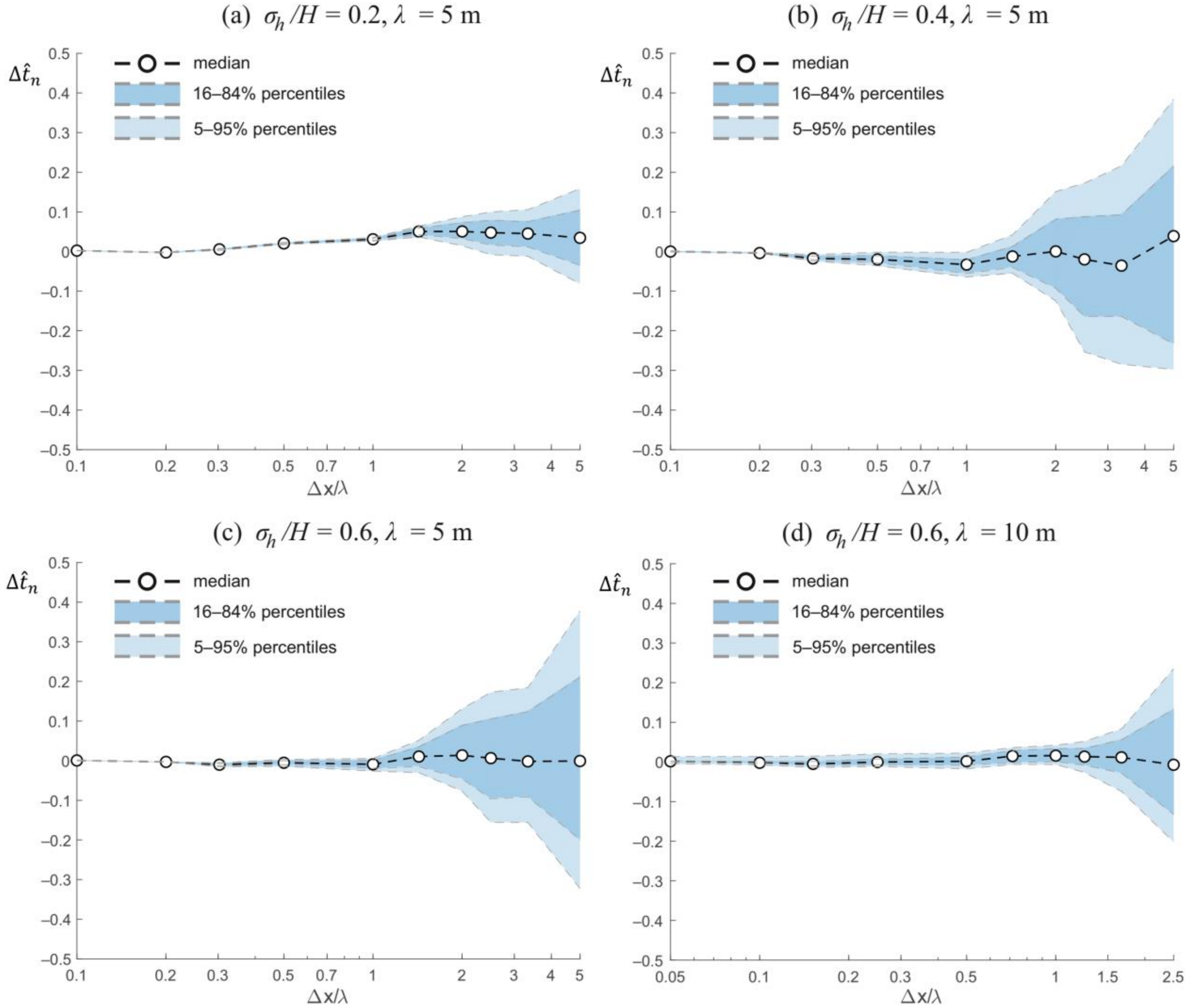

Figure 9. Relative error in the nominal residence time, $\Delta\hat{t}_{\mathrm{n}}$, as a function of the normalized grid size, $\Delta x/\lambda$, for wetlands with different bathymetric characteristics. Panels show results for (a) $\sigma_{\mathrm{h}}/H = 0.2$, $\lambda = 5$ m; (b) $\sigma_{\mathrm{h}}/H = 0.4$, λ = 5 m; (c) σ_{h}/H = 0.6, λ = 5 m; and (d) σ_{h}/H = 0.6, λ = 10 m. Symbols indicate the median error across realizations, with shaded bands corresponding to the 16th–84th and 5th–95th percentile ranges.

Overall, the results indicate that, on average, the nominal residence time is relatively insensitive to grid coarsening, with median errors typically within a few percent even when the grid size approaches or exceeds the bathymetric correlation length. For the case with moderate bed variability ($\sigma_h/H = 0.2$ Figure 9a), errors remain small and positive, and the spread across realizations only becomes significant when $\Delta x/\lambda \gtrsim 2$. Increasing the variance of bed elevation to $\sigma_h/H = 0.4$ (Figure 9b) leads to more variable outcomes, with median errors that are slightly negative at intermediate grid sizes and a much wider range of realizations at coarse resolution. A similar pattern is observed for $\sigma_h/H = 0.6$ and $\lambda =$ 5 m (Figure 9c), although the median error remains close to zero and the widening of the distribution is the most prominent effect.

Changing the correlation length alters the error behavior. For $\sigma_h/H = 0.6$ and $\lambda =$ 10 m (Figure 9d), the error distribution is narrow at fine resolutions, but at coarser grids the variability increases (with errors up to ± 0.4 for the 90% confidence interval) and both positive and negative outliers appear. Compared to the shorter correlation length case (Figure 9c), the larger λ reduces the bias in the median error but does not prevent the emergence of large deviations in individual realizations when $\Delta x/\lambda \gtrsim 2$.

In summary, these results suggest that while the nominal residence time is, on average, robust to grid coarsening, the uncertainty across realizations increases substantially as the grid size becomes larger than the correlation length, particularly for cases with higher bed elevation variance.

4.8.4.2.2 Variance of the Residence Time

Figure 10 shows the relative error in the variance of the residence time, $\Delta\widehat{\sigma}_t^2$, as a function of the normalized grid size $\Delta x/\lambda$. As in the case of the nominal residence time, the figure reports the median error together with percentile ranges that quantify the variability across realizations. The results indicate that the variance is systematically more sensitive to grid resolution than the nominal residence time, with errors becoming increasingly negative as $\Delta x/\lambda$ grows.

For weak bathymetric variability ($\sigma_h/H = 0.2$, Figure 10a), the errors remain small, with the median $\Delta\hat{\sigma}_t^2$ fluctuating near zero across all grid sizes. Although the spread increases for $\Delta x/\lambda > 1$, the error distribution remains largely centered, suggesting that variance is well preserved under coarse resolution when the bathymetry is relatively uniform.

As bathymetric variability increases, however, a clear trend of underestimation emerges. For $\sigma_h/H = 0.4$ (Figure 10b) and $\sigma_h/H = 0.6$ (Figure 10c), the median $\Delta\hat{\sigma}_t^2$ becomes increasingly negative with coarsening grid resolution, indicating that variance is consistently underestimated relative to the high-resolution reference. The spread of errors also widens substantially, with the 5th percentile dropping below -0.5 for $\Delta x/\lambda \geq 2$ in both cases. This indicates that coarse grids not only bias the variance but also introduce high variability between realizations, reflecting a loss of robustness.

The effect of increasing the correlation length (Figure 10d) slightly mitigates this sensitivity, at least for finer resolutions. For $\lambda = 10$ m, the errors remain relatively small for $\Delta x/\lambda < 0.5$, but as the resolution is degraded, the same pattern of negative bias and broadening distribution reappears. At the coarsest resolution, the median error approach -0.4, with extreme values nearly reaching -0.8.

Overall, these results highlight that the variance of residence times is far more vulnerable to loss of spatial detail than the nominal residence time. While nominal residence time errors remained relatively small even for coarse grids, variance shows a strong and systematic underestimation, particularly in wetlands with more variable bathymetry and shorter correlation lengths. This indicates that small-scale topographic variability plays a central role in generating dispersive flow paths and controlling residence time variability. When these fine-scale gradients are smoothed through coarse-graining, hydraulic heterogeneity diminishes, leading to a narrower predicted residence time distribution and reduced variance.

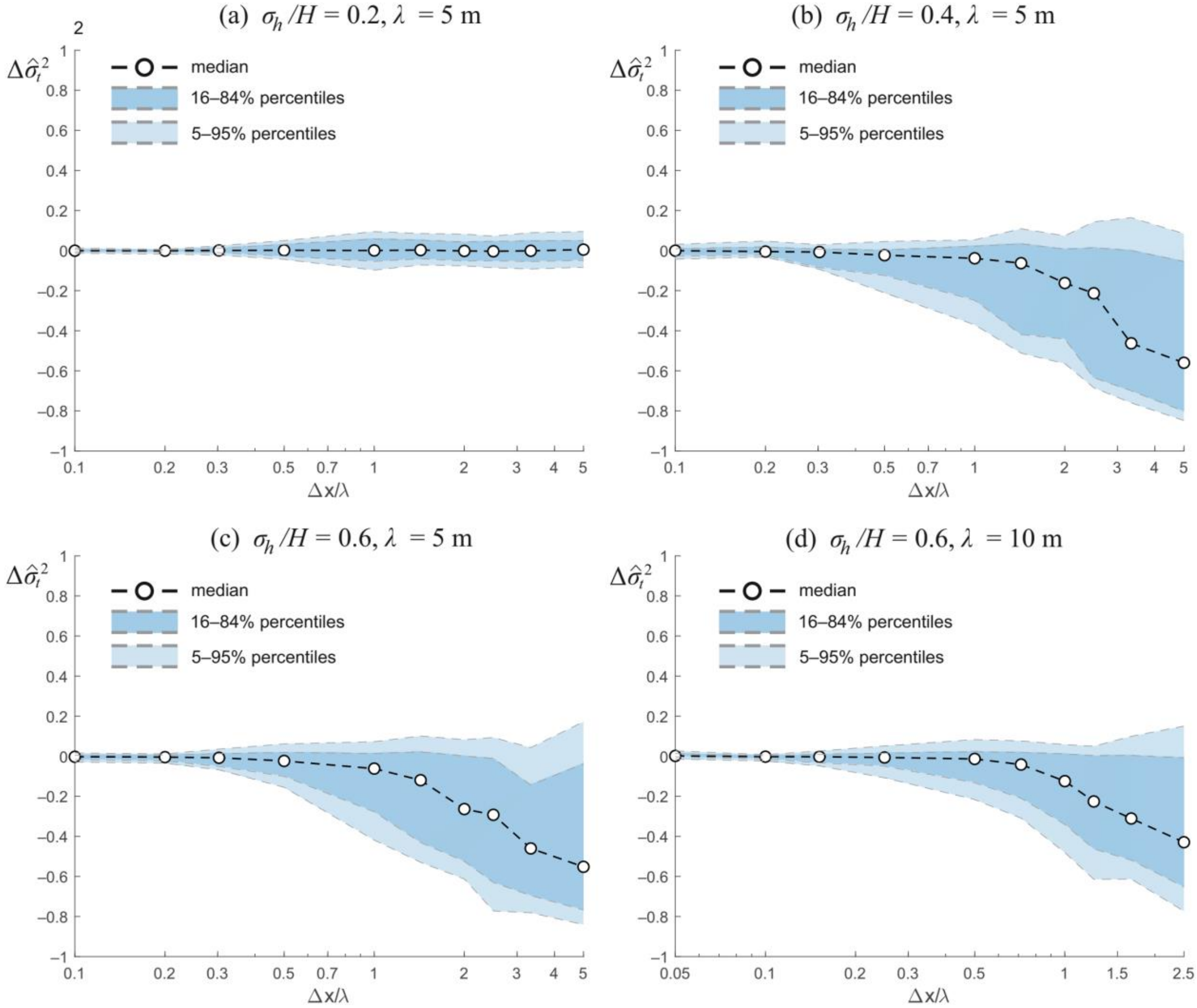

Figure 10. Relative error in the variance of the residence time, $\Delta\hat{\sigma}_t{}^2$, as a function of the normalized grid size, $\Delta x/\lambda$, for wetlands with different bathymetric characteristics. Panels show results for (a) $\sigma_h/H = 0.2$, λ = 5 m; (b) $\sigma_h/H = 0.4$, λ = 5 m; (c) $\sigma_h/H = 0.6$, λ = 5 m; and (d) $\sigma_h/H = 0.6$, λ = 10 m. Symbols represent the median error across realizations, while shaded bands indicate the 16th–84th and 5th–95th percentile ranges.

4.8.4.2.3 Outlet Concentration

Figure 11 shows the relative error in the predicted outlet concentration, $\Delta\hat{C}_{out}$, as a function of the normalized grid size, $\Delta x/\lambda$, across the different wetland scenarios. In contrast to the variance of the residence time, the behavior of $\Delta\hat{C}_{out}$ is less systematic, reflecting the fact that the outlet concentration is mostly dependent on the nominal residence time, and the uncertainty in C_{out} is a scaled version of the uncertainty in t_n.

For the case of low bathymetric variability ($\sigma_h/H = 0.2$, Figure 11a), the median error remains close to zero for all resolutions, with values fluctuating between slightly positive at finer grids and slightly negative at coarser grids. The spread across realizations, as indicated by the percentile bands, remains relatively narrow, suggesting that predictions of outlet concentration are generally robust when bathymetric variability is small.

As the bathymetric variability increases to $\sigma_h/H = 0.4$ (Figure 11b), a modest increase in the dispersion of $\Delta\hat{C}_{out}$ is observed, especially at larger grid sizes. The median error remains small and does not show a strong systematic bias, although the spread widens, indicating that the reliability of coarse models decreases with increasing bed variability.

For high bathymetric variability ($\sigma_h/H = 0.6$, Figure 11c), the effect of grid coarsening becomes more pronounced. The median error slightly increases with grid size, reaching values on the order of a few percent at $\Delta x/\lambda \gtrsim 1$, and the uncertainty band broadens considerably. In this case, the results exhibit a slight bias toward overestimating the outlet concentration. These patterns may reflect nonlinear effects of coarse-graining on depth–drag relationships and flow connectivity. However, given the complex, nonlinear interactions between bathymetry, hydraulics, and solute transport, it is difficult to provide a definitive explanation for the observed bias.

Finally, when the correlation length is increased to $\lambda = 10$ m while maintaining $\sigma_h/H = 0.6$ (Figure 11d), the overall trends remain similar, but the dispersion is somewhat reduced compared to the $\lambda = 5$ m case. The median error stays close to zero for fine resolutions and becomes slightly negative at coarse resolutions, while the uncertainty range remains moderate. This suggests that larger correlation lengths mitigate the sensitivity of outlet concentration predictions to grid resolution, even under strong bathymetric variability.

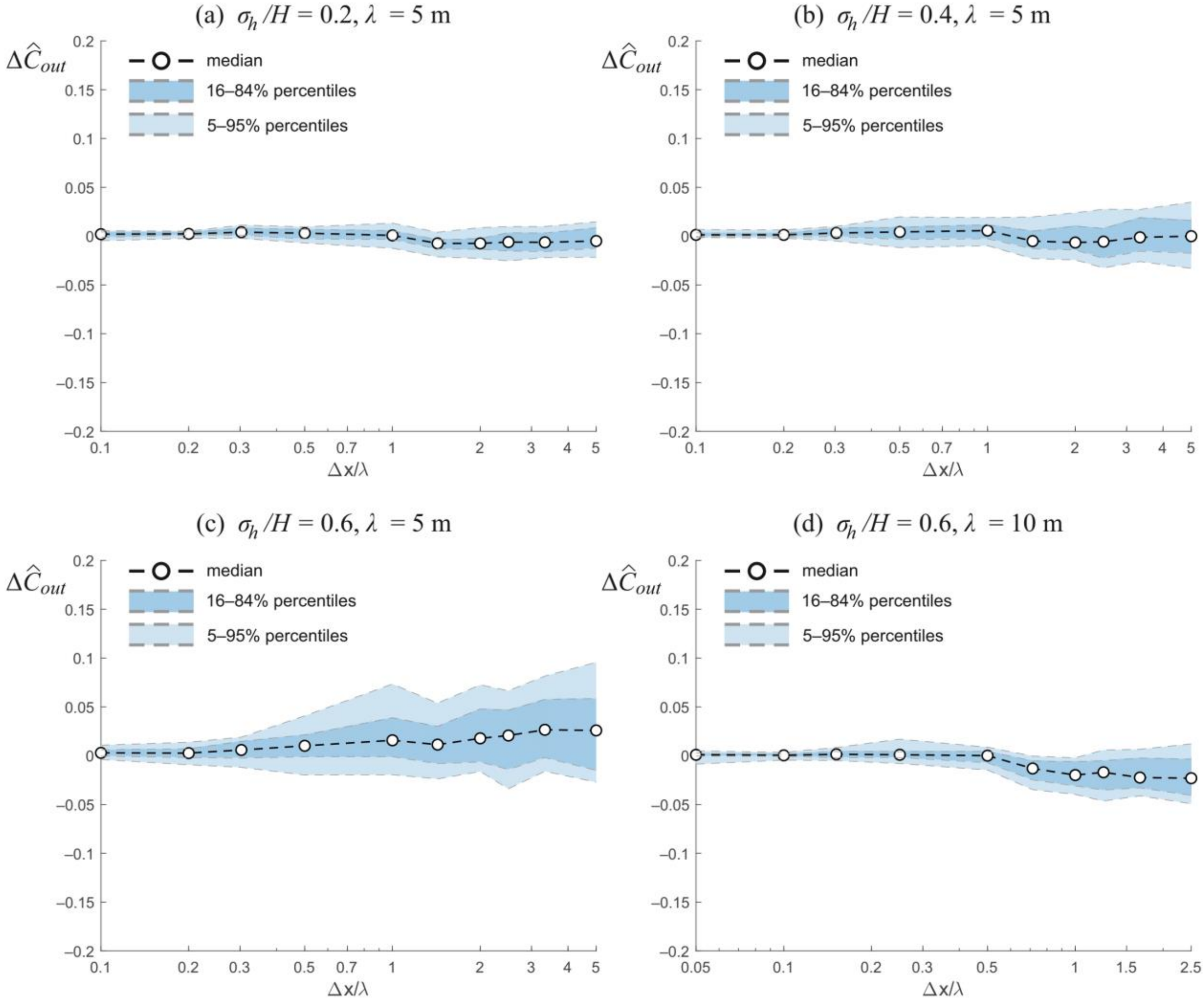
(a) $\sigma_h/H = 0.2, \lambda = 5$ m

(b) $\sigma_h/H = 0.4, \lambda = 5$ m

(c) $\sigma_h/H = 0.6, \lambda = 5$ m

(d) $\sigma_h/H = 0.6, \lambda = 10$ m

Figure 11. Relative error in the outlet concentration, $\Delta\hat{C}_{out}$, as a function of normalized grid size, $\Delta x/\lambda$, for wetlands with different bathymetric variability and correlation lengths. The results highlight that outlet concentration is less systematically biased by grid resolution than the variance of the residence time (Figure 10), with variations generally limited to a few percentage points. However, the associated uncertainty tends to increase with stronger bathymetric variability and coarser resolution, particularly when the bed elevation field is highly heterogeneous.

Overall, these results highlight that outlet concentration is less systematically biased by grid resolution than the residence time metrics, but the associated uncertainty can grow with increasing bathymetric variability and coarsening, particularly when the bed elevation field is highly heterogeneous.

4.8.4.2.4 Effect of a Non-Uniform Vegetation Distribution

We now examine the influence of vegetation data resolution on model error in a wetland with a flat bed and non-uniform vegetation distribution. In this configuration, the water depth is uniform, so variations in the nominal residence time are driven solely by the spatial heterogeneity of vegetation. We focus on a single vegetation scenario with an average density of $500\,\mathrm{stems\,m^{-2}}$, stem diameter $d = 3\,\mathrm{mm}$, standard deviation of stem density $\sigma_v = 300\,\mathrm{stems\,m^{-2}}$, and spatial correlation length $\lambda = 5\,\mathrm{m}$.

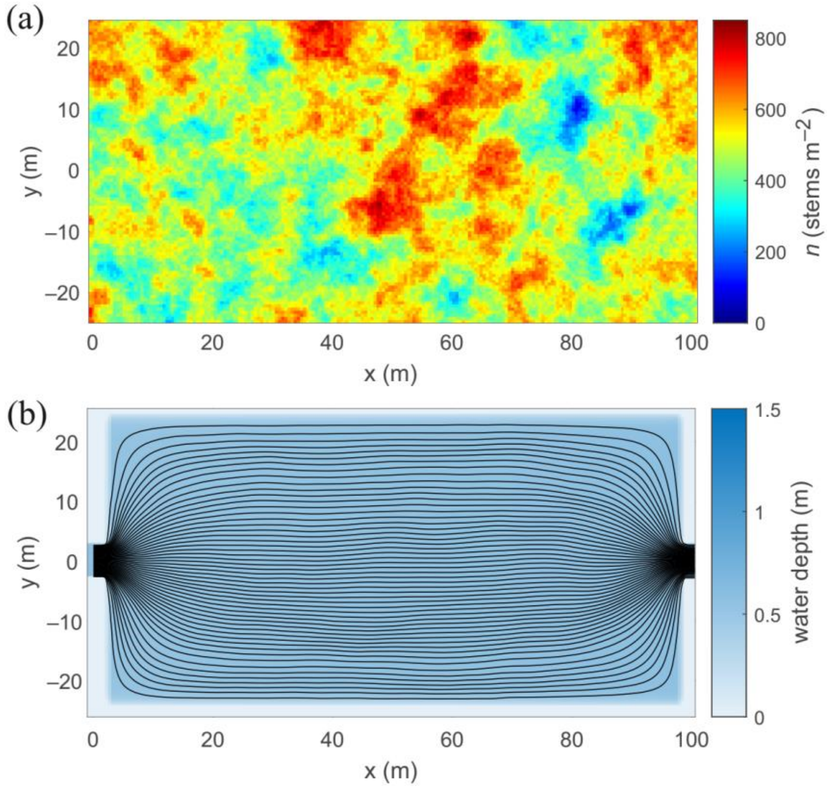

Figure 12. Example realization of a wetland with a flat bed, an average vegetation density of 500 stems $\mathrm{m^{-2}}$, a stem diameter of 3 mm, a standard deviation of 300 stems $\mathrm{m^{-2}}$, and a spatial correlation length of $\lambda = 5$ m: (a) vegetation density; (b) water depth and streamlines. The figure shows uniform water depth and streamlines, illustrating that flow patterns are largely unaffected by vegetation heterogeneity at this scale.

Figure 12 presents an example realization of such a wetland. The figure shows that water depth is essentially uniform, and streamlines are similar to those of a uniform wetland, indicating that the flow patterns are largely unaffected by vegetation heterogeneity at this scale. However, this outcome may not hold if vegetation distributions were to organize into larger-scale structures with reduced stem density along preferential pathways, in which case the flow would likely align with channels of minimum resistance while avoiding regions of higher resistance. This effect could be further amplified in the presence of correlations between bed topography and vegetation density, which, as discussed earlier, are not considered in this study.

Figure 13 quantifies the effect of vegetation data resolution on model error. In particular, Figure 13a shows the relative error in the variance of the residence time, $\Delta\hat{\sigma}_t^2$, as a function of the normalized grid size, $\Delta x/\lambda$. The median error is small for fine resolutions ($\Delta x/\lambda \lesssim 0.5$), but both the median and variability increase at coarser resolutions, reflecting greater uncertainty in predicting residence time variance when vegetation heterogeneity is coarsely represented.

Figure 13b reports the error in the outlet concentration, $\Delta\hat{C}_{out}$. In this case, errors remain relatively small across the range of resolutions, with median values close to zero. The variability increases modestly for coarser grids, but the overall magnitude of the error is limited.

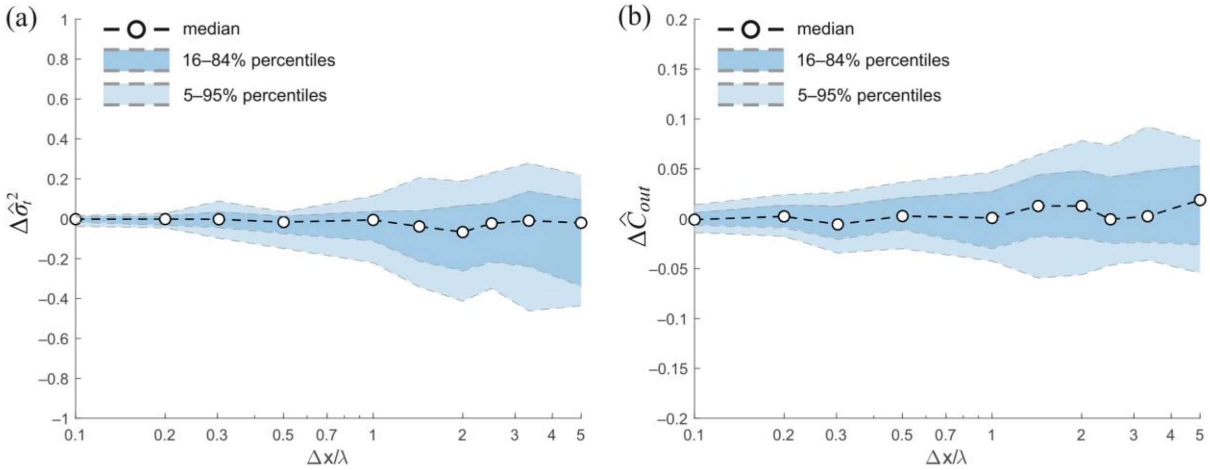

Figure 13. Model error as a function of the normalized grid size $\Delta x/\lambda$ for a wetland with a flat bed and heterogeneous vegetation (average density 500 stems m^{-2}, stem diameter 3 mm, standard deviation 300 stems m^{-2}, λ = 5 m). Panel (a) shows the error in the variance of the residence time, $\Delta\hat{\sigma}_t^2$, while panel (b) shows the error in the output concentration, $\Delta\hat{C}_{out}$. Coarse-graining the vegetation field slightly increases uncertainty in residence time and outlet concentration, but the relative error in solute removal remains mostly within 5%, indicating robustness of model predictions to vegetation resolution under the conditions considered.

In summary, while coarse-graining the vegetation field introduces some variability in the predicted residence time and a minor increase in uncertainty for outlet concentration, the effect on solute removal is limited, indicating that the model is relatively robust to the resolution of vegetation data for the conditions considered.

4.8.5 Discussion

4.8.5.1 Effect of bed topography

The results of this study highlight the significant role of bed topography in shaping wetland hydraulics and treatment performance. By demonstrating how the increased variance in water depth due to bed topography leads to greater variance in residence time and reduced hydraulic efficiency, the research aligns with previous findings on the crucial role of microtopography in influencing water flow and storage in wetlands (Diamond et al. 2020; Harvey et al. 2025). The observation that more heterogeneous bed topographies result in a wider range of hydraulic performances further supports the notion that microtopographic variability significantly impacts ecosystem functioning, as seen in studies by Smith et al. (2024) and Keiser et al. (2024).

For large variances of bed elevation, significant variations in performance were observed across realizations, which indicates that, for heterogeneous bed topographies with the same statistical parameters, the particular topography can make a significant difference on the hydraulic performance of a wetland. Considerable differences in hydraulic performance were also found by Savickis (2016) for a channelized wetland where the channelization is induced by differences in vegetation density. Although their study is limited to uniform bed topographies, their results show that the level of channelization – as produced by the difference in vegetation density in the channel and the surrounding, more highly vegetated zones – and the shape of the channel can significantly affect the hydraulic performance of a wetland. Similarly, for non-uniform bed topographies, we can expect that, for the same variance in bed elevation, the shape of the preferential flow pathways induced by bed forms are key to determining the performance of the wetland.

The interaction between bed topography and vegetation further shapes wetland performance, as previous works have emphasized (e.g., Sabokrouhiyeh et al. 2020; Zheng et al. 2021; Vulliet et al. 2024). Sabokrouhiyeh et al. (2020) investigated the effect of anisotropic vegetation patterns and found better concentration reduction efficiencies for wetlands with elongated patches of vegetation perpendicular to the flow direction compared to those obtained with patches parallel to the flow direction. This is likely due to the smaller fluxes of contaminant through the densely vegetated zones, where the removal rate is higher. Instead, the results presented in Figure 7 suggest better hydraulic efficiencies, i.e., a lower σ_t/t_n, for an elongated bed forms parallel to the flow direction. These findings are not in contradiction with each other, because contaminant removal ultimately depends on how the vegetation is distributed relative to the flow.

It must be stressed that the results presented in this work are based on the assumption of a uniform vegetation density all over the wetland. In actuality, there is often a correlation between bed elevation and vegetation density (Moser et al. 2007), with studies showing higher vegetation biomass in lower depth regions (Hudon 2004). Numerical simulations conducted by Sabokrouhiyeh et at. (2020) for rectangular wetlands with spatially random vegetation distributions have shown that the concentration reduction efficiency is primarily dependent on the average vegetation density, with relatively minor variations due to the spatial variability of vegetation density. In particular, Sabokrouhiyeh et at. (2020) found that the ensemble average of the total mass removal decreases for larger variances and correlation lengths of the vegetated field, which finds a physical explanation in the existence of preferential flow paths induced by variations in flow resistance as a result of the spatially varying vegetation density. It must be pointed out, however, that their study considered diversion wetlands in which the difference between the water surface elevation at the inlet and the outlet is imposed, or in other words, the average head gradient is imposed, while the flow rate through the wetland varies accordingly. Conversely, in the present study, we imposed the same flow rate in all simulations and let the water surface gradient vary accordingly. Under these conditions, the mass removal rate depends only on the concentration reduction efficiency, i.e., on the ratio of the outlet concentration to the inlet concentration, whereas in the work of Sabokrouhiyeh et at. (2020), the difference in the mass removal rate for wetlands with the same average vegetation density is due to differences in the flow rate through the wetland. Therefore, the presence of a variable vegetation density in a wetland with a non-uniform bed topography is unlikely to produce significant differences from the results found in this study for a uniform vegetation density.

The lack of correlation between bed topography and vegetation growth in our simulations stands in contrast to studies such as those by Sarkar et al. (2019) and Zhang et al. (2023), which showed that microtopographic variation strongly influenced vegetation composition and growth, either through altered flow regimes (Sarkar et al. 2019) or through changes in soil moisture and salinity (Zhang et al. 2023). In our analysis, we isolated the effect of bed topography by assuming a uniform vegetation distribution. This allowed us to focus specifically on the hydraulic implications of topographic heterogeneity, independently of the feedback from spatially variable vegetation. The differences in the treatment performance observed despite this simplification suggest that even in the absence of vegetation-topography correlations, the spatial arrangement of topographic features can significantly impact wetland function.

4.8.5.2 *Sensitivity of Wetland Model Outputs to Data Resolution*

The results show that the spatial resolution of topographic input data has a clear but selective influence on modeled wetland hydraulics. Coarse-graining the bathymetry primarily reduced small-scale variability in flow organization, reflected in a systematic underestimation of residence-time variance. This occurs because finer topographic details, such as small depressions and ridges, create localized storage zones and tortuous flow paths that enhance hydraulic dispersion. When these features are smoothed out, the model predicts more uniform velocities and narrower residence-time distributions. However, this simplification did not proportionally degrade treatment performance: the outlet concentration was relatively insensitive to the loss of topographic detail, remaining closely tied to the nominal residence time. This finding indicates that small-scale heterogeneity mainly affects intra-wetland transport dynamics rather than the overall treatment efficiency under the steady, idealized flow conditions examined here. Comparable sensitivity to bathymetric smoothing has been observed in ecological wetland models, where topographic roughness determines the persistence and extent of shallow-water habitats (Schaffer-Smith et al. 2018).

Vegetation heterogeneity played a comparatively minor role at small scales. Within the tested range of stem density variability, spatial patterns in vegetation resistance had limited impact on residence-time metrics or outlet concentrations. While local flow deviations occurred around patches of denser vegetation, these effects largely averaged out at the system scale. This suggests that, in shallow wetlands with moderate vegetation variability, the hydraulic influence of vegetation structure may be subordinate to that of bed topography. Nevertheless, in natural wetlands where vegetation forms large-scale patches, corridors, or main flow channels, its role in shaping preferential flow paths can be far more significant. For example, Savickis et al. (2016) showed that a main flow channel with lower vegetation density induces short-circuiting and reduces hydraulic efficiency, while channel sinuosity and the arrangement of lateral vegetated zones can mitigate these effects. Similarly, Sabokrouhiyeh et al. (2020) demonstrated that large, aligned vegetation patches promote preferential flow paths and affect contaminant removal, whereas alternating stem density perpendicular to the flow enhances mixing. These findings highlight that the hydraulic impact of vegetation is scale-dependent, and large-scale spatial organization can substantially influence intra-wetland transport dynamics, warranting targeted investigation.

The interpretation that treatment efficiency is less sensitive to small-scale spatial detail aligns with findings from field and modeling studies emphasizing the dominant role of bulk hydraulic behavior (Wörman and Kronnäs 2005; Sabokrouhiyeh et al. 2017; Dykes et al. 2025). For example, in full-scale vegetated cells of surface-flow constructed wetlands, Dykes et al. (2025) found that hydraulic inefficiencies were primarily driven by large-scale design factors, such as cell geometry, inlet–outlet configuration, and hydraulic loading, while sub-meter vegetation heterogeneity had comparatively little impact on treatment performance. Instead, vegetation influenced removal primarily through seasonal growth and climatic variability rather than fine-scale spatial variability. Sabokrouhiyeh et al. (2017) further demonstrated that, above a threshold stem density typical of treatment wetlands (≈ 300 stems m^{-2}), hydraulic performance metrics were largely insensitive to the exact value of vegetation density, supporting the notion that fine-scale vegetation details are secondary for overall hydraulic efficiency. Similarly, Guzman et al. (2018) and Persson (2005) observed that wetland topographies with islands or deep zones modify circulation, primarily by altering major flow paths rather than by small-scale surface roughness. Brovelli et al. (2011) further demonstrated that hydraulic conductivity heterogeneity at scales comparable to the system geometry strongly affects residence-time distributions, reinforcing that model sensitivity depends on the relative scale of spatial variability to overall system size.

From a modeling perspective, these results imply that moderate coarsening of topographic or vegetation data can be acceptable when predicting bulk hydraulic or treatment metrics, provided the grid spacing remains smaller than the dominant correlation length of the bed features. In contrast, metrics that depend on detailed mixing behavior, such as residence time variance or short-circuiting indices, require finer spatial resolution. This scale dependence mirrors similar findings in hydraulic modeling of wetlands and river systems (e.g., O'Sullivan et al. 2020; Hou et al. 2021; Zhang et al. 2022), where predictive accuracy deteriorates once the grid size exceeds key spatial correlation scales.

Future research should extend these analyses to explore how resolution effects interact with additional physical processes. Varying discharge conditions, submerged vegetation, or seasonally variable canopy structures could reveal nonlinear sensitivities absent under steady, uniform forcing. Coupling between topography and vegetation distribution (common in real wetlands) may also alter flow organization in ways not captured by the present approach. Incorporating such feedback in three-dimensional frameworks or field-validated models would help generalize the conclusions to more complex, natural systems.

4.8.6 Conclusions

This study highlighted the crucial role of bed topography in influencing the hydraulic performance of free water surface wetlands. Through Monte Carlo simulations, we demonstrated that greater topographic heterogeneity affects flow patterns and contaminant transport, increasing residence time variability and thereby reducing hydraulic performance. The reduction in performance was more pronounced in wetlands with smaller spatial correlation lengths, as they exhibited more complex flow patterns.

Contaminant transport analysis revealed that, while the average removal efficiency across wetlands with the same mean residence time does not vary significantly, greater topographic variability results in a higher variability of the removal efficiency, which is more pronounced under the conditions of lower vegetation density. This suggests that while bulk performance may be predictable based on the mean residence time and the average areal removal rate, the particular spatial configuration of bed features can significantly impact treatment reliability.

We also examined the effect of the spatial resolution of bathymetric and vegetation data on the prediction of residence time and solute treatment in shallow-water wetlands. Using synthetic wetlands with spatially correlated random fields for bed elevation and vegetation density, we quantified how coarse-graining the input data impacts model outputs. The median error in nominal residence time was generally small, although its variability across realizations increased with larger topographic heterogeneity. The variance of residence time was the most sensitive metric, exhibiting a tendency to be underestimated as the grid size increased. In contrast, errors in outlet concentration remained relatively small (<5\%) even for grid sizes up to 1–5 times the correlation length of the bed features, suggesting that outlet concentration is more strongly correlated with nominal residence time than with its variance.

For the range of vegetation stem density variability considered here, coarse-graining vegetation patterns had a less significant impact on both residence time metrics and outlet concentration compared to bathymetry. This result, however, may not hold if vegetation were organized into larger-scale structures with preferential low-density pathways, which would likely channel flow along paths of minimum resistance. Such configurations were not considered in this study.

A few important limitations should be noted. The results presented in this study were obtained under the assumption of uniform vegetation stem density and diameter across the wetland. The potential interaction between vegetation density and water depth, which was not explored here, represents an important direction for future research. In natural systems, vegetation structure and bed topography often covary, as vegetation tends to establish preferentially in zones of specific depth or flow conditions. Such spatial coupling can modify the local hydraulic resistance and feedback on flow organization, potentially amplifying or dampening the resolution effects observed in this study. For instance, correlations between elevated areas and sparse vegetation might enhance short-circuiting at coarse resolution, whereas vegetation concentrated in depressions could counteract flow acceleration by increasing resistance. Exploring these coupled effects would provide a more realistic understanding of how spatial heterogeneity influences model sensitivity to input resolution.

Moreover, the use of shallow-water and depth-averaged solute transport models, while computationally efficient, relies on a few simplifying assumptions. Vertical variations in flow and solute concentration are neglected, which may reduce accuracy in systems with strong stratification, highly heterogeneous vegetation, or vertical gradients at the inlet. As a result, the findings presented here should be interpreted within the limits of two-dimensional, depth-averaged dynamics, and caution should be exercised when extrapolating to wetlands where three-dimensional circulation or vertical mixing processes play a dominant role. These limitations should be considered when interpreting the results, especially for more complex or heterogeneous wetland systems.

Despite these limitations, the findings underscore the importance of accounting for bathymetric variability in wetland design, as strategically incorporating topographic diversity can enhance residence time distributions and improve contaminant removal. The work also provides a quantitative framework for evaluating how input data resolution influences the reliability of shallow-water wetland models, identifying conditions under which coarse-graining remains acceptable. In practical terms, the results indicate that when grid spacing or survey resolution is smaller than roughly half the dominant correlation length of bed topography, errors in hydraulic and treatment metrics remain within a few percent. Beyond this threshold, uncertainty increases rapidly, particularly in wetlands with highly variable microtopography. These insights provide a basis for selecting appropriate grid resolutions or survey intervals that reflect the spatial heterogeneity of the site.

4.8.7 References

Arheimer, Berit, and Hans B Wittgren. 2002. 'Modelling Nitrogen Removal in Potential Wetlands at the Catchment Scale'. Ecological Engineering 19 (1): 63–80. https://doi.org/10.1016/S0925-8574(02)00034-4.

Brovelli, A., O. Carranza-Diaz, L. Rossi, and D.A. Barry. 2011. 'Design Methodology Accounting for the Effects of Porous Medium Heterogeneity on Hydraulic Residence Time and Biodegradation in Horizontal Subsurface Flow Constructed Wetlands'. Ecological Engineering 37 (5): 758–70. https://doi.org/10.1016/j.ecoleng.2010.04.031.

Calhoun, Donna, and Randall J. LeVeque. 2000. 'A Cartesian Grid Finite-Volume Method for the Advection-Diffusion Equation in Irregular Geometries'. Journal of Computational Physics 157 (1): 143–80. https://doi.org/10.1006/jcph.1999.6369.

Cameron, Kimberley, Chandra Madramootoo, Anna Crolla, and Christopher Kinsley. 2003. 'Pollutant Removal from Municipal Sewage Lagoon Effluents with a Free-Surface Wetland'. Water Research 37 (12): 2803–12. https://doi.org/10.1016/S0043-1354(03)00135-0.

Carleton, J. N, T. J Grizzard, A. N Godrej, and H. E Post. 2001. 'Factors Affecting the Performance of Stormwater Treatment Wetlands'. Water Research 35 (6): 1552–62. https://doi.org/10.1016/S0043-1354(00)00416-4.

Chow, Ven Te. 1959. Open-Channel Hydraulics. McGraw-Hill Book Co.

Diamond, Jacob S., Daniel L. McLaughlin, Robert A. Slesak, and Atticus Stovall. 2020. 'Microtopography Is a Fundamental Organizing Structure of Vegetation and Soil Chemistry in Black Ash Wetlands'. Biogeosciences 17 (4): 901–15. https://doi.org/10.5194/bg-17-901-2020.

Dykes, Charlotte, Jonathan Pearson, Gary D. Bending, and Soroush Abolfathi. 2025. 'Hydraulic Efficiency and Mixing Dynamics in Surface Flow Constructed Wetlands: Influence of Design, Vegetation Phenology, and Climate Variability'. Water Research 285. https://doi.org/10.1016/j.watres.2025.124110.

Guzman, Celina Balderas, Samantha Cohen, Manoel Xavier, Tyler Swingle, Waishan Qiu, and Heidi Nepf. 2018. 'Island Topographies to Reduce Short-Circuiting in Stormwater Detention Ponds and Treatment Wetlands'. Ecological Engineering 117: 182–93. https://doi.org/10.1016/j.ecoleng.2018.02.020.

Harvey, J.W., J. Choi, W.W. Wilcox, M.C. Brown, and W. Lal. 2025. 'Biophysical Simulation of Wetland Surface Water Flow to Predict Changing Water Availability in the Everglades'. Ecological Engineering 212. Scopus. https://doi.org/10.1016/j.ecoleng.2024.107491.

Holland, Jeff F., Jay F. Martin, Timothy Granata, Virginie Bouchard, Martin Quigley, and Larry Brown. 2004. 'Effects of Wetland Depth and Flow Rate on Residence Time Distribution Characteristics'. Ecological Engineering 23 (3): 189–203. https://doi.org/10.1016/j.ecoleng.2004.09.003.

Hou, Jingming, Xinyi Li, Zhanpeng Pan, Junhui Wang, and Ruike Wang. 2021. 'Effect of Digital Elevation Model Spatial Resolution on Depression Storage'. Hydrological Processes 35 (10). https://doi.org/10.1002/hyp.14381.

Hudon, Christiane. 2004. 'Shift in Wetland Plant Composition and Biomass Following Low-Level Episodes in the St. Lawrence River: Looking into the Future'. Canadian Journal of Fisheries and Aquatic Sciences - CAN J FISHERIES AQUAT SCI 61 (April): 603–17. https://doi.org/10.1139/f04-031.

Jarihani, Abdollah A., John N. Callow, Tim R. McVicar, Thomas G. Van Niel, and Joshua R. Larsen. 2015. 'Satellite-Derived Digital Elevation Model (DEM) Selection, Preparation and Correction for Hydrodynamic Modelling in Large, Low-Gradient and Data-Sparse Catchments'. Journal of Hydrology 524: 489–506. https://doi.org/10.1016/j.jhydrol.2015.02.049.

Jiang, Long, and Ting Fong May Chui. 2022. 'A Review of the Application of Constructed Wetlands (CWs) and Their Hydraulic, Water Quality and Biological Responses to Changing Hydrological Conditions'. Ecological Engineering 174 (January): 106459. https://doi.org/10.1016/j.ecoleng.2021.106459.

Kadlec, Robert H., and Scott Wallace. 2008. Treatment Wetlands. 2nd ed. CRC Press. https://doi.org/10.1201/9781420012514.

Katsenovich, Yelena P., Adelaide Hummel-Batista, Alfredo J. Ravinet, and Jerry F. Miller. 2009. 'Performance Evaluation of Constructed Wetlands in a Tropical Region'. Ecological Engineering 35 (10): 1529–37. https://doi.org/10.1016/j.ecoleng.2009.07.003.

Keiser, Ashley D., Christina L. Davis, Montana Smith, Sheryl L. Bell, Erik A. Hobbie, and Kirsten S. Hofmockel. 2024. 'Depth and Microtopography Influence Microbial Biogeochemical Processes in a Forested Peatland'. Plant and Soil, ahead of print, August 12. https://doi.org/10.1007/s11104-024-06895-1.

Kotti, Irini P., Georgios D. Gikas, and Vassilios A. Tsihrintzis. 2010. ‘Effect of Operational and Design Parameters on Removal Efficiency of Pilot-Scale FWS Constructed Wetlands and Comparison with HSF Systems’. Ecological Engineering 36 (7): 862–75. https://doi.org/10.1016/j.ecoleng.2010.03.002.

Leer, Bram van. 1974. ‘Towards the Ultimate Conservative Difference Scheme. II. Monotonicity and Conservation Combined in a Second-Order Scheme’. Journal of Computational Physics 14 (4): 361–70. https://doi.org/10.1016/0021-9991(74)90019-9.

LeVeque, Randall J. 1997. ‘Wave Propagation Algorithms for Multidimensional Hyperbolic Systems’. Journal of Computational Physics 131 (2): 327–53. https://doi.org/10.1006/jcph.1996.5603.

Marion, Andrea, Vladimir Nikora, Sara Puijalon, et al. 2014. ‘Aquatic Interfaces: A Hydrodynamic and Ecological Perspective’. Journal of Hydraulic Research 52 (6): 744–58. https://doi.org/10.1080/00221686.2014.968887.

Meng, Panpan, Haiyan Pei, Wenrong Hu, Yuanyuan Shao, and Zheng Li. 2014. ‘How to Increase Microbial Degradation in Constructed Wetlands: Influencing Factors and Improvement Measures’. Bioresource Technology 157 (April): 316–26. https://doi.org/10.1016/j.biortech.2014.01.095.

Moser, Kurt, Changwoo Ahn, and Gregory Noe. 2007. ‘Characterization of Microtopography and Its Influence on Vegetation Patterns in Created Wetlands’. Wetlands 27 (4): 1081–97. https://doi.org/10.1672/0277-5212(2007)27[1081:COMAII]2.0.CO;2.

O’Sullivan, Antóin M., Kevin J. Devito, Jae Ogilvie, et al. 2020. ‘Effects of Topographic Resolution and Geologic Setting on Spatial Statistical River Temperature Models’. Water Resources Research 56 (12). https://doi.org/10.1029/2020WR028122.

Persson, J. 2005. ‘Improving Wetland Design’. Water 21, no. AUG.: 52.

Persson, J., N. L. G. Somes, and T. H. F. Wong. 1999. ‘Hydraulics Efficiency of Constructed Wetlands and Ponds’. Water Science and Technology 40 (3): 291–300. https://doi.org/10.1016/S0273-1223(99)00448-5.

Price, Jonathan S. 1993. ‘Water Level Regimes in Prairie Sloughs’. Canadian Water Resources Journal / Revue Canadienne Des Ressources Hydriques 18 (2): 95–106. https://doi.org/10.4296/cwrj1802095.

Sabokrouhiyeh, Nima, Andrea Bottacin-Busolin, Jevgenijs Savickis, Heidi Nepf, and Andrea Marion. 2017. ‘A Numerical Study of the Effect of Wetland Shape and Inlet-Outlet Configuration on Wetland Performance’. Ecological Engineering 105 (August): 170–79. https://doi.org/10.1016/j.ecoleng.2017.04.062.

Sabokrouhiyeh, Nima, Andrea Bottacin-Busolin, Matteo Tregnaghi, Heidi Nepf, and Andrea Marion. 2020. ‘Variation in Contaminant Removal Efficiency in Free-Water Surface Wetlands with Heterogeneous Vegetation Density’. Ecological Engineering 143 (January): 105662. https://doi.org/10.1016/j.ecoleng.2019.105662.

Sarkar, Priyanka, Tapati Das, and Dibyendu Adhikari. 2019. ‘Variation in Species Assemblages Due to Micro-Topography and Flow Regime Govern Vegetation Carbon Stock in Seasonal Floodplain Wetlands’. Ecological Processes 8 (1): 49. https://doi.org/10.1186/s13717-019-0201-9.

Savickis, J., A. Bottacin-Busolin, M. Zaramella, N. Sabokrouhiyeh, and A. Marion. 2016. ‘Effect of a Meandering Channel on Wetland Performance’. Journal of Hydrology 535 (April): 204–10. https://doi.org/10.1016/j.jhydrol.2016.01.082.

Schaffer-Smith, Danica, Jennifer J. Swenson, Matthew E. Reiter, and Jennifer E. Isola. 2018. ‘Quantifying Shorebird Habitat in Managed Wetlands by Modeling Shallow Water Depth Dynamics’. Ecological Applications 28 (6): 1534–45. https://doi.org/10.1002/eap.1732.

Seenath, Avidesh. 2018. ‘Effects of DEM Resolution on Modeling Coastal Flood Vulnerability’. Marine Geodesy 41 (6): 581–604. https://doi.org/10.1080/01490419.2018.1504838.

Serra, Teresa, Harindra J. S. Fernando, and Rodolfo V. Rodríguez. 2004. ‘Effects of Emergent Vegetation on Lateral Diffusion in Wetlands’. Water Research 38 (1): 139–47. https://doi.org/10.1016/j.watres.2003.09.009.

Smith, A.J., G.R. Guntenspergen, J.A. Carr, D.C. Walters, and M.L. Kirwan. 2024. 'Microtopographic Variation as a Potential Early Indicator of Ecosystem State Change and Vulnerability in Salt Marshes'. Estuaries and Coasts 47 (7): 2120–34. Scopus. https://doi.org/10.1007/s12237-024-01368-1.

Thackston, Edward L., F. Douglas Shields, and Paul R. Schroeder. 1987. 'Residence Time Distributions of Shallow Basins'. Journal of Environmental Engineering 113 (6): 1319–32. https://doi.org/10.1061/(ASCE)0733-9372(1987)113:6(1319).

Valiela, Ivan, John M. Teal, and Werner G. Deuser. 1978. 'The Nature of Growth Forms in the Salt Marsh Grass Spartina Alterniflora'. The American Naturalist 112 (985): 461–70.

Vulliet, Cécile, Jack Koci, Marcus Sheaves, and Nathan Waltham. 2024. 'Linking Tidal Wetland Vegetation Mosaics to Micro-Topography and Hydroperiod in a Tropical Estuary'. Marine Environmental Research 197 (May): 106485. https://doi.org/10.1016/j.marenvres.2024.106485.

Vymazal, Jan. 2013. 'Emergent Plants Used in Free Water Surface Constructed Wetlands: A Review'. Ecological Engineering, Plants in constructed, restored and created wetlands, vol. 61 (December): 582–92. https://doi.org/10.1016/j.ecoleng.2013.06.023.

Vymazal, Jan. 2014. 'Constructed Wetlands for Treatment of Industrial Wastewaters: A Review'. Ecological Engineering 73 (December): 724–51. https://doi.org/10.1016/j.ecoleng.2014.09.034.

Wang, Miaorun, Haojie Liu, Fereidoun Rezanezhad, Dominik Zak, and Bernd Lennartz. 2023. 'The Influence of Microtopography on Soil Carbon Accumulation and Nutrient Release from a Rewetted Coastal Peatland'. Geoderma 438 (October): 116637. https://doi.org/10.1016/j.geoderma.2023.116637.

Wörman, Anders, and Veronika Kronnäs. 2005. 'Effect of Pond Shape and Vegetation Heterogeneity on Flow and Treatment Performance of Constructed Wetlands'. Journal of Hydrology 301 (1–4): 123–38. https://doi.org/10.1016/j.jhydrol.2004.06.038.

Wu, Weiming. 2007. Computational River Dynamics. CRC Press. https://doi.org/10.4324/9780203938485.

Zhang, Dong-Qing, K. B. S. N. Jinadasa, Richard M. Gersberg, Yu Liu, Soon Keat Tan, and Wun Jern Ng. 2015. 'Application of Constructed Wetlands for Wastewater Treatment in Tropical and Subtropical Regions (2000-2013)'. Journal of Environmental Sciences (China) 30 (April): 30–46. https://doi.org/10.1016/j.jes.2014.10.013.

Zhang, Ke, Jiangbao Xia, Li Su, et al. 2023. 'Effects of Microtopographic Patterns on Plant Growth and Soil Improvement in Coastal Wetlands of the Yellow River Delta'. Frontiers in Plant Science 14 (March). https://doi.org/10.3389/fpls.2023.1162013.

Zhang, Xiaohe, Kyle Wright, Paola Passalacqua, Marc Simard, and Sergio Fagherazzi. 2022. 'Improving Channel Hydrological Connectivity in Coastal Hydrodynamic Models With Remotely Sensed Channel Networks'. Journal of Geophysical Research: Earth Surface 127 (3). https://doi.org/10.1029/2021JF006294.

Zhao, Fangxing, Xinwen Zhang, Zhenghe Xu, et al. 2024. 'Review of Hydraulic Conditions Optimization for Constructed Wetlands'. Journal of Environmental Management 370 (November): 122377. https://doi.org/10.1016/j.jenvman.2024.122377.

Zheng, Lilin, Xiaolong Wang, Dahui Li, Guoyu Xu, and Yufei Guo. 2021. 'Spatial Heterogeneity of Vegetation Extent and the Response to Water Level Fluctuations and Micro-Topography in Poyang Lake, China'. Ecological Indicators 124 (May): 107420. https://doi.org/10.1016/j.ecolind.2021.107420.

4.9 Hydrodynamic modelling of microplastic transport in river systems: Insights from a case study (UNIPD)

Contributors: Andrea Bottacin-Busolin, Nirman Bhagat, Andrea Marion - Department of Industrial Engineering, University of Padova

4.9.1 Abstract

Microplastics are persistent contaminants in fluvial sediments, yet the processes controlling their redistribution remain poorly understood. We use a numerical model, based on sediment-transport relationships, to simulate the settling, resuspension, and downstream transport of microplastic particles in two contrasting river systems over a one-year period. Simulations start from an initially uniform sediment concentration and assume no additional inputs, so that final distributions reflect only hydrodynamic transport and particle retention governed by river morphology and particle density. The model reproduces key patterns observed in previous empirical studies, including strong spatial heterogeneity in bed-sediment microplastic concentrations and pronounced redistribution during high-flow events. Low-density particles are widely mobilised even under moderate flows, whereas high-density particles accumulate preferentially in zones downstream of abrupt increases in shear stress. Channels with more spatially abrupt variations in shear stress, such as the Irwell, exhibit highly heterogeneous microplastic redistribution, whereas systems with more gradual hydraulic patterns, like the Mersey, show stronger downstream retention within depositional reaches. These results demonstrate that sediment microplastic concentrations are highly dynamic and event-driven, and that apparent changes at monitoring sites may reflect internal redistribution rather than changes in catchment inputs. The study highlights the value of physically based sediment-transport models for interpreting microplastic distributions in rivers and for identifying persistent retention zones.

4.9.2 Introduction

The pervasive presence of microplastics in aquatic environments has emerged as a significant environmental concern in recent decades (Thompson et al. 2004; Eerkes-Medrano et al. 2015). Microplastics, defined as plastic particles smaller than 5 mm in size, have been detected in various freshwater ecosystems worldwide, from urban rivers to remote streams (Wagner et al. 2014; Mani et al. 2015). The ubiquity of these particles in riverine systems is particularly alarming, as rivers serve as critical pathways for the transport of plastic debris from terrestrial sources to marine environments (Lebreton et al. 2017; Schmidt et al. 2017).

The global production of plastics has increased exponentially since the 1950s, reaching 359 million tonnes in 2018 (PlasticsEurope 2023). This surge in production, coupled with inadequate waste management practices, has led to a substantial influx of plastic waste into the environment (Jambeck et al. 2015). Recent estimates suggest that between 1.15 and 2.41 million tonnes of plastic waste enter the oceans via rivers annually (Lebreton et al. 2017). However, rivers are not merely conduits for plastic transport; they also act as temporary sinks and sources of microplastics, influencing their distribution and fate within catchments (Hurley et al. 2018; Windsor et al. 2019).

The presence of microplastics in riverine ecosystems poses potential risks to freshwater organisms through various mechanisms. Direct ingestion of microplastics has been observed in numerous aquatic species, potentially leading to physical harm and reduced feeding efficiency (Scherer et al. 2017; Triebskorn et al. 2019). Moreover, microplastics can act as vectors for the transport of persistent organic pollutants and other contaminants, potentially exacerbating their toxicological effects on biota (Rochman et al. 2013; Koelmans et al. 2016).

Despite the growing recognition of microplastic pollution in rivers, the physical processes governing their transport, deposition, and resuspension remain poorly understood (Kooi et al. 2018). Traditional sediment transport models have been widely used to describe the movement of natural particles in fluvial systems (Rijn 1984; García 2013). However, the applicability of these formulations to microplastics, which exhibit diverse shapes, sizes, and densities, is not well established (Hoellein et al. 2019; Waldschläger and Schüttrumpf 2019).

Recent field studies have provided valuable insights into the distribution and behavior of microplastics in rivers. Hurley et al. (2018) demonstrated that high-flow events can remobilize substantial quantities of microplastics stored in riverbed sediments, highlighting the dynamic nature of microplastic transport in fluvial systems. Similarly, Mani et al. (2015) observed variations in microplastic concentrations along the Rhine River, suggesting the influence of local sources and hydrodynamic conditions on their spatial distribution.

The complex interplay between hydrodynamic processes and microplastic transport necessitates the development of robust modeling approaches to predict their fate and behavior in rivers (Kooi et al. 2018). Such models can provide valuable tools for assessing microplastic accumulation patterns, identifying potential hotspots, and evaluating the effectiveness of mitigation strategies (Tibbetts et al. 2018). However, the development of accurate microplastic transport models faces several challenges, including the heterogeneity of particle properties, the influence of biofouling on particle behavior, and the limited availability of field data for model validation (Koelmans et al. 2016; Waldschläger and Schüttrumpf 2019).

Recent modeling efforts have attempted to address these challenges by incorporating microplastic-specific parameters into existing hydrodynamic and sediment transport frameworks. Nizzetto et al. (2016) developed a probabilistic model to simulate microplastic transport in the Danube River, considering various particle properties and environmental factors. Similarly, Besseling et al. (2017) proposed a spatially explicit model for nanoplastic transport in rivers, accounting for hetero-aggregation and sedimentation processes. These studies have provided valuable insights into the potential fate of microplastics in riverine systems, but further research is needed to validate and refine these modeling approaches across diverse environmental conditions.

The role of extreme weather events, such as floods, in the redistribution of microplastics within river networks is of particular interest (Hurley et al. 2018). Climate change projections suggest an increase in the frequency and intensity of extreme precipitation events in many regions (IPCC 2021), potentially altering the dynamics of microplastic transport and accumulation in rivers. Understanding the impact of these high-flow events on microplastic mobilization and downstream export is crucial for assessing long-term trends in microplastic pollution and developing effective management strategies (Windsor et al. 2019).

In light of these knowledge gaps, this study aims to evaluate the applicability of existing sediment transport formulations for representing microplastic transport, deposition, and resuspension in fluvial systems across contrasting flow regimes. By developing a coupled modeling framework that combines hydrodynamic simulations with a custom particle transport module, we seek to improve our understanding of microplastic dynamics in rivers and provide a foundation for predicting their long-term retention and mobility within catchments.

The Irwell–Mersey river network in Greater Manchester, UK, serves as a case study for this modeling approach. This urban river system has been the subject of previous microplastic investigations (Hurley et al. 2018), providing valuable field data for model comparison. By simulating both pre-flood and flood conditions during the winter of 2015, including December 2015 Boxing Day event, we aim to elucidate the impact of high-flow events on microplastic redistribution and downstream export.

4.9.3 Case study

Greater Manchester comprises four main river catchments: the Irwell, Upper Mersey, Lower Mersey, and Douglas. This study focuses on the Irwell (793 km²) and Upper Mersey (734 km²) catchments, which together include nearly 50 water bodies. The principal tributaries of the River Mersey are the Irwell, Tame, and Bollin. The River Irwell originates in the western Pennine uplands, where deeply incised valleys drain moorland peat soils. From its headwaters, the Irwell flows southward to its confluence with the River Roch at Radcliffe Ees, south of Bury. The Roch itself rises on Chelburn Moor in the Pennines and flows southwest before joining the Irwell. Downstream, the Irwell continues southeast through the urban core of Manchester, where it meets the Rivers Irk and Medlock.

The River Mersey is formed at the confluence of the Rivers Tame and Goyt in Stockport and is fed by three main tributaries: the Tame, Etherow, and Goyt (Figure 14). Each of these sub-catchments rises on the western slopes of the South Pennines and is characterised by steep, narrow headwater channels that transition into broader, low-gradient alluvial plains downstream. Both the Irwell and Upper Mersey ultimately discharge into the Manchester Ship Canal.

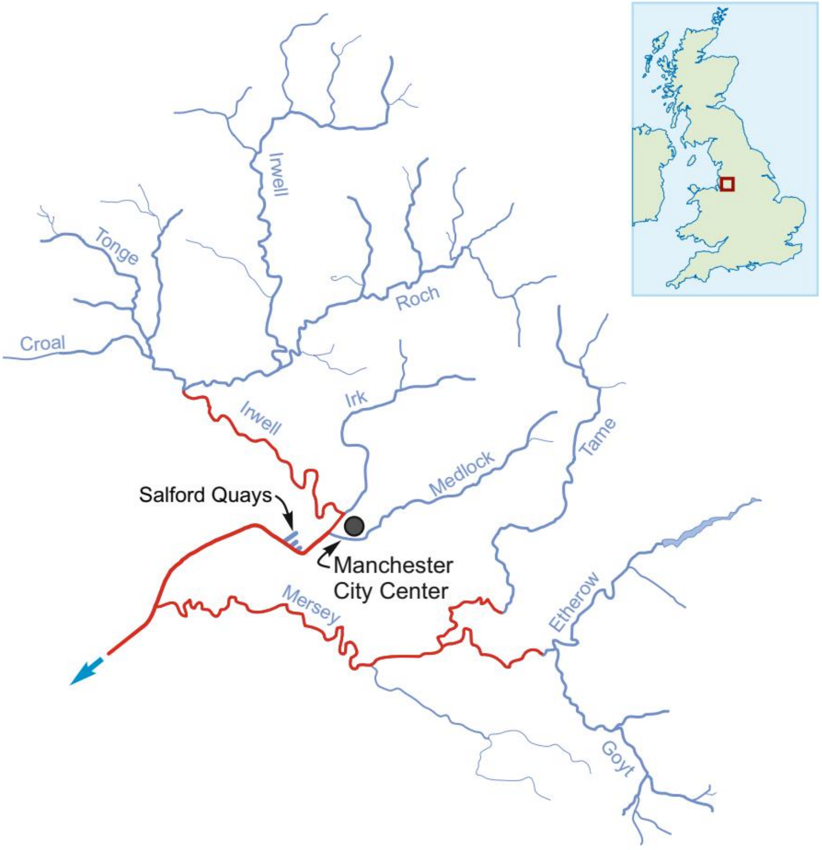

Figure 14. Case study river network. The channels selected for hydrodynamic and microplastic-transport simulations are shown in red.

Mean annual precipitation is 1,257 mm in the Irwell catchment and 1,150 mm in the Mersey catchment. Corresponding mean river discharges are 17.6 m^3s^{-1} at Adelphi Weir (Irwell) and 14.0 m^3s^{-1} at Ashton Weir (Mersey). The two catchments are among the most urbanised in the United Kingdom. Industrialisation along the main tributaries dates back to the 18th century, and its legacy remains evident in both hydromorphological alterations and pollutant accumulation. Regular deposition of physical waste and elevated microplastic concentrations have been documented along multiple reaches. Major population centres within the catchments include Manchester (530,300 inhabitants), Stockport (284,500), Salford (233,933), Rochdale (211,699), Bolton (139,403), Oldham (103,544), and Bury (60,718).

Topographically, the catchment area ranges from approximately 700 m a.s.l. in the uplands to 10 m a.s.l. near the outlet, while the main river reaches considered in this study lie between 300 m and 50 m a.s.l. Extensive suburban expansion over recent decades, together with numerous small industrial zones, has contributed to substantial non-point and point-source pollution. Industrial effluents, textile and plastic manufacturing waste, and urban runoff are major contributors to microplastic contamination within the Irwell and Upper Mersey systems.

4.9.4 Methods

4.9.4.1 Hydrodynamic model

Flow hydrodynamics in the river network was modelled using the software HEC-RAS (Hydrological Engineering Centre – River Analysis System), developed by the US Army Corps of Engineers. The simulations are based on the 1-D Saint Venant equations, including the continuity equation,

$$\frac{\partial A}{\partial t} + \frac{\partial Q}{\partial x} = 0 \tag{1}$$

and the momentum equation,

$$\frac{\partial Q}{\partial t} + \frac{\partial (Q^2/A)}{\partial x} + gA\frac{\partial h}{\partial x} = gA\big(S_b - S_f\big) \qquad (2)$$

where $\tau_b = \rho_w f u^2/8$ is the bed shear stress, $\tau_{c,e} = \gamma_{c,e}(\rho_s - \rho_w) g D \theta_{c,e}$ is the critical shear stress for erosion, $\gamma_e = 1$ is a user specified multiplier for erosion, $\gamma_{c,e} = 1$ is a user specified multiplier for critical erosion stress, and $\eta = 1.5$ is a user specified exponent for non-cohesive erosion stress.

$$S_f = \frac{Q|Q|n^2 P^{4/3}}{A^{10/3}} \qquad (3)$$

The river geometry used in the hydrodynamic model was derived from 1 m-resolution Digital Terrain Models (DTMs) made available by the UK Environment Agency. From the DTM, a few hundred cross-sections were extracted along each river reach, allowing for a detailed representation of channel geometry and topography. The roughness parameterisation was calibrated using stage observations from the River Flow Archive at selected control stations. This calibration resulted in Manning coefficients ranging from 0.025 to 0.045 s $\mathrm{m}^{-1/3}$, consistent with values typically associated with relatively smooth gravel-bed and alluvial channels.

Transient hydrodynamic simulations were driven by daily discharge hydrographs applied at the upstream boundaries and at lateral inflow locations. Because only daily data were available, the flood peaks used in the model are likely lower than the true instantaneous peaks that would appear in higher-resolution (e.g., hourly) records. This limitation should be kept in mind when interpreting the transport dynamics during high-flow periods. The simulations were carried out with a fixed time step of 1 s, ensuring numerical stability and time step independence. The full simulation period spans one year, from 15 June 2015 to 14 June 2016, matching the time window used for the microplastic transport analysis.

4.9.4.2 Estimation of upstream boundary flows and lateral inflows

In the hydraulic simulations, upstream boundary conditions for the Irwell, Tame and Goyt rivers were prescribed using observed discharge data obtained from the UK National River Flow Archive. These measured hydrographs were applied directly at the upstream nodes of the 1-D Saint Venant model, ensuring that the inflow signals entering the main river branches reflected authentic hydrological variability rather than modelled runoff.

To represent the additional runoff contributions generated within the model domain, distributed lateral inflows were estimated using a rainfall–runoff approach based on the SCS Curve Number method. The catchment was subdivided into a series of lateral subcatchments associated with individual reaches of the Irwell system. For each subcatchment, daily precipitation was transformed into surface runoff using the Curve Number method, which relates rainfall depth to runoff production according to land cover, soil type and antecedent moisture. These runoff depths were then converted into daily mean discharges according to the contributing area.

Because runoff generated in this way responds immediately to rainfall, a simple hydrologic routing procedure was applied to give the resulting hydrographs realistic timing and attenuation characteristics before they were introduced into the river model. This routing was implemented using a single linear reservoir for each subcatchment, which acts as a basic storage–release model. In practice, the linear reservoir smooths sharp variations in the raw runoff series and introduces a delay that reflects travel times through hillslope pathways, small drainage channels and the minor tributary network not explicitly represented in the hydraulic model. Each subcatchment was assigned a storage time constant consistent with its size, meaning that smaller areas produced more responsive routed inflows while larger areas exhibited slower, more attenuated hydrographs. The routed series were then used as lateral inflows along the corresponding river reaches.

A formal calibration of the linear reservoir routing was not undertaken, because the purpose of the routing step was not to reproduce detailed tributary hydrographs but to provide a physically plausible translation and attenuation of rainfall-derived runoff before it entered the river network. The storage constants assigned to each subcatchment were based on indicative values reported in the hydrological literature for catchments of similar size and physiographic characteristics, and were scaled according to subcatchment area so that smaller catchments responded more rapidly than larger ones. Sensitivity tests showed that the hydraulic model results were not strongly dependent on modest variations in these routing parameters, confirming that the chosen values were sufficiently robust for the intended use within the Saint Venant framework.

The same rainfall-runoff and routing procedure was used to estimate inflows from the River Medlock, which enters the Irwell system within the modelled domain. A dedicated Medlock subcatchment was defined, and its rainfall-driven discharge was generated and routed in the same manner as the distributed lateral inflows. The resulting Medlock hydrograph was inserted into the model at the appropriate confluence node.

Together, this approach provided a consistent hydrological forcing structure for the hydraulic simulations: gauged flows controlled the major upstream boundaries, while tributary and distributed inputs were supplied through rainfall-runoff modelling coupled with linear-reservoir routing to capture the essential timing and magnitude of runoff generated within the basin.

Figure 15 shows daily discharge records for the River Irwell at Adelphi Weir and the River Mersey at Ashton Weir over the period from 15 June 2015 to 14 June 2016. These hydrographs do not correspond to the upstream boundary conditions used in the hydraulic simulations; instead, they are included to illustrate the general flow behaviour in the catchment during the study period and to provide context for the hydrological conditions under which the model was run. Figure 15a presents the discharge record for the Irwell at Adelphi Weir, while Figure 15b shows the corresponding record for the Mersey at Ashton Weir.

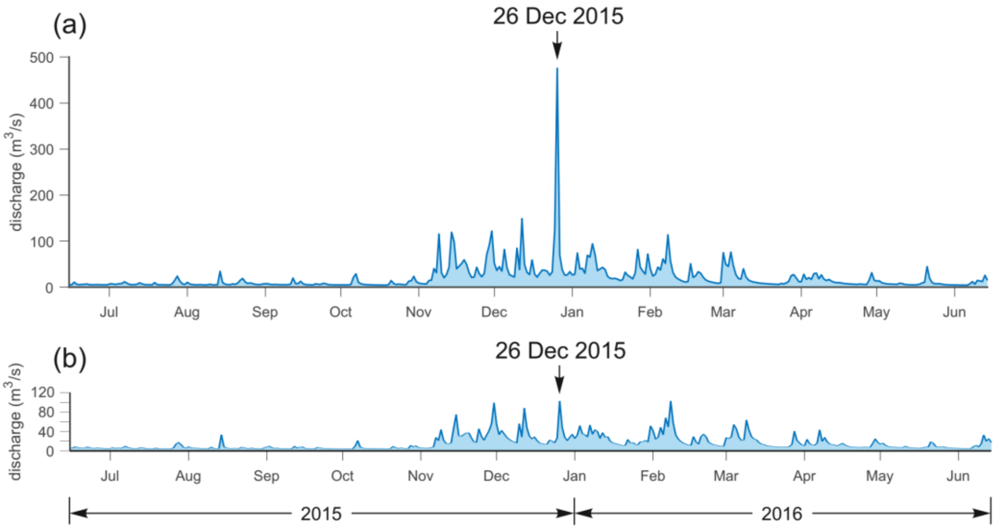

Figure 15. Daily discharge hydrographs for the study period from 15 June 2015 to 14 June 2016: (a) River Irwell at Adelphi Weir and (b) River Mersey at Ashton Weir. Both rivers show a prolonged low-flow period from June to late October (daily discharges ≈ 4–5 m^3s^{-1}), followed by a winter season characterised by multiple high-flow events. The largest flood occurred on 26 December 2015 (Boxing Day), with peak daily discharges of 476 m^3s^{-1} in the Irwell and 105 m^3s^{-1} in the Mersey. Daily values are shown because higher-resolution discharge data were not available; actual hourly peak flows during storm events were likely substantially higher.

Both time series exhibit a pronounced seasonal pattern. From mid-June to the end of October, the two rivers experience a sustained low-flow period, with typical daily discharges of approximately 4–5 m^3s^{-1}. This is followed by a winter period characterised by frequent high-flow events and several major discharge peaks. The most significant flood occurred on 26 December 2015 (Boxing Day), when the Irwell reached a peak daily discharge of 476 m^3s^{-1}, compared with 105 m^3s^{-1} in the Mersey. After the winter floods, both rivers returned to relatively low flows as the hydrological year progressed into late spring and early summer.

It is important to note that these hydrographs represent daily averaged discharges. Hourly peak flows during individual storm events would have been substantially higher; however, high-resolution data were not available for this study. As a result, daily discharge series were used for all model inputs.

4.9.5 Microplastic transport model

The microplastics transport model is based on the advection-dispersion equation with source/sink terms describing storage in the sediment bed and resuspension from it, and follows a formulation similar to that proposed by Knightes et al. (2019). The governing equations of the particle transport model are as follows:

$$\frac{\partial(C_wA)}{\partial t}+\frac{\partial(C_wQ)}{\partial x}-\frac{\partial}{\partial x}\left(DA\frac{\partial(C_wA)}{\partial x}\right)=v_rbC_s-v_sbC_w \qquad (4)$$

$$\frac{\partial(C_sA_s)}{\partial t}=-v_rbC_s+v_sbC_w \qquad (5)$$

where C_w is the concentration of microplastics in water, C_s is the concentration is the sediment, A is the flow cross-sectional area, A_s is the cross-sectional area of the sediment layer, b is the channel width, D is the longitudinal dispersion coefficient, v_s is the settling velocity, and v_r is the resuspension velocity.

Equations (4)–(5) represent a two-layer model where the upper layer is the river channel, and the lower layer is the sediment bed. Settling, deposition, erosion, and resuspension are modelled through the velocities v_s and v_r, which depend on particle parameters and the properties of the flow. The equations are solved using the flow profiles obtained from the HEC-RAS simulations. The combination of the 1-D unsteady flow simulations with the particle transport model provides a space and time dependent representation of the transport process.

4.9.5.1 Settling velocity

The settling velocity v_s is calculated as a function of particle density, water density and absolute viscosity, depending on the particle diameter, D:

$$v_s=\begin{cases}\dfrac{R_d}{18}\sqrt{g'D} & D\le 100\ \mu\text{m}\\ \dfrac{10}{R_d}\left(\sqrt{1+0.001R_d}-1\right)\sqrt{g'D} & 100\ \mu\text{m}<D\le 1\ \text{mm}\\ 1.1\sqrt{g'D} & D>1\ \text{mm}\end{cases}$$

where

$$R_d=\frac{D\sqrt{g'D}}{\mu/\rho_w}$$

is a reference Reynolds number based on the particle diameter D and the reduced gravitational acceleration,

$$g'=g\left(\frac{\rho_s}{\rho_w}-1\right)$$

μ is water viscosity, ρ_w is water density, and ρ_s is the particle density.

4.9.5.2 Non-cohesive resuspension

The resuspension velocity v_r is for the particles that are eroded from the sediment and enter (or re-enter) the water column. This is applicable when the bedload shear stress is greater than the critical shear stress $\tau_b>\tau_{c,r}$. Not all particles will experience resuspension, as this depends on the value of the shear stress compared to the critical shear stress. Following Knightes et al. (2019), the resuspension velocity is defined as:

$$v_r=f_rv_e$$

where:

$$f_r=\begin{cases}0 & \tau_b<\tau_{c,r}\\ \dfrac{\ln\frac{u_*}{v_s}-\ln\frac{u_{*,c,r}}{v_s}}{\ln 4-\ln\frac{u_{*,c,r}}{v_s}} & \tau_b\ge\tau_{c,r}\\ 1 & u_e>4v_s\end{cases}$$

where $u_*=\sqrt{\tau_b/\rho_w}$ is the shear velocity, $u_{*,cr}=\sqrt{\tau_{cr}/\rho_w}$ is the critical shear velocity for resuspension, and

$$\tau_{cr}=0.1\left(\frac{400v_s}{D_*}\right)/\left(\frac{\rho_w}{1000}\right)$$

is the critical shear stress.

4.9.5.3 Non-cohesive erosion

The van Rijn equation is used to calculate the non-cohesive erosion velocity, v_e:

$$v_e = E v_s$$

where:

$$E = 0.015 \gamma_e \frac{D}{k_s} R_d^{-0.2} \tau_*^{\eta}$$

is a proportionality constant, and

$$\tau_* = \begin{cases} \dfrac{\tau_b - \tau_{c,e}}{\tau_{c,e}} & \tau_b \geq \tau_{c,e} \\ 0 & \tau_b < \tau_{c,e} \end{cases}$$

where $\tau_b = \rho_w f u^2/8$ is the bed shear stress, $\tau_{c,e} = \gamma_{c,e}(\rho_s - \rho_w) g D \theta_{c,e}$ is the critical shear stress for erosion, $\gamma_e = 1$ is a user specified multiplier for erosion, $\gamma_{c,e} = 1$ is a user specified multiplier for critical erosion stress, and $\eta = 1.5$ is a user specified exponent for non-cohesive erosion stress.

4.9.5.4 Model implementation and application

The numerical particle-transport model was implemented in MATLAB, using a Fortran MEX routine to solve the advection–dispersion component of the governing equations. River profiles generated in HEC-RAS were imported into MATLAB to extract flow variables such as velocity, water depth, and bed shear stress. These fields were then interpolated onto the computational grid of the transport model.

The initial microplastic concentration in the sediment was assumed uniform, with no upstream particle input. The model computes resuspension and settling rates, allowing sediment-bound particles to be entrained when the local bed shear stress exceeds the critical value. Once in suspension, particles are transported downstream by advection and dispersion and may resettle further along the channel.

The model outputs two primary variables: (i) particle concentration in the water column and (ii) particle concentration in the sediment. Both are normalized by the initial sediment concentration. Because no upstream or lateral particle inputs are considered, surface-water concentrations quickly decline toward zero, increasing only during high-flow events that trigger resuspension. Given the limited long-term relevance of surface-water concentrations, this study focuses on microplastic concentrations in the sediment.

The advection-dispersion equation with source-sink terms is solved using a finite-volume scheme and a fractional-step time-integration method. The advective term is treated first, using a shock-capturing scheme with total-variation-diminishing slope limiters. The diffusive and source–sink terms are then solved with a first-order explicit method. A constant time step of 1 s is used. Simulations are performed for various particle diameters and specific gravities.

4.9.6 Results

4.9.6.1 Hydrodynamic conditions

Longitudinal profiles of flow depth and bed shear stress were computed for both the Irwell and Mersey study reaches under representative low-flow conditions and during the Boxing Day 2015 flood event. These profiles characterise the hydraulic forcing acting along each river corridor and provide the physical context for the subsequent transport analyses.

Under low-flow conditions, the Irwell exhibits substantial spatial variability in water depth along its 20 km study reach (Figure 16a). Depths are typically below 0.5–0.8 m, with deeper pools occurring intermittently. The corresponding shear-stress distribution (Figure 16b) reflects this heterogeneity: for much of the reach, shear stresses remain below 2 N m–2, but several short segments show markedly elevated values. Local peaks exceed 5 N m–2, and in a few constricted or shallow sections stresses rise above 8–10 N m–2, indicating zones of enhanced potential bed activity even during baseflow.

During the Boxing Day 2015 flood event, the hydraulic regime changes dramatically. Flow depths increase across the entire reach, often by an order of magnitude relative to low flow, and shear stresses rise accordingly (Figure 16a–b). Values exceeding 15–20 N m–2 become widespread, with local maxima surpassing 25–30 N–2. These conditions suggest extensive sediment mobilisation and efficient downstream transport during the peak of the event. Compared with low flow, the peak-flow shear-stress field is both more energetic and more spatially continuous, reflecting the strongly flushed hydraulic state of the river during the flood.

The Mersey reach displays a more irregular cross-sectional geometry, resulting in a highly heterogeneous flow-depth pattern under low-flow conditions (Figure 16c). Depths range from less than 0.3 m in shallow sections to over 0.8 m in local pools. The corresponding shear-stress profile (Figure 16d) shows a similarly patchy structure, with values typically below 2 N m–2 but several locations exceeding 5–7 N m–2. One segment near 15–16 km reaches nearly 20 N m–2, indicating locally intense hydraulic forcing even during baseflow.

During the Boxing Day flood, the Mersey experiences a substantial and widespread increase in flow depth, with long sections exceeding 2–3 m (Figure 16c). The shear-stress profile also intensifies markedly (Figure 16d). Stresses commonly exceed 10 N m–2 along extensive portions of the reach, and peak values of 20–30 N m–2 occur especially in the central and lower segments. These conditions imply a high degree of sediment entrainment potential throughout much of the system during peak discharge.

The two systems exhibit distinct hydraulic signatures. The Mersey generally sustains deeper flows and broader sections with moderately elevated shear stress, whereas the Irwell displays sharper, more localised peaks associated with narrow or constricted channel sections. During the Boxing Day flood, however, both rivers transition to hydraulically energetic states characterised by high and spatially extensive shear stresses. These contrasting and event-driven hydraulic regimes form the physical basis for the analyses presented in the following sections.

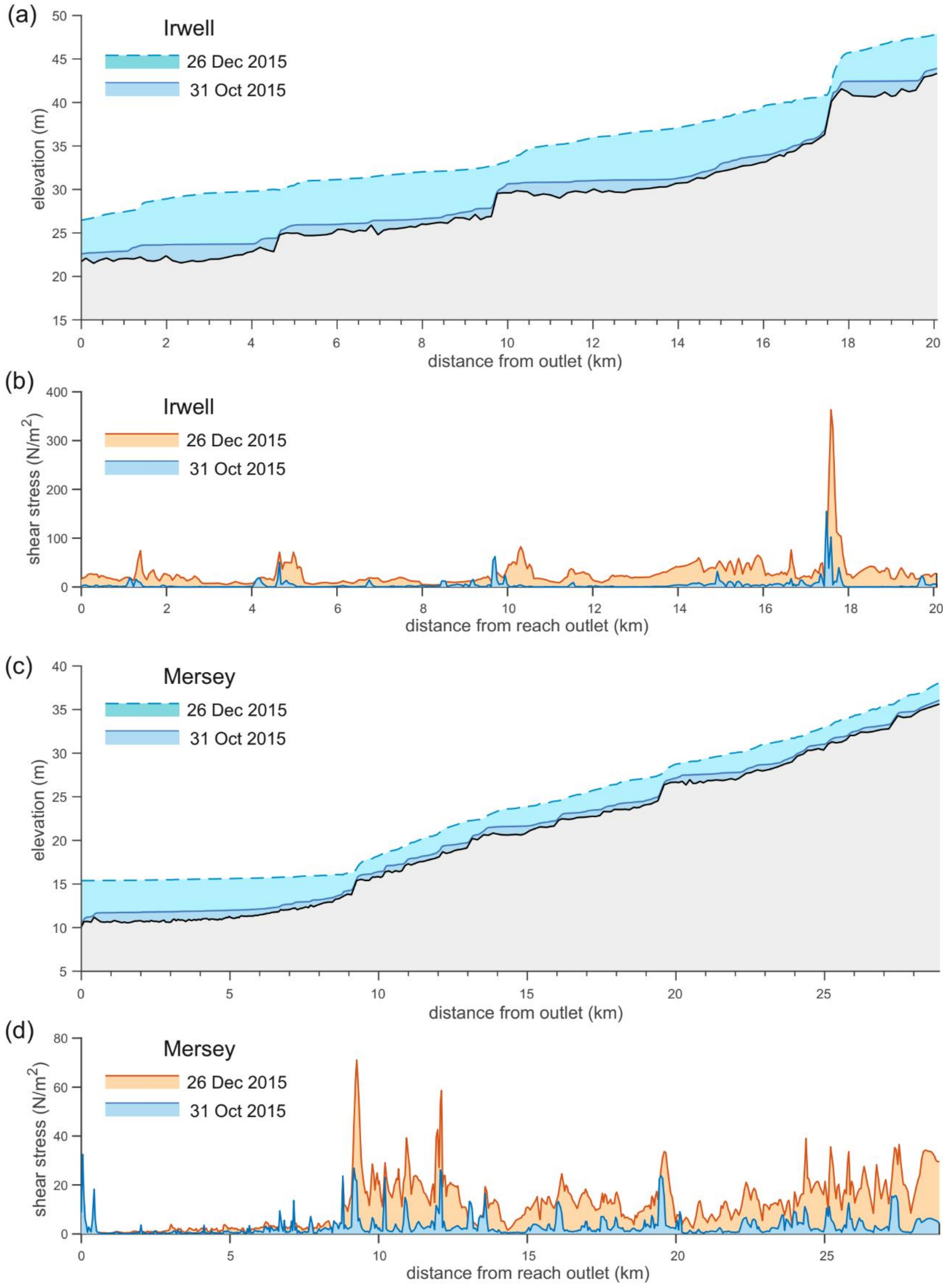

Figure 16. Longitudinal profiles of ground elevation, simulated water surface elevation, and shear stress for the Irwell (a-b) and Mersey (c-d) Rivers under low-flow conditions (1 October 2015) and during the Boxing Day 2015 flood. Ground elevation, extracted from a DTM, exhibits stepped morphology along both channels. Water surface profiles are obtained from hydraulic simulations driven by daily averaged discharges, and therefore represent mean conditions rather than instantaneous peak levels. Panels (a) and (c) show the ground and water surface elevation along the river reaches, whereas panels (b) and (d) present the corresponding shear stress distributions. The comparison between low- and high-flow states highlights substantial increases in water depth and shear stress during the flood event, indicating enhanced potential for sediment and microplastic transport.

4.9.6.2 Microplastic distributions

Figure 17 presents the simulated redistribution of microplastics in the bed sediment of the Irwell and Mersey Rivers over the one-year period from 15 June 2015 to 14 June 2016. The simulations begin from an initially uniform microplastic concentration and assume no further inputs, so that the final concentrations reflect only the effects of hydrodynamic transport, deposition, and re-entrainment driven by the observed flow regime. The reported values represent the ratio between the simulated concentration in the sediment at the end of the period and the initial value, C/C_0. These are shown for particles with diameter $d = 290$ µm, which is the average particle diameter found in the experimental analysis of Hurley et al. (2018), and a range of specific gravities.

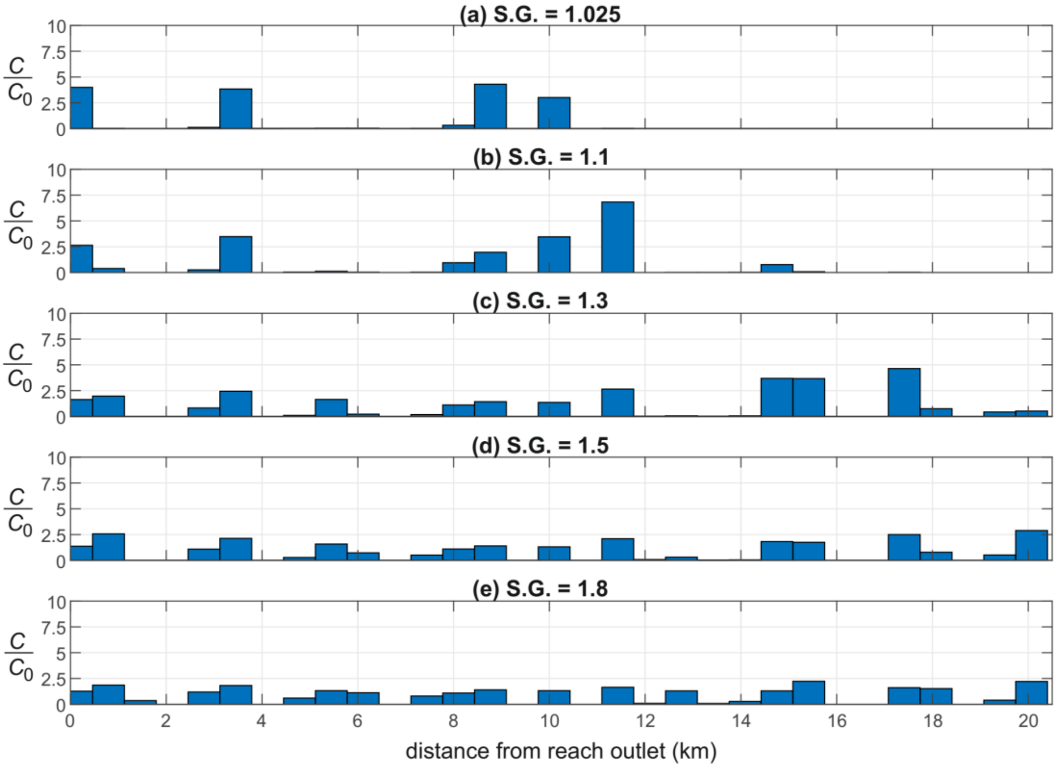

Figure 17. Normalized microplastic concentrations in the riverbed sediment along the Irwell River after one year of simulated transport (15 June 2015 to 14 June 2016). Simulations start from an initially uniform sediment concentration and assume no additional inputs during the year. Results are presented as the ratio between the final and initial concentrations, C/C_0, as a function of the distance from the downstream outlet. All simulations use microplastic particles with diameter $d = 290$ µm and consider a range of specific gravities, from 1.025 to 1.8.

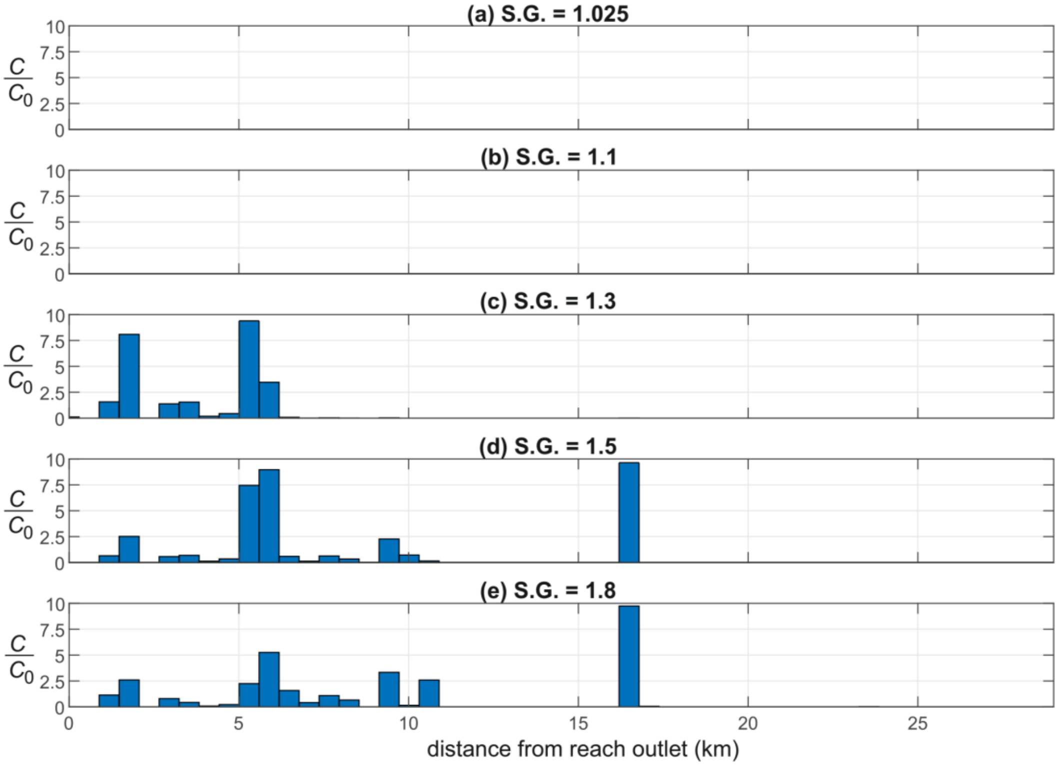

Figure 18. Normalized microplastic concentrations in the riverbed sediment along the Mersey River after one year of simulated transport (15 June 2015 to 14 June 2016). Simulations start from an initially uniform sediment concentration and assume no additional inputs during the year. Results are presented as the ratio between the final and initial concentrations, C/C_0, as a function of the distance from the downstream outlet. All simulations use microplastic particles with diameter $d = 290$ μm and consider a range of specific gravities, from 1.025 to 1.8.

For the Irwell River (Figure 17a), the longitudinal patterns reveal substantial spatial variability in the degree of microplastic retention and loss. For the lowest specific gravity considered (*s.g.* = 1.025), concentrations remain close to the initial value in only a few short segments, while most of the reach exhibits values approaching zero, indicating widespread mobilisation and downstream export. Several narrow zones, particularly near 0.1 km, 3.5 km, 8.8 km, and 10.1 km from the reach outlet, display values exceeding four times the initial concentration, suggesting localised trapping associated with channel morphology or reduced shear stress.

As particle density increases, the persistence of microplastics in the bed becomes more pronounced. For *s.g.* = 1.1, the overall pattern of depletion is still dominant, but multiple sections show moderate to strong accumulation, including peaks near 11.4 km and 14.1 km from the reach outlet. Heavier particles (*s.g.* = 1.3 and *s.g.* = 1.5) exhibit more frequent and more substantial retention, with pronounced concentration maxima at 12.1 km, 14.1 km, 17.4 km, and 19.4 km. The highest density class (*s.g.* = 1.8) further enhances this behaviour, producing consistent accumulation in downstream areas and several zones of moderate enrichment upstream. These trends indicate that particle density exerts a strong control on the balance between transport and retention, with heavier particles being more likely to remain in or return to the bed following high-flow events.

The Mersey River (Figure 17b) shows similar qualitative behaviour, characterised by strong winter-driven redistribution and clear sensitivity to particle density. Low-density particles experience widespread depletion along much of the river, while heavier particles show increasing spatial clustering and pronounced local enrichment. In both rivers, peak discharge events during the winter months play a dominant role in shaping the final concentration patterns, as they promote extensive remobilisation and subsequent redeposition once flows recede.

Overall, the results demonstrate that the longitudinal redistribution of microplastics is highly dynamic and strongly dependent on the hydrological regime and particle density. High-flow and flood events drive extensive mobilisation, while local channel characteristics and density-dependent settling velocities govern the locations of long-term retention. These patterns have important implications for identifying persistent microplastic hotspots and for understanding how episodic high-flow events shape long-term contamination profiles in river systems.

4.9.7 Discussion

Our simulations provide a mechanistic interpretation of the strong year-to-year changes in sediment microplastic concentrations documented empirically by Hurley et al. (2018) across the Irwell and upper Mersey catchments. Despite starting from an initially uniform microplastic load and assuming no additional inputs, the model reproduces three key patterns observed in their April–July 2015 to May–July 2016 dataset: (i) large overall reductions in bed-sediment microplastic concentrations following the 2015/16 winter floods, (ii) pronounced spatial heterogeneity and the formation or disappearance of localized hotspots, and (iii) density-dependent differences in mobilization and downstream redistribution. These agreements indicate that fluvial transport processes alone, without changes in source terms, are capable of producing the rapid sediment cleansing and spatial reorganization identified in the field.

4.9.7.1 Flood-driven mobilization and catchment-scale flushing

Hurley et al. (2018) reported substantial catchment-wide reductions in microplastic storage following the high-magnitude winter floods, with mean concentrations falling by 64% in the Irwell and 81% in the Mersey. Our simulations reproduce this strong flushing tendency. For both rivers, the normalized sediment concentration declines markedly at many locations, with most of the channel bed showing $C << 1$ by the end of the year. This is especially evident in the Mersey, where the model exhibits extensive near-zero concentrations across most of the reach, consistent with the high flushing efficiency measured by Hurley et al. Even in the Irwell—where hotspots persisted and some locations experienced temporary accumulation—the overall pattern reflects a strong net export of sediment-trapped microplastics under sustained high flows.

These results reinforce Hurley et al.'s (2018) conclusion that flood-related bed scour and hydraulic sorting are central controls on microplastic storage at the catchment scale. The agreement between our one-year simulations and the observed empirical changes across nearly the same hydrological interval (April 2015–July 2016) suggests that the dominant mechanisms governing bed storage are process-driven rather than source-driven. This finding is significant because Hurley et al. (2018) also documented catchment-wide declines in microbead concentrations, even in reaches where inputs from wastewater infrastructure are likely to remain high. Our simulations indicate that a single hydrological year with elevated winter flows is sufficient to deplete most of the initial sediment load, highlighting the sensitivity of microplastic retention to flow regimes and sediment mobility.

4.9.7.2 Spatial reorganization and hotspot dynamics

One of the central insights from Hurley et al. (2018) is the extreme spatial heterogeneity of microplastic contamination, including both persistent hotspots (e.g., the Tame, Tonge, and Roch) and sharp spatial transitions linked to land use, sewer overflows, and channel hydraulics. Our simulations, despite using a uniform initial sediment load and no source variability, produce comparably abrupt changes in concentration along both rivers. This is most evident in the Irwell, where several kilometres of minimal concentrations are interspersed with sharp peaks that exceed the initial concentration by factors of 2–4.

Because the model does not include any spatial variation in external inputs, these local maxima must arise from hydraulic controls, such as sediment sorting, local reductions in shear stress, and transient deposition during declining limbs of peak flows. Hurley et al. (2018) interpreted the spatial contrast between adjacent sites in the Irwell (for example, microbead-dominated sediments upstream and fragment-dominated sediments downstream of Manchester) as evidence for localized source influences and sewage infrastructure. Our results refine that interpretation by demonstrating that hydrodynamic controls alone can generate strong local contrasts, even in the absence of source heterogeneity. This implies that the observed hotspot variability in the field likely reflects an interaction of two factors: (i) spatial patterns in inputs and wastewater infrastructure, and (ii) reach-scale hydraulic sorting processes that amplify or suppress these inputs locally.

The simulations also show that heavier particles (s.g. ≥ 1.3) exhibit greater retention and more localized accumulation than low-density particles. This mirrors Hurley et al.'s (2018) empirical observation that higher-density microbeads and fragments were disproportionately retained at certain sites, including the Tame hotspot that intensified after the 2015/16 floods. The persistence of these high-density materials in predictable hydraulic retention zones lends further support to the notion that hotspot formation is governed by reach-scale topography and flow variability rather than simply by proximity to urban sources.

4.9.7.3 Density-dependent transport behaviour

Hurley et al. (2018) emphasized that microplastic density is a major determinant of in-channel storage, noting that 38% of the total stored mass consisted of seawater-buoyant plastics. They also reported distinctive post-flood changes in the relative abundance of microbeads, microfibres, and fragments, with fragments being preferentially removed. Our simulations help explain these patterns mechanistically.

For low-density particles (s.g. ≈ 1.025), concentrations rapidly decline along both rivers, with most sites showing near-complete removal within one year. This matches Hurley et al.'s (2018) documentation of widespread microbead and fragment flushing and the near-total cleansing of several headwater reaches. In contrast, particles with higher density (s.g. = 1.3–1.8) show markedly more complex behaviour: enhanced retention at mid-reach locations, increased trapping in low-shear zones, and even local accumulation exceeding initial levels. This aligns closely with Hurley et al.'s (2018) findings that some high-density microbeads increased from 14,000 to over 70,000 kg–1 at the Tame site after the floods, while most other locations saw declines.

Thus, the simulations confirm that density controls not only the overall likelihood of remobilization but also the spatial structure of subsequent sediment storage. Lighter particles are mobile across most of the hydrograph, whereas heavier particles respond in a highly episodic manner, mobilized only by the largest floods and often redeposited locally rather than exported.

4.9.7.4 Relationship between microplastic concentrations and shear stress

Comparison of the microplastic concentration profiles with the shear-stress profiles shows that the distributions of microplastics do not simply arise from the magnitude of shear stress, but from how shear stress changes along the river and how these changes interact with local morphology.

Along the Irwell, shear stress during the flood displays strong spatial variability, with several moderate peaks and one exceptionally high value of approximately 339 N m–2 at around 17.6 km upstream (Figure 16b). When examined together with the microplastic concentrations, a coherent pattern emerges: the largest microplastic accumulations tend to occur just downstream of major increases in shear stress, rather than immediately at the peak-stress locations themselves. These peaks represent upstream hydraulic "barriers" where the flow suddenly becomes much more competent. Microplastics travelling from upstream sections would have encountered these intense high-stress zones and been transported efficiently through them. The higher concentrations found downstream of these high-stress sections suggest that particles were delivered from upstream during peak flows but eventually settled as the flow decelerated downstream of the steep shear-stress gradients.

For example, immediately downstream of the extreme stress peak at 17.6 km from the reach outlet, the normalized concentration reaches one of its highest values at around 17.4 km. This supports the interpretation that sharp upstream increases in shear stress promote downstream deposition, where the flow transitions from highly energetic conditions to more moderate ones. In contrast, long stretches of uniformly low shear stress do not necessarily correspond to increased deposition, implying that local geomorphic controls (pool–riffle structures, channel widening, or bank irregularities) modulate the influence of hydraulic drivers.

The Mersey exhibits a more gradual shear-stress pattern, with much lower magnitudes (generally < 20 N m–2 compared to the Irwell, and only a few moderate peaks. Microplastic concentrations are strongly skewed towards the downstream portion of the reach. A major accumulation zone occurs within the first ~6 km from the outlet, corresponding to a combination of relatively low shear stress and favourable depositional conditions.

Upstream of ~8 km, where shear stresses increase slightly but remain moderate, concentrations drop to near zero and remain negligible all the way to the upstream boundary. This indicates that the downstream part of the Mersey provides effective retention zones, whereas the upstream sections, despite having modest shear stresses, lack the morphological features required to trap particles during and after the flood. The river thus behaves like a transport-dominated system upstream and a depositional system downstream.

4.9.7.5 Implications for microplastic export, river management, and source assessment

Hurley et al. (2018) estimated that 43 ± 14 billion microplastic particles were exported from the Irwell and Mersey catchments during the 2015/16 winter floods, including 17 ± 5.6 billion seawater-buoyant particles, equivalent to roughly 0.5–1% of the global surface ocean microplastic burden. Although our model does not explicitly compute fluxes, the widespread transition from initial concentrations to near-zero values along both rivers clearly reflects efficient export of the initial load. The simulated patterns therefore reinforce Hurley et al.'s (2018) conclusion that even modest catchments can export globally significant microplastic loads during a single hydrological year.

Finally, the model offers insight into how management strategies might interact with hydrological variability. Hurley et al. (2018) noted that recent microbead bans may allow rapid recovery of channel beds, provided that flood events mobilize contaminated sediments. Our results show that, even without the removal of ongoing inputs, fluvial processes themselves can reduce bed storage substantially during wet years. Conversely, in hydrological years with few high-magnitude events, heavy-density microplastics may persist in sediment stores, especially in retention-prone reaches. These findings suggest that long-term monitoring programs and sediment management strategies need to explicitly account for interannual hydrological variability and density-dependent differences in transport potential.

4.9.8 Conclusions

The numerical simulations presented here provide a mechanistic framework for interpreting the year-to-year changes in sediment microplastic concentrations documented by Hurley et al. (2018) in the Irwell-Mersey system. Starting from a uniform initial distribution and assuming no additional inputs, the model reproduces the strong spatial heterogeneity and substantial temporal variability observed in the field, demonstrating that internal redistribution driven by hydrodynamic forcing is sufficient to generate the patterns measured between 2015 and 2016.

The simulations confirm that winter high flows, particularly the December 2015 flood, exert dominant control on microplastic mobility, producing widespread erosion and redistribution of bed-stored particles. They also reveal pronounced density-dependent behaviour: low-density particles are readily mobilised and dispersed during moderate floods, while high-density particles require extreme events for significant transport. These mechanistic insights align closely with polymer-specific trends observed by Hurley et al. (2018), strengthening the conclusion that particle density is a first-order control on fluvial microplastic dynamics.

Comparisons between the two rivers highlight the influence of geomorphology on storage and transport. Although the study reaches have similar overall slopes, their hydraulic and morphological characteristics differ in ways that strongly affect microplastic dynamics. The Irwell displays more spatially abrupt variations in shear stress, with several sharp high-stress sections, whereas the Mersey shows broader, more gradual shear-stress patterns. These hydraulic differences contribute to the Irwell's more heterogeneous microplastic redistribution and the Mersey's stronger downstream retention.

Overall, the combined evidence indicates that sediment microplastic concentrations in fluvial systems are highly dynamic and strongly event-driven. Apparent increases or decreases at monitoring sites may reflect redistribution rather than changes in catchment loading. Consequently, assessments of sediment contamination should be interpreted within a hydrodynamic context, and modelling approaches such as the one presented here offer an essential complement to field-based monitoring. Together, these insights contribute to a more robust understanding of the processes governing the storage, mobility, and persistence of microplastics in riverine environments.

4.9.8.1 Ongoing and Future Work

Beyond the UK case study presented above, the authors have also developed (within the RETURN project) mass-transport models of microplastics and emerging contaminants, with a particular focus on one of the most pressing environmental challenges in the Veneto Region: understanding the propagation and fate of PFAS within the mid-Venetian river network. In particular, the Agno River (one of the most heavily contaminated streams in the area) has been selected as a priority system for detailed modelling.

The long-term objective is to construct a fully integrated model of PFAS transport in the Agno River. Given the complexity of this task and the time constraints of the current project phase, only the initial components of this modelling chain have been developed so far. The planned end-point is a two-dimensional, depth-integrated hydrodynamic model capable of representing surface-flow dynamics in gravel-bed rivers with complex geometries, including floodplains that become progressively activated as discharge increases. This hydrodynamic core will provide the foundation for a coupled contaminant-transport model that links surface advection-dispersion with hyporheic exchange processes, accounting for the role of streambed sediments as transient or long-term contaminant stores (see, e.g., Marion et al. 2008; Bottacin-Busolin 2019).

Developing such a modelling framework requires extremely detailed characterization of channel morphology and bed roughness elements (such as bars, bedforms, and clusters) that drive hyporheic flow paths. For this reason, the first stage of the work has focused on high-resolution topographic surveying of the active channel and adjacent floodplains, together with direct measurements of grain-scale and form-scale roughness. These surveys were conducted using drone-based photogrammetry technology acquired within the RETURN project (model: DJI Mavic 3E) with field support from AQUAPROGRAM.

Two initial reaches of the Agno River have now been fully surveyed and are being used to develop the first dedicated hydrodynamic models. These models will subsequently be coupled with the contaminant-transport component during the next phase of the work. This activity represents the concluding contribution of the Padua team to Task 3.1 of the RETURN project.

4.9.9 References

Besseling, Ellen, Joris T. K. Quik, Muzhi Sun, and Albert A. Koelmans. 2017. ‘Fate of Nano- and Microplastic in Freshwater Systems: A Modeling Study’. *Environmental Pollution* 220 (January): 540–48. https://doi.org/10.1016/j.envpol.2016.10.001.

Bottacin-Busolin, Andrea. 2019. ‘Modeling the Effect of Hyporheic Mixing on Stream Solute Transport’. *Water Resources Research* 55 (11): 9995–10011. https://doi.org/10.1029/2019WR025697.

Eerkes-Medrano, Dafne, Richard C. Thompson, and David C. Aldridge. 2015. ‘Microplastics in Freshwater Systems: A Review of the Emerging Threats, Identification of Knowledge Gaps and Prioritisation of Research Needs’. *Water Research* 75 (May): 63–82. https://doi.org/10.1016/j.watres.2015.02.012.

García, Marcelo H. 2013. *Sediment Transport and Morphodynamics*. May 6, 21–163. https://doi.org/10.1061/9780784408148.ch02.

Hoellein, Timothy J., Arial J. Shogren, Jennifer L. Tank, Paul Risteca, and John J. Kelly. 2019. ‘Microplastic Deposition Velocity in Streams Follows Patterns for Naturally Occurring Allochthonous Particles’. *Scientific Reports* 9 (1): 3740. https://doi.org/10.1038/s41598-019-40126-3.

Hurley, Rachel, Jamie Woodward, and James J. Rothwell. 2018. ‘Microplastic Contamination of River Beds Significantly Reduced by Catchment-Wide Flooding’. *Nature Geoscience* 11 (4): 251–57. https://doi.org/10.1038/s41561-018-0080-1.

IPCC. 2021. *Climate Change 2021 – The Physical Science Basis: Working Group I Contribution to the Sixth Assessment Report of the Intergovernmental Panel on Climate Change*. Cambridge University Press. https://doi.org/10.1017/9781009157896.

Jambeck, Jenna R., Roland Geyer, Chris Wilcox, et al. 2015. ‘Plastic Waste Inputs from Land into the Ocean’. *Science* 347 (6223): 768–71. https://doi.org/10.1126/science.1260352.

Knightes, Christopher D., Robert B. Ambrose, Brian Avant, et al. 2019. ‘Modeling Framework for Simulating Concentrations of Solute Chemicals, Nanoparticles, and Solids in Surface Waters and Sediments: WASP8 Advanced Toxicant Module’. *Environmental Modelling & Software* 111 (January): 444–58. https://doi.org/10.1016/j.envsoft.2018.10.012.

Koelmans, Albert A., Adil Bakir, G. Allen Burton, and Colin R. Janssen. 2016. ‘Microplastic as a Vector for Chemicals in the Aquatic Environment: Critical Review and Model-Supported Reinterpretation of Empirical Studies’. *Environmental Science & Technology* 50 (7): 3315–26. https://doi.org/10.1021/acs.est.5b06069.

Kooi, Merel, Ellen Besseling, Carolien Kroeze, Annemarie P. van Wezel, and Albert A. Koelmans. 2018. ‘Modeling the Fate and Transport of Plastic Debris in Freshwaters: Review and Guidance’. In *Freshwater Microplastics : Emerging Environmental Contaminants?*, edited by Martin Wagner and Scott Lambert. Springer International Publishing. https://doi.org/10.1007/978-3-319-61615-5_7.

Lebreton, Laurent C. M., Joost van der Zwet, Jan-Willem Damsteeg, Boyan Slat, Anthony Andrady, and Julia Reisser. 2017. ‘River Plastic Emissions to the World’s Oceans’. *Nature Communications* 8 (1): 15611. https://doi.org/10.1038/ncomms15611.

Mani, Thomas, Armin Hauk, Ulrich Walter, and Patricia Burkhardt-Holm. 2015. ‘Microplastics Profile along the Rhine River’. *Scientific Reports* 5 (1): 17988. https://doi.org/10.1038/srep17988.

Marion, A., M. Zaramella, and A. Bottacin-Busolin. 2008. ‘Solute Transport in Rivers with Multiple Storage Zones: The STIR Model’. *Water Resources Research* 44 (10). https://doi.org/10.1029/2008WR007037.

Nizzetto, Luca, Gianbattista Bussi, Martyn N. Futter, Dan Butterfield, and Paul G. Whitehead. 2016. ‘A Theoretical Assessment of Microplastic Transport in River Catchments and Their Retention by Soils and River Sediments’. *Environmental Science: Processes & Impacts* 18 (8): 1050–59. https://doi.org/10.1039/C6EM00206D.

PlasticsEurope. 2023. *Plastics – the Fast Facts 2023*. PlasticsEurope. https://plasticseurope.org/knowledge-hub/plastics-the-fast-facts-2023/.

Rijn, Leo C. van. 1984. ‘Sediment Transport, Part II: Suspended Load Transport’. *Journal of Hydraulic Engineering* 110 (11): 1613–41. https://doi.org/10.1061/(ASCE)0733-9429(1984)110:11(1613).

Rochman, Chelsea M., Eunha Hoh, Tomofumi Kurobe, and Swee J. Teh. 2013. ‘Ingested Plastic Transfers Hazardous Chemicals to Fish and Induces Hepatic Stress’. *Scientific Reports* 3 (1): 3263. https://doi.org/10.1038/srep03263.

Scherer, Christian, Nicole Brennholt, Georg Reifferscheid, and Martin Wagner. 2017. ‘Feeding Type and Development Drive the Ingestion of Microplastics by Freshwater Invertebrates’. *Scientific Reports* 7 (1): 17006. https://doi.org/10.1038/s41598-017-17191-7.

Schmidt, Christian, Tobias Krauth, and Stephan Wagner. 2017. ‘Export of Plastic Debris by Rivers into the Sea’. *Environmental Science & Technology* 51 (21): 12246–53. https://doi.org/10.1021/acs.est.7b02368.

Thompson, Richard C., Ylva Olsen, Richard P. Mitchell, et al. 2004. ‘Lost at Sea: Where Is All the Plastic?’ *Science* 304 (5672): 838–838. https://doi.org/10.1126/science.1094559.

Tibbetts, Joseph, Stefan Krause, Iseult Lynch, and Gregory H. Sambrook Smith. 2018. ‘Abundance, Distribution, and Drivers of Microplastic Contamination in Urban River Environments’. *Water* 10 (11): 1597. https://doi.org/10.3390/w10111597.

Triebskorn, Rita, Thomas Braunbeck, Tamara Grummt, et al. 2019. ‘Relevance of Nano- and Microplastics for Freshwater Ecosystems: A Critical Review’. *TrAC Trends in Analytical Chemistry* 110 (January): 375–92. https://doi.org/10.1016/j.trac.2018.11.023.

Wagner, Martin, Christian Scherer, Diana Alvarez-Muñoz, et al. 2014. ‘Microplastics in Freshwater Ecosystems: What We Know and What We Need to Know’. *Environmental Sciences Europe* 26 (1): 12. https://doi.org/10.1186/s12302-014-0012-7.

Waldschläger, Kryss, and Holger Schüttrumpf. 2019. ‘Effects of Particle Properties on the Settling and Rise Velocities of Microplastics in Freshwater under Laboratory Conditions’. *Environmental Science & Technology* 53 (4): 1958–66. https://doi.org/10.1021/acs.est.8b06794.

Windsor, Fredric M., Isabelle Durance, Alice A. Horton, Richard C. Thompson, Charles R. Tyler, and Steve J. Ormerod. 2019. ‘A Catchment-Scale Perspective of Plastic Pollution’. *Global Change Biology* 25 (4): 1207–21. https://doi.org/10.1111/gcb.14572.

4.10 Effects of microplastics (MPs) on the interactions between plant and pollinating insects (UNIFI)

Contributors: I. Colzi, S. Falsini, C. Gonnelli, A. Papini

4.10.1 Introduction

The widespread presence of microplastic (MP) contamination is receiving increasing attention at ecosystem level, since these pollutants interact with terrestrial organisms that mediate significant ecosystem services and functions, such as terrestrial fungi or several invertebrates e.g., pollinating insects. The effects of MPs on insects are particularly relevant given the prevalence of these organisms in the environment and the fact that they provide key ecosystem services: above all, pollinators are inextricably linked to the natural environment and the production of foods, they maintain a genetically diverse angiosperm flora within most ecosystems and are, thus, essential for food crop pollination and human as well as livestock food security around the world. Pollination is essential for the sexual reproduction of all seed plants and provides benefits to the human population. Despite recent studies have shown a direct MP-toxicity on pollinators, it remains to understand if the plant-pollinator interaction may be affected by MP pollution.

The communication between plants and pollinators is reciprocally beneficial for each other, as pollinators enhance plant reproductive success through pollen export and collection, while nectar and pollen serve as nutrition for pollinators, which are called floral rewards. Flowering plants developed and evolved various characteristics to attract or influence the success of pollinators, including different floral features such as pigmentation, floral signals, floral pattering, floral scents, and nectar secondary metabolites. The adaptation of floral traits is vital for the attraction of pollinators, and accordingly, any interferences with this adaptation may have great impacts on pollination process. Pollinators learn to find flowers with high quality or abundant nectar and it has been shown that they can learn to avoid visiting flowers with nectar containing toxic compounds. The insects can associate floral traits with the taste of secondary metabolites in nectar or with the negative consequences of accidentally ingesting toxic compounds. It is therefore it possible that MPs in the soil modify the plant floral and nectar characteristics consequentially interfering with the memory and the behaviour of insects.

4.10.2 Case study description

The impact of MPs on ecological interactions was studied using *Viola tricolor* as a model for plant–pollinator relationships. The effects of MPs were investigated through specific experiments in controlled conditions of temperature, light and humidity to standardize the environmental conditions.

4.10.3 Methodologies

Specific experiments were performed to assess the possible effects of MP-polluted soils on plant flower traits involved in attracting pollinating insects, such as odor emission, flower number and color, and nectar patterns (Fig. 1).

4.10.3.1 Experimental methods

Plants of *V. tricolor* have been cultivated in pots containing commercial soil artificially polluted with certified MPs purchased from chemical companies. Two different plastic types were selected by choosing among those generally reported in literature for agricultural soils, namely polyvinyl chloride (PVC), and polyethylene terephthalate (PET). The different plastics were tested separately to highlight differences in the phytotoxicity of the materials.

During the cultivation, plant physiology and development was monitored by periodical measurements of growth parameters (e.g. shoot height, number of leaves, leaf traits through pictures) and photosynthetic efficiency (Fig. 1). Such measurements were used to identify signs of plant stress. At the flowering stage the plants were used for the analysis of volatile organic compound (VOC) emission to identify any modification in the odor emission profile due to MP treatment. Moreover, plants were sampled for further analyses (Fig. 1): i) number of total flowers per plant; ii) flower phenotypical characteristics, such as size, colour intensity, specific patterns; iii) amount of nectar produced through graduated glass capillary tubes; iv) chemical and nutritional characteristics of nectar, such as sugars and secondary metabolites.

All the measurements of MP-treated plants were compared with control plants grown in non-contaminated soils, therefore allowing to univocally identify changes in flower and nectar characteristics induced by MP pollution.

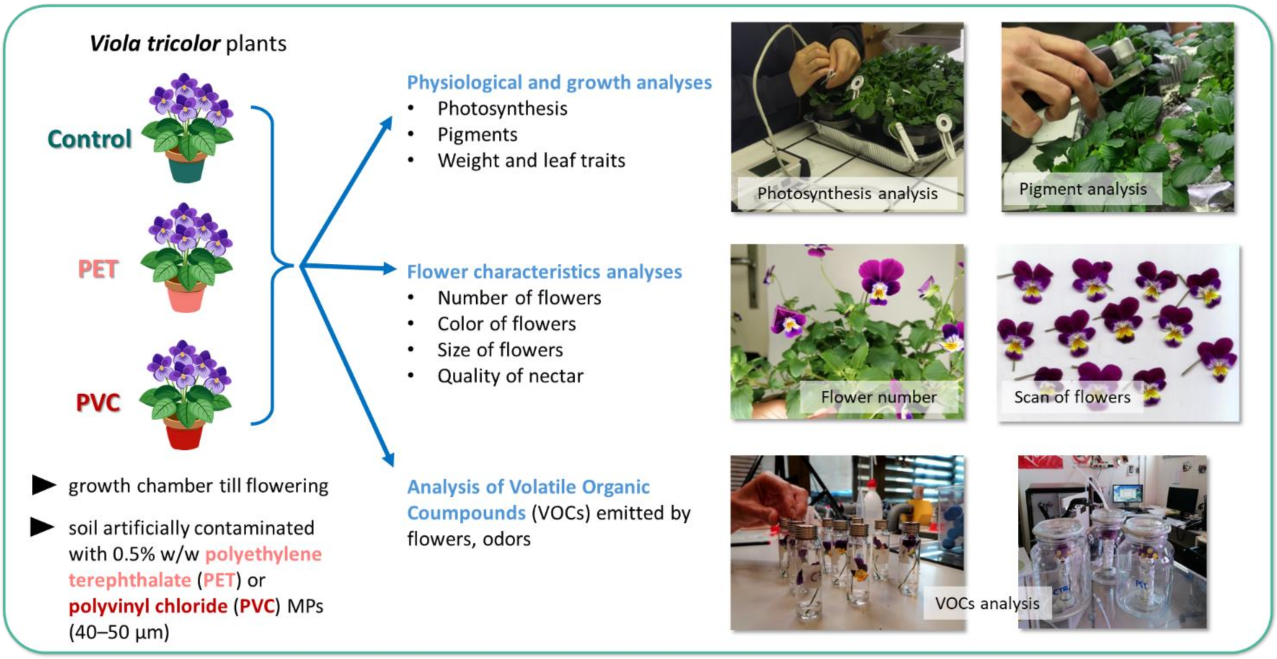

Figure 1: Schematic representation of the experimental setup and performed analyses.

4.10.4 Results

MP-contaminated soils caused several alterations compared with controls (Fig. 2).

Regarding physiological and growth parameters, plants treated with MPs generally showed a lower photosynthetic efficiency and chlorophyll content, and a reduction of several leaf traits such as leaf area and thickness, suggesting that plants suffered some toxicity from MP soil pollution.

Regarding the effects on flower characteristics that may be involved in attracting pollinating insects, several alterations were found in plants grown in soils contaminated with MPs in respect to controls:

- a lower number of flowers;
- flowers with different pattern of colorations (more yellow flowers).
- Alterations in the profile of the VOCs emitted by flowers. In particular, some compounds were emitted in a lower quantity, but some terpenes were more abundant;
- Alteration in the nectar quality. In particular, nectar was richer in sugar content

These findings suggested that soil MP contamination may cause interferences in the plant-pollinator interactions with possible consequences for the pollination process.

Understanding the effects of MP contamination on ecological interaction is important to assess possible ecosystem-level consequences, such as altered interactions between plants and other organisms, including pollinators. However, no studies have been performed in this specific direction. Pollinators, such as honeybees and wild solitary and social bees, interact with plants, air, soil, and water basins, and are therefore directly exposed to MPs when foraging (Balzani et al., 2022). MPs have been found in honey, in several plant species foraged by bees (Diaz-Basantes et al., 2020; Liebezeit & Liebezeit, 2013, 2015) and on the cuticle of honeybees (Edo et al., 2021). Recently, laboratory studies have investigated toxicity of MP on individual honeybees, showing varying results from low, moderate to high effects on survival

(Balzani et al., 2022; Buteler et al., 2022; Edo et al., 2021; K. Wang et al., 2021). However, such studies have the limitations to use quite artificial laboratory conditions, by feeding the pollinators with sucrose solutions containing concentrations of MPs. Not much importance has been yet posed in considering more realistic conditions.

Gaining knowledge about the effect of MPs on plant-pollinator interactions is essential considering that pollinators, especially bees, are relentlessly decreasing worldwide (Goulson, 2019; Potts et al., 2010) due to a multitude of stressors caused by anthropogenic activity, such as habitat disruption, parasites and diseases, lack of food, pesticides (Hladik et al., 2018), and climate change (Goulson et al., 2015). Wide research is necessary to understand if MPs may represent an additional hazard for bees and to keep safe these organisms as important as they are at risk.

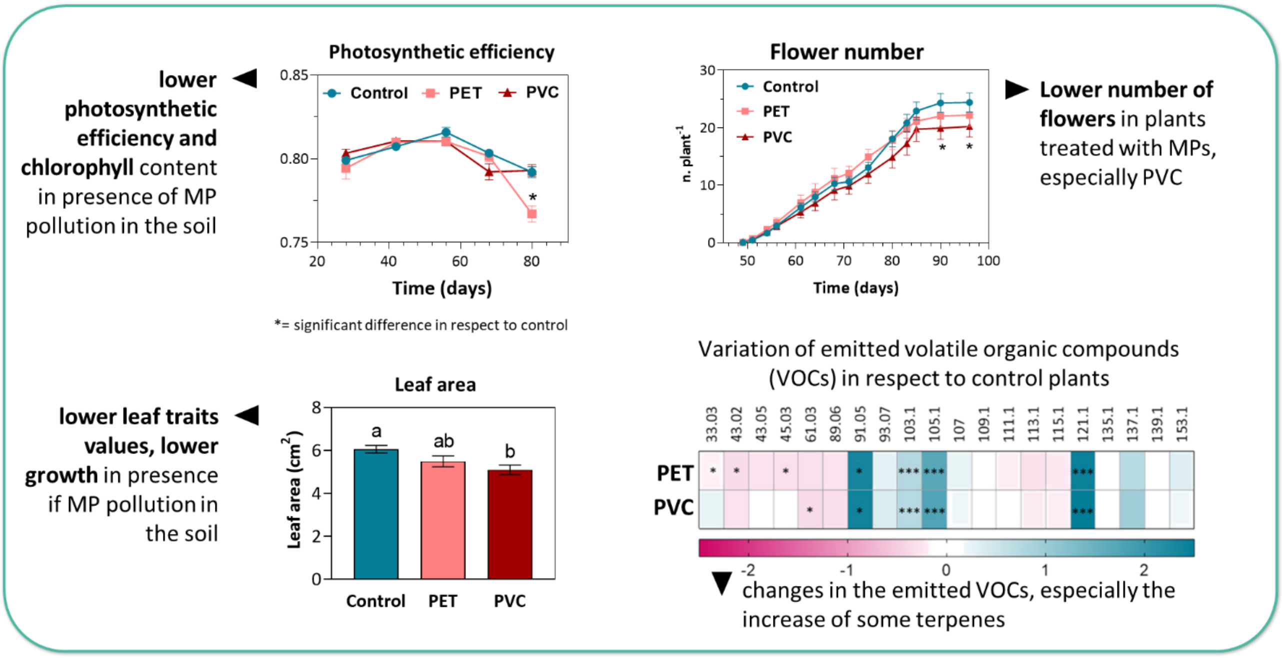

lower photosynthetic efficiency and chlorophyll content in presence of MP pollution in the soil

Lower number of flowers in plants treated with MPs, especially PVC

*= significant difference in respect to control

Variation of emitted volatile organic compounds (VOCs) in respect to control plants

lower leaf traits values, lower growth in presence if MP pollution in the soil

changes in the emitted VOCs, especially the increase of some terpenes

Figure 2: Main results obtained from the experiments.

4.10.5 Scientific products and dissemination

18-20 September 2024. Poster presentation at the Mini symposia of the International Conference "XVII FISV Congress" in Padova: "The third wheel in the plant-pollinator relationship: the presence of microplastics in the soil – the BeeSafe project" Colzi I., Chiavacci B., Pecorini V., Taiti C., Calabrese D., Nepi M., Guardigli G., Bazihizina N., Brunetti C., Baracchi D., Gonnelli C.

27 Novembre 2024. Oral presentation at the Workshop "Le piante e la biodiversità urbana e peri-urbana: sfide e come valorizzarla" of Fondazione per il Futuro delle Città. Title of presentation: Interazioni pianta-impollinatori a rischio per le microplastiche. Ilaria Colzi

4.10.6 References

P. Balzani, G. Galeotti, S. Scheggi, A. Masoni, G. Santini, and D. Baracchi, "Acute and chronic ingestion of polyethylene (PE) microplastics has mild effects on honey bee health and cognition," Environmental Pollution, vol. 305, 2022, doi: 10.1016/j.envpol.2022.119318.

M. Buteler, A. M. Alma, T. Stadler, A. C. Gingold, M. C. Manattini, and M. Lozada, "Acute toxicity of microplastic fibers to honeybees and effects on foraging behavior," Science of the Total Environment, vol. 822, 2022, doi: 10.1016/j.scitotenv.2022.153320.

M. F. Diaz-Basantes, J. A. Conesa, and A. Fullana, “Microplastics in honey, beer, milk and refreshments in Ecuador as emerging contaminants,” Sustainability (Switzerland), vol. 12, no. 12, 2020, doi: 10.3390/SU12145514.

C. Edo, A. R. Fernández-Alba, F. Vejsnæs, J. J. M. van der Steen, F. Fernández-Piñas, and R. Rosal, “Honeybees as active samplers for microplastics,” Science of the Total Environment, vol. 767, 2021, doi: 10.1016/j.scitotenv.2020.144481.

D. Goulson, E. Nicholls, C. Botías, and E. L. Rotheray, “Bee declines driven by combined Stress from parasites, pesticides, and lack of flowers,” Science, vol. 347, no. 6229. 2015. doi: 10.1126/science.1255957.

D. Goulson, “The insect apocalypse, and why it matters,” Current Biology, vol. 29, no. 19. 2019. doi: 10.1016/j.cub.2019.06.069.

M. L. Hladik, A. R. Main, and D. Goulson, “Environmental Risks and Challenges Associated with Neonicotinoid Insecticides,” Environ Sci Technol, vol. 52, no. 6, 2018, doi: 10.1021/acs.est.7b06388.

G. Liebezeit and E. Liebezeit, “Origin of synthetic particles in honeys,” Pol J Food Nutr Sci, vol. 65, no. 2, 2015, doi: 10.1515/pjfns-2015-0025.

G. Liebezeit and E. Liebezeit, “Non-pollen particulates in honey and sugar,” Food Additives and Contaminants - Part A, vol. 30, no. 12, 2013, doi: 10.1080/19440049.2013.843025.

S. G. Potts, J. C. Biesmeijer, C. Kremen, P. Neumann, O. Schweiger, and W. E. Kunin, “Global pollinator declines: Trends, impacts and drivers,” Trends in Ecology and Evolution, vol. 25, no. 6. 2010. doi: 10.1016/j.tree.2010.01.007.

K. Wang et al., “Gut microbiota protects honey bees (Apis mellifera L.) against polystyrene microplastics exposure risks,” J Hazard Mater, vol. 402, 2021, doi: 10.1016/j.jhazmat.2020.123828.

4.11 Study of the potential impact of MPs on plant resistance to pathogens (UNIFI)

Contributors: I. Colzi, S. Falsini, C. Gonnelli, A. Papini

4.11.1 Introduction

Plants are inevitably affected by this new class of pollutants since plants are sessile organisms and cannot escape all environmental challenges during their lifespan. A wide variety of negative effects caused by MPs on plants have already been reported. However, plant response to MPs is greatly variable, depending on multifaceted MP characteristics and specific plant capacity to interact with MPs. Moreover, stressors seldom come alone in natural environments, and plants are always exposed to a combination of them. Joint exposure of plants to MPs and other stressful conditions has started to be studied. This is essential for a correct understanding of MP hazardousness and/or toxicity, since, in general, combined stressors may have more severe effects on plants. For example, joint treatments with MPs and trace metals, especially cadmium and lead, may alter element bioavaiability in environmental matrices and aggravate their toxic effects on plants. Often, MPs magnify the impacts of other stresses on plant organisms and communities, such as in the case of acid rain, drought and heat.

Among the possible stress that can be found in environments, biotic stressors are a main cause of global agricultural yield losses, and plant communities are expected to be increasingly exposed to dangerous diseases in the current climate change scenario. Foyer et al. (2016) demonstrated that various plant defence responses against abiotic stressors (e.g., reduced growth, redox regulation, production of specialised metabolites) could positively influence resistance to aphid infestation. Furthermore, the simultaneous presence of environmental contaminants, other than plastics, and biotic stress agents has been reported to possibly lead to cross-tolerance (Poschenrieder et al. 2006). MPs are abundant in both natural environments and agroecosystems; however, to the best of our knowledge, only two recent studies have investigated the combination of MPs with biotic stress, both suggesting higher plant susceptibility to the stressors (Cao et al. 2024; Bouaicha et al. 2024).

Since agriculture is moving towards sustainability targets, it appears impelling to understand the possible consequences that MPs may cause on disease resistance mechanisms and how soil pollution with MPs may affect the plant innate immune system. Enhanced pathogen susceptibility, for instance, would have consequences in terms of crop losses and enhanced use of plant protection products.

4.11.2 Case study description

To shed light on the potential impact of MPs on plant-pathogen interaction, the model plant *Arabidopsis thaliana* was grown in the presence of two widely diffused types of MPs, polyvinyl chloride (PVC), and polyethylene terephthalate (PET), at two environmentally relevant concentrations. The plants were then exposed to different pathogens to explore whether MPs: (i) affect plant resistance to *Botrytis cinerea*, a generalist fungal pathogen; (ii) influence the production of antimicrobial compounds (i.e., phytoalexins) and reactive oxygen species (ROS) after exposure to cerato-platanin (CP), a fungal protein with well-known PAMP activity.

4.11.3 Methodologies

Specific experiments were performed in controlled conditions of temperature, light and humidity to standardize the environmental conditions.

4.11.3.1 Experimental methods

Microplastic soil pollution was simulated in the laboratory using previously standardised methodologies. Commercial soil was artificially polluted with certified MPs (PET and PVC) purchased from chemical companies. These types of plastic were chosen because of their large presence in natural and agricultural soils. They were directly added to the substrate without further treatment at two environmentally realistic concentrations that are commonly used for testing in controlled conditions, that is, 0.2% and 0.5% MPs/dry soil (w/w).

Plants of *A. thaliana* were grown in such polluted soils for 3 weeks in a climatic chamber, during which different parameters of plant growth and physiology (photosynthetic efficiency, malondialdehyde concentration, chlorophyll content, etc.) were monitored at different times (Fig. 1). Three-week-old *A. thaliana* plants were then exposed to two different biotic stressors: the fungal pathogen *Botrytis cinerea* and the cerato-platanin protein, a fungal protein produced by the ascomycete *Ceratocystis platani* and used as a model molecule to simulate plant-pathogen interactions (Fig. 1). To evaluate the effects of MPs on plant defense mechanisms, different plant responses induced by the fungal pathogens were investigated: necrotic lesion diameter, phytoalexin production, ROS production, specialized metabolite profiles (Fig. 1).

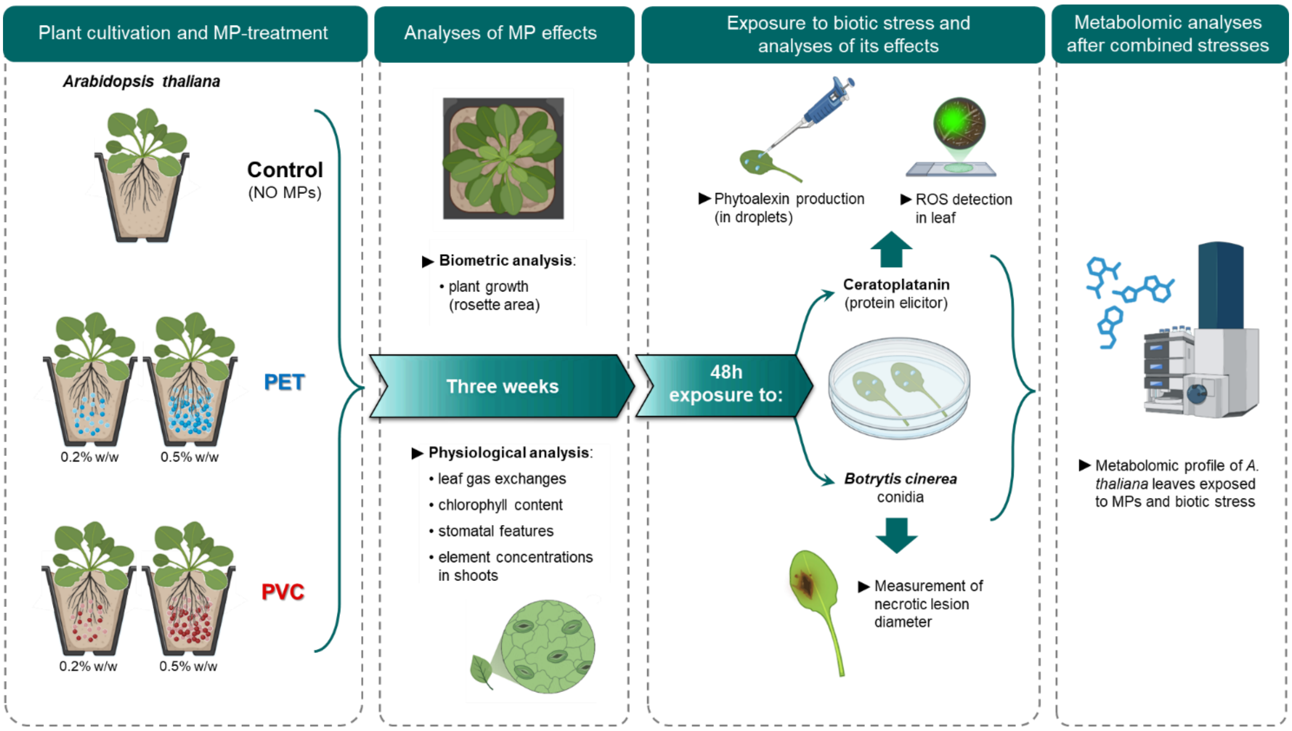

Figure 1: Schematic representation of the experimental setup and performed analyses.

4.11.4 Results

The results reported mild effects on *A. thaliana* growth and rosette development of MPs at low (realistic) doses together with a reduced accumulation of some nutrients (i.e. Zn, Mn etc.). MP has mild effects also on plant physiology, inducing a stimulation of stomatal conductance.

Interestingly, the study revealed possible interactions between MPs and pathogen stress in plants. PVC (0.2%) triggered a primed state in *A. thaliana*, enhancing its response to *B. cinerea* infection and cerato-platanin (Fig. 2). This was demonstrated by decreased lesion size, enhanced ROS generation, and elevated camalexin synthesis following PAMP elicitation, and increased levels of defensive isothiocyanate and phenylpropanoid metabolites. It seems, therefore, that MPs altered plant specialized metabolism influencing the response to biotic stress. Specific polymer-concentration combinations may carry a significant priming effect, activating defensive responses against fungal pathogens. Fine regulation of these effects by specialised metabolites is also likely, and some possible metabolic interactions were highlighted.

Many other factors can play a role in influencing the ecological and agronomic implications of exposure to MPs. For example, domestication can diminish both constitutive and inducible defences (Córdova-Campos et al. 2012; Moreira et al. 2018; Soltis et al. 2018), and this may change the capacity to cope with biotic stress in crop species, even under an MP-induced priming.

In conclusion, the results indicate that MPs also affect soil structure, ionome balance, and specialised metabolite accumulation. However, MPs did not provide an unambiguous response, underscoring challenges in formulating a model of plant response to MPs when exposed to pathogens.

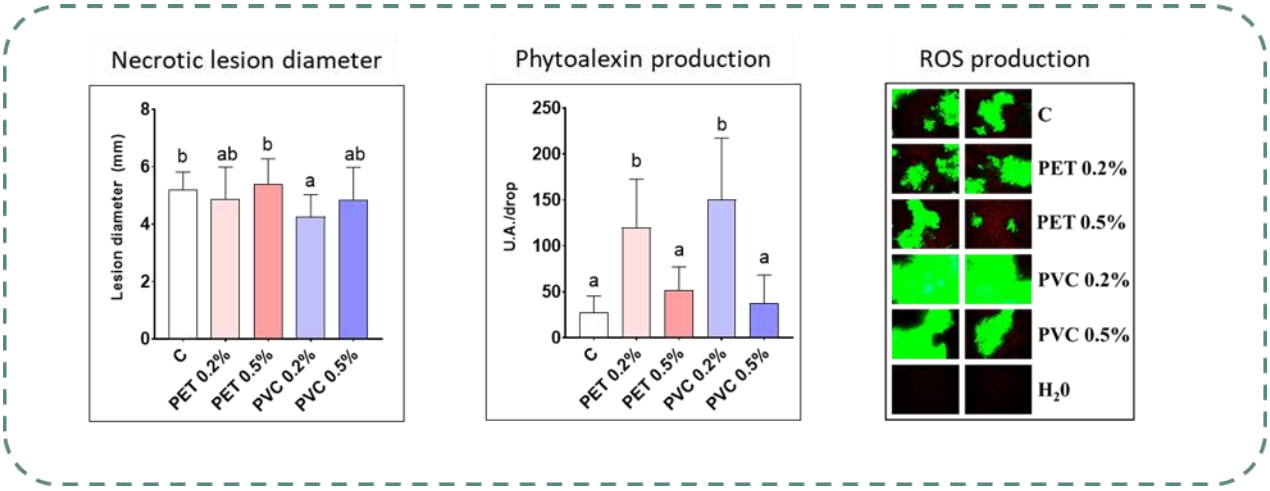

Figure 2: Main results obtained from the experiments.

4.11.5 Scientific products and dissemination

Dainelli M., Colzi I., Giosa D., Gargiulo G., Lo Passo C., Pernice I., Falsini S., Ristori S., Pignattelli S., Miniati A., Morandi P., Buti M. (2025). Coding and non-coding transcripts modulated by transparent and blue PET micro-nanoplastics in *Arabidopsis thaliana*. Plant Physiology and Biochemistry 220, 109409. https://doi.org/10.1016/j.plaphy.2024.109409

Dainelli M., Cicchi C., Baccelli I., Boutet S., Colzi I., Coppi A., Luti S., Pignattelli S., Pollastri S., Loreto F., Pazzagli L., Corso M., Gonnelli C. (2025). Microplastics in the Soil at Sub-Toxic Concentrations Cause Metabolic Changes Decreasing Fungal Pathogen Susceptibility in *Arabidopsis thaliana*. Physiol Plantarum 177(3), e70312. https://doi.org/10.1111/ppl.70312

16-19 September 2025. Poster at the "XIV Congress of the Italian Society of Plant Biology" in Palermo: "Microplastics in the soil at sub-toxic concentrations cause metabolic changes decreasing fungal pathogen susceptibility in *Arabidopsis thaliana*" Dainelli M, Cicchi C., Baccelli I., Boutet S., Colzi I., Coppi A., Luti S., Pignattelli S., Pollastri S., Loreto F., Pazzagli L., Corso M., Gonnelli C.

4.11.6 References

Bouaicha, O., M. Maver, T. Mimmo, S. Cesco, and L. Borruso. 2024. "Microplastic Influences the ménage à Trois Among the Plant, a Fungal Pathogen, and a Plant Growth-Promoting Fungal Species." Ecotoxicology and Environmental Safety 279: 116518.

Cao, X., C. Wang, X. Luo, et al. 2024. "Nano-and Microplastics Increase the Occurrence of Bacterial Wilt in Tomato (Solanum lycopersicum L.)." ACS Nano 18: 18071–18084.

Córdova-Campos, O., R. M. Adame-Álvarez, J. A. Acosta-Gallegos, and M. Heil. 2012. "Domestication Affected the Basal and Induced Disease Resistance in Common Bean (Phaseolus vulgaris)." European Journal of Plant Pathology 134: 367–379.

Foyer, C. H., B. Rasool, J. W. Davey, and R. D. Hancock. 2016. "Cross-Tolerance to Biotic and Abiotic Stresses in Plants: A Focus on Resistance to Aphid Infestation." Journal of Experimental Botany 67: 2025–2037.

Moreira, X., L. Abdala-Roberts, R. Gols, and M. Francisco. 2018. “Plant Domestication Decreases Both Constitutive and Induced Chemical Defences by Direct Selection Against Defensive Traits.” Scientific Reports 8: 12678.

Poschenrieder, C., R. Tolrà, and J. Barceló. 2006. “Can Metals Defend Plants Against Biotic Stress?” Trends in Plant Science 11: 288–295.

Soltis, N. E., S. Atwell, G. Shi, et al. 2018. “Crop Domestication and Pathogen Virulence: Interactions of Tomato and Botrytis Genetic Diversity.” Plant Cell 31, no. 2: tpc.00857.2018.

4.12 Enzymatic degradation and anaerobic co-digestion of commercial bioplastics + food waste and related potential environmental issues (UNIROMA1)

Contributors: M. Falzarano, A. Polettini (DICEA, University of Rome “La Sapienza”)

4.12.1 Introduction

The possibility of treating bioplastics together with the OFMSW is one of the main advantages in the progressive substitution of conventional plastics with bioplastics. However, there are currently many issues related to the management of bioplastic residues to which scientific literature has not given a comprehensive answer yet. For instance, an incomplete degradation could lead to the formation of micro-bioplastics that can in turn affect the quality of the final compost/digestate and be carried into the environment. A deeper knowledge of the biodegradation mechanisms of bioplastics is needed to understand if there are any technological adjustments that can be made in full-scale plants to allow their operation. The effect of anaerobic digestion of commercial bioplastic products and food waste with and without enzymes was investigated. The aim of the experimental campaign was to simulate degradation conditions of a full-scale anaerobic digestion plant and to evaluate the potential benefits and drawbacks linked to the presence of bioplastics. The possibility of using enzymes as a pre-treatment or a boost during anaerobic digestion was investigated. Moreover, a literature review on enzymatic degradation of bioplastics was conducted to evaluate the state of the art in terms of enzymes used and effects on different biopolymers.

4.12.2 Methodologies

In this study the investigation was carried out in two phases. The first phase was aimed at a detailed review of literature studies and related findings related to the enzymatic degradation of bioplastic materials. The second phase involved experimental investigations on the biological and enzymatic degradation of selected bioplastic items, where the testing conditions were selected based on the preliminary literature investigation conducted during the first phase.

4.12.2.1 Literature review of enzymatic degradation of bioplastics

In this phase of the study we aimed at reviewing the relevant scientific literature on enzymatic degradation of different types of biopolymers using data search and analysis methodologies meant to be clearly defined, systematic, reproducible and transparent. The study was structured to achieve multiple targets, including 1) summarising the main findings of the scientific community on the title topic; 2) identifying common research trends and related advance as well as potential knowledge gaps; 3) conducting a meta-analysis of collected data using appropriate statistical techniques in order to explore as quantitatively as possible how and to what extent the relevant underlying factors affect the enzymatic degradation of bioplastic materials.

To meet such targets, a combination of systematic literature review and meta-analysis of data was adopted according to well-established and codified methods of data search, categorization and processing (see e.g. (Mengist et al., 2020; Page et al., 2021; Paul and Barari, 2022; Snyder, 2019)).

The bibliographic search was conducted in the Web of Science (WoS) database, which was chosen as a well-acknowledged reference database in the fields of, among others, chemical/biological science and engineering. The search strategy was designed to capture both generic and polymer-specific studies by combining keywords related to enzymatic and hydrolytic degradation processes with terms describing the effects of degradation on the main properties of various biopolymers mainly of the aliphatic polyesters family. The database was accessed in March 2025 and the literature search was then refined and updated for inclusion of the latest scientific references in January 2026. Boolean operators and wildcard characters were employed to maximize the sensitivity of literature search while maintaining thematic relevance. The search was conducted in the “Topic” field, which includes title, abstract and author keywords using the following search query: (("enzym* degradation" OR "enzym* hydrolysis" OR "enzym* depolymerization") AND (PLA OR "polylactic acid" OR polylactide OR PCL OR "polycaprolactone" OR PBS OR "poly(butylene succinate)" OR PBSA OR "poly(butylene succinate-co-adipate)" OR PHA OR "polyhydroxyalkanoate*" OR PHB OR "polyhydroxybutyrate" OR "biodegradable polyester*") AND ("mechanism*" OR "kinetic*" OR "mass loss" OR "molecular weight" OR "crystallinity" OR morpholog* OR "surface erosion" OR "bulk erosion")).

The selection of relevant studies was conducted according to the PRISMA (Preferred Reporting Items for Systematic Reviews and Meta-Analysis) guidelines (Page et al., 2021) on the basis of predefined eligibility criteria, and exclusion of manuscripts was done at different stages where the following conditions applied (Batten and Brackett, 2021; Mengist et al., 2020):

- duplicated manuscripts (early access/final paper versions, corrigendum versions, indexing errors)
- inaccessible manuscripts
- non-qualified sources (grey literature, no peer-review or similar)
- ineligibility based on title and abstract screening (non-enzymatic biodegradation, non-biobased polymers, not relevant context)
- ineligibility based on full-text screening (out-of-scope papers, absence of experimental results on enzyme applications, lack of primary/original research data, lack of sufficient methodological rigour, detection of evident inconsistencies or errors in data reporting)

Data extraction was conducted manually for manuscripts in the final list of eligible papers with a focus on the information, characteristics and properties listed in Table 1, which were arranged in an Excel database used for further in-depth analysis of the extracted data. When data was only available in the manuscript in graphical form, WebPlotDigitizer, a semi-automatic computer vision-assisted software capable of extracting data from images (Rohatgi, 2024), was employed to collect data in numerical format. Reconciliation of data from different sources in some instances required unit conversion with the aim of reporting the numerical results – when feasible – as homogeneously as possible. The accuracy of each data entry was checked by at least three of the authors of the present manuscript in parallel and independently from each other in order to avoid any potential bias in data collection, classification and interpretation.

Table 1. Definition and description of categorical and numeric variables included in the database

Group of variables	**Specific variable**	**Description**	**Variable code**	**Variable type (categorical/ numeric)**
1. BP type and composition	1.1 BP type	Type of bioplastic	BP	C
	1.2 BP blend	Bioplastic sub-type (individual polymer, copolymer or blend)	BP_blend	C
	1.3 BP composition	Composition of bioplastic	BP_composition	C
2. BP processing	2.1 BP production method	Method of production of copolymer or blend	BP_blend/copolym_produc	C
	2.2 BP transformation	Method of processing of BP before the enzymatic treatment	BP_transform	C
3. BP properties	3.1 BP form	Physical form of the BP	BP_form	C
	3.2 BP surface area	Surface area of the BP tested	BP_size_surfacearea	N
	3.3 BP thickness	Thickness of the BP tested (when applicable)	BP_size_thickn	N
	3.4-3.6 BP molecular weight	Molecular weight of the BP tested (M_w, M_n, M_v)	BP_Mw (3.4) BP_Mn (3.5) BP_Mv (3.6)	N N N
	3.7 BP crystallinity	Crystallinity of the BP tested	BP_crystallinity	N
	4.1 Enzyme type	Specific type of enzyme	Enzyme_type	C

4. Enzyme type and characteristics	4.2 Enzyme source	Source of enzyme	Enzyme_source	C
	4.3 Enzyme production	Method of enzyme production	Enzyme_production	C
5 Testing conditions	5.1 Working volume	Working volume	Working_vol	N
	5.2 BP concentration	BP concentration	BP_conc	N
	5.3-5.4 Enzyme concentration	Enzyme concentration	Enzyme conc_(mg/mL) (5.3) Enzyme conc_(U/mL) (5.4)	N N
	5.5-5.6 Enzyme dosage	Enzyme dosage per unit of BP mass	Enzyme dosage_(mg/mgBP) (5.5) Enzyme dosage_(U/mgBP) (5.6)	N N
	5.7 Buffer/solvent solution	Type of buffer/solvent solution	Buffer_solvent_solution	C
	5.8 Initial pH	Initial pH	Initial_pH	N
	5.9 Final pH	Final pH	Final_pH	N
	5.10 pH control method	Method of pH control	pH_ctrl_method	C
	5.11 Degradation time	Duration of the enzymatic degradation test	Degr_time	N
	5.12 Temperature	Temperature	Temperature	N
6. Results	6.1 Mass loss	BP mass loss after enzymatic degradation	Mass_loss	N
	6.2 Monomer conversion method	Analytical method adopted to measure BP conversion into monomers	Monomer_convers_meth	C
	6.3 Monomer conversion yield	Yield of BP conversion into monomers (%)	Monomer_convers_perc	N
	6.4 Oligomer conversion method	Analytical method adopted to measure BP conversion into oligomers	Oligomer_convers_meth	C
	6.5 Oligomer conversion yield	Yield of BP conversion into oligomers (%)	Oligomer_convers_perc	N
	6.6 Molecular weight change method	Analytical method adopted to measure molecular weight change	Mol_w_change_meth	C
	6.7 Molecular weight change	Molecular weight change after enzymatic degradation (%)	Mol_w_change_perc	N
	6.8 Crystallinity change method	Analytical method adopted to measure crystallinity change	Crystall_change_meth	C
	6.9 Crystallinity change	Crystallinity change after enzymatic degradation (%)	Crystall_change_perc	N
	6.10 Microscopic change method	Analytical method adopted to measure changes in microscopic characteristics	Microsc_meth	C
	6.11 Microscopic change	Changes in microscopic characteristics after enzymatic degradation	Microsc_change	C
	6.12 Chemical structure change method	Analytical method adopted to measure changes in chemical structure	Chemstruct_meth	C
	6.13 Chemical structure change	Changes in chemical structure after enzymatic degradation	Chemstruct_change	C

	6.14 Chemical structure change method	Analytical method adopted to measure other changes in material properties	Othtechn_meth	C
	6.15 Chemical structure change	Other changes in material properties after enzymatic degradation	Othtechn_change	C

An initial general appraisal of the collected scientific literature on the enzymatic degradation of bioplastics was carried out to point out specific research hotspots, trends and relevant features. The main aspects addressed in the bibliographic analysis included: 1) volume and time evolution of the scientific production; 2) geographical distribution of the collected studies; 3) frequency and network of recurring keywords to pick out hot topics and thematic clusters. The analysis of recurring words in paper text, abstract and keywords list was performed by means of the bibliometric mapping software VOSviewer (van Eck and Waltman, 2010) after reconciling and merging similar keywords.

In a second phase of the analysis aimed at a systematic review of the collected information, the data was first analysed for factor levels and related size, statistical parameters of the frequency distribution of values (for numeric variables), combinations of operating conditions adopted in the enzymatic treatment experiments, type of analytical techniques adopted to assess the effects of enzymatic degradation as well as measured performance of the enzymatic degradation process. To this aim, different tools of data extraction and analysis available in MS Excel and R software (packages ggplot2 (Wickham, 2016), networkD3 (Allaire et al., 2025) and dplyr (Wickham et al., 2023)) were employed. To explore patterns, relationships and clusters within the literature results, the statistical technique known as recursive partitioning was applied. This is a non-parametric statistical technique based on binary regression tree algorithms. A regression tree is constructed by recursively partitioning the data set into two homogeneous groups (son nodes) according to a specified criterion, and then splitting the nodes up further on each of the branches. On each node the response is fitted by the node average, which implies defining a stepwise constant fitted response surface. Recursive partitioning (Hothorn and Zeileis, 2015) thus involves separating statistical groups progressively decreasing in size and increasing in internal homogeneity in terms of the statistical distribution of the response variable. In the present case, splitting was implemented using a conditional inference criterion, implying testing the global null hypothesis of independence between any of the input variables and the response. If the null hypothesis cannot be rejected, the splitting procedure at that node is stopped, and this becomes a terminal node of the tree; otherwise, the input variable exhibiting the strongest association with the response (as measured by the corresponding p-value) is selected and a binary split in it is implemented. The splitting procedure continues until each node becomes a terminal node according to the above mentioned condition.

4.12.2.2 Experimental investigation of anaerobic biodegradation and enzymatic degradation of bioplastic products

During the experimental investigation the degradation of some disposable bioplastic items was assessed under thermophilic anaerobic conditions in co-digestion with synthetic food waste (FW). The tests were arranged to simulate a long-term scenario in which the weight component of bioplastics is extremely abundant (50-75 % of the substrate). The characterization of each bioplastic type was carried out by scanning electron microscopy (SEM), thermogravimetric analysis (TGA) and Fourier transform infrared (FTIR) spectroscopy prior to degradation. Bioplastic samples were also treated with enzymes simulating two scenarios: i) an enzymatic pre-treatment prior to anaerobic digestion and ii) the combined use of digestate and enzymes during the biodegradation process. These tests were carried out based on the main findings collected with the literature review.

Six different bioplastic products were selected (cup1, cup2, plate, knife, shopper bag and coffee capsule) and characterized for their composition. Cup1 and the plate were PLA-based, cup2 and the coffee capsule were a mixture of PLA and PBS, while the knife and the shopper were mainly made of PLA and PBAT. All items were manually cut into 2 ×2 cm squares. Synthetic FW was prepared by blending 10% of meat, 65% of fruit and vegetables, 10% of bread and 15% of cooked pasta (wet weight basis). Lipase from *Candida Rugosa* was purchased from Sigma Aldrich. The digestate was collected from a full-scale anaerobic digestion plant. The tests were conducted at 55 °C by monitoring biogas evolution and composition (H_2, CH_4, CO_2) using gas chromatography. Blank tests were conducted to evaluate the residual biogas production of the inoculum. Each type of bioplastic item was tested individually with FW using F/M = 1 $gVS_{substrate}/gVS_{inoculum}$ (with $VS_{substrate}$ being the sum of the VS of FW and bioplastics) and setting FW at 50% of the substrate on a wet weight basis. Cup1 and FW were also tested at F/M = 1 $gVS_{substrate}/gVS_{inoculum}$ and FW at 25%, and with F/M = 0.5 $gVS_{substrate}/gVS_{inoculum}$ and FW at 50% and 25% respectively. In addition, FW was digested alone with the inoculum at different F/M ratios (0.5 and 1 $gVS_{substrate}/gVS_{inoculum}$). The degree of material disintegration was evaluated by sieving the digestate at 0.84 mm; the plastic fragments retained were carefully rinsed with deionized water and then dried at 35 °C until constant weight. FT-IR analyses were carried out on the clean residual fragments with LUMOS II (Bruker Optik GmbH) equipped with a single reflection germanium ATR cell. The spectra were recorded with 256 scans in the mid infrared range (400–4000 cm^{-1}) at a resolution of 4 cm^{-1}. The enzymatic pre-treatment with lipase was carried out on cup1. The cup was cut in 1.5x1.5 cm^2 and placed in 0.25 L glass reactor with 100 ml of TrisHCl buffer at different concentrations of lipase (0.5, 2 and 10 mg/ml). The reactors were placed in a thermostatic shaker at 38 °C for 4 days. The bioplastic fragments were then collected, washed with deionized water and then put in 0.5 L glass reactors with digestate. The reactors were placed in a thermostatic bath at 55 °C until plateau was reached. The F/M ratio was kept equal to 1 for all tests. The anaerobic digestion with enzymes was carried out on Cup1, SH and PL. Lipase was added to the digestate at two concentrations (0.5 and 10 mg/ml). Glass reactors of 0.5 L were filled with digestate and bioplastics were added at F/M = 1. The reactors were placed in a thermostatic bath at 55 °C until the plateau was reached.

4.12.3 Results

4.12.3.1 Main findings from the literature analysis

The results of literature search based on the search query specified in Materials and Methods showed a total number of 1459 matching records, which were reduced to 1366 unique articles after duplication check, and further down to 1363 after removing manuscripts that were not accessible in their full-text version. Exclusion based on source qualification removed 14 articles, while 1027 were further discarded based on title and abstract screening, with 322 full-text articles being finally assessed for eligibility. Full-text screening led to the removal of additional 230 manuscripts due to insufficient focus on bio-based/biodegradable polymers (58), lack of quantitative data on degradation effects (115), irrelevant research focus (e.g., synthesis/application only (26)), methodological limitations or evident flaws/errors in the description of experimental methods/conditions and in the reporting of data (31). Ultimately, 92 studies were included in the final list of analysed papers.

As depicted in Figure 1, the selected papers spanned the time horizon 1996-2025 (a) and the main contributing countries (b) included Japan (25 articles), China (22), Italy (9), Thailand (7), United States (6), France (5) and South Korea (5); overall, the remaining countries contributed by 42 additional articles. The analysis of keywords identified the following most frequently adopted (> 25 occurrences) words (retained words = 63): *enzym* (87), biodegrad* (52), PLA (50), degrad* (38), polyester* (36), lactic acid (35), hydroly* (27). Figure 1 c) shows the co-occurrence network for keywords displaying a minimum number of 5 occurrences, where the node label size is proportional to the number of occurrences and the line thickness reflects the strength of the link between each pair of keywords. The keyword network was found to be structured in three different clusters: a first cluster (in red) including keywords mainly related to the type of biopolymers tested, their chemical structure and physical, mechanical and microscopic properties, a second group (in green) mainly associated to bioplastics production/processing methods and related conditions, and a third cluster (in blue) including information on enzymes used, enzyme production methods and enzymatic degradation products.

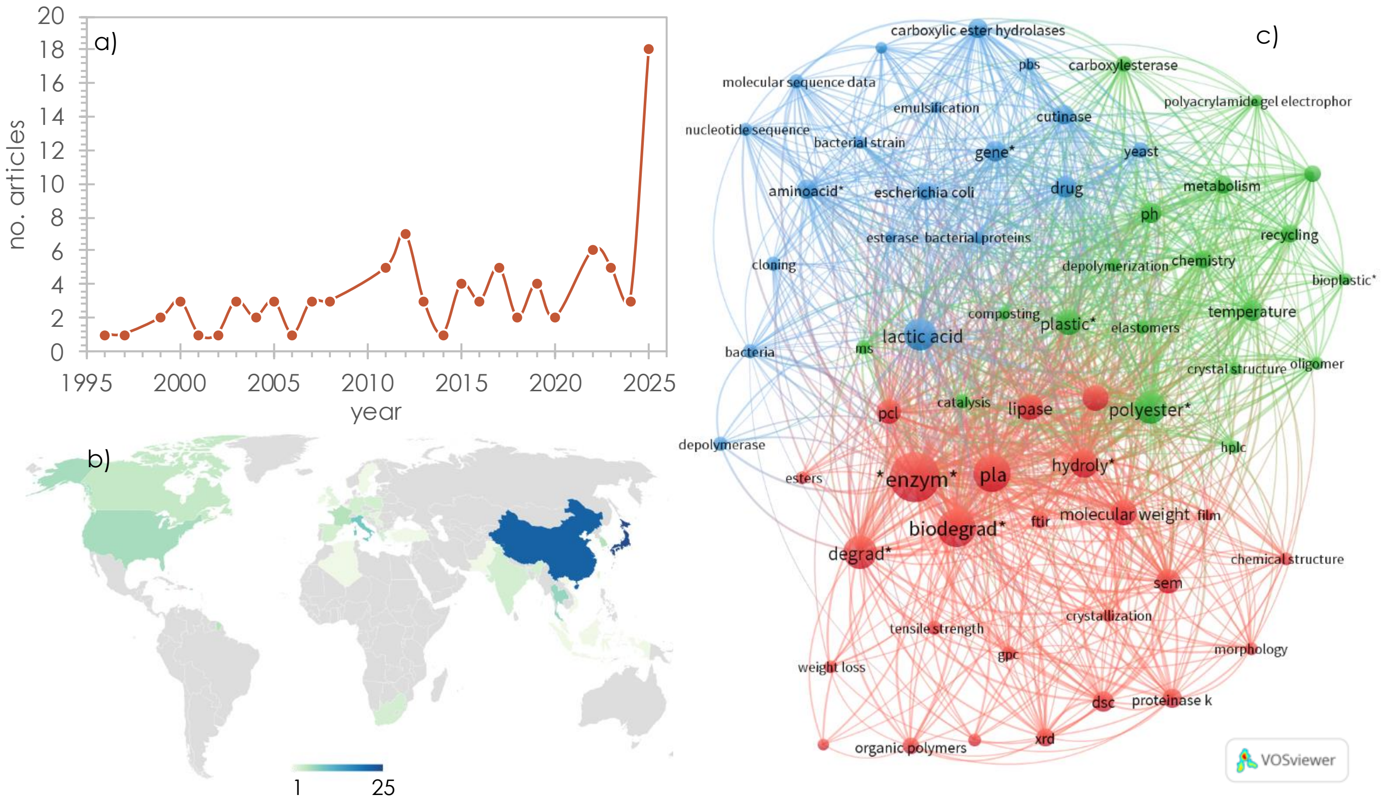

Figure 1. (a) time trend of published articles; (b) contributing countries (color shades indicate the number of papers per country); (c) keyword co-occurrence network.

Overall, the database built from the literature data contained 2648 rows with a total of 58,180 individual entries (excluding empty cells). The database is currently available at the link https://docs.google.com/spreadsheets/d/1vPttemPpF7069DVqpxpiN3CuYQcfmRTb/edit?usp=sharing&ouid=117195305257319988835&rtpof=true&sd=true (password-protected file; password to be requested to alessandra.polettini@uniroma1.it). The number of selected papers focusing on specific polymers as well as the number of data entries by polymer and enzyme type are shown in Table 2, which points out at PLA, PCL, PBS, PBSA and PHB as the most widely investigated biopolymers, and at lipase, proteinase K, cutinase and protease as the most commonly tested enzymes.

Table 2. Number of selected articles and observations by polymer and enzyme type.

Polymer type	**no. articles**	**no. observ.**
PLA	62	1261
PCL	24	359
PBS	11	144
PBSA	8	89
PHB	7	102
PBAT	4	33
PLA + additives	5	136
PHBV	3	38
PCL + PLA	3	73
PES	2	32
Mater-Bi®	1	17
PCHC	1	68
PEAz	1	6
PHD	1	2
PHHx	1	2

Enzyme type	**no. observ.**
Lipase	1030
Proteinase K	544
Cutinase	509
Protease	163
Depolymerase	115
Esterase	70
Unspecified	41
Diastase	32
Enzyme mix (Alcalase + Savinase + 3 Lipases)	27
Proteinase K + Savinase	25
Lipase + Cutinase	17
Subtilisin	15
Proteinase K + Lipoxidase	9
Proteinase K + Lipase	8
Trypsin	8

PHN	1	2
PHO	1	2
PHB + PTMG	1	4
PHB+ PTMG + PLA	1	4
PHB + PCL	1	4
PHB + PCL + PLA	1	4
PCL + PEO	1	6
PCL + PEO + PCL	1	6
PCL + PPDO	1	12
PCL + PBS	1	32
PCL + PU	1	30
PBAT + PVA	1	8
PBS + PVA	1	6
PCL + (PCL/PLA copolym.)	1	7
PCL + blend	1	10
PPSu	1	3
PPTA	1	21
PLA + PBSA	1	3
PPSu + PCL	1	25
PLA + PEAz	1	24
PLA + PVA	1	6
PLA + PHB	1	36
PLA + TPU	1	8
PLA + TPU + additives	1	14
PLA + PBSA + additives	1	9

α-Amylase	6
β-Glucanase	6
Talipase	6
Pectin methylesterase	5
Roosepase	5
Alcalase	4
Lipoxidase	2
Protease + Lipase	1

The experimental conditions of the enzymatic degradation tests were found to vary over notably large ranges, which on one side reflects the variety of the experimental approach adopted in the examined studies and on the other side anticipates a large variability of the associated experimental results. Overall, the main statistical parameters of the frequency distribution of the testing conditions (group 5 of variables in Table 1) were the following (in the order **min–max**, *average*, first and third quartiles; total no. of observations):

- working volume: **0.5–3500;** *115*; 3; 20 [mL]; no. = 1976
- BP concentration: **0.5–100,000;** *6806*; 10; 10,000 [mg/L]; no. = 1476
- enzyme concentration: **0.000001–180;** *2.0*; 0.05; 0.5 [mg/mL]; no. = 1653
- enzyme dosage: **0.00002–186;** *6.5*; 0.005; 3 [mg/mg BP]; no. = 1011
- initial pH: **3.9–12;** *7.7*; 7.0; 8.5; no. = 2149
- degradation time: **0–2688;** *231*; 12; 168 [h]; no. = 2644
- temperature: **10–110;** *39.4*; 37; 40 [°C]; no. = 2648

For some of the operating conditions, namely the duration of the degradation experiments, temperature, initial pH and working volume, Figure 2 also reports the box plots for the available numeric observations grouped by biopolymer type. It should however be noted that the number of datapoints varied largely depending on the biopolymer tested and in some cases the information regarding the operating conditions of interest was even not retrieved in the analysed publications. The operating variables that are not reported in Figure 2 were excluded from the graphical representation as their numerical values were found to be either too scattered across the different biopolymer types or of too low sample size to provide a meaningful statistical distribution.

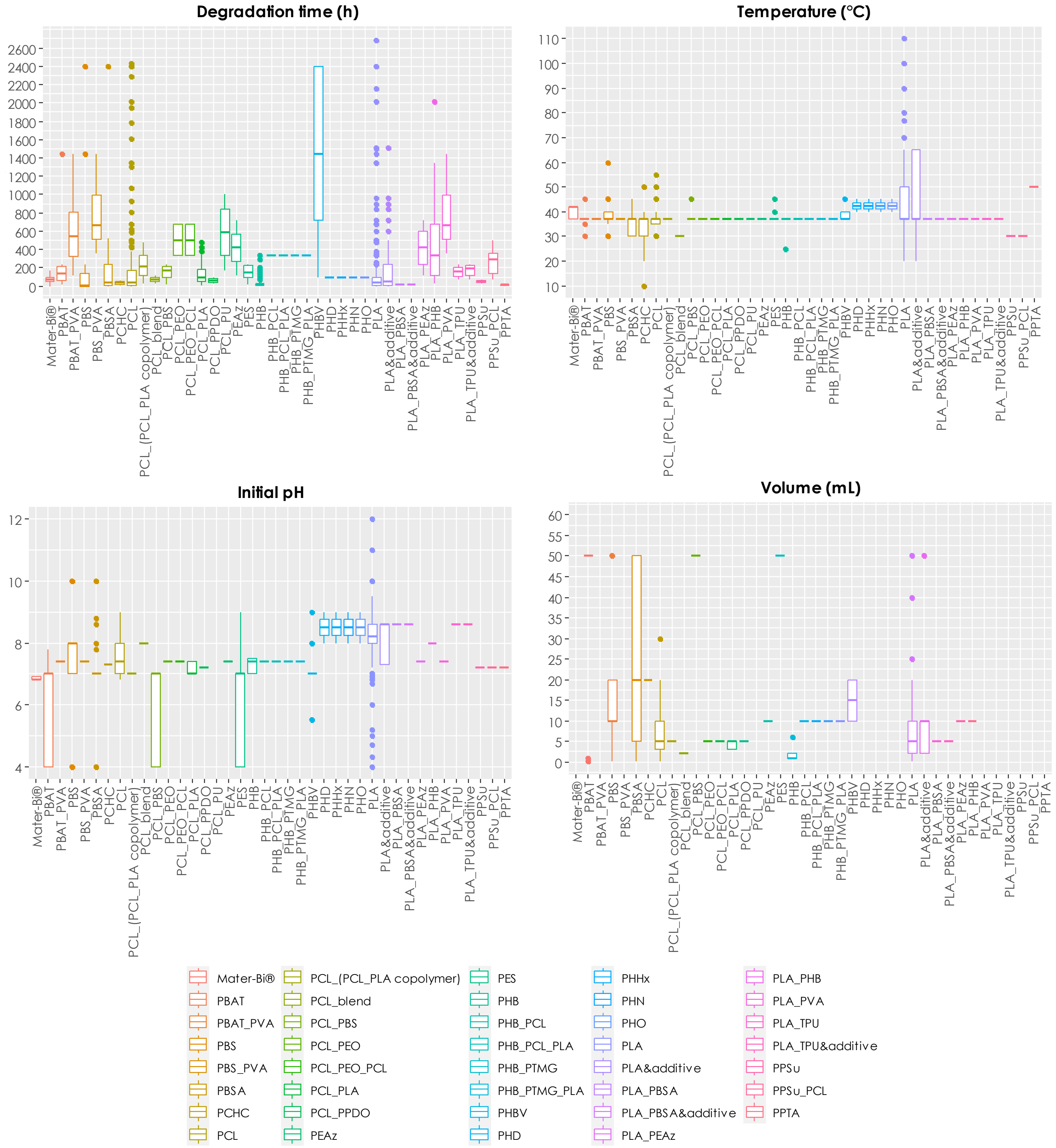

Figure 2. Box plots of the operating conditions (degradation time, temperature, initial pH and working volume) of the enzymatic degradation tests by polymer type (note: due to scale adjustment, the maximum working volume recorded for PCL [2000 mL] and PLA [3500 mL] are not visible in the plot)

Other attempts at categorizing the dataset were made by reporting the combinations of biopolymer type and related physical form, enzyme type adopted and nature of buffer/solvent solution used in the tests, as depicted in Figure 3 in the form of Sankey diagrams for the main polymers identified in Table 2.

In most cases the polymer form adopted during the enzymatic degradation experiments was obtained by the application of a variety of preliminary physical, chemical and thermal processes, alone or in mutual combination (see Table 3). Figure 3 shows that the biopolymers were mostly tested, as a result of the pre-treatments applied, as films as the typical material form that displays a surface area suitable to promote adequate surface erosion of the material; for PLA and other PLA blends/mixtures, a significant number of samples was also found to be investigated both in the powder form and as emulsion in appropriate solutions. As far as the type of enzyme used for the degradation experiments was concerned, inspection of Figure 3 reveals that lipase was applied to a wide array of polymers, while other enzymes were adopted for a smaller range of applications. More specifically, cutinase was most commonly used for degrading PLA and PBS, proteinase K was the prevalent enzyme used for PLA and, to a much lesser extent, PBSA degradation, while protease was tested predominantly on PLA-based polymers.

Table 3. Types of processing methods reported in the literature and related number of datapoints retrieved

BP processing method	no. observations
None/unspecified	788
Thermomechanical compaction (hot/cold pressing)	464
Casting/Film formation	365
Thermal moulding and post-treatments (quenching, ageing, crystallization, stretching)	279
Emulsification	355
Physical processing (sonication, hydrolysis, drying, size reduction, ageing)	165
Extrusion/continuous forming (electrospinning, fiber alignment, fiber drawing, spin coating)	96
Emulsification + Casting/Film formation (melting, quenching)	56
dissolution + casting + drying	30
Physical processing + Emulsification	18
Physical processing	16
drying + hot pressing	8
Annealing	7
Thermomechanical compaction + Emulsification	1

In most cases, the enzymatic degradation experiments were run at fixed pH conditions, requiring the use of specific buffer solutions in the reaction system. The pH of the system is known as an important parameter for enzyme-based depolymerization of bioplastics, as pH dictates the ionization state of the enzyme's catalytic triad and the polymer surface charge. More specifically, pH fluctuations modulate the protonation of functional groups within the active sites of the polymer and affect properties such as solubility, directly influencing the enzyme-substrate binding affinity and the subsequent hydrolysis of ester bonds (Jendrossek and Handrick, 2002); on the other hand, the accumulation of acidic degradation products (e.g. lactic acid from PLA) can trigger a pH drop, potentially leading to partial unfolding or irreversible denaturation of the enzyme if no adequate buffer is provided (Cui et al., 2022). For the set of articles analysed in the present study, Tris-HCl and phosphate buffers by far dominated the range of buffer solutions used in the enzymatic degradation experiments (see Figure 3); in a few cases, such species were also used in combination with other solutions to optimize enzyme attack to the polymers and inhibit potential side effects.

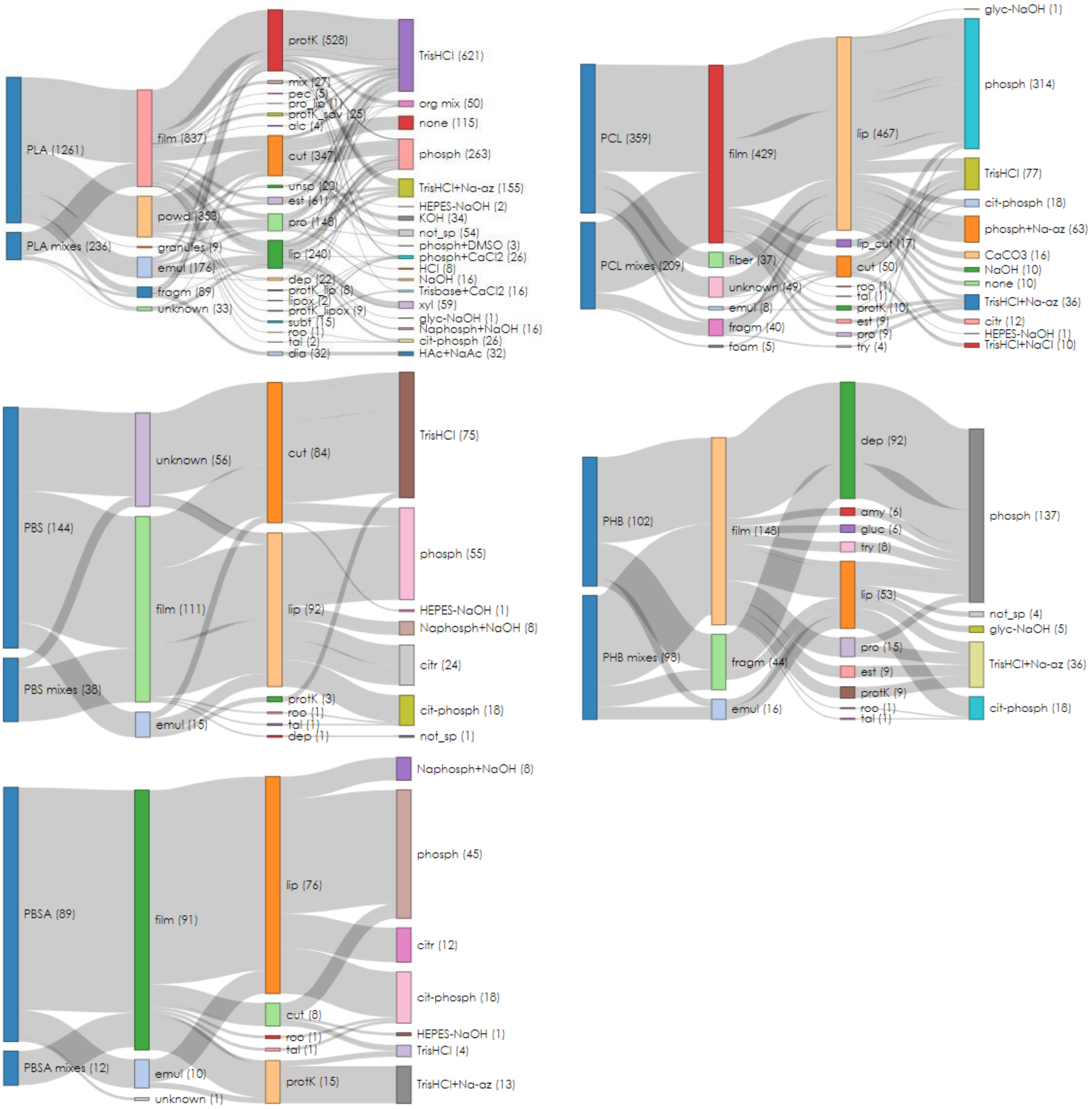

Figure 3. Sankey diagram of the combinations of materials tested grouped by biopolymer type (number of individual datapoints in brackets)

Another feature taken for data analysis involved the type of analytical methods used to detect and measure the effect of enzymatic degradation. In general, it was found that the outcomes of enzyme-based degradation were estimated both from the viewpoint of biopolymer properties changes and from that of the degradation products formed. As illustrated in Table 4, a total of eight classes of analytical methods were identified, including mass loss, analysis of monomers and oligomers formation, molecular weight changes, crystallinity changes, morphological surface characteristics, chemical structure and other miscellaneous techniques. Overall, 31% of the papers adopted mass loss as the main characterization technique, while morphological and monomers analyses accounted for 19% and 12% of the cases. Most commonly, a single analytical method (28% of articles) was adopted for the characterization of process effects, while manuscripts using the combination of two or three techniques accounted for, respectively, 23% and 21% of the total number of papers analysed. Mass loss and monomers analysis were adopted in 41% and 26% of the cases in which a single analytical method was employed. When a combination of two analytical techniques was used, the most common methods included again mass loss (83%) along with morphological analyses (44%). In the case of three analytical methods used, mass loss was found to dominate the range of cases (95%) and was mostly combined with morphological analyses (76%) and measurements of crystallinity changes (28%).

Table 4. Number of manuscripts using different analytical techniques to assess the effects of enzymatic degradation

	no. of combined analytical methods adopted					
Analytical method	**1**	**2**	**3**	**4**	**5**	**6**
Mass loss	11	19	20	15	3	1
Analysis of monomers (1)	7	5	7	5	2	1
Analysis of oligomers (2)	4	5	5	4	1	1
Molecular weight changes (3)	1	1	3	5	0	1
Crystallinity changes (4)	0	2	7	8	2	0
Microscopic characterization (5)	0	10	17	11	3	1
Chemical structure changes (6)	0	2	3	8	2	0
Other (7)	4	2	1	8	2	1
Total	**27**	**46**	**63**	**64**	**15**	**6**

(1) HPLC, lactic acid enzymatic assay, thin-layer chromatography, NMR + MS, GPC, lactate biosensor, spectrophotometric measure, CZE, MALDI-TOF MS

(2) NMR + MS, CZE, DOC, GPC, HPLC, MALDI-TOF-MS, turbidity

(3) GPC, SEC

(4) DSC, FTIR, TGA, WAXD, WAXS, XRD

(5) Reflected light microscopy, SEM, 3D optical profilometry, AFM

(6) DSC, FTIR, NMR, XRD

(7) AFM, FTIR, DSC, UV-VIS spectroscopy, NMR, MS, mechanical strength, TGA, water absorption, water contact angle, turbidity

As far as the assessment of the enzymatic treatment effects was concerned, the only variables for which a significant number of datapoints was available included mass loss and monomer production (the latter only in the case of PLA). These were therefore selected as the candidate response variables for meta-analysis of the selected literature results, with the aim of providing a quantitative interpretation of the effects of factors governing the enzymatic degradation of bioplastic materials. The observed ranges of measured mass loss values for different combinations of pairs of categorical variables are reported in Figure 4 in terms of heat maps of values and related number of observations. Inspection of the experimental data revealed a large variability of the results of enzymatic degradation depending on the biopolymer properties, the specific treatment conditions adopted and most likely other hidden factors that were not fully documented in the analysed documents.

The results of the statistical analysis of mass loss conducted using recursive partitioning are reported in Figure 5 for PLA and PCL as examples. In summary, the results of the analysis show that the most influential factors on mass loss included enzyme type, pH and treatment duration. For PLA, the combination of operating conditions the yielded the largest degree of enzymatic degradation (grouped in node 10, average mass loss = 93.3%) was: enzyme type = (enzyme mix, protease, proteinase K + savinase), $pH > 8$, $T \leq 37$ °C. For PCL the highest mass loss (detected in node 3) was 58.7% and corresponded to the combination $pH \leq 7.2$ and degradation time ≤ 480 h.

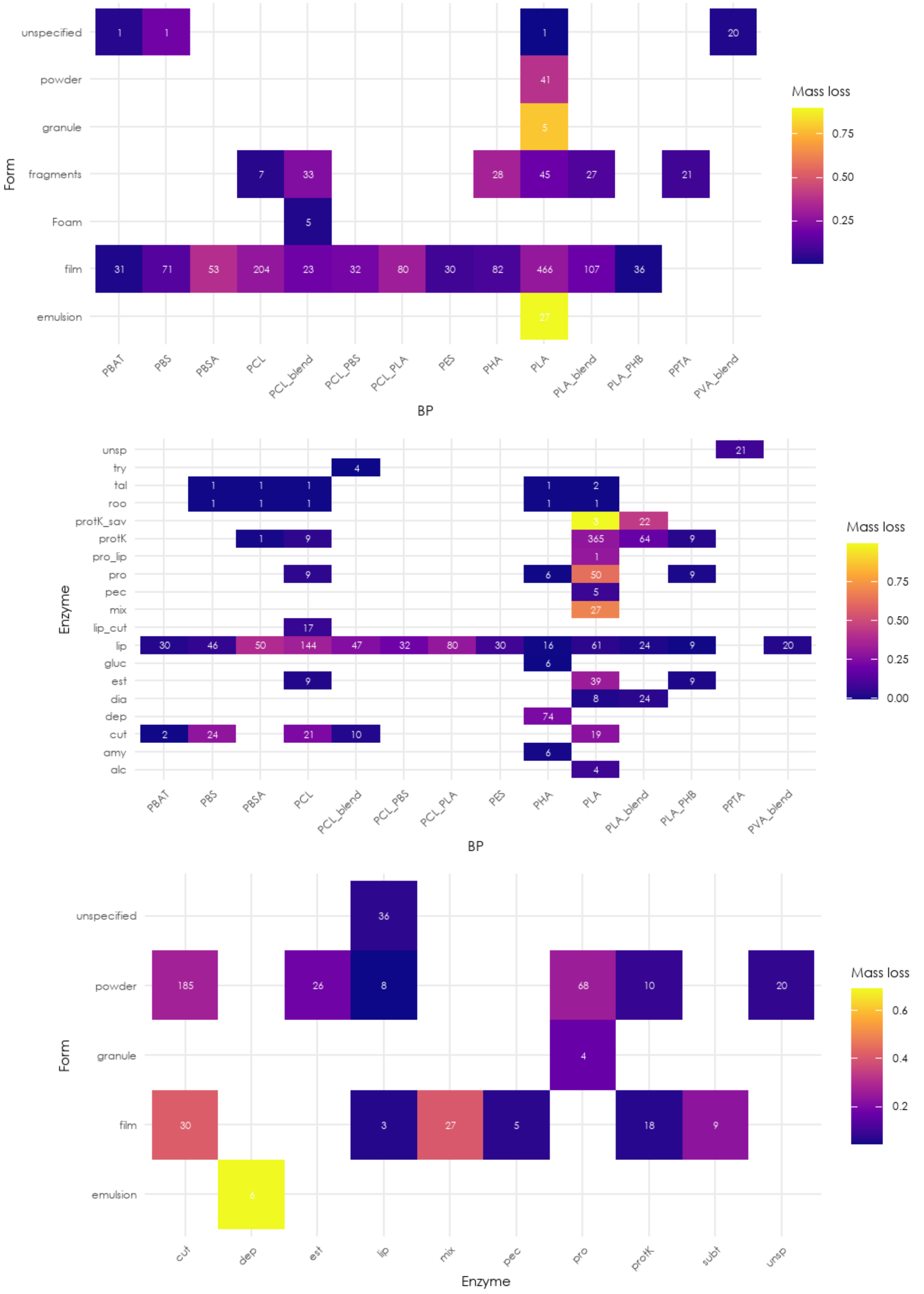

Figure 4. Heat maps for mass loss as a function of BP type, BP form and enzyme type (colours denote the average mass loss for each pair of variables, while numeric values indicate the corresponding number of observations)

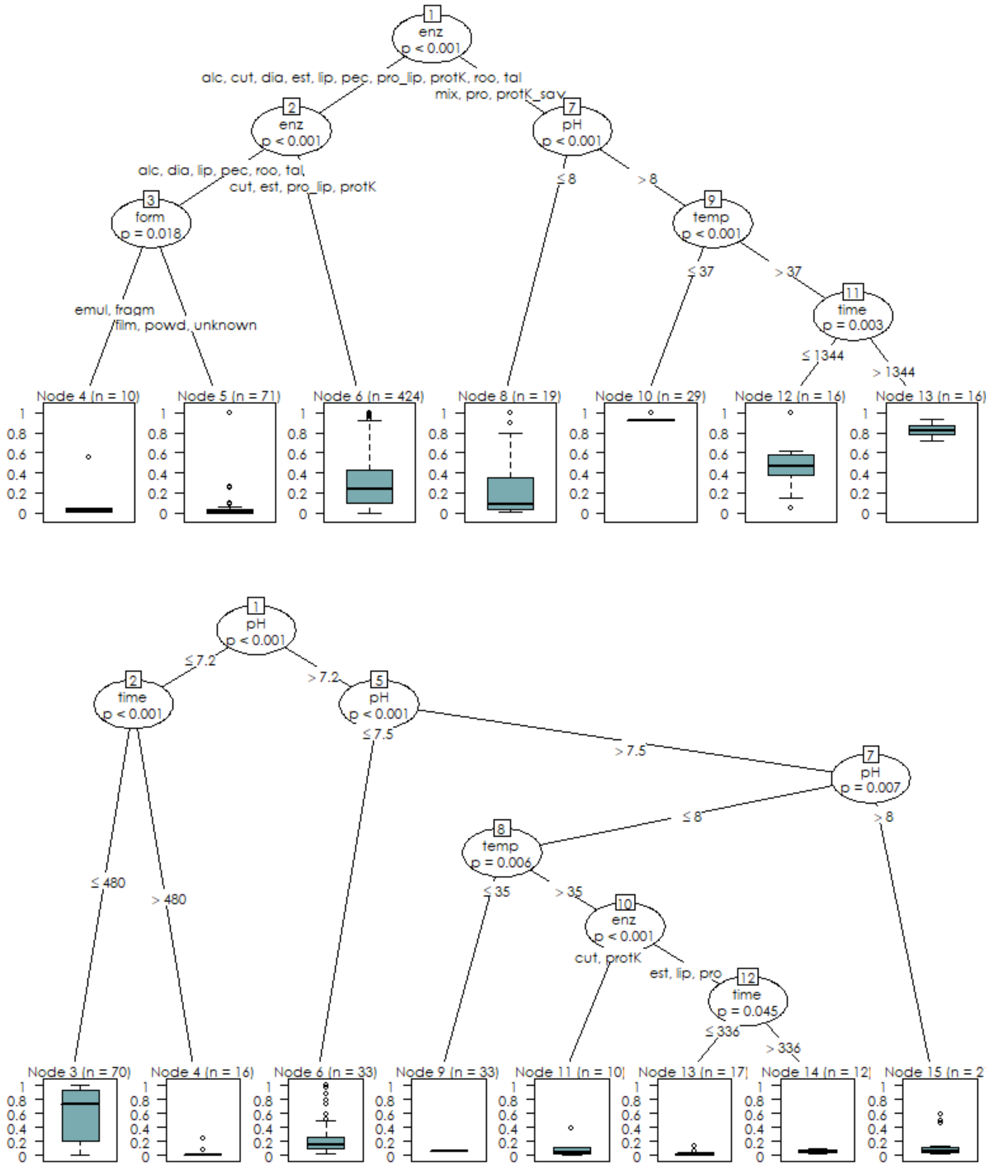

Figure 5. Regression trees obtained from recursive partitioning of mass loss data for PLA (top) and PLC (bottom). The number of data points (n) and the statistical distribution of mass loss (indicated by the associated box plots) are shown for each terminal node, while the average mass loss is provided at each splitting point. All values are reported as fractions of the initial mass.

4.12.3.2 Main results of the experimental investigation

Thermophilic tests were found to have reached completion after 38-55 days. Biogas evolution in co-digestion clearly showed two separate degradation stages (Figure 6), of which the first one was ascribed to readily biodegradable constituents of FW, while the second phase may include the bioplastic contribution to biogas generation. This was in accordance with mono-digestion tests, where bioplastics show a lag time of about 10 days (data not shown). The biogas yield and kinetics were found to be strictly dependent on the polymeric matrix. However, variations of the F/M ratio did not influence substrate degradation. Synthetic food waste degradation was not affected by bioplastic presence.

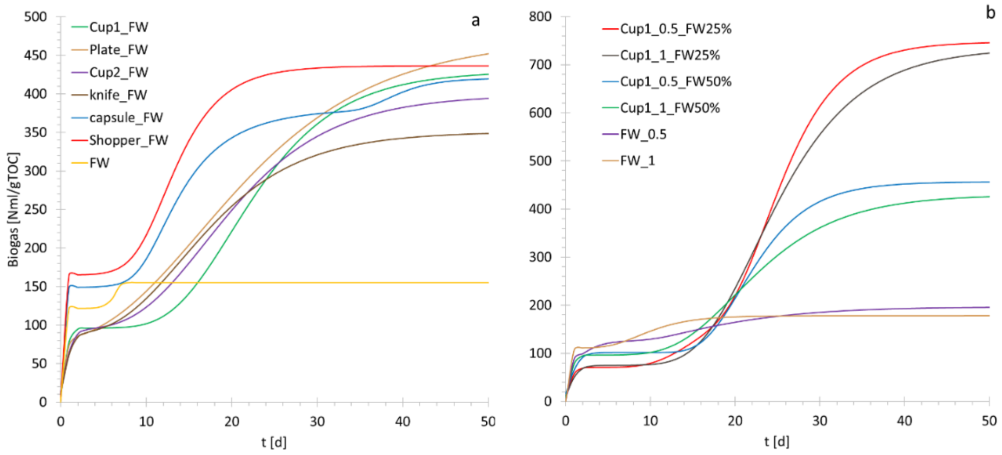

Figure 6. The figure shows the biogas evolution in terms of Nml/gTOC where gTOC refers to the sum of the organic carbon content associated with bioplastics and synthetic FW. The figure on the left (a) shows the biogas evolution of the tests F/M = 0.5 gVSsubstrate/gVSinoculum and FW at 50%; the figure on the right (b) shows the biogas evolution for the tests on Cup1 at varying F/M (0.5 and 1) and FW percentages (25%, 50% and 100%).

A review of the literature on the enzymatic degradation of bioplastics reveals a pronounced lack of harmonization among existing test methodologies. Overall, lipases are the most extensively studied enzymes, and polylactic acid (PLA) is the most frequently examined biopolymer. However, the limited availability of comparable datasets, combined with the high variability and inconsistency of reported results, precludes drawing robust correlations or generalizable conclusions.

Results from anaerobic digestion of cup1 after enzymatic pre-treatment show limited effects on biogas yield and kinetics (see Figure 7).

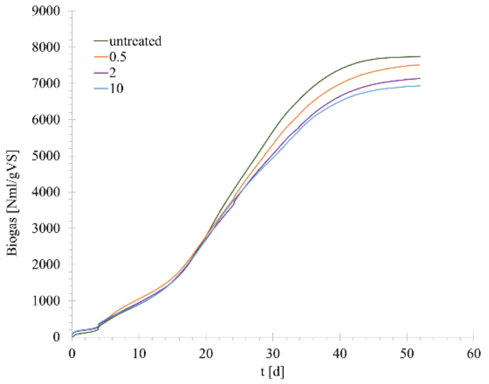

Figure 7. Biogas evolution of tests on cup1 after enzymatic pre-treatment with lipase at different concentrations (0.5, 2 and 10 mg/ml). The curves refer to the data collected during the anaerobic degradation process with digestate at 55 °C. Untreated Cup1 was also digested for comparison.

The biogas evolution measured during anaerobic digestion tests with the addition of lipase is shown in Figure 8. The presence of lipase appeared to accelerate the process kinetics in the very first moment of the test ($t < 5$ d). However, a decrease in process kinetics was observed with increasing concentrations of lipase for all tested products. No significant effects were observed concerning the final biogas yield. In general, a negative synergy between digestate and lipase was observed.

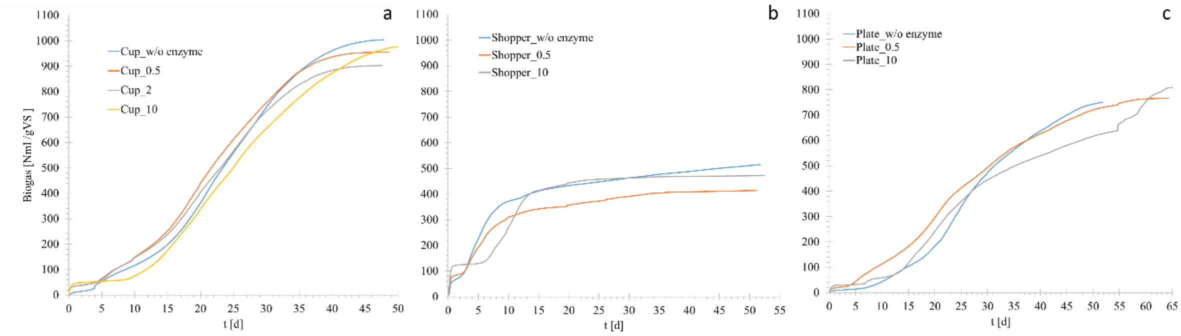

Figure 8. Biogas evolution of anaerobic digestion tests with lipase on Cup1, SH and PL. Lipase was mixed with digestate at different concentrations (0.5, 2 and 10 mg/ml). Biogas evolution measured during anaerobic digestion tests on the bioplastic items without lipase is also shown for comparison.

4.12.4 Main outcomes and implications

- A large database was built that contained the results from 92 experimental studies on various combinations of biopolymers and enzymes under a range of testing conditions
- Different data categorization, representation and interpretation tools were used to provide a thorough and in-depth analysis of extracted data
- A number of clusters and trends in the collected data from literature search were isolated, which are deemed to be useful for the purpose of identifying the most appropriate conditions to maximize the degree of bioplastic degradation through enzyme-based treatment
- Bioplastics can be co-treated with OFMSW, but operational uncertainties remain. Bioplastics can be co-treated with OFMSW without compromising food-waste degradation, but incomplete breakdown and the risk of micro-bioplastic formation introduce operational and environmental uncertainties.
- Polymer-dependent degradability: Anaerobic degradation performance varies mainly with polymer composition (PLA, PBS, PBAT), while changes in F/M ratio exert minimal influence, underscoring material chemistry as the key determinant of bioplastic behavior.
- Limited benefits of enzymatic treatments: Neither enzymatic pre-treatment nor lipase addition during digestion substantially improved biogas yield, and higher enzyme doses even reduced process kinetics, indicating limited applicability of such strategies in full-scale systems.
- Inconsistent knowledge base: The literature on enzymatic bioplastic degradation remains fragmented, with poorly harmonized methodologies and scattered results that hinder reliable interpretation and comparison.
- Improved understanding of degradation mechanisms is essential for full-scale implementation. To support the integration of bioplastics into existing organic waste treatment infrastructures, further research is required to clarify degradation pathways, optimize process conditions, and evaluate the long-term fate of residual fragments. Harmonized testing frameworks are needed to allow reliable comparison among studies and guide technological adjustments in full-scale facilities.

4.12.5 Scientific products and dissemination

Publications:

Journals

Falzarano M., Polettini A., Pomi R., Rossi A., Zonfa T., Bracciale M.P., Gabrielli S., Sarasini F., Tirillò J. (2025). Anaerobic Biodegradation of Polylactic Acid-Based Items: A Specific Focus on Disposable Tableware Products, *Materials* **18**(5), paper no. 1186. https://doi.org/10.3390/ma18051186.

Conference Proceedings

Falzarano M., Polettini A., Pomi R., Rossi A., Zonfa T. (2024). Assessing the microbial and enzymatic degradation of bioplastic products, In: Proc. *SIDISA 2024, 12th International Symposium on Environmental Engineering*, Palermo (IT), 1-4 October 2024.

Dissemination

Olscher C., Falzarano M., Polettini A., Zafiu C., Part F. (2025). Circular plastics and advanced composites: stakeholder workshop on circular business models, In: Proc. *Sardinia 2025, Twentieth International Symposium on Waste Management, Resource Recovery and Sustainable Landfilling*, S. Margherita di Pula (IT), 13-17 October 2025, paper F04(1), ISBN: 9788862650472, ISSN: 2282-0027.

4.12.6 Electronic annex: database of literature results on enzymatic degradation of bioplastics:

Database available at the link:

https://docs.google.com/spreadsheets/d/1vPttemPpF7069DVqpxpiN3CuYQcfmRTb/edit?usp=sharing&ouid=117195305257319988835&rtpof=true&sd=true

(password-protected file; password to be requested to alessandra.polettini@uniroma1.it)

4.13 Bioplastics degradation under anaerobic conditions (UNIFI)

Contributors: Claudio Lubello, Pietro Pelleschi (DICEA, University of Florence)

4.13.1 Introduction

The global dependence on conventional petroleum-based plastics has created an **enormous environmental burden**, characterized by persistent accumulation in landfills and natural ecosystems, leading to soil and water pollution, and the formation of microplastics [1, 2]. Consequently, there is an urgent need for sustainable alternatives. **Bioplastics** are a promising class of materials developed to address this issue.

Bioplastics are defined based on one or both of the following criteria: their origin (derived wholly or partially from **renewable biomass** sources like starch, cellulose, or vegetable oils) and/or their end-of-life characteristics (their capacity for **biodegradation**) [3]. This category is diverse and includes materials like:

- **Bio-based non-biodegradable plastics:** Such as bio-polyethylene (Bio-PE) or bio-polyethylene terephthalate (Bio-PET), which are chemically identical to their fossil counterparts but derived from biological feedstock.
- **Bio-based and biodegradable plastics:** The most relevant group for waste management, including **Polylactic Acid (PLA)** and **Polyhydroxyalkanoates (PHAs)**.
- **Fossil-based biodegradable plastics:** Such as Polybutylene Adipate Terephthalate (PBAT) [4].

The primary appeal of biodegradable bioplastics lies in their potential to be converted into benign end-products, such as CO_2**, water, and biomass**, through microbial action in specific environments, offering a path toward a circular economy [5].

Biodegradation is a naturally occurring process where microorganisms (bacteria, fungi, and algae) consume and break down complex organic materials into simpler substances. This process is highly dependent on the surrounding **environmental conditions**, particularly the presence of oxygen.

- **Aerobic Biodegradation:** Occurs in the presence of oxygen, resulting in CO_2 , water, and new biomass. This is typical in composting.
- **Anaerobic Biodegradation:** Occurs in the absence of oxygen, resulting in **biogas** (a mixture of CH_4 and CO_2), water, and new biomass.

The rate and extent of bioplastic biodegradation are determined by the **material's chemistry** (e.g., molecular weight, crystallinity, and hydrophilicity) and the **activity of the microbial community** [5].

While some bioplastics, like **PHAs**, have shown excellent anaerobic biodegradability, converting rapidly and with high methane yield comparable to organic standards [9], others present challenges:

- **PLA:** Due to its high melting point and crystallinity, PLA typically requires **thermophilic conditions** (temperatures >50 °C) to hydrolyze effectively within the typical retention times of AD plants. At mesophilic temperatures (around 35 °C), its degradation rate is often too slow for practical application [10].
- **PBAT and PCL:** These materials exhibit good biodegradability under both aerobic and anaerobic conditions, though degradation rates vary significantly based on the specific AD inoculum [11].

Research efforts are focused on improving the anaerobic degradability of bioplastics through material modification (e.g., lower molecular weight, blending) and by optimizing AD process parameters (e.g., temperature, microbial selection, pre-treatment) to maximize sustainable waste management [1, 7].

In this chapter, the results of the biodegradability of certain commercial products composed of bioplastics are described, in comparison with organic substrates that are typically biodegradable under anaerobic conditions in solid waste treatment plants. The aim is to highlight differences in behavior and to assess the actual feasibility of directing bioplastics collected through conventional separate collection systems to anaerobic digestion.

4.13.2 Materials and Methods

The instrument used for the anaerobic tests is the Ritter Biogas Batch Fermentation System.

It is composed of an air-heated oven inside which 18 reactors of 1 L each are placed, which are thus maintained at the chosen temperature for the test (up to a maximum of 52 °C). The configuration makes it possible to easily extract the reactors from the oven for visual checks during the test, without compromising the process.

Each reactor is equipped with a motor which, connected to a stirring blade, allows the mixing of the material according to the indicated stirring speed. The gas produced flows through a conduit towards the measurement system.

The measurement of biogas production takes place through the MilliGascounters, which are directly connected to each of the reactors. The internal operation is based on an oscillating chamber mechanism (double chamber) combined with a packing liquid: the gas, which reaches the base of the device, forms bubbles that rise through the packing liquid and collect in the measuring chamber, which actually has two alternative compartments. When one compartment is completely filled with gas, the hydrostatic thrust causes it to tilt, discharging the excess gas and causing the other compartment to begin filling. Each tilting event generates an electrical impulse recorded by the digital counting unit. The measured gas volume is derived from these impulses: each impulse corresponds to a known volume of the compartment (the volumetric calibration is different for each instrument, which is individually calibrated).

In order to have a direct measurement of the biomethane produced, it is possible to install CO_2 traps.

Data acquisition is automated through the RIGAMO software, which allows for the real-time recording of the gas volume and flow rate produced, with the possibility of later exporting the data.

4.13.2.1 Sample Preparation

For these tests, the inoculum used was the digestate from the FORSU treatment plant at Casa Sartori (Montespertoli, FI). At the time of sampling, the digesters were operating at a temperature of 48.7 °C, while the HRT (Hydraulic Retention Time) of the plant was between 21–28 days, thus simulating actual operating conditions. Tests were carried out over a duration of 28 days under thermophilic conditions (52 °C).

In the laboratory, the measurement of Total Solids (TS) in the digestate was performed by heating in an oven at 105 °C for 24 h. From the three samples analyzed, an average value of TS = 16.29 % was obtained.

After characterization of the inoculum, the preparation of the samples was carried out. For these tests, different types of bioplastics and food waste were used, specifically:

- Bioplastic bag (film)
- Bioplastic cutlery (rigid)
- Paper cup with plastic lamination
- Fruit peels (apple and orange), both whole and chopped into small pieces

The experimental scheme involved, in addition to one reactor for each sample analyzed, a reactor loaded only with digestate (blank), and one with cellulose in the form of filter paper discs together with digestate (positive control).

Each 1 L reactor was filled with 650 mL of digestate (corresponding to 60–70 % of the volume), with a solids content of approximately 105 g. ISO standards suggest working with a ratio of 1/2 or 1/4 between the substrate and the amount of TS in the digestate:

- For the FORSU samples, in the form of fruit peels, a ratio of about 1/4 was used, by adding approximately 25 g of sample to the reactor.
- For the other materials analyzed, considering their actual presence in organic waste, this value would be too high. Therefore, approximately 3.5 g of material was added, corresponding to a ratio of about 1/30.

Table of samples used:

Digester	Sample	Weight [g]	TS [%]	TS [g]	VS/TS [%]	VS [g]
D_2	blank	0	0%	0.00	0%	0.00
D_6	cellulose	3.64	95%	3.46	95%	3.29
D_10	bag	3.58	100%	3.58	80%	2.86
D_11	cup	3.59	100%	3.59	70%	2.39
D_13	cutlery	3.57	100%	3.57	75%	2.68
D_15	whole peels	26.42	20%	5.28	90%	4.76
D_17	chopped peels	26.28	20%	5.26	90%	4.73

4.13.3 Results and Discussion

The following graphs show, both in terms of cumulative values and relative to TS, the amount of biogas produced after 28 days for each of the samples. The net biogas produced by the various samples is obtained by subtracting the biogas produced by the reactor filled only with digestate.

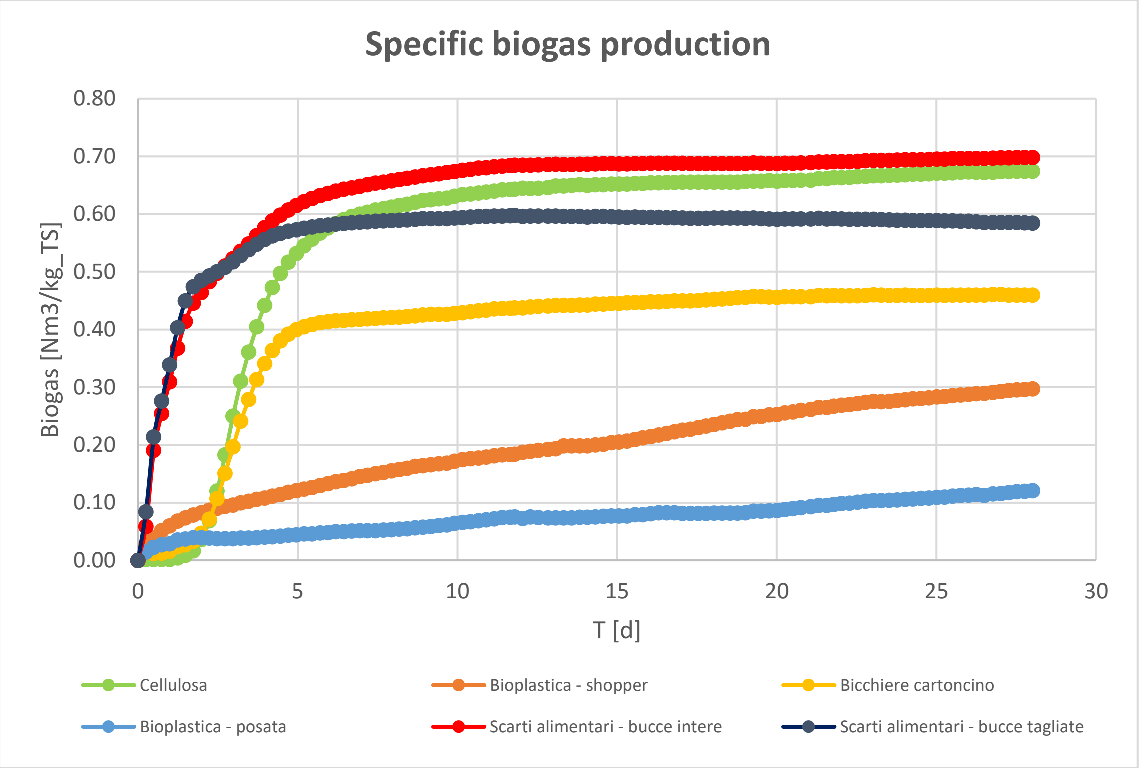

The results obtained show the different behavior of the materials analyzed during anaerobic digestion:

- Simple substrates such as fruit are rapidly degraded by microorganisms (in this case, the different particle size of the material does not influence the process, leading instead to results that are contrary to expectations).
- Cellulose is also completely degraded during the test; however, it can be observed that the kinetics are different, and biogas production begins only a few days after the start of the test.
- A similar behavior is shown by the paper cup, which nevertheless produces a smaller amount of biogas.
- Bioplastics, on the other hand, show a much slower degradation, failing to reach the plateau within 28 days. Moreover, the behavior varies depending on the type of bioplastic: rigid bioplastic produces less biogas (and therefore undergoes less degradation) compared to film bioplastic.

By recovering and weighing the residues of the samples at the end of the test, it is possible—given the initial weight inserted—to estimate the degradation of the different substrates during the experiment. The residue analysis shows that no cellulose or fruit peel residues (of either type) were present, indicating complete degradation. The other samples display varying degrees of degradation, as can be observed in the following photos.

Bioplastic bag

Bioplastic cutlery

Paper cup with plastic lamination

In the following table, the degradation values obtained are reported:

Digester	Sample	Initial weight [g]	Final weight [g]	Degradation [%]
D_2	blank	0	0	-
D_6	cellulose	3.64	0	100%
D_10	bag	3.58	2.23	27%
D_11	cup	3.59	0.27	93%
D_13	bioplastic cutlery	3.57	3.24	9%
D_15	whole peels	26.42	0	100%
D_17	chopped peels	26.28	0	100%

4.13.4 References

[1] Kümmerer, K. (2019). The environmental chemistry of synthetic polymers–a new focus. *Science*, 366(6470), 1198-1199.

[2] Geyer, R., Jambeck, J. R., & Law, K. L. (2017). Production, use, and fate of all plastics ever made. *Science Advances*, 3(7), e1700782.

[3] European Bioplastics. (2020). *Bioplastics facts and figures*.

[4] Hatti-Kaul, R., Nilsson, L., & Zhang, B. (2020). Designing plastics for circular economy: Biodegradation in the open environment. *ACS Sustainable Chemistry & Engineering*, 8(23), 8936-8951.

[5] Emadian, S. M., Onay, T. T., & Demirel, B. (2017). Biodegradation of bioplastics in natural environments. *Waste Management*, 59, 526-536.

[6] De Meester, S., Ragaert, P., & Van Geem, K. M. (2018). The environmental performance of plastics from a lifecycle perspective: A critical review. *Science of The Total Environment*, 640-641, 107-117.

[7] Caldeira, C., De Meester, S., & Govaert, E. (2019). Potential of anaerobic digestion to treat biodegradable plastic waste: A review. *Waste Management*, 97, 18-29.

[8] Appels, L., Van Der Heyden, P., Degrève, J., Van Impe, J., & Dewil, R. (2011). Anaerobic digestion of waste sludge: a review. *Applied Environmental Biotechnology*, 1(2), 1-15.

[9] Koller, M., Chiellini, E., & Braunegg, G. (2013). Anaerobic digestion of polyhydroxyalkanoates. *Polyhydroxyalkanoates: Production, properties and applications*, 141-164.

[10] Rudnik, E. (2019). *Polylactide (PLA): biodegradable polymer for sustainable development*. CRC Press.

[11] Jendrossek, D., & Handrick, R. (2002). Microbial degradation of polyhydroxyalkanoates. *Annual Review of Microbiology*, 56(1), 403-422.

4.14 Identification and classification of micro-bioplastics (MBPs) in anaerobic digestion by SWIR hyperspectral imaging (UNIROMA1)

Contributors: G. Capobianco, E. Gorga, S. Serranti (DICMA); M. Falzarano, A. Polettini (DICEA)

4.14.1 Introduction

The aim of this research was to develop a rapid and efficient analytical strategy capable of identifying residual plastic fragments (i.e., micro-bioplastics - MBPs) within the final product of anaerobic digestion. In line with the European Union Directive (EU) 2019/904, bioplastics (BPs) are gradually replacing fossil-based plastics in several applications, especially in packaging materials and disposable items. The most widely used commercial formulations include blends based on thermoplastic starch (TPS) or polylactic acid (PLA), produced in different variants depending on the specific copolymer or additives used (e.g., polybutylene succinate - PBS, talc - $Mg_3Si_4O_{10}(OH)_2$, etc.). The main strength of biodegradable materials lies in their compatibility with biological end-of-life treatments, such as anaerobic digestion. However, the overall efficiency of their co-digestion with organic waste is still a matter of ongoing research. In particular, large-scale digesters may require technical adaptations to ensure optimal treatment performance and preserve the quality of the final product. A critical concern is the potential formation of degradation byproducts, such as MBPs, during the biodegradation process. These particles can persist in the digestate and potentially enter the environment when the material is applied to soil. Such contamination could pose a risk to plant systems and agricultural productivity, with potential implications for human health through the food chain. Therefore, a rapid methodology that allows for the quality assessment of the final product of anaerobic digestion is essential. However, developing analytical methodologies capable of identifying MBPs in complex organic matrices represents a significant challenge, primarily due to the heterogeneity of these materials and the masking effects of surrounding organic matter. In this context, an efficient analytical strategy based on short-wave infrared hyperspectral imaging (SWIR-HSI: 1000–2500 nm) combined with chemometrics was developed to rapidly and non-destructively identify MBPs deriving from different single-use BP objects within the anaerobic digestate to assess its quality.

4.14.2 Case study description

Four representative everyday BP objects were selected and investigated as representative samples: a coffee capsule (CA), a cup (CU), a plate (PL) and a shopper bag (SH). In particular, CA was composed of polylactic acid (PLA) + polybutylene succinate (PBS) + $Mg_3Si_4O_{10}(OH)_2$, CU was composed of a Mater-Bi® commercial formulation based on PLA + PBS + $Mg_3Si_4O_{10}(OH)_2$, PL was composed by PLA + $CaCO_3$ fillers and SH was composed of a Mater-Bi® commercial formulation based on PLA/thermoplastic starch (TPS) + polybutylene adipate terephthalate (PBAT). Specifically, Mater-Bi® is a brand of biodegradable and compostable BPs developed and produced by Novamont (Terni, Italy), available in different grades that may include TPS and biodegradable polyesters in variable percentages. These BP objects were mechanically ground with a mill and subsequently sieved to obtain two particle size classes: < 0.5 mm and 0.5–1 mm. To simulate real environmental conditions, the anaerobic digestate was sampled from a full-scale digestion plant that treats mixtures of organic residues derived from food industries. This digestate was sieved at 0.84 mm to eliminate coarse fraction. The MBPs were placed onto individual cellulose filters that previously coated with a thin layer of digestate and dried at room temperature. In total, eight different samples were obtained, one for each BP object (CA, CU, PL and SH) and particle size classes (< 0.5 mm and 0.5-1 mm). Before acquiring the hyperspectral images, the cellulose filters were placed between two glass Petri dishes to improve surface uniformity.

4.14.3 Methodologies

4.14.3.1 Analytical methods

The HSI analyses were carried out at the Raw Materials Laboratory (RawMaLab) of the Department of Chemical Engineering, Materials & Environment (DICMA) of Sapienza University of Rome (Rome, Italy). Hyperspectral images of the eight different samples were acquired in the SWIR range (1000-2500 nm) by

Specim SISUChema XL™, equipped with an ImSpector™ N25E imaging spectrograph (Specim Ltd, Finland) using two different configurations for the image acquisitions: a 31 mm lens with a 50 mm field of view (FOV) and a spatial resolution of 150 μm/pixel and a "macro-lens" with a 10 mm of FOV and a spatial resolution of 30 μm/pixel.

4.14.3.2 Modelling approaches

After the acquisition of hyperspectral images, the modelling approaches followed these main phases: preprocessing of spectra to highlight the differences between the various classes of materials, exploratory data analysis through Principal Component Analysis (PCA), development of the classification model using a calibration dataset, application of the classification model to a validation dataset and finally, evaluation of the classification model performance.

Specifically, the acquired hyperspectral images were preprocessed using PLS toolbox (version 9.2; Eigenvector Research, Inc., Wenatchee, WA, USA) and MIA toolbox (version 3.1; Eigenvector Research, Inc., Wenatchee, WA, USA) running in MATLAB® environment (version 9.12 – R2022a, The Mathworks, Inc., Natick, MA, USA). In order to build the classification models, from the hyperspectral images sixteen different portions were selected and assembled into mosaics images, eight for the calibration dataset and eight for the validation dataset (Figure 1).

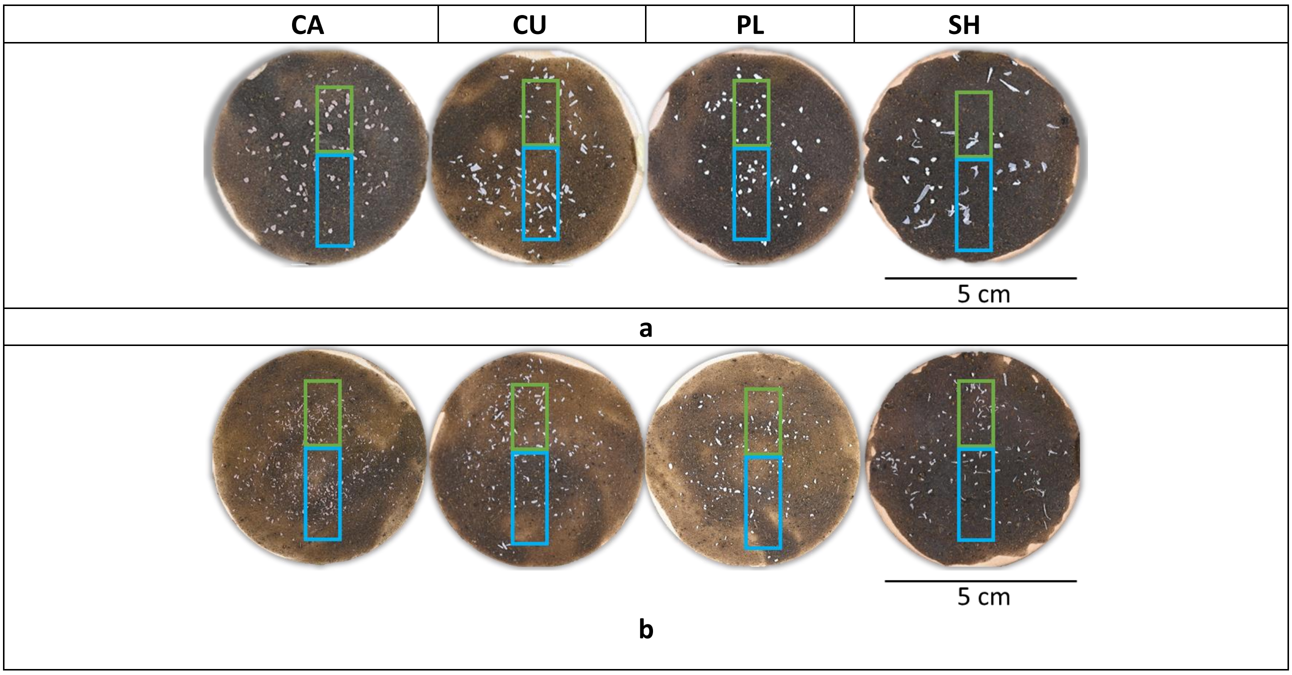

Figure 1. The analyzed samples consisted of cellulose filters with powered MBPs of two different sizes: 0.5-1 mm (a) and < 0.5 mm (b). The green and blue boxes highlighted the portions used to build the calibration and validation datasets, respectively.

Different pre-processing strategies (i.e. Standard Normal Variate (SNV), Gap-Segment Derivative and Mean Center) were selected in order to remove physical phenomena and optimize the recognition of materials. To explore the data, define classes and evaluate the best algorithms for the classification model, a Principal Component Analysis (PCA) was carried out. Starting from the results obtained with the exploratory analysis, a hierarchical classification approach based on Partial Least Squares-Discriminant Analysis (PLS-DA) classification method was adopted for the identification of the 5 selected materials (i.e., digestate matrix and four different MBPs type). Finally, the classification performances of the developed classification model were evaluated using a pixel-based approach. For this purpose, sensitivity and specificity performance metrics were used. More in detail, sensitivity describes the model's capability to correctly identify classes and specificity describes the model's capability to correctly reject classes. Both sensitivity and specificity range from 0 to 1, with a value of 1 indicating perfect predictive performance.

4.14.4 Results

The average raw reflectance spectra obtained by SWIR-HSI are reported in Figure 2 and show the different spectral trends of the 5 studied classes (i.e., matrix, CA, CU, PL and SH).

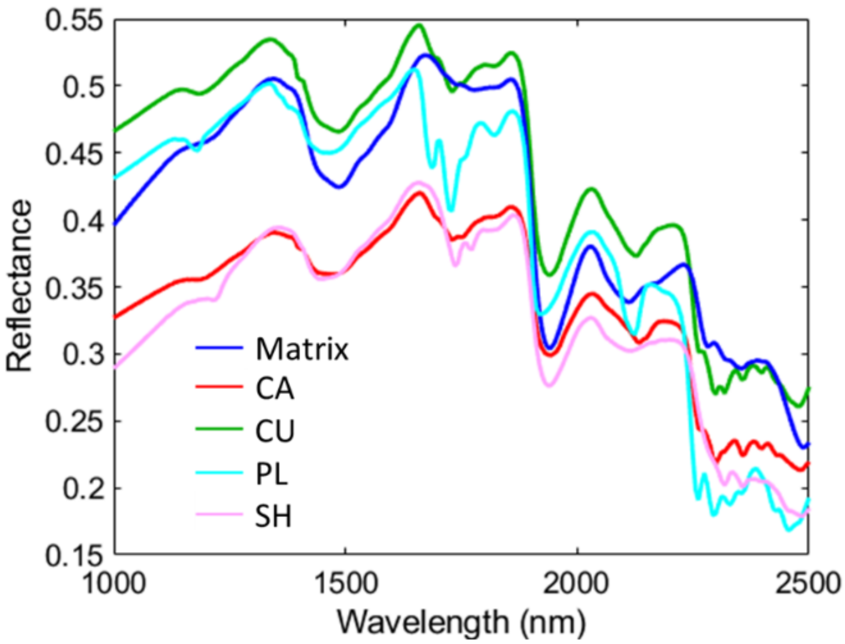

Figure 2. Average raw reflectance spectra of the 5 studied classes (i.e., matrix, CA, CU, PL and SH) acquired in the SWIR range.

Starting from the spectra preprocessing and PCA results, a 5-class classification model based on 4 PLS-DA rules was developed and structured as illustrated in Figure 3.

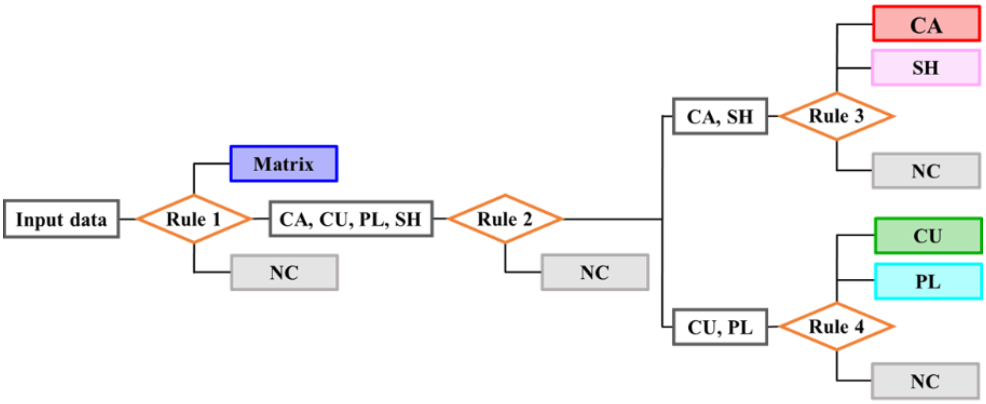

Figure 3: Dendrogram of the hierarchical classification model based on 4 PLS-DA rules. For each rule, the different outputs are shown as matrix, CA, CU, PL, SH and NC (Not Classified).

The performance in calibration and cross-validation phases shows satisfactory results with values from 0.96 to 1.00 for specificity and values from 0.91 to 1.00 for sensitivity. These results consistently demonstrate reliable discrimination between the digestate matrix and the different MBP classes.
Subsequently, the Hi-PLS-DA model was applied to a validation dataset acquired at 150 µm/pixel and 30 µm/pixel spatial resolution to define both the capabilities and limitations of the two different configurations in relation to the two particle size classes (< 0.5 mm and 0.5–1 mm). The classification results show an overall good correspondence between the source RGB images and the corresponding false-color prediction maps (Figure 4). However, the prediction maps show few local variations associated with spatial detection limits, spectral interference related to transparency, matrix variability due to heterogeneous digestate composition and edge effects caused by spectral mixing at the borders of the MBPs.

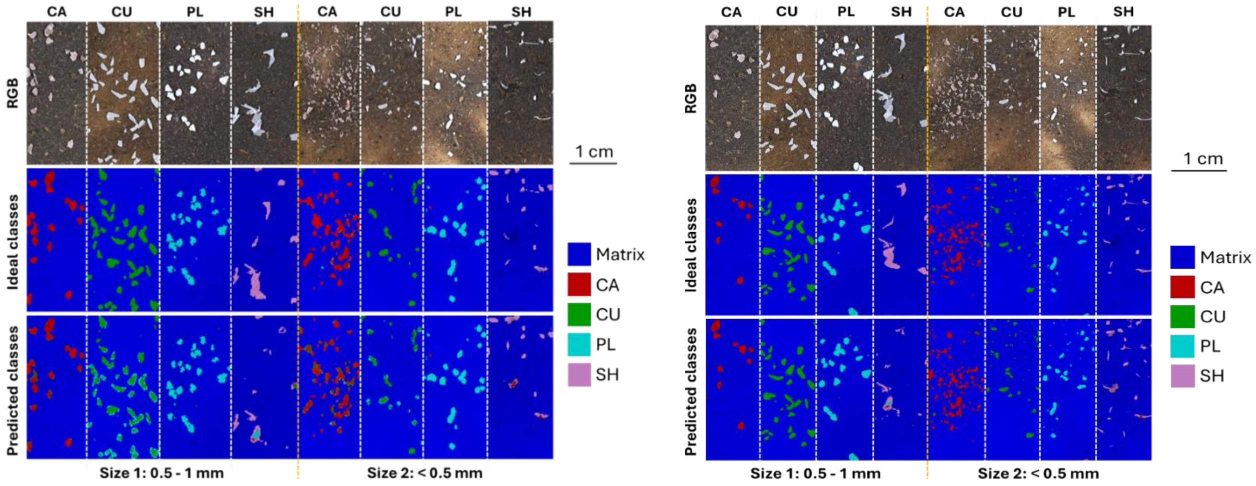

a **b**

Figure 4: Comparison between the source RGB images and the ideal and predicted hyperspectral false-color maps of the validation dataset acquired at 150 µm/pixel (a) and 30 µm/pixel (b) resolution.

The performance parameters in prediction phase confirm the optimal classification capability with sensitivity ranging from 0.92 to 1.00 and specificity from 0.83 to 1.00. Comparing the false-color hyperspectral maps of the validation dataset acquired at 150 µm/pixel (Figure 4a) and 30 µm/pixel (Figure 4b) resolutions, it is evident that the higher spatial resolution (30 µm/pixel) reduces boundary artifacts and improves the detection of MBP particles belonging to size 2 (< 0.5 mm). However, the Hi-PLS-DA model remains sufficiently powerful to provide reliable qualitative monitoring even at the lower spatial resolution (150 µm/pixel). In conclusion, the results confirm the robustness and reliability of the proposed SWIR-HSI strategy coupled with Hi-PLS-DA classification model. Overall, the results obtained demonstrate not only accurate detection of MBPs presence within the complex digestate matrix but also the model's capability to discriminate among different BP polymer types.

4.14.5 Scientific products and dissemination

Publications:

Capobianco G., Cucuzza P., Gorga E., Falzarano M., Bonifazi G., Pomi R., Polettini A., Serranti S. - Development of a hyperspectral imaging-based strategy for detecting micro-bioplastics in anaerobic digestate (*Manuscript submitted to Spectrochimica Acta, Part A: Molecular and Biomolecular Spectroscopy*).

Serranti, S., Capobianco, G., Cucuzza, P., & Bonifazi, G. (2024). Efficient microplastic identification by hyperspectral imaging: A comparative study of spatial resolutions, spectral ranges and classification models to define an optimal analytical protocol. *Science of the Total Environment*, *954*, 176630. https://doi.org/10.1016/j.scitotenv.2024.176630

Conference proceedings indexed in Scopus:

Capobianco, G., Falzarano, M., Bonifazi, G., Polettini, A., Pomi, R., Rossi, A., & Serranti, S. (2024). Characterization of disposable Mater-Bi® bioplastic by hyperspectral imaging for anaerobic biodegradation monitoring. In *Algorithms, Technologies, and Applications for Multispectral and Hyperspectral Imaging XXX* (Vol. 13031, pp. 207-213). SPIE. https://doi.org/10.1117/12.3014862 SPIE Defense + Commercial Sensing Conference (21-25 April 2024, National Harbor, Maryland, United States).

Presentations at International Conferences:

Gorga E., Capobianco G., Cucuzza P., Falzarano M., Bonifazi G., Polettini A., Pomi R., Serranti S. - Application of Hyperspectral Imaging and Chemometric Techniques for the Identification of Micro-Bioplastics During Anaerobic Biodegradation – CSI25: Colloquium Spectroscopicum Internationale (27-31 July 2025, Ulm, Germany).

Gorga E., Serranti S., Capobianco G., Bonifazi G. - Identification and Classification of Microplastics by a Micro-Hyperspectral Imaging Scanner Prototype - NIR2025: 22nd International Conference on Near Infrared Spectroscopy (8-12 June 2025, Rome, Italy).

Dissemination:

Capobianco G., Falzarano M., Bonifazi G., Gorga E., Polettini A., Pomi R., Rossi A., Serranti S. - Hyperspectral imaging to monitor anaerobic degradation of bioplastic products - RETURN Dissemination Workshop (19-21 June 2024, Bari, Italy)

Capobianco G., Falzarano M., Bonifazi G., Polettini A., Pomi R., Rossi A., Serranti S. - Classification of Mater-Bi® bioplastics in anaerobic sludge by SWIR hyperspectral imaging - RETURN Dissemination Workshop (1-2 February 2024, Turin, Italy)

Falzarano M., Capobianco G., Bonifazi G., Bracciale M.P., Polettini A., Pomi R., Rossi A., Sarasini F., Serranti S., Tirillò J., Zonfa T., Metodologie per la valutazione della biodegradabilità di prodotti in bioplastica, Workshop SHARESCIENCE2024, Sapienza University of Rome, 15-16 February 2024.

Gorga E., Bonifazi G., Capobianco G., Cocozza P., Serranti S. - Development of spectral sensing methodologies for monitoring and rapid identification and classification of macro- and microplastics dispersed in terrestrial and marine environments – RETURN Spoke VS4 Plenary Meeting (30-31 October 2025, Rome, Italy).

Pagliaccia B., Santini G., Lubello C., Maisto G., Gori R., Francalanci S., Polettini A., Falzarano M., Cincinelli A., Sforzi L., Serranti S., Capobianco G., Gorga E., Falsini S., Colzi I., Rizzo A. - Microplastics: from the detection to the characterization of their effects into the environment - RETURN Dissemination Workshop (19-21 June 2024, Bari, Italy).

Serranti S., Capobianco G., Cucuzza P., Gorga E., Bonifazi G. - Definition of the optimal analytical protocol for the rapid and efficient characterization of microplastics by hyperspectral imaging - RETURN Dissemination Workshop (27-29 November 2024, Bologna, Italy).

4.15 Effects of bioplastics and bioplastics digestion residues on model plants growth in soils (UNIROMA1, UNIFI)

Contributors: M. Falzarano, A. Polettini, I. Colzi, S. Falsini, B. Chiavacci

4.15.1 Introduction

Soil can be affected by both direct and indirect contamination from bioplastics. In the first case, single-use bioplastic items may be directly littered on the soil. In the second case, bioplastic residues can be transported to the soil through digestate coming from anaerobic digestion processes. These residues can accumulate and persist in soil, altering its structure and affecting the organisms living within it. However, the current understanding of the potential contamination associated with bioplastics is still limited. The present study aim was to investigate the effects on model plants growing in soils contaminated with bioplastic fragments or bioplastics digestion residues.

4.15.2 Methodologies

An open-air experimental campaign was conducted to simulate the impact of bioplastics and digestate on soil and plant growth. For the experiment, two sets of 25 cm diameter pots were prepared: Set1 was filled with soil mixed with bioplastics, while Set2 contained soil mixed with digestate. The soil was collected from Sarno river basin and mixed with universal potting soil (70:30 on a total solids basis). Three different bioplastic products were selected: a plate (PL), a coffee capsule (CA) and a shopper bag (SH). The products were characterized using a combination of FT-IR and TGA, and the results showed the following compositions: PL was primarily PLA (polylactic acid) with carbonate fillers; CA was mainly composed of PLA and PBS (polybutylene succinate) with talc fillers; and SH consisted mainly of PLA and PBAT (polybutylene adipate terephthalate).

For Set1 (soil mixed with bioplastics), a 1:100 ratio was used, so 500 gTS of soil were mixed with 5 gTS of bioplastics. Additionally, PL was mixed at ratios of 1:1000 and 1:50, meaning 500 gTS of soil were mixed with 0.5 gTS and 10 gTS of PL, respectively. A blank test with only soil was added to the set. This was done to assess whether the concentration had any additional effects on plant growth.

For Set2 (soil mixed with digestate), anaerobic digestion was previously performed on the selected bioplastic products at 55 °C for 30 days using an inoculum to substrate ratio equal to 1. After 30 days, the following biodegradation degrees were observed for PL, CA, and SH: 63%, 21%, and 29%, respectively. The corresponding disintegration degrees were 64%, 31%, and 62%. The final digestate was then collected and mixed with soil using the same ratios as in the first set. Specifically, a 1:100 ratio by total solids was used for the digestate from the treatment of PL, CA, and SH. Additionally, 1:100 and 1:50 ratios were used for the digestate from the treatment of PL. A blank test with soil and blank digestate (digested anaerobically for 30 days at 55 °C without bioplastics) was added to the set.

The pots were placed on a roof and exposed to natural environmental conditions for 1 year. Samples from both sets were taken after 4 (t1), 8 (t2) and 12 (t3) months of exposure.

The samples from Set1 were sieved to recover the bioplastic fragments and to evaluate the overall mass loss. The fragments were then placed back, except for a few that were retained for subsequent chemical characterization by FT-IR. TOC (Total Organic Carbon) analyses were performed on soils from both sets.

Soil samples from Set 1 and Set 2, collected after 4 (t1), 8 (t2), and 12 (t3) months of exposure, were used to test plant cultivation and to identify potential toxic effects of bioplastics at different stages of natural degradation. For the test, lettuce (*Lactuca sativa*) was selected as an agronomically and commercially relevant species due to its rapid growth and edible biomass. This choice allowed us to evaluate the effects of bioplastics both in terms of possible reductions in plant biomass (and therefore economic impact) and in terms of the nutritional quality of the edible tissues.

For the experiment, pots were prepared containing the different soil types mixed with bioplastics and digestate collected at the various exposure times. Lettuce seeds were sown directly into the soils and grown for three weeks in a growth chamber under controlled light, temperature, and humidity. To monitor plant physiological status and potential toxicity symptoms, physiological parameters were measured, including photosynthetic efficiency and chlorophyll content in the leaves.

After three weeks, plants were harvested and weighed to determine the effects of bioplastic-contaminated soils on growth and biomass production. Mineral content analyses were performed on the edible leaves to assess potential impacts on the nutritional value of lettuce.

Set1	Set2
Control	Control_dig
PL_0.1	PL_0.1_dig
PL_1	PL_1_dig
PL_2	PL_2_dig
CA_1	CA_1_dig
SH_1	SHdig_1

PL = plate
CA = coffee capsule
SH = shopper bag

dig = mixed with digestate

Figure 1. Summary (on the left) of the soils used for the plant cultivations (on the right)

4.15.3 Results

Mass loss revealed a negligible disintegration of bioplastic fragments of Set1 after all the sampling events. In Figure the preliminary results of TOC analysis are shown. It can be observed that in Set2 a drastic reduction of TOC content was registered in t2 (Figure b).

FT-IR analyses of bioplastic fragments retrieved from Set1 are shown in Figure . A slight reduction in PL peaks was observed after 8 and 12 months for all the bioplastic concentration tested. SH samples show an additional peak around 1650 cm^{-1} when compared to the untested material that indicates a progressive accumulation of biofilm on the surface. SH samples became very brittle in time and it was impossible to clean the surface without damaging it.

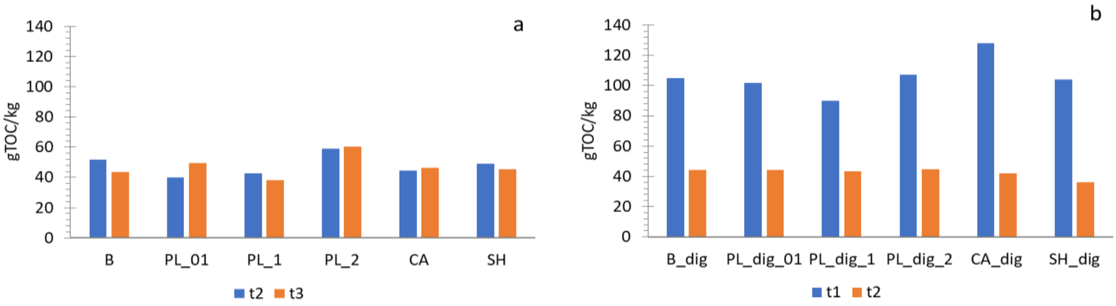

Figure 2. TOC content in samples of Set1 (a) and Set2 (b)

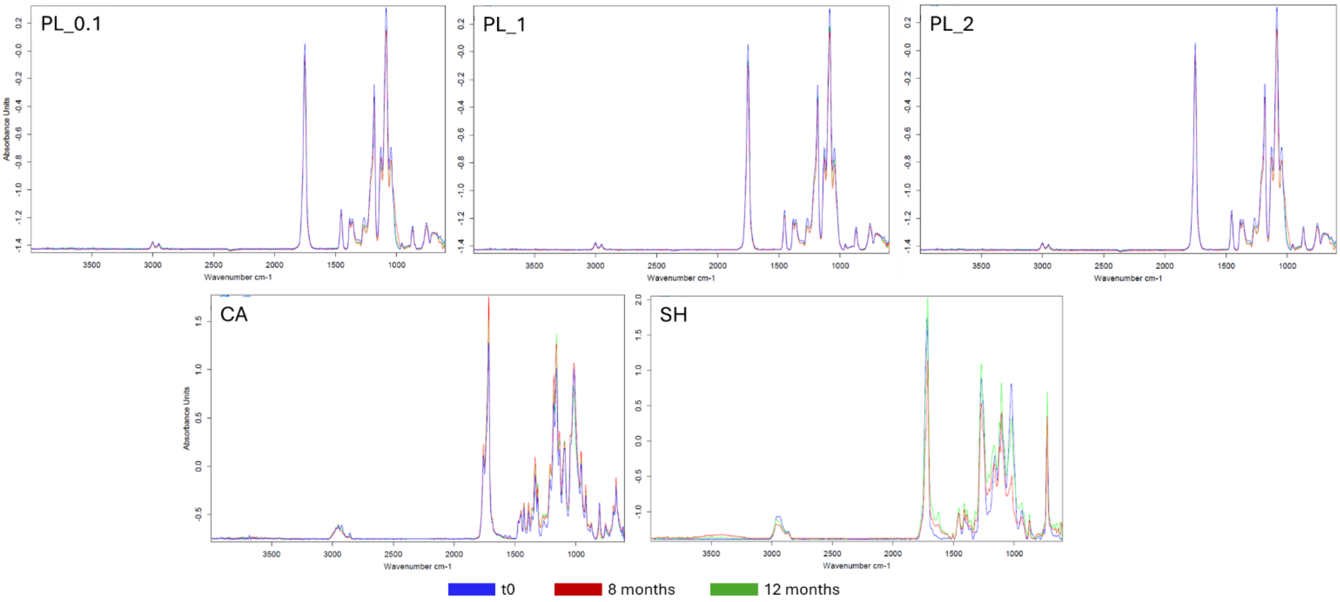

Figure 3. FT-IR analysis of residual bioplastics after 8 and 12 months in soil.

The plant cultivation test revealed some mild effects associated with bioplastic contamination. Representative results are shown in Figure 4, which reports the effects observed in plants grown on soils collected after 8 months of exposure (t2). All plants, from both soils of set1 and set2, showed no visible symptoms of phytotoxicity, such as chlorosis (yellowing leaves), which was also confirmed by the optimal values of photosynthetic efficiency and chlorophyll content. Only two soils mixed with digestate (Set 2: CA and SH) caused a slight decrease in leaf chlorophyll content, although the reduction was not statistically different from the control plants.

Although bioplastic contamination did not induce significant physiological alterations, some effects were observed in growth parameters. All types of bioplastics caused a reduction in plant growth compared with plants cultivated in control soils, as indicated by the fresh biomass values reported in Figure 4. However, statistically significant differences were detected only for two soils: PL_1 from Set 1 and SH_1_dif from Set 2.

These results suggest that, despite the absence of visible toxicity symptoms and despite plants maintaining an apparently good physiological status, soils contaminated with bioplastics may nonetheless reduce plant biomass production, with consequences for crop yield. Beyond the economic impact, this reduction could also have implications for human and environmental health, as growers may be unknowingly induced to use higher amounts of chemical products or growth stimulants to compensate for yield losses caused by undetected bioplastic contamination.

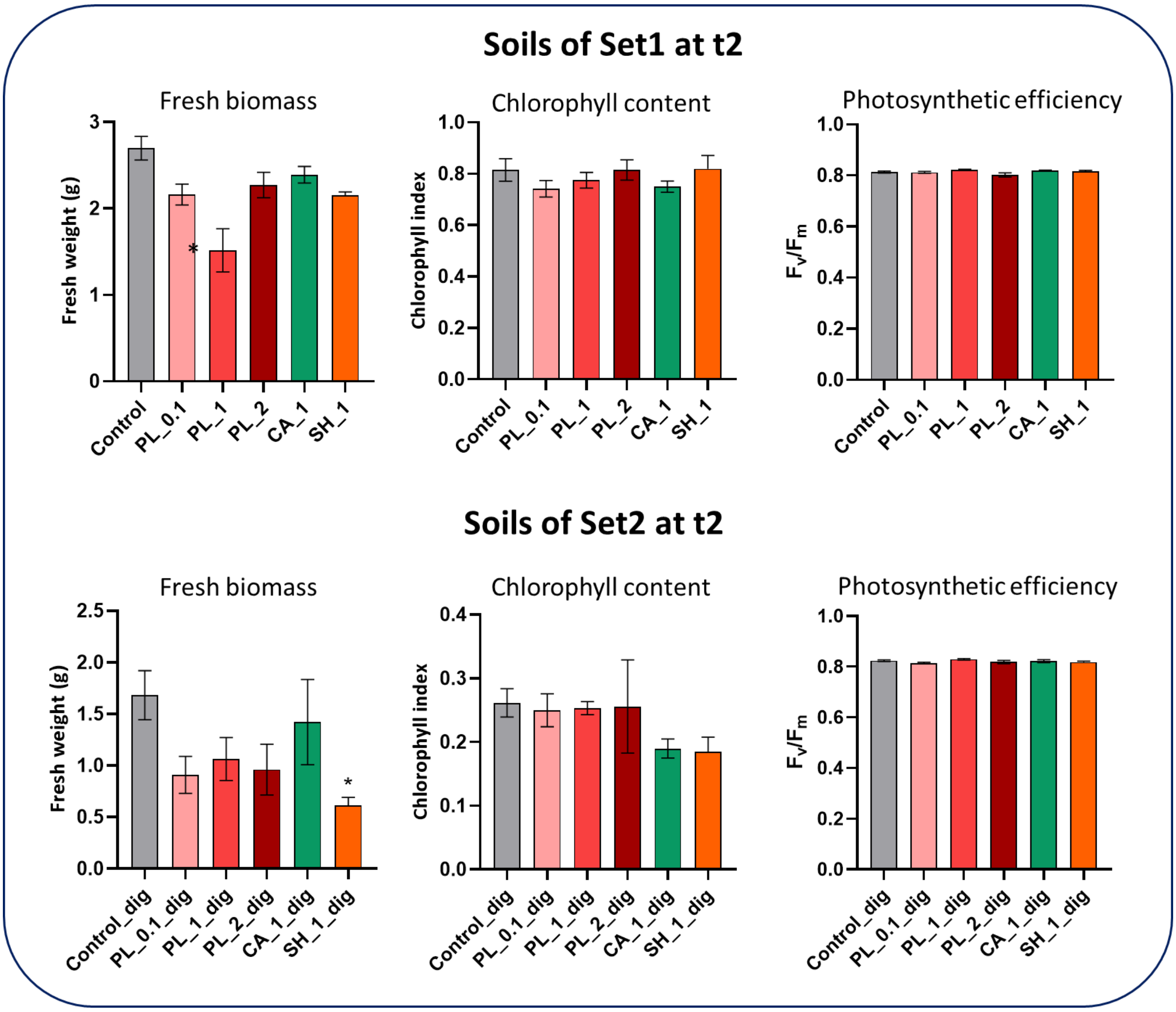

Figure 4. Mean values of growth (fresh biomass) and physiological (chlorophyll content and photosynthetic efficiency) parameters of plants cultivated in soils contaminated with bioplastics and taken after 8 months of exposure (t2).

4.16 Micropollutant fate in the water environment: integrated risk assessment and targeted mitigation strategies (POLIMI)

Contributors: Manuela Antonelli, Beatrice Cantoni, Jessica Ianes

4.16.1 Introduction

Integrated Urban Water Systems (IUWS) are increasingly challenged by the combined effects of climate change, urbanization, and the growing presence of macro- and micro-pollutants, some of them addressed also as contaminants of emerging concern, in wastewater and stormwater streams. Within this context, Combined Sewer Overflows (CSOs) represent one of the most critical and uncertain pollutant sources in urban areas, as they occur episodically during rainfall events and discharge untreated mixtures of wastewater and runoff directly into receiving waters. These short-duration, high-volume discharges often coincide with reduced river dilution and can therefore create acute environmental pressures. At the same time, continuous discharges from Wastewater Treatment Plants (WWTPs) represent a persistent background load, especially for highly soluble and persistent chemicals.

Micropollutants, such as pharmaceuticals (PHARMS), pesticides (PESTS), Per- and Poly-fluoroalkyl Substances (PFAS), alkylphenols, phthalates, Heavy Metals (HMs), Polycyclic Aromatic Hydrocarbons (PAHs), have gained attention due to their widespread occurrence, low removal efficiency in conventional treatment systems, and potential chronic environmental effects. Their behavior in IUWS is strongly influenced by hydrological variability, in-sewer processes, and treatment dynamics. The complex interaction between hydraulic processes, pollutant transport, and chemical fate in urban water systems poses a significant challenge to regulators and water managers. Climate change exacerbates this complexity, as increasing rainfall intensity and prolonged droughts alter both pollutant mobilization and river dilution capacity. Moreover, the recent recast of the EU Urban Wastewater Treatment Directive (UWWTD, 2024) introduces stricter limits on wet-weather discharges, demanding that total pollutant loads released during such events remain below 2% of the annual dry-weather load.

In response to the challenges of understanding and managing micropollutants in urban water systems, these deliverable advances integrated methodologies for assessing contaminant fate and environmental risks. By combining probabilistic risk evaluation, mechanistic dynamic modelling, and full-scale monitoring, the study improves our understanding of CSO-related hazards, the behavior of micropollutants under wet- and dry-weather conditions, and the potential impacts of climate change and mitigation strategies. This holistic approach supports decision-making by identifying key contaminant sources, pathways, and critical points within urban water systems, ultimately providing robust tools for designing targeted monitoring campaigns and informing sustainable and resilient urban water management strategies.

4.16.2 Methodology

The methodological approach combined probabilistic analysis based on literature data, monitoring-based characterization and dynamic modelling to address the different temporal and spatial scales of micropollutant generation, transport and discharge.

4.16.2.1 Quantitative Risk assessment approach

The common step of all these approaches was the quantification of environmental risk contribution of different sources for different contaminants. Chronic environmental risk was estimated through the Risk Quotient (RQ) calculated as follows:

$$RQ_{i,j} = \frac{C_{i,j}}{TL_j} \cdot \frac{V_i \cdot n_i}{Q_R \cdot t} \qquad \text{Eq. 1}$$

where:

- i is the discharge source, e.g. CSO, WWTP by-pass (BP), WWTP effluent (EFF),
- j is one micropollutant that may cause chronic toxicity,
- $C_{i,j}$ is the distribution of the concentration of the j micropollutant in the discharge I,
- V_i is the distribution of the annual volume released in the river by each discharge,
- n_i is the number of structures per discharge,
- Q_R is the distribution of the river annual average flowrate,
- t is the reference time (1 year),
- TL_j is the Toxic Level for the j micropollutant, that is the minimum value between the Annual Average Environmental Quality Standards (AA-EQS), set by the European Parliament in 2013, and the lowest Chronic Predicted No-Effect Concentration ($\text{PNEC}_{\text{chronic}}$), collected from the NORMAN database.

Probabilistic assessment of wet vs dry-weather discharges from literature data

The probabilistic assessment was based on a literature-derived IUWS archetype that included multiple CSO structures, WWTP bypass, treated WWTP effluent and a receiving water body. For each source, probability distributions of flows and micropollutant concentrations were constructed from collected literature data to reflect inherent variability and uncertainty. This study focused on 12 micropollutants from different classes: 3 HM, 3 PHARMS, 3 PESTS, 3 PAH. RQ values were calculated through Monte-Carlo simulations, allowing propagation of uncertainty originating from concentration distributions, discharge volumes, dilution factors and the number of overflow structures. Various percentiles were extracted from these probability distributions for the parameterization of the archetype IUWS. In particular, six scenarios were identified related to climate changes: three pollution levels were accounted using the distributions for the 50th, 75th, 95th percentiles (C50, C75, C95) of the micropollutants concentration distributions; three dilution scenarios (Safe, Medium, and Worst) were derived from the distributions of the river dilution factor.

Monitoring campaign

The monitoring part of the work consisted of an extensive wet- and dry-weather sampling campaign at a full-scale WWTP (210,000 population equivalent, with 13% from industrial sources) in the outskirt of Milan city, discharging into the Seveso River. Eleven monitoring campaigns were performed from February to November 2023: four campaigns in dry-weather conditions (WWTP influent and effluent), seven campaigns in wet-weather conditions (WWTP bypass and effluent). A total of ten rain events were monitored. The 78 monitored parameters included:

- 7 conventional pollutants: electric conductivity at 25°C (EC), total suspended solids (TSS), chemical oxygen demand (COD), ammonium nitrogen (N-NH_4^+), nitrate nitrogen (N-NO_3^-), total phosphorous (TP), *Escherichia coli* (*E. coli*);
- 15 metals (Al, Fe, Zn, B, Ni, Cu, Pb, Mn, Cr, Co, V, Hg, Se, Cd, Tl);
- 52 micropollutants: 23 pesticides, 25 PFAS, and 4 other micropollutants previously detected in Milan groundwater, e.g. Mebicar, 2-Methyl 5-Methylthio 1,3,4-Thiadiazole (MMtTD), Dimetridazole (DMZ), and Tris(2-chloroethyl) phosphate (TCEP).

Ecotoxicity was also analyzed through immobilization on *Daphnia magna*.

Integrated Hydraulic and Pollutant Transport Modeling

An IUWS model was developed for the catchment in the outskirt of Milan monitored in the monitoring campaign. The catchment (22.5 km²) is mostly combined (87%). It includes 29 CSO structures discharging to the Seveso River, a small, low-flow watercourse highly sensitive to wet-weather events.

The model was implemented in WEST (DHI A/S), adopting the IUWS_MP model library, which simulates hydraulic processes and pollutant fate in sewers, WWTPs, and the receiving water. The model incorporates:

- rainfall–runoff generation and routing through a three-tank-in-series conceptual structure.
- CSO and bypass activation based on hydraulic thresholds and dynamic inflow conditions,
- pollutant generation, accumulation, and wash-off from impervious areas,
- fate and transport processes in sewers (sorption, biodegradation, sediment resuspension),
- WWTP treatment dynamics, including removal, biodegradation, and sorption of micropollutants,
- instantaneous mixing with the river downstream of the discharge point for surface water quality assessment.

Model simulations were performed for a full hydrological year with a 15-minute resolution, under both baseline and scenario conditions. Calibration was achieved using high-frequency field measurements of flowrate and concentrations of conventional pollutants (COD, TSS, NH_4^+, TP), three metals (Cu, Pb, Zn) micropollutants (Terbutryn (TRB), TCEP, and Mebicar) obtained from the monitoring campaign. Table 1 summarizes the main classes of pollutants and the fate processes included in the model.

Table 1. Summary of the target micropollutant classes and modeled fate processes in the IUWS model

Pollutant class	Target pollutants	Main sources	Key modeled processes	Primary removal mechanism
Conventional	COD, NH_4, TP, TSS	Domestic wastewater	Sedimentation, biodegradation	Biological treatment
Heavy metals	Cu, Pb, Zn	Runoff, corrosion, industrial inputs	Sorption/desorption, sedimentation	Settling, sorption
Organic micropollutants	Terbutryn (TRP), TCEP, Mebicar	Building materials, domestic use	Biodegradation, adsorption	Partial biodegradation

4.16.3 Results

The proposed risk-based procedure proved to be effective to identify micropollutants sources and exposure routes as useful support tool for planning monitoring campaigns and mitigation strategies also in future climate change scenarios.

Comparing pollution from wet and dry weather discharges

Looking at the first task (risk derived from CSOs), comparing the risk contribution of wet weather discharges to the wastewater treatment plant effluent, the RQ probabilistic distribution was used to evaluate which streams and micropollutants are more responsible for chronic environmental risk. The probabilistic analysis revealed that CSOs and WWTP bypasses are major contributors to chronic environmental risks for several micropollutant classes, particularly PAHs and heavy metals. Across all dilution scenarios, CSOs consistently displayed RQ distributions exceeding the threshold of 1 for PAHs, with Benzo(a)pyrene showing the highest risk. The WWTP effluent represented the dominant source for pharmaceuticals, reflecting their high solubility and persistence, while CSOs became relevant for this class only under worst-case dilution conditions. Heavy metals also showed high risk contributions from CSOs when dilution was limited. Pesticides exhibited comparatively lower risk, though individual compounds such as diuron occasionally exceeded thresholds.

Since in the literature there is a lack of standardization of the risk assessment procedure, this study investigated the sensitivity of the risk estimate to the input parameters variability and the risk assessment choices, such as the percentile of micropollutant's concentration used for the exposure assessment, or the different percentiles of the RQ distribution. Figure 1 shows the sensitivity indices accounting for the impact of the variability and uncertainty of different input parameters on the final risk estimate. The analysis confirmed that river dilution is the most influential driver of risk variability: median RQ values differed by up to four orders of magnitude between safe and worst-case dilution scenarios, whereas differences due to pollutant concentration percentiles were comparatively small. Secondly, an accurate monitoring of micropollutant concentration in CSOs and effluent can effectively reduce risk estimation uncertainties. This outcome led to the design of the monitoring campaign.

Monitoring campaign

Out of the 78 compounds analyzed, 3/19 metals, 12/23 pesticides, and 18/25 PFAS were below the LOQ (Level of Quantification) in all samples of all streams. A higher number of pollutants was detected in the dry weather influent (28) and the bypass (42), compared to the effluent (27 in dry and wet weather).

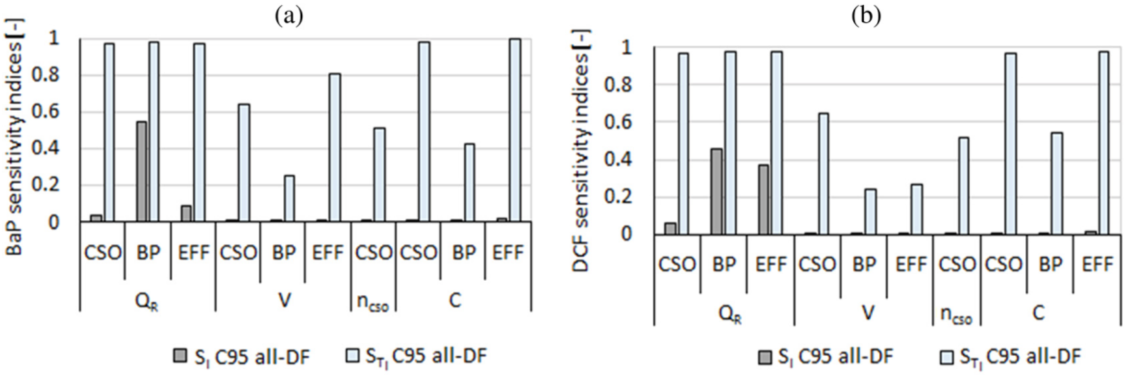

Figure 1. Sensitivity first order Index (in grey) and Global Sensitivity Index (in light blue) values for (a) Benzo-a-Pyrene (BaP) and (b) diclofenac (DCF) in all Dilution Factor scenarios (Ianes et al., 2024a).

The concentrations and discharged volumes were used to estimate the risk in wet weather (due to by-pass and WWTP effluent) and in dry weather (comparing the potential risk at the WWTP influent to the actual risk at the WWTP effluent). Figure 2 reports the RQ distributions for all the detected conventional pollutants, metals and micropollutants highlighting the warning thresholds (RQ=0.1 in orange) and the risk presence threshold (RQ=1 in red).

Looking at the median values, the risk posed by the bypass is higher than that of the effluent for all the conventional pollutants and metals. Those with RQ > 1, exceeding the discharge limit for WWTP effluents, are: *E. coli*, TSS, TP, Al, COD, Fe, Cu, $N\text{-}NH_4^+$, Zn. For some micropollutants (BAM, LM6, MEBICAR, DMZ, MMtTD), the effluent poses higher risks due to higher concentrations with respect to the bypass. Moreover, due to dilution, also micropollutants with higher concentrations in the bypass than in the effluent, can pose higher risks in the effluent than in the bypass, such as TCEP. Among the micropollutants, only TRB always poses a risk, with the bypass posing higher risk than the effluent. On average, the effluent poses higher risks for all other micropollutants compared to the bypass. However, when looking at the highest percentiles of the risk in the bypass, due to the high variability in concentration and dilution across different events, higher RQs can be observed compared to the effluent for TBA, DST-TBA, MET, TCEP, and PFHxA.

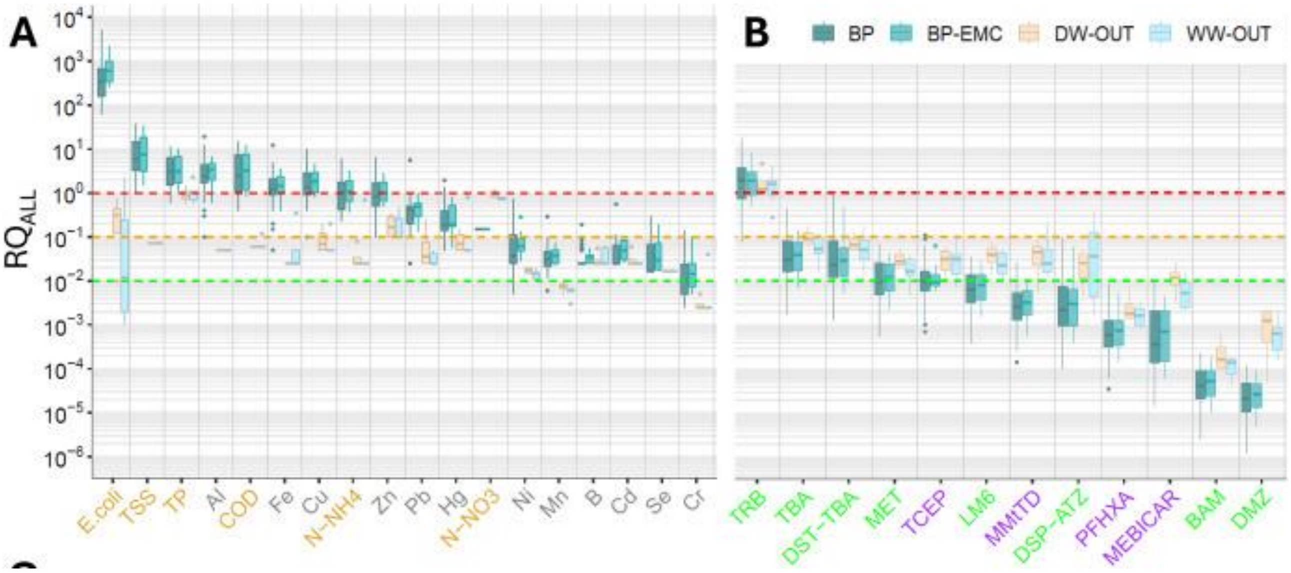

Figure 2. RQs calculated for conventional pollutants and metals (a) and for micropollutants (b) (Ianes et al., 2024b).

These findings hold significant implications for WWTP monitoring and management strategies. This analysis underscores the necessity of including bypass streams into intervention plans to minimize environmental micropollutant contamination. Furthermore, developing predictive models that incorporate factors like rainfall characteristics and historical pollutant data can provide valuable insights for risk assessment and decision-making.

Integrated Hydraulic and Pollutant Transport Modeling

Given the results of the risk assessment performed on the monitoring campaign data, it was clear the need for implementing a modeling framework able to combine hydraulic and pollutant transport in the sewer to plan possible mitigation strategies able to reduce the environmental risk due to wet weather discharges.

The developed model was calibrated and validated with data coming from the monitoring campaign described above. The model achieved good agreement between measured and simulated data across all compartments, as shown in Figure 3. About the calibration, the main outcome are:

- Hydraulic calibration: Mean Absolute Relative Error (MARE) between 2–8% for dry-weather flows; CSO activation and deactivation timing accurately reproduced for multiple rainfall events.
- Water quality calibration: the model captured concentration dynamics for both conventional and micropollutants, including dilution peaks and pollutant wash-off events. Minor underestimation was observed for lead and TCEP concentrations, attributed to variability in industrial inflows and limited wet-weather data.

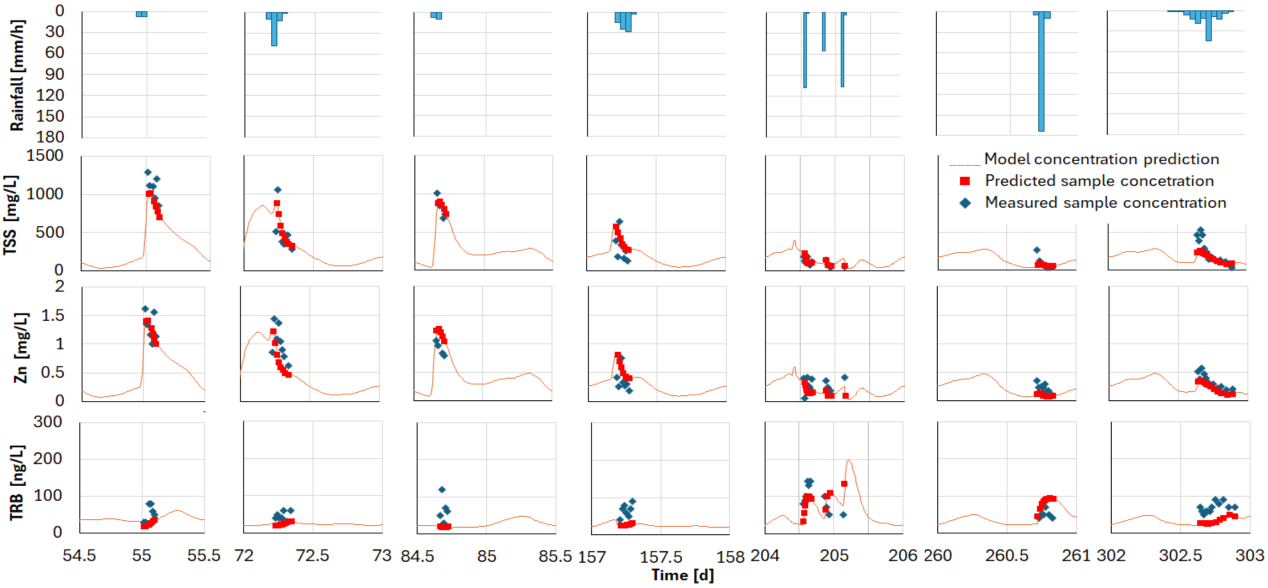

Figure 3. Predicted concentrations of one representative for each conventional, metals and micropollutants classes in the influent bypassed flow, along with the measured rainfall each 350 hour at the closest station to the WWTP, for each of the monitored rain events.

The application of the model showed to be a useful tool to evaluate the source apportionment of the risk. The annual pollutant balance under baseline conditions (2023) revealed that CSOs and WWTP bypasses accounted for only 13% of total discharged volume but contributed up to 65% of COD, TSS, and NH_4^+ loads to the Seveso River. For micropollutants, wet-weather discharges contributed between 30-50% of annual loads for Cu, Pb, Zn, and TRB, while WWTP effluent dominated emissions of TCEP and Mebicar. The WWTP removal efficiency exceeded 90% for conventional pollutants but was below 50% for most micropollutants, confirming the persistence of these compounds even in tertiary-treated effluents.

Moreover, compared to the monitoring campaign, the integration of a model into the assessment can support the evaluation of different scenarios. In particular, two different mitigation strategies (first-flush retention tanks and sewer separation with infiltration systems) and a climate change scenario were considered.

First-flush retention tanks reduced pollutant loads from wet-weather discharges by 40-70%, achieving system-wide reductions up to 42% for conventional pollutants. However, benefits for micropollutants were marginal (<10%), due to their poor removal in WWTP treatment stages. Additionally, temporary overloading of the WWTP during tank emptying caused short-term quality deterioration in effluent.

Sewer separation with infiltration achieved substantial reductions in both wet-weather discharge volumes and loads, reaching 96% reduction in pollutants when applied to 75% of the catchment. Intermediate levels (25-50%) yielded only moderate improvements. Despite its environmental effectiveness, this strategy entails high infrastructural and economic costs.

The model results under the drought and rainy year scenarios highlighted the dual effect of climate change. In drought conditions, discharge volumes decreased by 60%, but the river's dilution capacity dropped by more than 50%, leading to elevated concentrations and increased RQ values for Zn, Pb, and TCEP. In rainy conditions, pollutant loads increased by 30-60%, but higher flowrates improved dilution, resulting in lower average RQ values and better compliance with EQS limits.

In conclusion, the proposed risk-based approach combining probabilistic assessment with literature data, monitoring campaign and modelling approaches enabled:

- the identification of priority pollutants and sources for targeted monitoring;
- the quantification of the efficiency and trade-offs of mitigation strategies under varying climate conditions;
- the support for risk-based regulation, emphasizing hydraulic control (dilution, storage) as critical to reducing environmental impacts.

4.16.4 Scientific products and dissemination

Published Papers:

Ianes, J., Cantoni, B., Remigi, E. U., Polesel, F., Vezzaro, L., & Antonelli, M. (2023). A stochastic approach for assessing the chronic environmental risk generated by wet-weather events from integrated urban wastewater systems. Environmental Science: Water Research & Technology, 9(12), 3174-3190.

Ianes, J., Cantoni, B., Remigi, E. U., Polesel, F., Vezzaro, L., Antonelli, M. (2024). Monitoring (micro-)pollutants in wastewater treatment plants: Comparing discharges in wet- and dry-weather. Environmental Research, 263, 120132.

Ianes, J., Cantoni, B., Polesel, F., Remigi, E. U., Vezzaro, L., Antonelli, M. (2024). Modeling an integrated urban wastewater system to assess (micro-)pollutant discharge under dry- and wet-weather: mitigation strategies and climate change scenarios. Under review in Journal of Environmental Management.

Presentations at conferences:

Ianes, J., Cantoni, B., Remigi, E. U., Polesel, F., Vezzaro, L., & Antonelli, M. (2023). Assessing the contribution of wet-weather discharges on micropollutants release by urban catchments. 11th IWA International Conference on Efficient Urban Water Management "Efficient2023", Bordeaux (France), 13-15 September 2023.

Ianes, J., Cantoni, B., Scana, F., Delli Compagni, R., Remigi, E. U., Polesel, F., Vezzaro, L., & Antonelli, M. (2023). An integrated modelling framework to assess cascade water reuse in urban areas. 11th IWA International Conference on Efficient Urban Water Management "Efficient2023", Bordeaux (France), 13-15 September 2023.

Ianes J., Polesel F., Cantoni B., Remigi E.U., Vezzaro L., Antonelli M. (2024). An integrated modelling framework for predicting wet-weather discharges pollution. Proc. of the 34th Annual Meeting of the Society of Environmental Toxicology and Chemistry - Europe (SETAC Europe), 5th-9th May 2024, Seville (Spain). Accepted as poster (abstract 3.18.P-Mo289), pp. 1 (www.setac.org)

4.17 Risk-based approaches for managing multiple water (re-)use scenarios: from gaps to a one-health approach (POLIMI)

Contributors: Manuela Antonelli, Beatrice Cantoni, Luca Penserini, Jessica Ianes

4.17.1 Introduction

Water scarcity, climate change, and rapid urbanization have driven the adoption of strategies aimed at optimizing water resources, among which multiple water uses in urban areas and wastewater reuse play a central role. These practices are essential for sustainable water management but introduce complex challenges related to contaminant transfer, cross-contamination, and associated risks for both ecosystems and human health.
Multiple water uses in urban areas involve cascading applications of water within interconnected systems, where the same water resource is used sequentially for different purposes. These complex networks increase the likelihood of cross-contamination, as water flows through multiple compartments without complete removal of micropollutants at each stage. The overlapping of uses amplifies uncertainties regarding contaminant fate and transport, making risk management more challenging.

Wastewater reuse refers to the intentional recovery and application of treated wastewater for beneficial purposes. Direct reuse happens when treated wastewater is applied directly for agricultural irrigation without intermediate dilution or blending. This practice maximizes resource efficiency but increases the likelihood of contaminant transfer to soils and crops. Indirect reuse happens when treated wastewater is discharged into surface water before being abstracted for irrigation. While this approach provides natural attenuation, it introduces the exposure of the water receptor to the discharge. Both forms of reuse can lead to the presence of contaminants of emerging concern (CECs), such as pharmaceuticals and personal care products, alkylphenols, PFAS, which may persist even after conventional treatment. These contaminants can reach the natural water bodies with potential impacts to ecosystems. Receiving waters are also used for drinking water production, requiring a wise management to minimize impacts on consumers' health. Moreover, during the irrigation CECs can accumulate in soils and crops, ultimately reaching humans through the food chain.

Traditional concentration-based monitoring provides information on contaminant presence but does not adequately capture the cumulative risk arising from these interconnected pathways. To address this gap, a risk-based approach is here proposed to integrate environmental and human health endpoints in a one-health perspective, evaluates exposure scenarios, and supports prioritization of mitigation strategies, focusing on wastewater reuse and multiple urban water use under a unified risk assessment perspective.

4.17.2 Methodology

The methodological approach adopted across the studies is grounded in a risk-based framework integrating environmental and human health endpoints under a One Health perspective. This framework addresses the complexity of interconnected compartments - wastewater, surface water, groundwater, soil, crops, and humans - where CECs and other pollutants circulate through reuse and cascading water uses. The framework consists of four main steps:

- problem formulation, identifying relevant contaminants and endpoints. For wastewater reuse, pharmaceuticals and antibiotics were prioritized; for urban water systems, PFAS and PAHs were selected due to persistence and toxicity;
- exposure assessment, mapping pathways for contaminant transfer: for reuse, oral ingestion via drinking water and food was considered, while for urban systems, aquatic ecosystem exposure was assessed;
- hazard assessment, defining toxicological thresholds: Health-Based Guidance Values (HBGV) for human health, Predicted No-Effect Concentrations (PNEC) for ecosystems;
- risk characterization, calculating risk indices (Benchmark Quotient for human health, Risk Quotient for environment and antibiotic resistance) using deterministic and probabilistic approaches, including Monte Carlo simulations to propagate uncertainty.

As for the environmental risk assessment, the Risk Quotient (RQ) was estimated as the ratio between environmental concentration (MEC) and the Predicted No-Effect Concentration (PNEC), as follows:

$$\mathrm{RQ} = \frac{MEC}{PNEC}$$

As for human health risk assessment, the Benchmark Quotient (BQ) was calculated as the contaminant exposure concentration (C_{EXP}), typically originating from crop or drinking water consumption, divided by its reference dose (RfD), as follows:

$$\mathrm{BQ} = \frac{C_{EXP}}{RfD}$$

Risk values (RQ or BQ) lower than 0.1 indicates the absence of appreciable concern, between 0.1 and 1 indicates that further investigation might be warranted, and higher than 1 indicates the presence of a risk.

Modeling impacts of multiple urban water (re-)uses

An integrated model-based approach was applied to evaluate the impact of transitioning to water-wise cities on urban water quality. The assessment encompasses multiple strategies such as stormwater separation, use of Groundwater Heat Pumps (GHPs), reclaimed water for irrigation, and their implications on micropollutants release into a surface river under different scenarios. The study assumed as archetype city for the “water-wise city” transition, evaluating the occurrence and fate of three micropollutants: PFOA, PFOS (both in the family of PFAS) and pyrene (in the family of PAHs). Concentration data were collected from literature and open-source monitoring repositories. The fate of these micropollutants from the different water sources in the case study was predicted adopting the Integrated Urban Wastewater and Stormwater (IUWS_MP) model library in the software WEST (DHI A/S, Denmark). The simulated concentrations of micropollutants at five monitoring points along the waterway were used to evaluate environmental risk contributions of different sources.

Modeling impacts of wastewater reuse

A critical review of the existing literature was performed with the aim of analyzing the proposed methodologies for assessing impacts from reclaimed wastewater reuse in agriculture. Firstly, a conceptual framework was built to evaluate the environmental compartments involved in the reclaimed wastewater reuse system, the models used to assess reuse impacts and the main target variables analyzed in scientific literature focused on reuse.

Data collected from different studies were then used to assess the risk due to pharmaceuticals in different compartments of the reclaimed wastewater reuse system.

4.17.3 Results

The proposed risk-based procedure was applied in different scenarios to identify micropollutants sources and exposure routes and evaluate the efficiency of mitigation strategies.

Modeling impacts of multiple urban water (re-)uses

The assessment of multiple water uses in urban areas was carried out through dynamic modeling, where the transition towards a water-wise city introduces new water fluxes and reuse opportunities. The model simulated the fate of micropollutants under different management and climate scenarios, focusing on three contaminants: PFOA and PFOS (representing PFAS) and pyrene (representing PAHs), selected due to their persistence, toxicity, and relevance to urban water systems.

To capture the spatial variability of risk along the interconnected waterways, five monitoring points were defined within the modeled system (Figure 1). The **INLET** point represents the upstream canal entering the city, providing baseline water quality before any urban influence. The **POST_GHP** point is located downstream of the last discharge of groundwater extracted for geothermal heat pumps. The **POST_SW** point is positioned immediately after the discharge from the separate stormwater sewer system. The **POST_WWTP** point is situated downstream of the wastewater treatment plant effluent discharge. Finally, the **OUTLET** point marks the end of the natural canal before it enters the receiving river, integrating the cumulative effects of all upstream discharges and processes such as dilution and sedimentation.

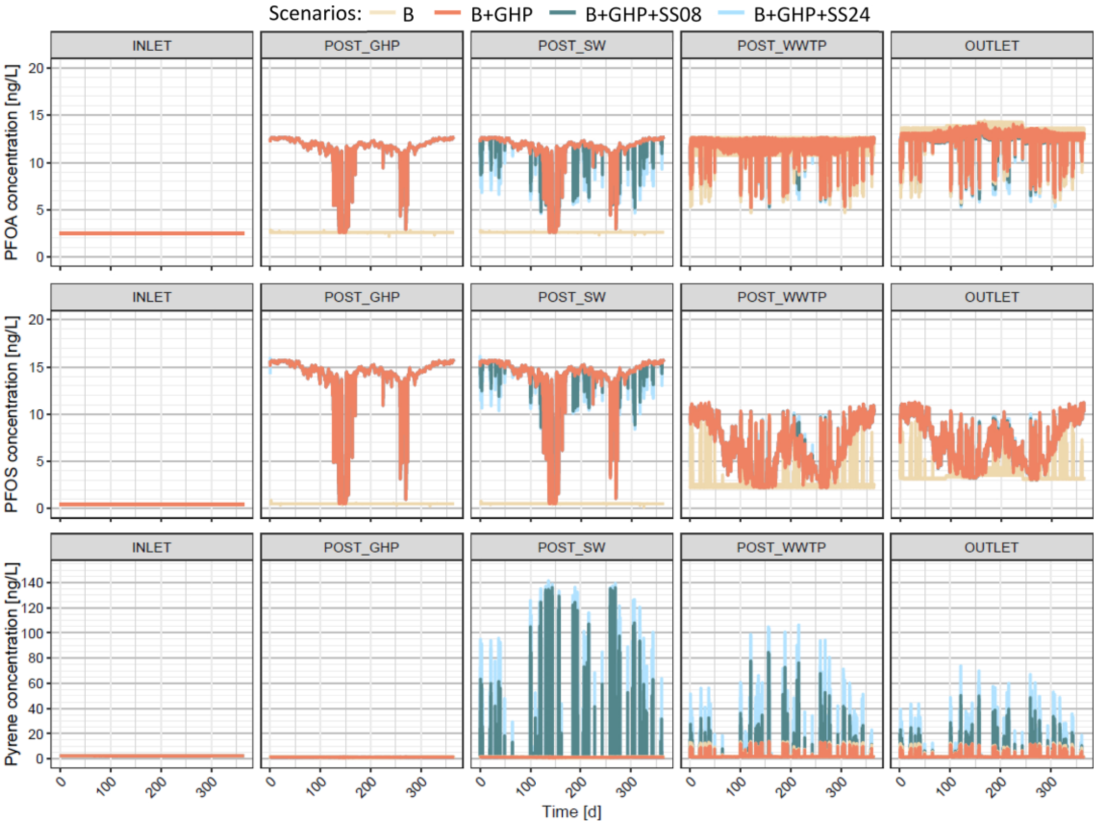

Figure 1. 1-hour resolution concentration at each monitoring point (INLET, POST_GHP, POST_SW, POST_WWTP, OUTLET), for PFOA, PFOS, and pyrene (Ianes et al., 2024).

The simulation results revealed distinct behaviors for the selected contaminants. PFAS concentrations were dominated by the soluble fraction and exhibited chronic risk (RQ > 1) at locations downstream of the WWTP discharge in all scenarios, including the baseline. The introduction of groundwater discharges through heat pumps increased PFAS concentrations at POST_GHP, with seasonal fluctuations linked to energy demand.

Conversely, stormwater separation produced a dilution effect for PFAS but introduced pyrene into the system. Pyrene concentrations spiked at POST_SW during wet-weather events, reaching levels that triggered acute risk exceedances when large areas of the catchment were converted to separate sewers. These exceedances persisted downstream, although attenuation occurred due to sedimentation processes.

These findings underscore the complexity of managing water quality in interconnected urban systems. The spatially resolved risk assessment across the five monitoring points highlights the need for targeted mitigation strategies at critical locations, particularly stormwater discharge points and WWTP effluent outlets, to ensure that the transition towards a water-wise city does not compromise environmental safety.

Main literature gaps in wastewater reuse evaluation

To understand the complexity of risks associated with wastewater reuse and compare them with risk due to drinking water consumption, we first conceptualized the anthropic water system through a schematic representation of all relevant compartments and their interconnections (Figure 2a). The diagram reports the number of studies investigating the concentrations of two CECs in those compartments. Links show the number of studies analyzing two compartments simultaneously. It is clear that, not only the compartments themselves but also the numerous links between them remain poorly studied in the scientific literature. These gaps in knowledge are critical because they hinder our ability to fully characterize contaminant transfer and cumulative risk across the system. Moreover, Figure 2b shows that only a very small fraction of studies that proposed a risk assessment application in wastewater reuse have simultaneously addressed environmental and human health risks, despite the evident need for integrated assessments. Most existing research focuses on isolated endpoints, which limits the effectiveness of risk management strategies and regulatory frameworks.

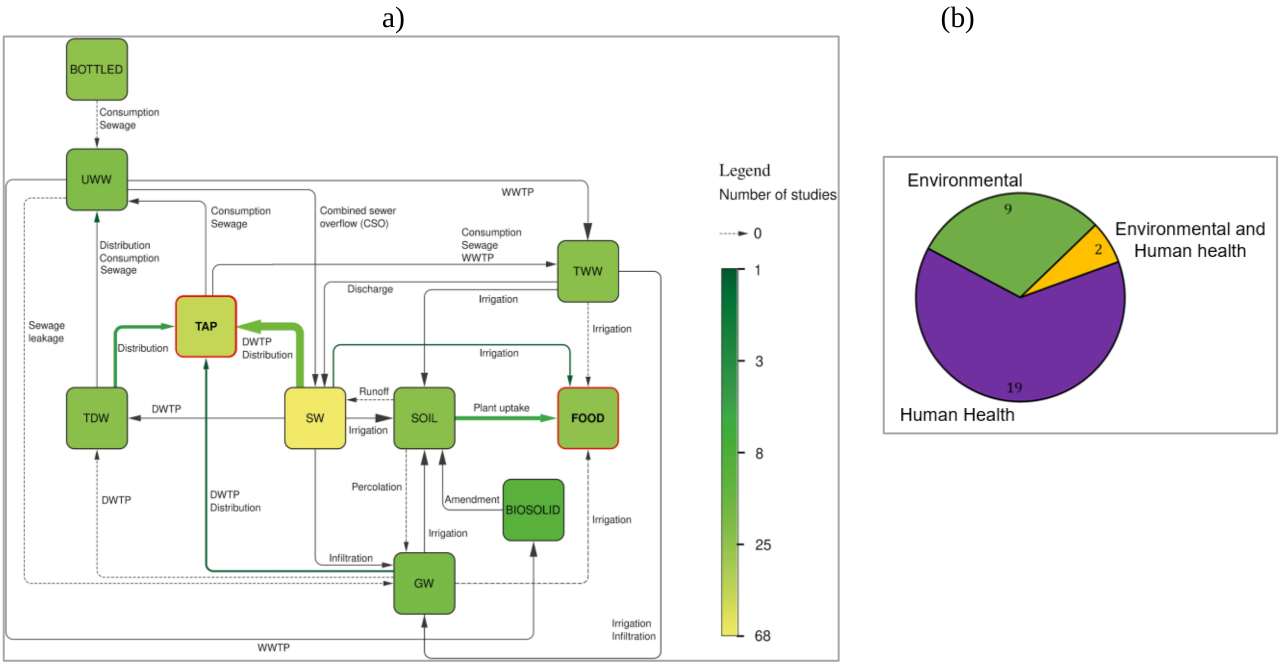

Figure 2. (a) Environmental compartments and cause-effect links investigated in literature for BPA and NP. Nodes and edges are colored depending on the number of literature studies investigating such compartment or link (Penserini et al., 2023); (b) Distribution of the studied endpoints for studies applying risk assessment to wastewater reuse (Penserini et al., 2024).

Proposed approach for wastewater reuse management

Given the highlighted gaps, we analyzed the occurrence and distribution of CECs across the interconnected compartments looking at data coming from WWTPs currently not applying quaternary treatments, such as ozonation and adsorption on activated carbon. Boxplots of measured concentrations for carbamazepine (CBZ) and diclofenac (DCF) (Figure 3a) reveal the high variability of concentrations across compartments - from treated wastewater and surface water to edible crops - underscoring the complexity of contaminant fate and transport.

However, concentration data alone do not provide sufficient insight into the actual risk posed by these contaminants. For this reason, a risk-based approach was applied to translate concentrations into risk indices, enabling a more meaningful prioritization of hazards. The results in Figure 3b show that diclofenac and carbamazepine exhibit markedly different risk profiles across compartments, with diclofenac often exceeding environmental risk thresholds in surface waters, while human health risk from drinking water and crop consumption being negligible.

These findings highlight the importance of moving beyond concentration-based monitoring towards integrated risk assessment frameworks. More specifically, using a One-Health approach looking simultaneously to human health and environmental risk allow decision-makers to identify which contaminants and pathways should be addressed first, ensuring that mitigation efforts target the most critical sources of risk rather than those that merely exhibit higher concentrations.

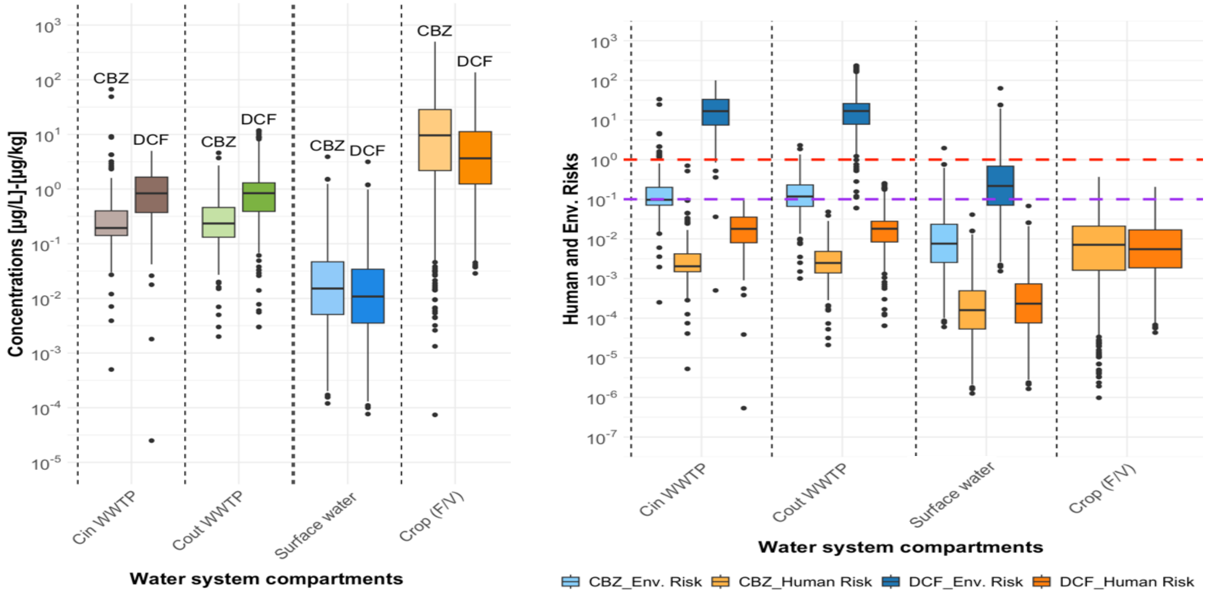
(a) (b)

Figure 3. Distribution of (a) concentration and (b) human health and environmental risk for carbamazepine and diclofenac in differente wastewater reuse compartments (Desca et al., 2025).

4.17.4 Scientific products and dissemination

Published Papers:

Ianes, J., Cantoni, B., Scana, F., Compagni, R. D., Polesel, F., Remigi, E.U., Vezzaro L., Antonelli, M. (2024). Implications of the transition towards water-wise approaches in urban areas: Elucidating the risk from micropollutants release. *Journal of Environmental Chemical Engineering*, *12*(3), 112676

Penserini, L., Cantoni, B., Gabrielli, M., Sezenna, E., Saponaro, S., Antonelli, M. (2023). An integrated human health risk assessment framework for alkylphenols due to drinking water and crops' food consumption. *Chemosphere*, *325*, 138259.

Penserini, L., Cantoni, B., Antonelli, M. (2024). Modelling the impacts generated by reclaimed wastewater reuse in agriculture: From literature gaps to an integrated risk assessment in a One Health perspective. *Journal of Environmental Management*, *371*, 122715.

Presentations at conferences:

Penserini, L., Cantoni, B., & Antonelli, M. (2023). Reclaimed wastewater reuse impacts: from literature data gaps to integrated risk modelling. 6th IWA International Conference on eco-Technologies for Wastewater Treatment (ecoSTP2023), Girona (Spain), 26-29 June 2023.

Penserini L., Cantoni B., Sezenna E., Saponaro S., Antonelli M. (2024). Assessing the Risk of Wastewater Reuse in Agriculture: Is Irrigated Crops' Food the main Exposure Route for Alkylphenols compared to Drinking Water? Proc. of the IWA Conference on "Wider-Uptake of Water Resource Recovery from Wastewater Treatment (ICWRR2024), Palermo (Italy), 18th-21st June 2024, pp. 1-4 (https://icwrr2024.org/)

Penserini L., Cantoni B., Antonelli M. (2024). From Literature Gaps to Integrated Risk Assessment: Unveiling the Complexity of Wastewater Reuse Impact Models. Proc. of the IWA Conference on "Wider-Uptake of Water Resource Recovery from Wastewater Treatment (ICWRR2024), Palermo (Italy), 18th-21st June 2024, pp. 1-4 (https://icwrr2024.org/)

Ianes J., Penserini L., Sezenna S., Saponaro S., Cantoni B., Antonelli M. (2024). The fate of micropollutants in the water environment from sources to humans: planning removal treatments and assessing the risk in a one-health approach. Proc. of SIDISA 2024 - XII International Symposium on Environmental Engineering, Palermo (Italy), 1st-4th October 2024, pp. 813-816 (https://www.sidisa2024.org/)

Desca A., Ianes J., Penserini L., Cantoni B., Antonelli M. (2025). The fate of micropollutants in the water environment from sources to humans: integrated risk assessment and targeted mitigation strategies in a one-health approach. Proc. of 7th IWA International Conference on ecotechnologies for wastewater treatment (ecoSTP2025), 23rd-26th June 2025, Stockholm (Sweden), pp. 1-4. Accepted as oral presentation (https://www.ecostp2025.org/) (https://doi.org/10.5281/zenodo.17415176)

4.18 Direct measurements of hydrocarbon vapor emissions in sites subject to hydrocarbons' contamination by means of dynamic flux chambers: results from seasonal field campaigns in a real site (UNIPA)

Contributors

D. Di Trapani, G. Viviani, A. Cosenza, F. De Marines, M. Russo Tiesi (University of Palermo)

I. Verginelli (University of Rome Tor Vergata)

F. Villani, S. Frisario, A. Modica (Eni Rewind)

4.18.1 Introduction

The contamination of environmental matrices represents nowadays a major concern due to the potential risk to humans, water, ecosystems or other receptors (Islam et al., 2017). Soil pollution due to petroleum hydrocarbons represents a major threat affecting soils globally mainly due by the mutagenic, carcinogenic, and toxic characteristics of such contaminants (Gidudu and Chirwa, 2020). Health Risk Analysis (HRA) procedure provides a quantitative assessment of the risk representing a useful tool to manage the risk. Indeed, depending on the severity of the risk as well as on current or planned use, the contaminated site might be subject to risk management measures, represented by remediation and/or security actions.

The Italian Legislation that regulates the reclamation of contaminated sites (Legislative Decree No. 152/2006) establishes the operational procedure aimed at verifying the actual level of contamination of a site and its eventual classification as “contaminated site” due to the potential risk to humans and/or water systems. The latter derives from the application a HRA carried out in agreement to the ASTM Standard (ASTM, 2000). The site investigation is of paramount importance since it implies the collection of prominent site-specific data and information about the contamination level, the pollutants migration pathways and the target exposure, thus enabling the build-up of an accurate Conceptual Site Model (CSM). This aspect is of particular concern in case of volatile organic compounds (VOCs) in soil of groundwater, such as petroleum hydrocarbons, since the vapor transport assumes a major role for the assessment of health risk for the selected targets, referring to inhalation pathway.

Traditionally, the applied “fate&transport” models are in general non-reactive diffusive, not considering the recurrence of reactive phenomena, related to biodegradation in the subsurface (Verginelli et al., 2018). In this light, the direct measurement of volatile compound emissions from the subsurface is becoming increasingly important in site contamination assessment procedures, both within human health risk assessment and in the design of remediation measures and subsequent post-remediation monitoring (Di Trapani et al., 2025).

The SNPA Guidelines 15/2018, “Design of Vapor Monitoring at Contaminated Sites”, include flux chambers among the applicable techniques for soil gas monitoring at sites contaminated by volatile compounds. Open dynamic flux chambers are instruments that allow the estimation of fluxes of volatile pollutants emitted from the subsurface, providing a direct measurement of emissions to the atmosphere. Such measurements play a key role in risk assessment, as they enable the determination of actual emissions of volatile substances from the subsurface, overcoming estimates based on conservative models generally adopted in assessments derived from concentrations measured in soils and groundwater.

Within this framework, the objective of the present study was to evaluate the performance of three different types of dynamic flux chambers for the measurement of VOC emissions from the subsurface of a site located in southern Italy. The study was conducted in an area characterized by the presence of aromatic hydrocarbons and volatile organochlorinated compounds in the subsurface, through the implementation of two monitoring campaigns carried out in two different seasons. This report describes the activities performed during the monitoring campaigns and presents and discusses the results obtained.

4.18.2 Description of case study and experimental campaigns

Monitoring activities were carried out at an Italian site characterized by the presence of aromatic hydrocarbon compounds and volatile organochlorinated compounds in the subsurface (Figure 1).

The campaigns involved three monitoring points, identified as Point 1, Point 2, and Point 3, at which different types of commercially available dynamic flux chambers were deployed (whose characteristics are described in more detail below):

- Point 1: dynamic chamber 1 (DC1);
- Point 2: dynamic chamber 2 (DC2);
- Point 3: dynamic chamber 3 (DC3).

To assess the potential effect of seasonality on VOC flux measurements, the monitoring activities were structured into two separate campaigns conducted during periods of the year characterized by different environmental conditions. Specifically, the first campaign was carried out in July 2025, representative of summer conditions, while the second campaign was conducted in October 2025, representative of autumn conditions. During the campaigns, repeated measurements were performed throughout the day to obtain a mean value (with associated uncertainty) of the daily average fluxes.

It is worth noting that the flux chamber identified as DC1 is of property of Palermo University and was purposely purchased within the RETURN Project.

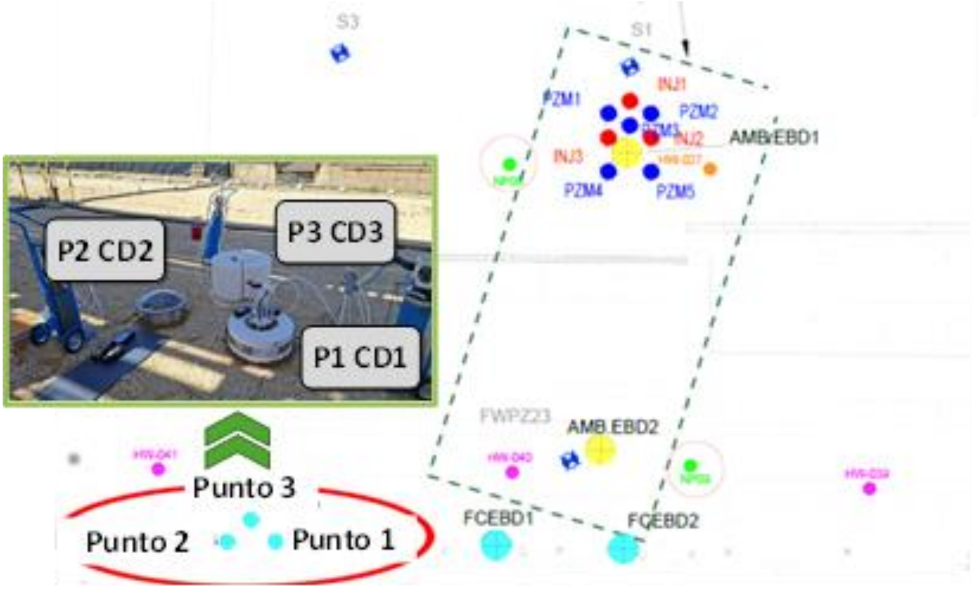

Figure 1. Panoramic view of the sampling area and location of the monitoring points.

The monitoring strategy adopted an integrated approach, including an initial screening using a static accumulation chamber, followed by the quantification of individual VOC fluxes by means of different types of dynamic flux chambers. In the following Figure 2 a panoramic view of the monitory area prepared for the monitoring campaigns carried out in summer (Figure 2a) and autumn (Figure 2b), respectively, is reported.

Figure 2. Panoramic view of the sampling area during summer (a) and autumn (b) campaign.

Specifically, in the area selected for the experimental activities, accumulation chamber measurements were carried out in accordance with the SNPA Guideline 15/2018, by establishing a grid of points around the main point of interest. At the end of the screening phase, three monitoring points were identified for the deployment of the dynamic flux chambers. Prior to sampling, the chambers were purged for approximately one hour until stabilization of the environmental parameters was achieved. Sampling during both campaigns was performed using vacuum bottles at −30 bar. In Figure 3 a particular of the vacuum bottle is shown.

Figure 3. Detail of a vacuum bottle used for gas sampling

4.18.3 Description of the flux chambers used

4.18.3.1 Static accumulation chamber

The static accumulation chamber used for screening measurements consists of a Teflon-coated steel chamber with a bell-shaped structure, 20 cm in diameter and with a volume of approximately 3.4 L. The chamber is closed at the top and connected to an external enclosure housing a rechargeable battery, a gas recirculation pump, gas analyzers (PID and IR sensors), and the control electronics for data acquisition and transfer via Bluetooth connection. Figure 4 shows the static accumulation chamber used during the screening phases.

The operating principle of the static accumulation chamber is based on the extraction of gases present inside the chamber by means of a recirculation pump, which directs the flow toward non-destructive sensors (specifically IR for CO_2 and PID for VOCs). After the VOC and CO_2 concentrations are measured, the gases are reintroduced into the chamber. Under these conditions, the gas concentration inside the measurement volume increases over time according to an approximately linear relationship. Therefore, the emission flux can be determined from the slope of the concentration–time curve according to the following equation (1):

$$F = \left(\frac{dC}{dt}\right) \cdot \frac{V}{A} \tag{1}$$

where:

F: emission flux ($\text{ppm} \cdot s^{-1} \cdot m^{-2}$)

V: volume of the accumulation chamber (m^3)

A: surface area of the chamber in contact with the ground (m^2)

The conversion from ppm to molar fluxes is then performed as a function of environmental parameters (temperature and pressure).

Figure 4. View of the accumulation chamber used during the preliminary screening activities

4.18.3.2 Dynamic flux chambers

During the monitoring campaigns carried out, three different types of dynamic flux chambers were used in order to evaluate the performance of the method through a direct comparison of the results obtained. Figure 5 provides an overview of the three flux chambers employed.

The operating principle of dynamic flux chambers is based on the injection of an inert gas (nitrogen) into the chamber, while an equivalent amount of gas exits through a vent. After several air exchanges (generally 3–4 renewals of the internal volume), the system reaches steady-state conditions.

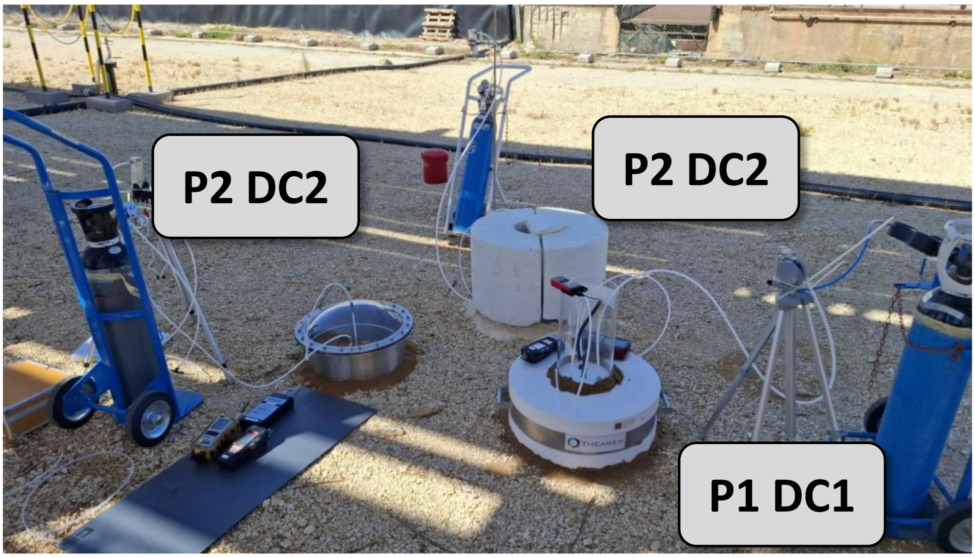

Figure 5. View of the dynamic flux chambers used in the experimental monitoring campaigns

Once the internal conditions have stabilized, gas sampling from the chamber can be performed (in this specific case using vacuum bottles), and the flux of the compounds of interest can be determined according to the following equation (2):

$$F_i = \frac{C_{fc,i} \cdot Q_{in}}{A_{fc}} \tag{2}$$

where:

F_i: emission flux of the i-th compound ($\mu g \cdot m^{-2} \cdot h^{-1}$)

C_{fc,i}: steady-state concentration of the i-th compound ($\mu g \cdot m^{-3}$)

Q_{IN}: flow rate of the carrier gas injected into the chamber ($m^3 \cdot h^{-1}$)

A_{fc}: surface area of the chamber in contact with the ground (m^2)

The dynamic flux chamber identified as DC1 featured a circular cross-section with a flat top, equipped with a wind-shielding system, constructed entirely from inert material (PTFE), with walls and cover of sufficient thickness, and a helical carrier gas injection system. The chamber had an internal diameter of 50 cm and an internal height of 20 cm, corresponding to a usable volume of 39.25 L.

The dynamic flux chamber identified as DC2 was constructed with a vertical section in stainless steel and a dome made of transparent material (polymethyl methacrylate, PMMA). The chamber had an internal diameter of 40 cm, corresponding to a usable volume of 25 L.

The dynamic flux chamber identified as DC3 was externally made of stainless steel and internally lined with a PTFE film. Its geometric characteristics were as follows: internal diameter of 49.5 cm, covered surface area of 0.192 m², internal height of 26.5 cm, corresponding to a usable volume of approximately 41 L. Figure 6 shows a detailed view of the three flux chambers used.

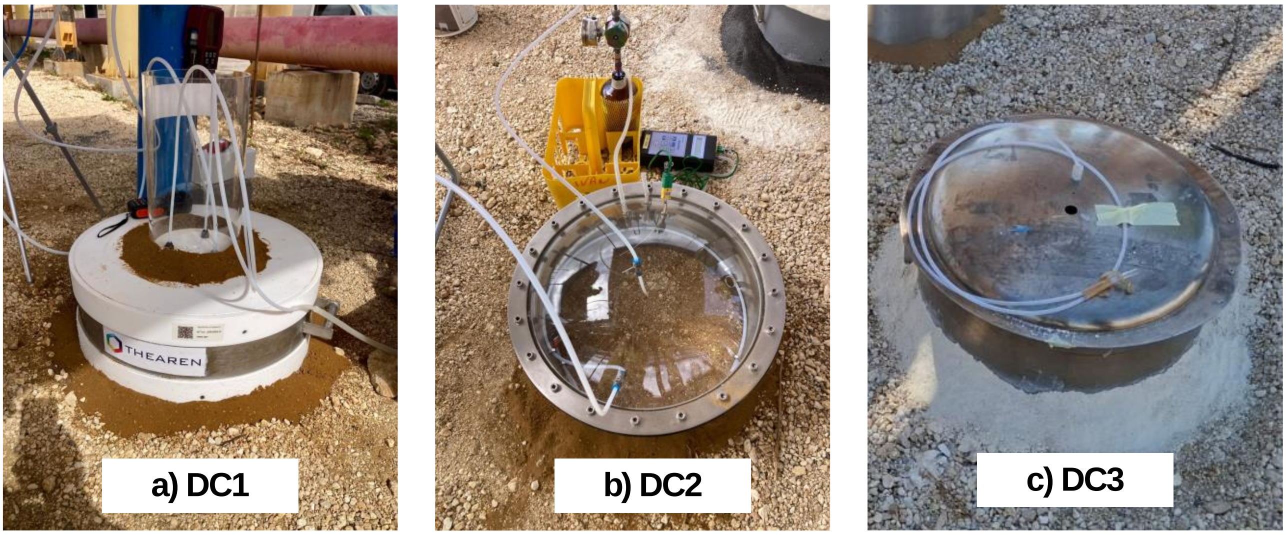

Figure 6. Detailed view of the three different flux chambers used: a) chamber CD1 (property of Palermo University), b) chamber CD2 and c) chamber CD3.

4.18.4 Analytical Methods

Chlorinated organic compounds and aromatic compounds were analysed by the three laboratories using gas chromatography/mass spectrometry (GC/MS) in accordance with EPA Method TO-15A (2019), Category 0, for the determination of volatile organic compounds (VOCs).

With regards to hydrocarbon compounds (aliphatic hydrocarbons C5–C8, aliphatic hydrocarbons C9–C12, and aromatic hydrocarbons C9–C10), these were analysed by gas chromatography/mass spectrometry (GC/MS) in accordance with the MADEP APH 2009 method.

4.18.5 Results

4.18.5.1 Summer field campaign

As discussed, the summer field campaign has been preceded by a preliminary screening characterization of VOC and CO_2 fluxes. The VOC fluxes measured with the static accumulation chamber, as screening analysis, resulted comparable in the three sampling points, thus suggesting a contamination distribution quite homogeneous in the selected monitoring area. (Figure 7).

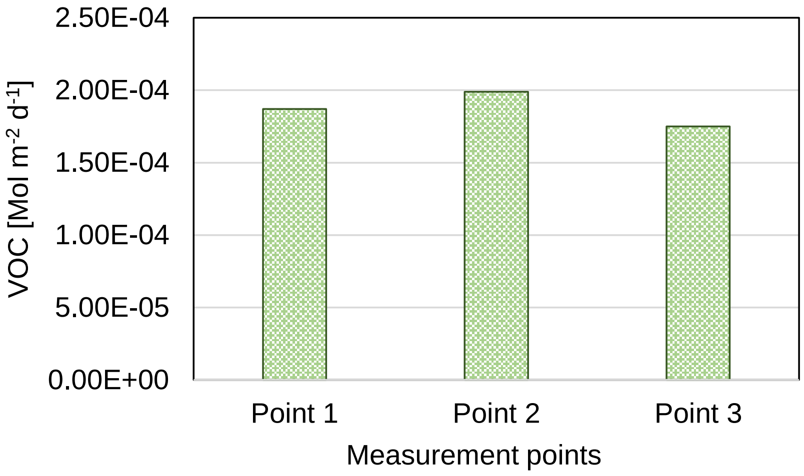

Figure 7. VOC fluxes measure with the static accumulation chamber prior to summer campaign

Figure 8 shows the average values of the measured fluxes for the different target compounds obtained using the various flux chambers employed. The error bars represent the standard deviations associated with the replicates performed during the monitoring campaigns.

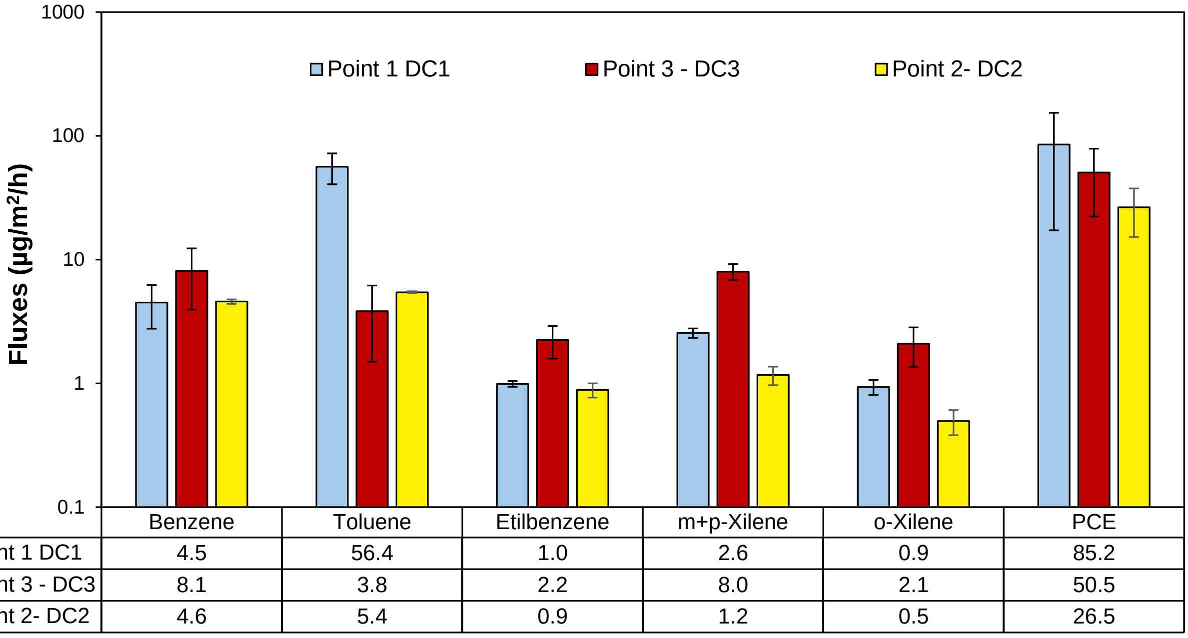

	Benzene	Toluene	Etilbenzene	m+p-Xilene	o-Xilene	PCE
▢ Point 1 DC1	4.5	56.4	1.0	2.6	0.9	85.2
🟥 Point 3 - DC3	8.1	3.8	2.2	8.0	2.1	50.5
🟨 Point 2- DC2	4.6	5.4	0.9	1.2	0.5	26.5

Figure 8. Contaminant fluxes measured with the dynamic chambers in the summer campaign.

The comparison among the mean flux values obtained with the three measurement systems highlights, for most of the analysed compounds, good agreement among the results, which are statistically comparable in terms of mean ± standard deviation. However, some outliers are present for specific compounds (e.g., toluene), showing greater variability among the different systems.

Overall, a slight tendency toward flux underestimation is observed for the CD3 chamber, whereas a slight tendency toward overestimation is associated with the CD2 chamber.

4.18.5.2 Autumn field campaign

As for the summer campaign, also in this case the monitoring of contaminant fluxes has been preceded by screening VOC and CO_2 measurements carried out with a static accumulation chamber. Figure 9 presents the results of the screening conducted during the second monitoring campaign using the accumulation chambers. The outcomes obtained are consistent with those observed during the summer campaign with regards to the preliminary measurements carried out using these devices.

Specifically, the total VOC fluxes measured at the three investigation points remain comparable, indicating a substantially homogeneous distribution of contamination across the surveyed area. However, during the autumn campaign, the total flux values were slightly lower than those recorded in the summer campaign, likely due to differing environmental conditions, particularly temperature and atmospheric pressure, characteristic of the autumn period.

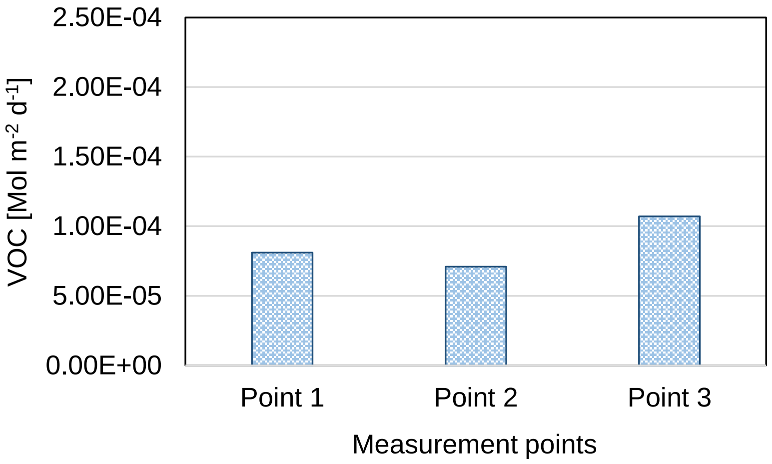

Figure 9. VOC fluxes measure with the static accumulation chamber prior to autumn campaign

Figure 10 shows the average flux values measured for the different target compounds using the various flux chambers employed. The error bars represent the standard deviations associated with the replicates performed during the monitoring campaigns.

In this campaign, the quantitative comparison of the mean fluxes shows greater data variability compared to that observed in the first campaign. Some compounds, in particular o-xylene and PCE, exhibited significant differences among the three systems. Most of these outliers were observed in the fluxes measured with the CD2 chamber, which provided higher values compared to the other systems, whereas the CD3 chamber generally returned lower values, confirming the trend already observed in the results of the summer campaign.

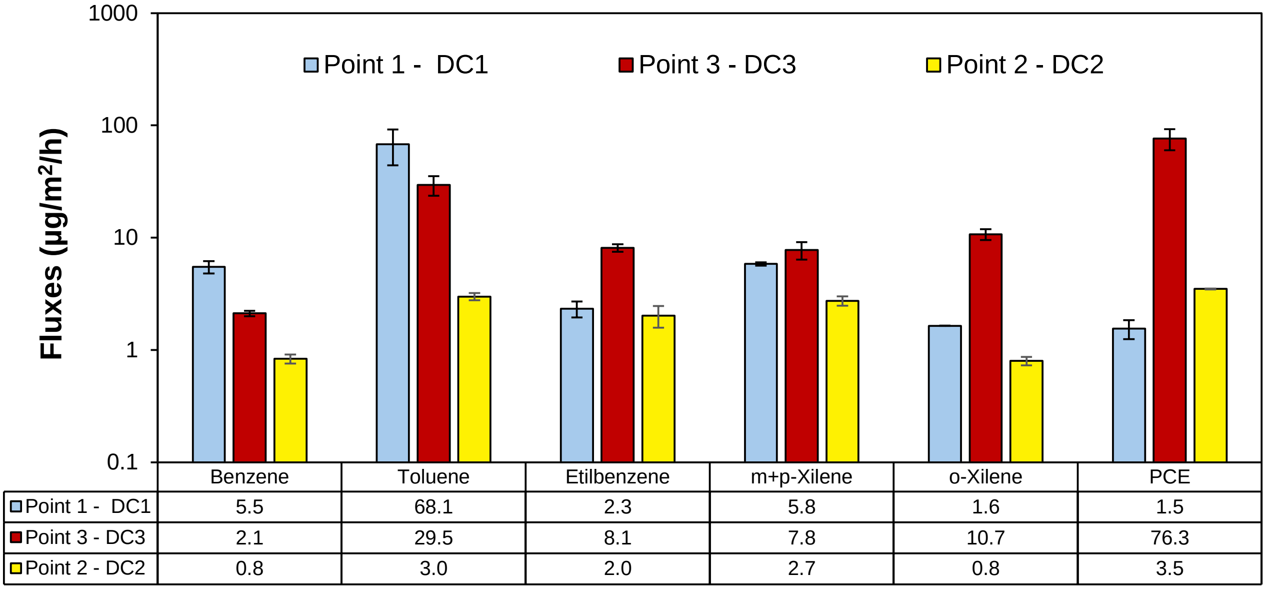

	Benzene	Toluene	Etilbenzene	m+p-Xilene	o-Xilene	PCE
Point 1 - DC1	5.5	68.1	2.3	5.8	1.6	1.5
Point 3 - DC3	2.1	29.5	8.1	7.8	10.7	76.3
Point 2 - DC2	0.8	3.0	2.0	2.7	0.8	3.5

Figure 10. Contaminant fluxes measured with the dynamic chambers in the autumn campaign.

4.18.6 Discussion of the results achieved

Tables 1 and 2 report the average emission fluxes for the target compounds measured during the two monitoring campaigns (July 2025 and October 2025) using the three types of dynamic flux chambers. For each compound and system, mean values and standard deviations are provided, reflecting intra-day measurement variability.

Table 1. Comparison of the fluxes (average values) measured with the different flux chambers in the summer campaign (± standard deviation)

Summer campaign				
Compound	**Units**	**Point 1 DC1 (UNIPA)**	**Point 2 DC2**	**Point 3 DC3**
Benzene	µg/m²/h	4.5 ± 1.7	8.1 ± 4.2	4.6 ± 0.2
Toluene	µg/m²/h	56.4 ± 15.7	3.8 ± 2.3	5.4 ± 0.1
Etilbenzene	µg/m²/h	1.0 ± 0.1	2.2 ± 0.7	0.9 ± 0.1
m+p-Xilene	µg/m²/h	2.6 ± 0.2	8.0 ± 1.2	1.2 ± 0.2
o-Xilene	µg/m²/h	0.9 ± 0.1	2.1 ± 0.7	0.5 ± 0.1
PCE	µg/m²/h	85.2 ± 67.9	50.5 ± 28.3	26.5 ± 11.2

🟩 Same order of magnitude (< factor 3)

🟦 High outlier (> factor 3)

Due to the inherently high variability of VOC fluxes from the subsurface, which typically follow log-normal distributions, measurements were considered consistent if comparable within a factor of 3. This criterion was also used to identify outliers in the tables, distinguishing values higher or lower than those of the other systems. Cells are color-coded as follows: green indicates values within the same order of magnitude (deviation < factor 3), blue indicates higher outliers (> factor 3), and pink (only in the second campaign) indicates lower outliers (> factor 3 below other systems).

In the first campaign, most compounds, including benzene, ethylbenzene, o-xylene, and PCE, exhibited mean fluxes of the same order of magnitude, although some showed high standard deviations, reflecting notable temporal variability. Only two higher outliers were observed: toluene measured with the UNIPA DC1 chamber and m+p-xylene measured with the DC2 chamber, both exceeding the other systems by more than a factor of 3. Such discrepancies are likely due to a combination of factors, including the natural heterogeneity of subsurface VOC release, differences in chamber design, and variations in flow and sampling handling.

Overall, the first campaign data show a slight tendency of the DC3 chamber to report lower fluxes, while the DC2 chamber shows a slight overestimation trend; however, most measurements remain within the defined comparability limits.

The results of the second campaign present an overall similar picture, but with a higher frequency of outliers, reflecting greater variability of emission fluxes during the autumn period. Many of the measured values remain comparable within a factor of 3. However, a total of five outliers were observed in this campaign—three higher and two lower—primarily associated with measurements performed using the DC2 and DC3 chambers.

Table 2. Comparison of the fluxes (average values) measured with the different flux chambers in the autumn campaign (± standard deviation)

Autumn campaign				
Compound	**Units**	**Point 1 DC1 (UNIPA)**	**Point 2 DC2**	**Point 3 DC3**
Benzene	μg/m^2/h	5.5 ± 0.7	2.1 ± 0.1	0.8 ± 0.1
Toluene	μg/m^2/h	68.1 ± 24.1	29.5 ± 5.9	3.0 ± 0.2
Etilbenzene	μg/m^2/h	2.3 ± 0.4	8.1 ± 0.6	2.0 ± 0.4
m+p-Xilene	μg/m^2/h	5.8 ± 0.2	7.8 ± 1.4	2.7 ± 0.3
o-Xilene	μg/m^2/h	1.6 ± 0.0	10.7 ± 1.2	0.8 ± 0.1
PCE	μg/m^2/h	1.5 ± 0.3	76.3 ± 16.3	3.5 ± 0.0

🟩 Same order of magnitude (< factor 3)

🟦 High outlier (> factor 3)

🟪 Low outlier (> factor 3)

Specifically, for certain aromatic compounds (e.g., ethylbenzene and o-xylene) and PCE, the DC2 chamber produced substantially higher values compared to the other systems, while the DC3 chamber showed lower values for some parameters (e.g., benzene and toluene). These differences are consistent with observations from the first campaign and further indicate a modest tendency for the two systems to overestimate and underestimate fluxes, respectively.

Overall, the comparative analysis of the two campaigns indicates that the three types of dynamic flux chambers generally provide comparable results, particularly when interpreted in light of the high intrinsic variability of VOC emission fluxes from the subsurface. The observed discrepancies, including the occurrence of outliers, are consistent with the complexity of the phenomenon under investigation and with the constructional and operational differences among the measurement systems.

4.18.7 Conclusions

The emission profiles obtained using the three types of dynamic flux chambers were largely consistent in terms of identified compounds, with minor differences attributable to the different limits of quantification achieved by the participating laboratories. Concentrations above the LOQ for BTEX and PCE were detected by all systems, enabling a robust comparison of chamber performance.

Given the high intrinsic variability of subsurface VOC emission fluxes, typically described by log-normal distributions, and considering the spatial separation of the measurement points, fluxes were considered comparable when within the same order of magnitude (factor of 3). Based on this criterion, approximately 80% of the measured data were comparable across systems. Outliers (≈20% of the dataset) were mainly observed during the second monitoring campaign and were predominantly associated with the DC2 and DC3 chambers.

Across both campaigns, a slight tendency toward flux overestimation by the CD2 chamber and underestimation by the CD3 chamber was observed. However, these differences remain consistent with the inherent complexity of VOC emissions from the subsurface and with constructional and operational differences among the chambers, including materials, potential memory effects, and gas injection, mixing, and venting configurations.

Overall, despite the limited number of monitoring campaigns, the results demonstrate good general reliability of dynamic flux chambers for direct measurement of subsurface VOC emissions, supporting their application in contaminated site characterization and human health risk assessment.

4.18.8 Scientific products and dissemination

Di Trapani, D.; Bifulco, S.; Capodici, M.; Cosenza, A.; De Marines, F.; Farina, M.; Verginelli, I.; Viviani, G. Direct Measurements of Petroleum Hydrocarbon Vapors in the Risk Assessment Procedure: The Case of a Contaminated Italian Site. Sustainability 2025, 17, 4189. https://doi.org/10.3390/su17094189.

Di Trapani, D., Multiscale modeling framework for contaminants transport and reaction with uncertainty quantificationIn: Lipizer, M., Solidoro, C., & Tognolli, A. (2025, dicembre 9). Spoke 4 Degrado ambientale. Sintesi dei risultati ottenuti. Book of Abstracts: Spoke 4 Degrado Ambientale. Sintesi Dei Risultati Ottenuti. https://doi.org/10.5281/zenodo.17864607.

Di Trapani Daniele, Cosenza Alida, De Marines Federica, Frisario Silvia, Modica Alfonso, Verginelli Iason, Villani Federico, Viviani Gaspare. Direct Measurements of Vapour Emissions in Contaminated Site by Means of Dynamic Flux Chambers: the Case Study of an Italian Site. Poster Session in Return Final Meeting: Comunicazione, Disseminazione e Valorizzazione dei Risultati. 3-5 dicembre 2025. Napoli (NA).

Di Trapani, D., Cosenza, A., De Marines, F., Frisario S.A., Modica, A., Verginelli, I., Villani, F., Viviani, G. MONITORAGGIO DI FLUSSI EMISSIVI IN UN SITO ITALIANO: CONFRONTO TRA DIVERSE TIPOLOGIE DI CAMERE DI FLUSSO DINAMICHE. In Sicon 2026: Esperienze negli interventi di risanamento. Rome, 11-13 February 2026. ISBN: 978-88-7850-030-3

Acknowledgements

Authors warmly thank Dr. Luca Spinelli for his precious contribution during field operations and data processing.

References

ASTM. Standard Guide for Risk-Based Corrective Action, Designation: E-2081-00. 2000. Available online: https://store.astm.org/e2081-22.html (accessed on 20 January 2026).

Di Trapani, D.; Bifulco, S.; Capodici, M.; Cosenza, A.; De Marines, F.; Farina, M.; Verginelli, I.; Viviani, G. Direct Measurements of Petroleum Hydrocarbon Vapors in the Risk Assessment Procedure: The Case of a Contaminated Italian Site. Sustainability 2025, 17, 4189. https://doi.org/10.3390/su17094189.

Gidudu, B.; M. Nkhalambayausi Chirwa, E. Application of Biosurfactants and Pulsating Electrode Configurations as Potential Enhancers for Electrokinetic Remediation of Petrochemical Contaminated Soil. Sustainability 2020, 12, 5613. https://doi.org/10.3390/su12145613.

Islam, M.N.; Jung, S.K.; Jung, H.-Y.; Park, J.-H. The feasibility of recovering oil from contaminated soil at petroleum oil spill site using a subcritical water extraction technology. Process Saf. Environ. Prot. 2017, 111, 52–59. https://doi.org/10.1016/j.psep.2017.06.015.

Legislative Decree N: 152/2006; Norme in materia ambientale (G.U. n. 88 14 aprile 2006). Istituto Poligrafico e Zecca dello Stato: Roma, Italy, 2006 (In Italian).

SNPA. Progettazione del monitoraggio dei vapori nei siti contaminati; Linea Guida SNPA 15/2018; SNPA: Roma, Italy, 2018; ISBN978-88-448-0922-5 (In Italian).

Verginelli, I.; Pecoraro, R.; Baciocchi, R. Using dynamic flux chambers to estimate the natural attenuation rates in the subsurface at petroleum contaminated sites. Sci. Total Environ. 2018, 619–620, 470–479. https://doi.org/10.1016/j.scitotenv.2017.11.100